SPATIAL AND SEASONAL VARIATION IN THE PERFORMANCE OF ALGORITHMS FOR DERIVING IN-WATER PROPERTIES FROM OCEAN COLOUR

by

Anthony Guy Westbrook, BSc. Hons.

A thesis submitted to the University of Plymouth in partial fulfilment of the requirements for admittance to the degree of

DOCTOR OF PHILOSOPHY

Undertaken at:

Institute of Marine Studies
University of Plymouth
Faculty of Science
Drake Circus
Plymouth
Devon
UK
PL4 8AA

In collaboration with:

Natural Environment Research Council
Centre for Coastal and Marine Sciences
Plymouth Marine Laboratory
Prospect Place
West Hoe
Plymouth
Devon
UK
PL4 3DH

March 2000

ABSTRACT

SPATIAL AND SEASONAL VARIATION IN THE PERFORMANCE OF ALGORITHMS FOR DERIVING IN-WATER PROPERTIES FROM OCEAN COLOUR

Anthony Guy Westbrook, BSc. Hons.

The on-going calibration and validation of visible satellite imagery remains a core activity of the scientific community in pursuit of high quality data characterising the oceanic chlorophyll field, providing input to models assessing primary productivity and the potential role of the oceans in climatic regulation. This work serves to examine the operational characteristics of semi-analytical algorithms that are designed to derive key optical properties from space born observations of ocean colour.

The collection of water samples contemporaneously with precision profiled radiometry conforming to similar spectral bands to those of the NASA Sea Viewing Wide Field of view Sensor (SeaWiFS) was planned and executed, with appropriate field sampling techniques developed in accordance with the SeaWiFS Ocean Optics protocols (Mueller and Austin, 1995). Data were collected during extensive fieldwork sampling at a near coastal survey site and during two deep Atlantic research programmes.

Historical and recently developed algorithms designed to retrieve the diffuse attenuation coefficient at 490*nm* and chlorophyll-*a* pigment concentrations from upwelling radiances were applied to the optical data, to compare the mathematically retrieved in-water properties with the values measured *in-situ*. The radiometric data were then used to generate general and local algorithm modifications to assess possible differences in the mathematically retrieved values. Statistical analyses of the errors in mathematical retrieval of in-water properties identified structured variability resulting from the empirical approach to algorithm generation, supporting the point of view that locally constrained algorithms provide a method of achieving significantly improved results.

The problems associated with the derivation of semi-analytical algorithms are then discussed and errors analysed. The new algorithms generated here are found to compare well with their source data and with work by other investigators. Systematic variability was found within the data sets and the affect this has on the determinations is discussed.

It is suggested that data users be afforded details of the equations employed in the production of readily available remote sensing products, placing them in a position where they are better able to assess the data in the context of their work.

CONTENTS

LIST OF FIGURES

LIST OF TABLES

ACKNOWLEDGEMENTS

I am glad of this opportunity to express my gratitude to a number of people for their help and support during this study; without them, much of this work could not have been attempted, let alone bought to a satisfactory conclusion.

I thank my supervisors Dr. D. A. Pilgrim (University of Plymouth) and Prof. J. Aiken (Plymouth Marine Laboratory) for their advice, guidance, and encouragement. I am particularly indebted to Dr. Aiken for resourcing my work and enabling access to the PML research vessel *RV Squilla*, and particularly for placing his trust in me, supporting my participation in the two oceanographic cruises undertaken: AMT-1 on *RRS James Clark Ross*, and PRIME on *RRS Discovery*.

I am also indebted to Dr R. Barlow, Dr. A. J. Bayle, Mr. G. F. Moore, Dr. S. Lavender, Dr. C. Gallienne, Mr. M. Pinkerton, Mr. N. Rees and Dr. S. Gibb for their general help and discussion during the course of my training and research. Dr. S. Gibb in particular for supplying the PRIME core pigment data set. My thanks must also go to Ms. Georgina Spyres who was an enthusiastic participant in the DOC experiments undertaken in the Plymouth Sound area.

I am indebted to Dr. Stanford B. Hooker of NASA for his guidance and for funding my trip to CHORS (San-Diego), and to Dr. C. Trees for his hospitality and assistance with the AMT-1 HPLC pigment analysis once there.

I thank the Masters and crews of *RV Squilla*, *RRS James Clark Ross* and *RRS Discovery* for their professionalism and flexibility during the fieldwork programmes.

My thanks must also go to my friends and family for their never ending encouragement, and for always pretending to be impressed by my exploits.

My fondest thanks go to Penny for support far beyond that which I had any right to expect during the writing up of this project.

And to Megan, Bronwyn and Mark, who mean more to me than they will ever know.

DECLARATIONS

At no time during the registration for the degree of Doctor of Philosophy has the author been registered for any other University award.

This study was financed with the aid of a studentship from the Natural Environment Research Council (NERC) and carried out in collaboration with Plymouth Marine Laboratory (PML).

A programme of advanced study was undertaken which included, at the University and PML, the development of advanced computing skills for the logging and subsequent analysis of large data sets, as well as knowledge of the hardware required for the study. Experience of shipboard techniques was gained during two deep sea cruises and an intense period of inshore work.

Regular scientific meetings were attended at which work was presented and or discussed; nineteen main scientific meetings were attended, ten conferences/workshops were attended at which 9 talks/papers/posters were presented and ten papers/abstracts were published or have been submitted or are in press. Eight contract reports have been submitted and accepted. A contribution to a text book 'Optical techniques in Oceanography' is in preparation.

PUBLICATIONS:

Robins, D.B., Bale A.J., Moore G.F., Rees N. W., Hooker S.B., Gallienne C.P., Westbrook A.G., Maranon E., Spooner W.H., and Laney S.R., (1996): AMT-1 Cruise Report and Preliminary Results. NASA Technical memorandum 104566, Vol. 35, Hooker S.B. and Firestone E.R., eds. NASA Goddard Space Flight Centre, Greenbelt, Maryland, 87 pp.

Lavender S., Westbrook A.G., Moore G.F. and Bottrell H., (1996). Plymouth Atmospheric Correction Experiment (PACE), 23rd International Remote Sensing Society Conference, Reading, UK. 8pp.

Aiken J, Bale A. J., Barlow R. G., Holligan P., Hooker S. B., Moore G. F., Trees C. C., Westbrook A. G., (1997). Phytoplankton pigment determination, inter-province pigment and bio-optical variability: implications for the accuracy of remote sensing algorithms of ocean colour. SeaWiFS workshop, January 1997.

Lavender S., Westbrook A.G., Aiken J. and Pilgrim D.A., (1997). The derivation of water leaving radiances during PACE. Proceedings of the Third International Remote Sensing Conference, Copenhagen, Denmark. 6pp.

Westbrook A.G., Pilgrim D.A. and Aiken J., (199X). Seasonal study of the diffuse attenuation coefficient in the Western English Channel. Journal of Optics, submitted.

Westbrook A.G., Pinkerton M.P., Aiken J. and Pilgrim D.A., (1999). Simulated Performance of remote sensing ocean colour algorithms during the 1996 PRIME cruise. Deep Sea Research PRIME special issue, accepted.

Westbrook A. G., Aiken J. and Pilgrim D.A., (1998). Spatial variation in the performance of algorithms for the interpretation of remotely sensed measurements of ocean colour during the first Atlantic Meridional Transect (AMT-1). Applied Optics and Optoelectronics, Proceedings of the Applied Optics Divisional Conference of The Institute of Physics, Brighton (talk, paper bound in proceedings). 6pp.

Ludbrook G.D., Scott A.M., Westbrook A.G, Aiken J. and Lavender, S.J., (1998). Coincident LIDAR, Satellite and surface measurements of the optical properties of UK littoral waters. Applied Optics and Optoelectronics, Proceedings of the Applied Optics Divisional Conference of The Institute of Physics, Brighton (talk, bound in abstract book).

Aiken J., Hooker S., Moore G., Westbrook G., Gibb S. & Cummings D., (1998). Validation of the SeaWiFS operational algorithm for phytoplankton pigment concentrations. Applied Optics and Optoelectronics, Proceedings of the Applied Optics Divisional Conference of The Institute of Physics, Brighton (talk, bound in abstract book).

Aiken J., Hooker S., Moore G. & Westbrook G., (1998). Validation of the SeaWiFS pre launch algorithm for the diffuse attenuation coefficient. Applied Optics and Optoelectronics, Proceedings of the Applied Optics Divisional Conference of The Institute of Physics, Brighton (talk, bound in abstract book).

TECHNICAL REPORTS:

Defence Evaluation and Research Agency (DRA Malvern)

Report 1: Presentation of Results

Westbrook A.G. and Aiken J., (June 1997). OBANEX- Field log and preliminary data report.

Report 2: Data processing

Westbrook A.G. and Aiken J., (August 1997). OBANEX - Results of preliminary data processing, 14pp.

Report 3 (final): Data analysis

Westbrook A.G. and Aiken J., (February 1998). OBANEX: analysis of results, 21pp.

Defence Evaluation and Research Agency (DRA Winfrith)

The determination of Seawater Optical Properties from Satellite Remote Sensors

Report 2:

Aiken J., Westbrook A.G., Moore G.F., (Period April 1st. 1997 to 31 March 1998). Report: Optical Algorithms, contract SSDW1/443, 50pp.

Report 3:

Aiken J., Westbrook A.G., Pinkerton M. and Moore G.F., (November 1998). Optical properties of Celtic sea littoral waters: Yr. 2 progress report, contract SSDW1/443, Period April 1st. 1998 to 30 November 1998. 10pp.

EUROPEAN UNION CONTRACT REPORTS

Pinkerton M., Westbrook A.G., Aiken J. and Moore G.F., (November 1998). Concertation on European validation experiment for coastal shelf water remote sensing (CEVEx), final report. 17pp.

Pinkerton M., Westbrook A.G., Aiken J. and Moore G.F., (November 1998). Coastal region long term measurement for colour remote sensing development and validation (COLORS) annual report. 8pp.

Pinkerton M., Westbrook A.G., Aiken J. and Moore G.F., (November 1998). Coastal Surveillance through Observations of Ocean Colour (Coast/ooc): annual report, 4pp.

SUMMARY OF CONFERENCES / MEETINGS / PLANNING MEETINGS ATTENDED:

1. London 1994 - Royal Society meeting of the participants of the Joint Global Ocean Flux Study, JGOFS, programme, London, UK. October 1994 (attended).

2. UoP 1995 - A meeting of the Participants of the Plymouth Environmental Research Consultancy, PERC, University of Plymouth, March 1995. Presented preliminary results from the radiometry component of a structural survey of the tidal plume emanating from the river Teign, South Devon (talk, presentation of data).

3. Southampton 1995 - SeaWiFS Exploitation Initiative, SEI, meeting of special topic participants and principal investigators. James Reynolds Centre, Southampton, UK. March 1995 (attended).

4. Plymouth - First Atlantic Meridional Transect workshop, Plymouth, Devon, UK. February 1996. Presented preliminary analyses of the AMT-1 cruise HPLC pigment data (presentation and poster).

5. North Wales - First PRIME cruise workshop, Plas Menai, Bangor, North Wales, UK. December 1996. Presented the preliminary results of the optical work undertaken during the second half of the trip (talk).

6. Plymouth - The Second AMT workshop, Plymouth, Devon, UK. February 1997. Participant in discussions regarding future biological sampling strategies (attended, participated in discussion group).

7. Aberdeen June 1997 - Meeting of the Institute of Physics, University of Aberdeen, Scotland, UK. Presented paper: Seasonal study of the diffuse attenuation coefficient in the Western English channel (talk).

8. Copenhagen 1997- Presented poster: The derivation of water leaving radiances during PACE, at the Third International Remote Sensing Conference, Copenhagen, Denmark.

9. PML August 1997- A meeting with personnel from the Defence Evaluation and Research agency, DERA. Presented the second data analysis report arising from the LIDAR ground truthing exercise carried out on board *RV Calanus* out of Dunstafnage Marine Laboratory, Oban (Presentation of results and discussion of future data analysis).

10. Bristol September 1997 - Second PRIME cruise workshop, Bristol University, UK. Presented and submitted the paper: Spatial performance of algorithms for the remote sensing of ocean colour during the 1996 PRIME cruise (talk, participated in synthesis paper discussion group, submitted paper for publication in Deep Sea Research).

11. Brighton March 1998 - Institute of Physics conference 'Ocean Optics 3' in Brighton, presented 3 papers.

12. DRA Winfrith February 1998 - A meeting with personnel from the Defence Evaluation and Research agency (DERA). Discussion of on going PML contract: determination of optical properties of coastal waters.

13. DRA Malvern March 1998 - Discussion with personnel from the Defence Evaluation and Research agency (DERA) regarding a proposal to undertake research into the location of sub-surface inhomoginaity in physical structure using air borne multi-spectral imagery. Discussion of proposed research.

14. Italy (Venice) May 1998 - Participated in EU project: Concertation on European validation experiment for coastal shelf water remote sensing (CEVEx). Travelled to the Joint Research Centre (Ispra) then on to Venice to carry out an inter-comparison with JRC personnel into radiometric deployment techniques at the 'Aqua Alta' facility outside the Venetian lagoon.

15. PML 1998 - Assisting with the planning and procurement of sampling equipment and techniques in support of the biological sampling of the 7$^{th.}$ Atlantic Meridional Transect, providing instruction where required.

16. Plymouth 1998 - Participation in the planning and execution of the Coastlooc helicopter remote sensing campaign. Organised and directed ship operations, co-ordinating personnel; prepared and executed optical and water sampling.

17. PML October 1998 - Planning and execution of the EU project: Coastal region long term measurement for colour remote sensing development and validation, COLORS, (project continues to October 2000). Participation in the design, planning and execution of the bio-optical field sampling.

18. PML October 1998 - Planning and execution of field sampling from the upper reaches of the Tamar estuary to the mouth of the river at the Plymouth breakwater. A range of data were collected by a team of 5 scientists plus two crew on board the PML/MBA research vessel *RV Tamaris*. The objective was to characterise the dissolved organic component of the waters sampled in terms of UV absorption. A comprehensive suite of ancillary measurements were collected. This experiment is being written up and will be presented for peer review and publication.

19. Italy (JRC-Ispra) October 1998 – Field sampling methodology workshop in support of COLORS. Participation in the planning and execution of the bio-optical field sampling with particular reference to inter calibration techniques of the Wetlabs *ac*-9 multi channel transmissometer.

Signed. A. G. Wetbrook .....Date. 21/3/00

1. AIMS AND OBJECTIVES

The research presented in this thesis was undertaken through the sponsorship of the Natural Environment Research Council (NERC) as part of the SeaWiFS Exploitation Initiative (SEI). The work was funded in recognition of the importance to the research community of continued investigation into the quality of satellite derived observations of key bio-optical parameters of the surface mixed layer that may be determined by satellite remote sensing.

The aim of this project is to optimise the performance of published algorithms used to derive specific remotely sensed products from the colour of the oceans. Several algorithms are available (for features such as the 490*nm* diffuse attenuation coefficient and chlorophyll-*a*) but they are spatially and temporally limited. In order to address these limitations this project will:

- Collect high quality bio-optical data for use within the algorithms;
- Use that data to construct the empirical relationship between the in-water parameters and the radiometric input;
- Assess the error distribution between the retrieved and measured variables to compare existing and new algorithms (which have arisen from this work) and to describe any improvement.
- In addition, using the approach to pigment grouping by Bidigare *et al.* (1990), and analysis by Aiken *et al.* (1995), investigate the influence of pigment groups other than chlorophyll-*a* on ocean colour and the feasibility of retrieving these parameters from the radiometry.

1.1 Introduction

The activities of mankind are changing the atmospheric concentration and distribution of greenhouse gases and aerosols. This can produce a radiative forcing by changing the characteristic reflection or absorption patterns of solar radiation by the Earth's surface and atmosphere, or the consequent emission and absorption of terrestrial radiation (Houghton *et al.*, 1996). One such gas is carbon dioxide, CO_2.

Away from the influence of land, the many hued nature of the ocean surface when viewed remotely results from the presence and activities of microscopic organisms that make up the base of the marine food chain (Aiken *et al.* 1992; Kirk, 1994; Ikeda and Dobson, 1995). The autotrophic organisms that make up the phytoplankton use CO_2, one of the building blocks of life, through its role in the process of photosynthesis (Williamson, 1990; Hall and Rao, 1991; Hooker *et al.*, 1992; Kirk, 1994). Increasing atmospheric concentrations of CO_2 could cause enhanced growth in marine primary producers, with associated increases in carbon fixation and the subsequent removal of excess CO_2 from the atmosphere (Williamson, 1990; Watson *et al.*, 1991; Aiken *et al.*, 1992; Robins *et al.*, 1996).

The greenhouse effect is a natural process that keeps the planet Earth in moderate temperature regulation, as without heat-absorbing gases in the atmosphere the average surface temperature would be 33°C colder than the present figure which, excluding Antarctica, is 15°C (Williamson, 1990; Houghton *et al.*, 1996).

The CO_2 concentration in the atmosphere has increased markedly over the past 100 years due to anthropogenic inputs; an observed increase of 50ppmv (from 310ppmv to 360ppmv) has been observed between 1955 and 1995 at Mauna Loa, Hawaii (Asrar and Greenstone, 1995). Aided by contributions from other

greenhouse gases, such as methane, nitrous oxide, halocarbons and ozone, this trend is continuing at a rate which is expected to produce significant world-wide warming of between 0.9 and 3.5°C by the year 2100. Even the lower projection requires an average rise greater than any seen in the last 10,000 years (Houghton *et al.*, 1996). CO_2 is removed from the atmosphere by a number of processes that operate on different time scales, and is subsequently transferred to various reservoirs, some of which eventually return it to the atmosphere (Houghton *et al.*, 1996). The fastest process is the uptake by vegetation in the terrestrial and marine biosphere, with long term removal of part of this CO_2 to the ultimate sink, the deep ocean sediments. Carbon is fixed in plant and animal material through primary and secondary production then by the processes of deep-water chemistry, ecology and sedimentation (Lalli and Parsons, 1997).

The two major bio-optical variables derived from ocean colour data are the near-surface chlorophyll-*a* concentration, units: $mg\ m^{-3}$, and the diffuse attenuation coefficient at 490*nm*, *Kd*(490*nm*), units: m^{-1}. The former parameter leads to maps of global phytoplankton distributions which can be used as data input for models to estimate the role of the oceans in the regulation of atmospheric CO_2 (Aiken *et al.*, 1992). *Kd*(490*nm*) describes the biologically mediated absorption of light within the surface layers of the sea; a high attenuation coefficient means that light is absorbed rapidly with depth as a result of material in the water. This process can cause significant heating and affect the physical structure of the upper water-column (Sathyendranath *et al.*, 1991). Research by Zaneveld *et al.* (1993) indicates that *Kd*(490*nm*) can also be used to estimate the depth of the euphotic zone, at which the downwelling photosynthetically available radiation (PAR)

between 400-700*nm*, has fallen to 1% of its surface value (Morel and Berthon, 1989).

The birth of satellite oceanography was probably in August 1964 at Woods Hole Oceanographic Institute (WHOI) when a meeting entitled "Oceanography from Space" was held. After various experiments, the Coastal Zone Colour Scanner, CZCS, was incorporated into the NIMBUS-7 satellite which was operational from 1978 until 1986. This was the first dedicated ocean colour viewing system which was intended as a proof of concept sensor only but produced a time series of global imagery with an accompanying ground truthing calibration and validation effort (a process where by remotely sensed observations are matched with contemporaneous observations made *in-situ*). This extended beyond its anticipated operational phase (Austin and Petzold, 1981; Clark, 1981; Holligan *et al.*, 1989).

The success of the CZCS mission set the scene for future ocean colour viewing satellites. The Modular Optoelectronic Scanner (MOS), designed and built by the Institute for Space Research (Germany), was launched 21 March 1996 onboard the Indian Remote sensing Satellite (IRS-P3), and has been providing colour imagery over 17 spectral channels covering the visible and infra red, IR. The repeat cycle is 24 days and the satellite is not dedicated solely to ocean colour viewing as it also carries sensors dedicated to extra terrestrial research.

The Ocean Colour Temperature Scanner (OCTS) was launched by the National Space Development Agency of Japan (NASDA) on board the Advanced Earth Observing Satellite (ADEOS). This sensor successfully collected ocean colour data from August 17 1996 until June 30 1997 when a power failure prematurely ended the mission. The OCTS radiometer had eight narrow spectral bands in the visible and 4 in the IR, with a repeat cycle of three days.

The National Aeronautic and Space Administration (NASA) Sea viewing Wide-Field-of-view Sensor (SeaWiFS), carried on the ORBIMAGE 2 satellite, was successfully deployed in August 1997 and the first images were received during September of the same year. The radiometer has eight narrow spectral bands, six in the visible range and two in the near IR (see Table 1.1). The sun-synchronous polar orbit allows a global repeat visit every 24 hours. It is the high level specification of the SeaWiFS radiometer and the sophistication of the accompanying ground truthing calibration and validation experiments (building upon all that had been learned through the CZCS mission) which enabled the project goals for sensor performance to be met as reported by McClain *et al.* (1998).

With the advent of sophisticated satellite observation systems in the last 15-20 years, oceanography has entered a new era. It is now possible to routinely obtain ocean basin-wide information within a few hours of observation of mixed layer phytoplankton biomass distributions from ocean colour (Smith and Baker, 1978; Robinson, 1985; Williamson, 1990; Hooker *et al.*, 1992; Aiken *et al.*, 1995). This may be achieved to an accuracy of +/-35% over the range of 0.05 to 50 $mg\ m^{-3}$ (Hooker *et al.*, 1992) using the optical signature of the ubiquitous phytoplankton pigment chlorophyll-*a*. From these data it is possible to investigate the surface mixed layer of the marine biosphere to quantify its variability and to obtain baseline data against which future spatial and temporal patterns of change may be assessed (Hooker *et al.*, 1992; Lalli and Parsons, 1993; Houghton *et al.*, 1996). These data form one of the inputs into the increasingly sophisticated coupled atmospheric and oceanic general circulation models (GCMs) which are the tools of future climate change prediction (Houghton *et al.*, 1996).

Table 1.1. The SeaWiFS band set and some in-water characteristics to which they relate.

Band	SeaWiFS Wavelength, *nm*, and centre, λ	Approxi-mate Colour	In-water phenomena to which the bands relate (description is from shorter wavelengths to longer wavelengths). Interpretation based on data collected by Bidigare *et al.* (1990).
1	402-422 (412)	Violet	• dissolved organic material (DOM) high absorption (decreases with longer wavelength) • phytoplankton pigment low absorption
2	433-453 (443)	Blue	• chlorophyll-*a* (CHL-*a*) maximum blue absorption • increasing carotenoid absorption • increasing chlorophyll-*b* (CHL-*b*) absorption • increasing chlorophyll-*c* (CHL-*c*) absorption
3	480-500 (490)	Blue	• CHL-*a* minimum absorption • CHL-*b* decreasing absorption • CHL-*c* decreasing absorption • Photosynthetic carotenoids (PSC) high absorption • Photoprotective carotenoid (PPC) high absorption (decreasing)
4	500-520 (510)	Blue/ Green	• CHL-*a* increasing absorption • CHL-*b* minimum absorption • CHL-*c* minimum absorption • PPC minimum absorption. • PSC decreasing absorption
5	545-565 (555)	Green	• CHL-*a*, CHL-*b* and CHL-*c* increasing absorption • PSC low absorption (decreasing) • PPC zero absorption • DOM low absorption
6	660-680 (670)	Red	• CHL-*a* red absorption maximum • CHL-*b* and CHL-*c* decreasing absorption • DOM low absorption
7	745-785 (765)	Infra red	• atmospheric correction • Phytoplankton pigment zero absorption • DOM zero absorption
8	845-885 (865)	Infra red	• atmospheric correction

It is the interpretation of these input parameters that forms the focus of this work, which further explores the relationship between the light field as it would be viewed by SeaWiFS, and the optical properties of the medium driving the remotely sensed observations through modelling of data collected *in-situ*. This work therefore serves three purposes:

(i) to provide data for the calibration and validation of SeaWiFS;

(ii) to test existing algorithms relating ocean colour imagery to in-water properties (see chapter 3);

(iii) to assess the performance characteristics of new algorithms arising from the field measurements collected (see chapter 8).

The proposed work plan was centred on the collection of contemporaneous in-water data (the apparent optical properties of the medium, AOP, and phytoplankton pigments) and remotely sensed observations. Because the delayed launch of SeaWiFS (three years) meant that it was only possible to collect the in-water observations presented here, no satellite ground truth match-ups were possible.
As is the case in soil with terrestrial plants growing on land, natural seawater forms a medium in which a range of photosynthetic flora grow, these organisms are highly diverse and vary in colour, albeit often very subtly. With this in mind, the field sampling phase of the work presented here covered a diverse range of bio-optical regimes. It follows that the attenuation of light in one locality that is attributable to a given in-water dominant algal group, and hence pigment(s), may not be so at another location where the water has a different phytoplankton composition and hence pigment assemblage. If additional material not related to the standing algal crop is also present in the water, then its colour will also become a function of the

prevailing sedimentology as well as dissolved organic material (of both organic and inorganic origin) (Jerlov, 1968; Gordon and Morell 1983; Dyer,1986; Kirk, 1994; Aiken *et al.*, 1995). The presence of these materials within the particulate and dissolved fractions of seawater leads to the concept of type case 1 and type case 2 waters, a summary of which is presented in figure 1.1. This study was involved primarily with sampling in type case 1 waters.

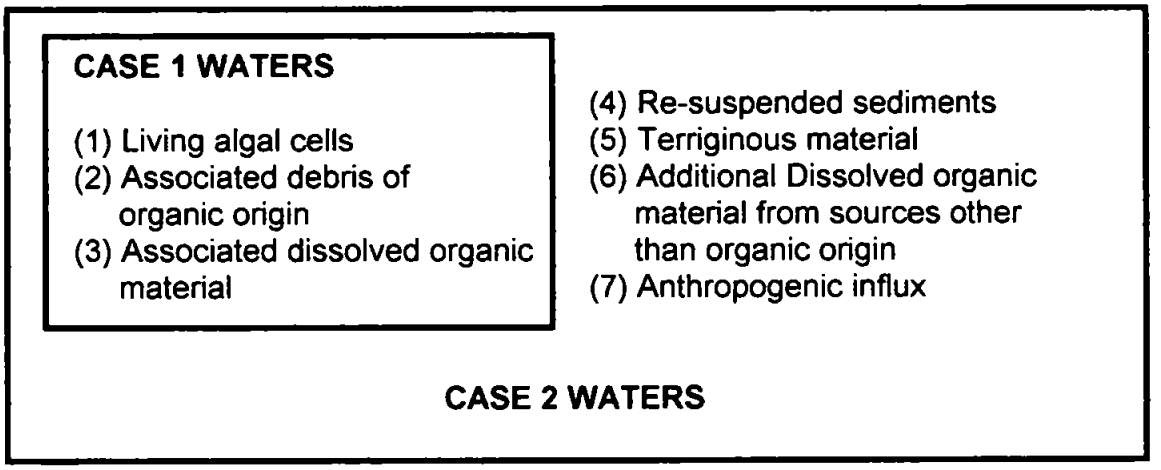

Figure 1.1. The broad optical classification of water types (Gordon and Morel, 1983).

1.2 Introduction to the field sites

The field work was carried out in three parts:

(i) a seasonal study at a near coastal site (station L4) in the western English Channel from January to September 1995;

(ii) a spatial variability study from the UK to the Falkland Islands, the Atlantic Meridional Transect during the first cruise of the programme (AMT-1) from September to October 1995;

(iii) a second spatial variability study from Iceland to a station at 20°W / 37°N near the Azores during June and July 1996. The latter work was in support of the Natural Environment Research Council (NERC) Plankton Reactivity in the Marine Environment (PRIME) study.

The following sub-sections provide a general understanding of the location of the sampling sites.

1.2.1 Coastal fieldwork campaign at station L4, Plymouth

Station L4 is located in the western English Channel at 50°15.0'*N* / 04°13.0'*W* and sampling at this site has been extensive over several decades by staff of the Marine Biological Association, MBA, and more recently their sister organisation, Plymouth Marine Laboratory, PML. Data collection in support of this study was undertaken coincident with continuing MBA-PML sampling programmes using the research vessel *Squilla* (Holligan and Harbour, 1977; Lavender *et al.*, 1996; Pond *et al.*, 1996; Lavender *et al.*, 1997).

The sampling programme ran weekly from January to September 1995, weather and ship availability permitting. Figure 1.2 shows a map of the sampling site location.

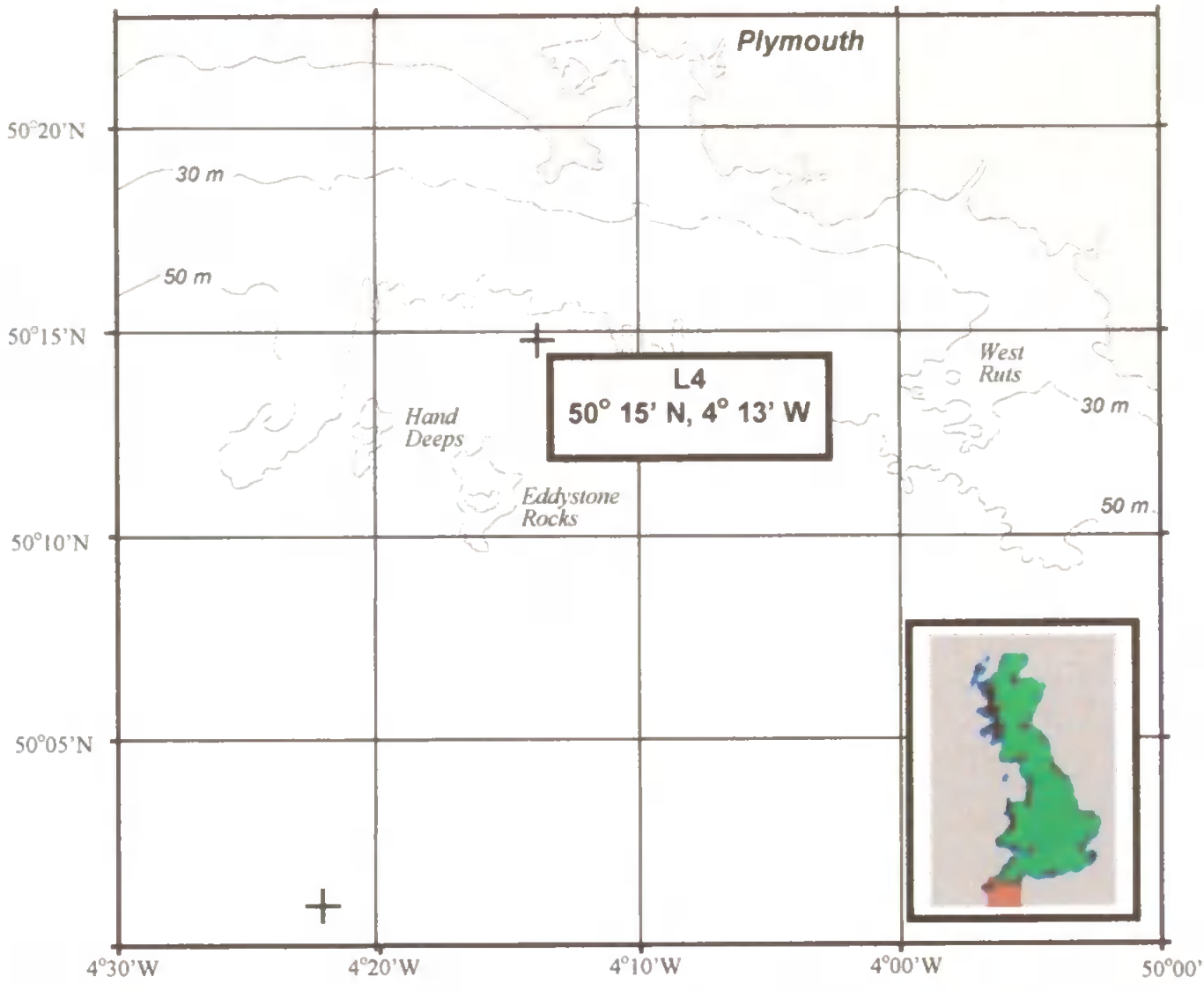

Figure 1.2. The location of the L4 sampling site off Plymouth in the western English Channel, and inset the general location of the site within the British Isles.

1.2.2 The first Atlantic Meridional Transect, AMT-1

AMT-1 crossed the Atlantic Ocean from 52°*N* to 52°*S* aboard the British Antarctic Survey (BAS) vessel *RRS James Clark Ross* (Robins *et al.*, 1996; Westbrook *et al.*, 1998), see figure 1.3. In the North Atlantic the cruise track left the western approaches to the European continental shelf in a westerly direction until reaching the 20°*W* meridian before turning south. Apart from an unscheduled visit to

Madeira, the track maintained this heading until 9.24°*N* / 20°*W* before turning south west, traversing the south Atlantic oceanic gyre. The track then followed the Brazilian coast at a distance of approximately 200 nautical miles. After a logistics stop in Montevideo (Uruguay) the last section of the cruise programme terminated at Stanley, Falkland Islands. The AMT-1 pigment data collected during this work have been incorporated into the NASA SeaWiFS algorithm generation data base.

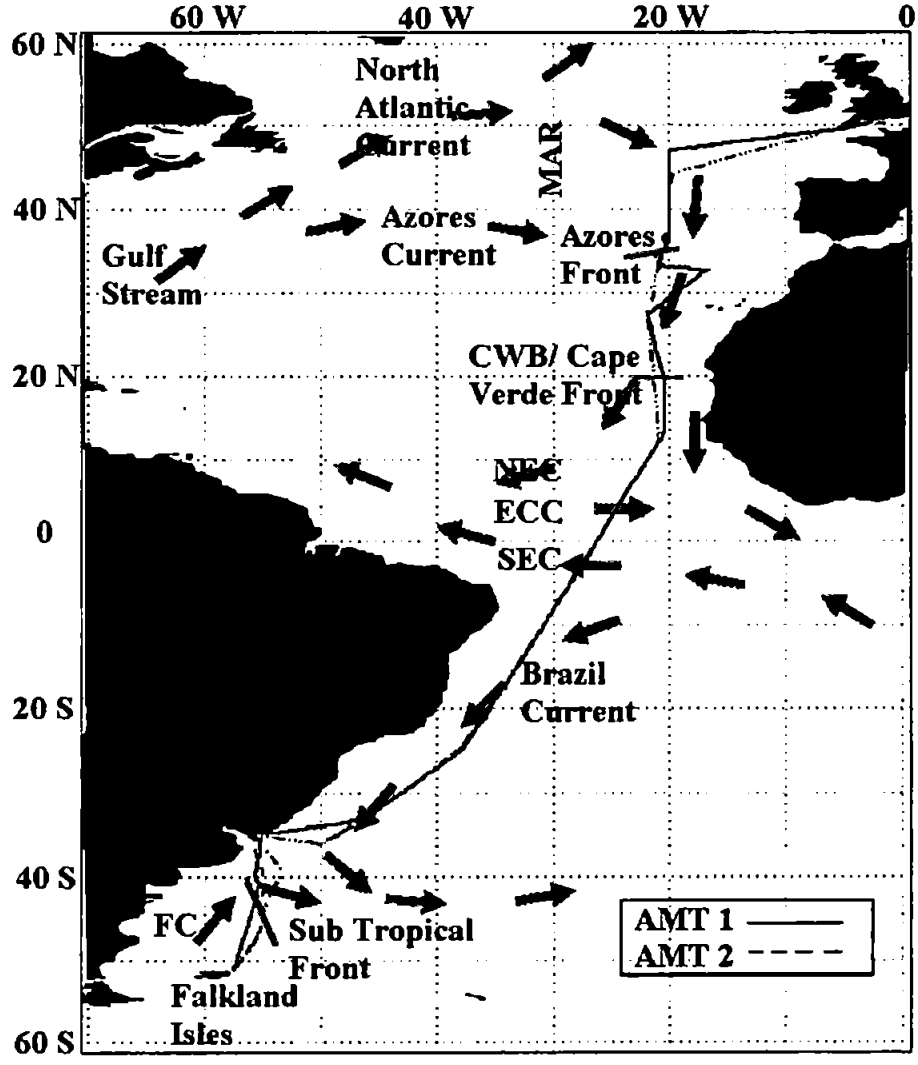

Figure 1.3. *RRS James Clark Ross* cruise track during AMT-1 (23/09/1995 to 24/10/1995), including the major regional current features. Key: NEC-North Equatorial Current, ECC-Equatorial Counter Current, SEC-South Equatorial Current, FC-Falklands Current, CWB- Central Water mass Boundary, MAR-Mid Atlantic Ridge.

1.2.3 The Plankton Reactivity in the Marine Environment (PRIME) cruise

The research cruise on board *RRS Discovery* from Iceland to 37°*N* / 20°*W* during May and June 1996 was part of the PRIME study, which was concerned with the role of plankton in the food chain and associated biogeochemical cycling.

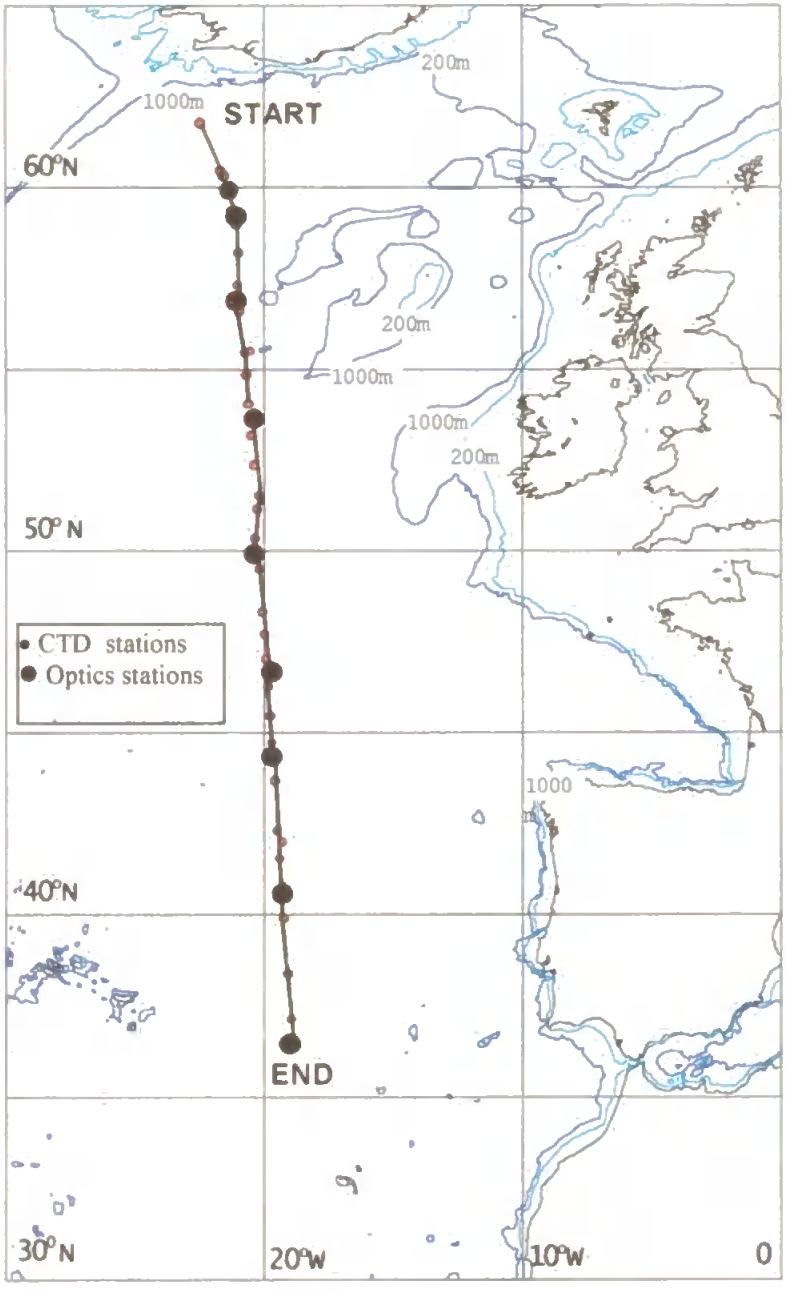

Figure 1.4. *RRS Discovery* cruise track, July 2 to July 21 1996.

The cruise was divided into three parts. Firstly a process study on a cold core eddy south of Iceland was undertaken; secondly, a survey of the physical and biological structure of the waters along the 20°*W* meridian from 60°*N* to 37°*N* (see figure 1.4); and thirdly an eight day Lagrangian time-series process survey at 37°*N* / 20°*W*. The work described here was carried out during the second and third parts of the cruise (Westbrook *et al.*, 1999).

1.3 Thesis overview

Chapter two is gives the reader a background in the fundamentals of both in-water and air-water interface optical theory as applicable to ocean colour remote sensing calibration and validation exercises (satellite 'match ups' or 'ground truth'). Also covered is a description of the analytical basis of the two band algorithm and the various radiometric inputs and a section introducing the optical characteristics of the main constituents usually encountered while undertaking contemporaneous bio-optical sampling is also included. In chapter 3 the algorithms under consideration are discussed. In Chapter 4 the optical methodologies that were developed in preparation for the field sampling and concurrent instrument calibration are introduced and explained. In chapter 5 the sampling quality control procedures employed during data analysis and the statistical test used to demonstrate how the algorithms perform are presented. Algorithm performance is assessed in terms of statistically significant differences in the shape of the error distribution of the measured versus retrieved parameter(s).

In Chapter 6 an introduction to the phytoplankton pigments identifiable by HPLC is given, as well as details of the sampling, storage and analysis procedures

employed. Chapter 7 contains the results arranged by field work session, and in chapter 8 the analysis and interpretation of these results is illustrated.
In chapter 9 conclusions of the research are drawn, with suggestions for future work. Some proposed solutions to technical problems encountered are presented in appendix 2, while appendix 3 contains selected publications arising out of this and other work executed during the period covered by this research.

2. OPTICAL THEORY

In this section the optical theory employed in later chapters is presented. The text follows the definitive work presented in Kirk (1994) with some reference to Mobley (1994).

2.1 LIGHT AND ITS PROPERTIES

Electromagnetic radiation is energy emitted from a body and varies as a function of the thermodynamic state of that body. The energy emanates as electromagnetic waves, the length of which distinguish the various components of the electromagnetic spectrum e.g. gamma waves ($\approx 0.03\text{Å}$) , X-rays ($\approx 3\text{Å}$), visible light ($\approx 555nm$), RADAR ($\approx 30cm$) and radio waves ($\approx 300m$). The bandwidth of the emitted spectrum depends upon the inherent energetic state of the source and may change as, for example, the body cools. This study is concerned with the visible band from $400nm$ (deep violet) to $700nm$ (dark red). This band constitutes 38% of the solar irradiance incident at the Earth's outer atmosphere, and the use of the light in this narrow band by autotrophic organisms makes it essential for life on Earth (Kirk, 1994).

2.1.1 The geometric notation describing the light field

Consider a downward and upward beam of light, both in the same vertical plane. The downward beam has zenith angle θ, the upward beam has nadir angle θ_n, (equivalent to a zenith angle of $180^\circ - \theta_n$). Assuming that the x-y plane is the vertical plane of the

sun, or any other reference vertical plane, then ϕ is the azimuth angle for both beams of light (Kirk, 1994), as illustrated in figure 2.1.

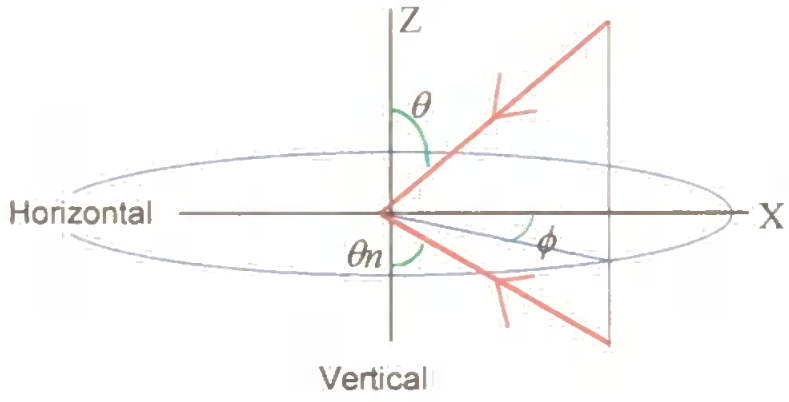

Figure 2.1. The angles defining direction within a light field.

2.2 PROPERTIES OF THE LIGHT FIELD

Energy is emitted from a light source as electromagnetic radiation in accordance with the geometric convention outlined in figure 2.1. The following section details how this radiating energy is quantified, with particular reference to those quantities used to characterise ocean colour in the context of remote sensing.

2.2.1 Radiant energy

Radiant energy is that carried by an electromagnetic wave. It is a measure of the capacity of the wave to do work by force upon a medium or body, heating it or changing its state. The unit of energy is the joule.

Radiant energy = $F(\lambda)$ (J) (2.1)

2.2.2 The radiant flux

The radiant flux, Φ, is the flow of energy with respect to time past a fixed location in space, so is measured in $J\ s^{-1}$ or *Watts*.

$\Phi(\lambda) = dF(\lambda)/dt$ (W) (2.2)

2.2.3 The radiant intensity

The radiant intensity, $I(\lambda)$, is a measure of radiant flux upon an infinitesimally small point in space per unit of solid angle in a specified direction:

$I(\lambda,z) = d\Phi/d\omega$ $(W\ sr^{-1})$. (2.3)

2.2.4 Radiance

It is not practicable to derive a value of $I(\lambda)$ from equation 2.3, as it assumes an infinitesimally small detector area, which produces an insoluble equation. However, we can consider a radiance meter that has geometric dimensions describing the measurement cone (refer to figure 2.2), then the photodiode detector will have an

area, A (m^2), at the apex of the cone. By dividing the radiant intensity by A it is possible to quantify the radiance component of the light field. Radiance is the energy per unit time per unit solid angle incident upon an elemental area, A, from the direction (θ, ϕ):

$$L(\lambda,z,\theta,\phi) = dI(\lambda,z,\theta,\phi)\ /dA \quad (Wm^{-2}sr^{-1}) \tag{2.4}$$

2.2.5 Upwelling radiance

The special case of upwelling radiance, $Lu(\lambda,z,\theta,\phi)$, is of particular importance as this is a measurement of the vertically back-scattered light field that is ultimately viewed from space (as shown in figure 2.2).

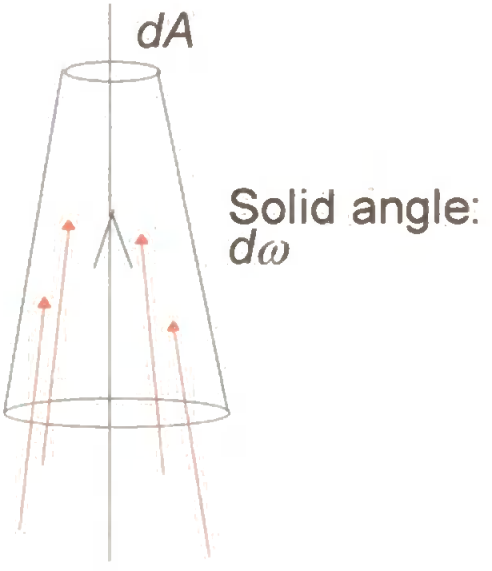

Figure 2.2. Upwelling radiance.

2.2.6 Radiant flux density (Irradiance)

Irradiance, E, is the radiant flux incident upon an elemental surface of unit area, A, divided by the irradiated surface area of that element, dA, m^{-2}. Therefore:

$$\text{Irradiance, } E(\lambda,z) = d\Phi / dt \cdot dA \quad (Wm^{-2}) \tag{2.5}$$

In a light field the radiance intensity gives a measure of the energy from the point of view of a small area viewing a cone. An alternative approach is to measure the entire energy falling on that same point if it were considered to be a sphere of infinitely small surface area. The total energy incident on the surface of this sphere would therefore be equivalent to the radiant intensity received over dω, which for a sphere is 4π steradians.

An irradiant light field is highly scattered by the constituent components of the medium and may be described as a light field that will not form a shadow. Irradiance is measured by one of two instrument types (i) vector irradiance meters or

(ii) scalar irradiance meters:

(i) Downwelling vector irradiance is measured using a flat cosine collector over a viewing angle of $0 \leq \theta \leq \pi/2$ and $0 \leq \phi \leq 2\pi$. Vector irradiance is therefore measured in the vertical with the instrument viewing vertically upwards measuring downwelling irradiance, $Ed(\lambda, z)$, therefore:

$$Ed(\lambda,z) = \int_{2\pi} L(\lambda,z,\theta,\phi).\cos\theta.d\omega \tag{2.6}$$

where $\int_{2\pi} d\omega = \int_{\theta=0}^{\pi/2} \int_{\phi=0}^{2\pi} d\theta \cdot d\phi$

Radiometers incorporating cosine collectors to measure $Ed(\lambda, z)$ must be deployed vertically in the water. NASA protocols require a limit of 10° as the maximum angle for $Ed(\lambda,z)$ data (Mueller and Austin, 1995). This is further discussed in section 4.2.3.

(ii) Scalar irradiance detectors measure the magnitude from all directions of a solid sphere that the sensor is designed to view.

Instruments measuring scalar irradiance are favoured for studies of primary production, as they present realistic values of the light received by the plant cells, which make use of light regardless of its direction of propagation.

2.3 TRANSMISSION THROUGH THE AIR / SEA BOUNDARY

To propagate the light field through the air-water interface the effects of (i) refraction and (ii) reflection at the boundary need to be considered. These effects are summarised in figure 2.3.

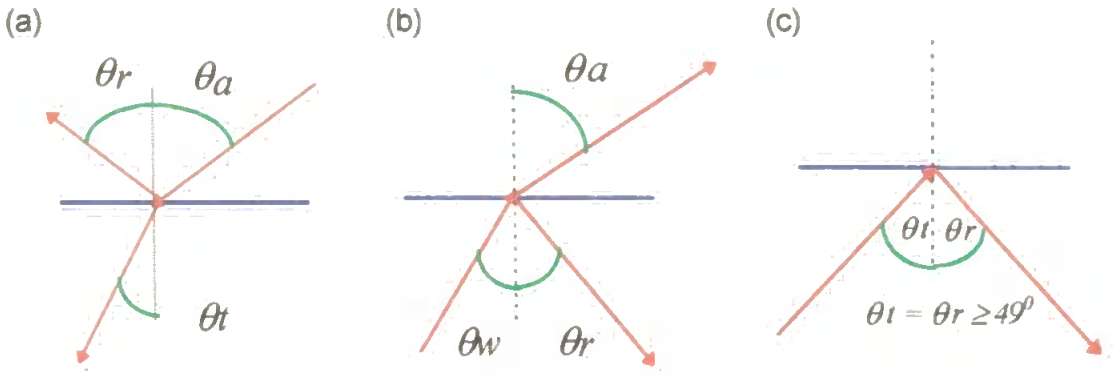

Figure 2.3. (a) An incident beam of light at zenith angle, θ_a, is partly reflected and partly refracted as it passes through the air/sea interface. (b) A light beam from below at nadir angle, θ_w, is refracted away from the vertical as it passes through into the air. A small part of the beam is reflected downwards again at the water-air boundary. (c) A light beam incident from below at a nadir angle greater than 49° undergoes complete internal reflection at the water-air boundary (Kirk, 1994).

2.3.1 Refraction at the boundary

As light passes from the air through to the water it is slowed by the refractive index of water, n_w (the ratio of the speed of light in water to that in a vacuum), with the result that the portion of the incident beam passing through the surface is bent towards the normal. This change in angle is governed by Snell's law (equation 2.7):

$$\frac{\sin\theta_a}{\sin\theta_w} = \frac{n_w}{n_a} \qquad (2.7)$$

where θ_a and θ_w are the respective angles between the normal and the incident transmitted beams and where n_w and n_a are the refractive indices of water and air

respectively, the ratio of which is 1.33 (and hence 0.75 when passing from water to air).

2.3.2 Reflection at the boundary

The dependence of reflectance, *r*, of unpolarized light on the zenith and azimuth angle of the incident light in at the air / water interface (θ_a) is given by Fresnel's equation (see equation 2.8)

$$r = \frac{1\sin^2(\theta_a - \theta_w)}{2\sin^2(\theta_a + \theta_w)} + \frac{1\tan^2(\theta_a - \theta_w)}{2\tan^2(\theta_a + \theta_w)} \qquad (2.8)$$

The reflectance is a function of zenith angle and is shown in table 2.1 for various angles of incidence. Note that for angles up to 50° the reflectance is small, increasing rapidly after this angle.

Table 2.1. Change in reflectance (%) with zenith angle, (Kirk, 1994).

Zenith angle of incidence, θ_a (degrees).	**Reflectance, r (%).**	**Zenith angle of incidence, θ_a (degrees).**	**Reflectance, r (%).**
0	2	50	3.3
5	2	55	4.3
10	2	60	5.9
15	2	65	8.6
20	2	70	13.3
25	2.1	75	21.1
30	2.1	80	34.7
35	2.2	85	58.3
40	2.4	87.5	76.1
45	2.8	89	89.6

2.4 INHERENT OPTICAL PROPERTIES

When a photon of light enters water it will be either scattered or absorbed, (figure 2.4). The absorption and scattering properties of water for any given wavelength are expressed in terms of the absorption coefficient, the scattering coefficient and volume scattering function. These are the inherent optical properties of the water itself, i.e. are not a function of the geometric structure of the light field that may pervade it (Kirk, 1994; Mobley, 1994).

The contributory factors of attenuance of a radiant flux are expressed by equation 2.9 and illustrated in figure 2.4.

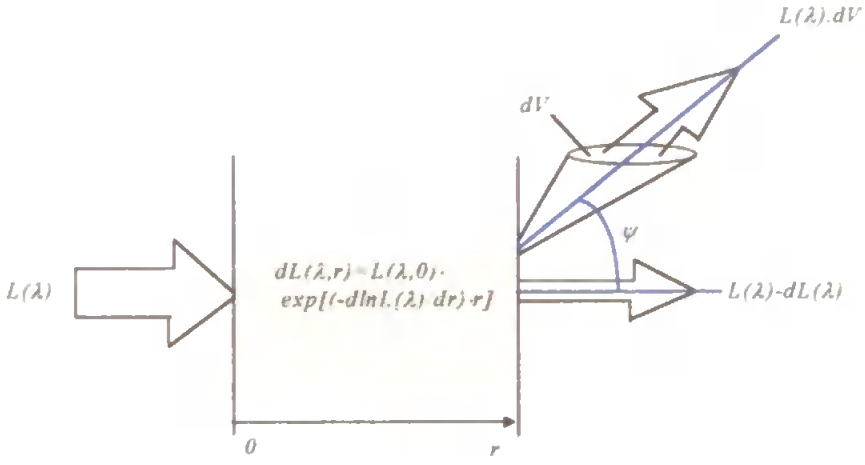

Figure 2.4. The combined effects of absorption and scattering upon an incident radiant light field, L, of wavelength, λ, when passing through solid element of a medium (of length r).

$$c = a + b \qquad (m^{-1}) \tag{2.9}$$

where c is the beam attenuation coefficient which comprises the absorption coefficient, a, and the scattering coefficient, b. From figure 2.4 $\frac{dL(\lambda)}{L(\lambda)} = A(\lambda)$, the attenuance, related to c (λ) by dividing by the distance along the path the beam is travelling through the medium, dr. Thus, as shown in figure 2.4, the diminution of an incident radiant beam of light by a scattering and absorbing medium will result in a portion being attenuated in accordance with equation 2.10.

$$c(\lambda) = \frac{A(\lambda)}{dr} \qquad (m^{-1}) \tag{2.10}$$

The portion of the beam scattered out of the direction of propagation, at angle ψ, is represented in figure 2.4 by $L(\lambda).dV$ and may be described by the volume scattering function, β, from equation 2.11.

$$\beta(\lambda,\psi) = \frac{dL(\lambda,\psi)}{L(\lambda)\cdot dV} \tag{2.11}$$

Equation 2.11 is integrated over all angles (0 to 4π) to derive the total volume scattering coefficient, $b(\lambda)$, described in equation 2.12.

$$b(\lambda) = \int_{4\pi} \beta\ (\lambda,\Psi)\cdot d\omega \qquad (m^{-1}) \tag{2.12}$$

When viewed from above the colour of the ocean is purely the result of the back-scattering of the incident light field (the portion of the downwelling light field scattered in the upwelling direction). It is possible to distinguish between scattering in the forward, b_f, and backward, b_b, directions as shown in equation 2.13:

$$b(\lambda) = b_f(\lambda) + b_b(\lambda) \tag{2.13}$$

Forward scattering is over $0 \leq \psi \leq \pi/2$ and backward scattering over $\pi/2 \leq \psi \leq \pi$, hence b_f and b_b are described by equations 2.14 and 2.15 respectively (Kirk, 1994).

$$b_f = 2\pi \int_0^{\pi/2} \beta(\psi)\sin(\psi)d\psi \tag{2.14}$$

and

$$b_b = 2\pi \int_{\pi/2}^{\pi} \beta(\psi)\sin(\psi)d\psi \tag{2.15}$$

2.4.1 Scattering mechanisms

A photon is scattered when it interacts with some component of a medium in such a way that it diverges from its original path. The scattering of photons serves to increase their path length through the medium and hence increase the likelihood of the photon

being absorbed. The effect of scattering is therefore to intensify the attenuation process.

The scattering of light in natural waters is an important aspect of marine optics. In the atmosphere and very pure liquids the majority of scattering is over small forward angles. In the purest oceanic waters there are complicated chemical relationships between the dissolved minerals, suspended particulates and biological constituents which cause photons to diverge in various ways and many directions. Some of these are shown in figure 2.5 (Kirk, 1994).

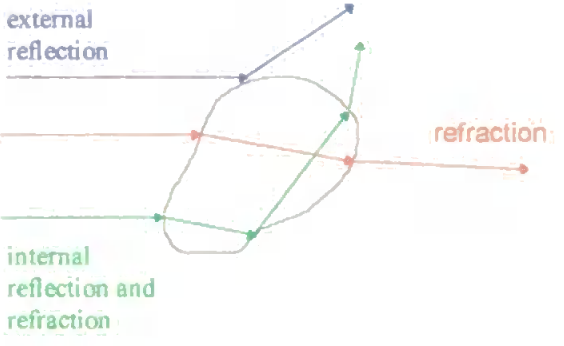

Figure 2.5. Light interaction with of a particle suspended in a water body resulting in scattering.

The amount of scattering within a medium depends upon the relative size of the spherical equivalent particle radius, r, and the wavelength, λ, of the incident radiation and may take the form of (i) scattering by density fluctuations, termed molecular or Rayleigh scattering, for $r<<\lambda$, and/or (ii) scattering due to suspended particulates, for $r>>\lambda$.

2.4.1(i) Scattering due to density fluctuations

The Rayleigh model applies to particles that are small relative to the wavelength of light, e.g. gases with only weak inter-molecular associations. For a gas molecule that lies within a light field, a dipole is induced by the electric vector and as the dipole oscillates at the excitation frequency the molecule emits quanta in all directions, thus light is scattered the same amount in the forward and backward directions.

It is not appropriate to apply this theory to liquids as the strong interactions between the molecules make it impossible to consider them individually as discrete scatterers. Due to density fluctuations, however, the resultant localised inhomogeneities can be regarded as dipoles and behave as such in their interaction with light (Kirk, 1994).

2.4.1(ii) Scattering by suspended particulate material

Mie scattering provides an approach to predict the scattering by particles of any equivalent spherical size, particularly those of size greater than the wavelength of visible light. Even the clearest natural waters contain relatively high levels of particulates (e.g. sediments or phytoplankton). Natural waters have a particle size distribution that increases approximately exponentially towards the smaller particulates, i.e. the number of particles greater than D is proportional to $1/D^{\gamma}$, where γ is a constant that varies between 0.7 to 6, depending upon the water body (Kirk, 1994).

As with Rayleigh scattering, Mie theory considers the oscillations set up in a polarizable body by the incident light field, and the light re-radiated by the body as a result of these oscillations (Kirk, 1994). The particle is considered to interact with light as a series of multi-poles within the particle, with overall scattering being the additive effect of these multi-poles. Mie theory predicts that most of the scattering is in the forward direction, within small angles of the incident beam axis.

Where the medium contains particles of large and irregular size relative to the wavelength of light, the potential outcome is illustrated in figure 2.5 where all or some of an incident beam of light is either reflected at the surface of the particle upon entry, is refracted upon passage through the particle before becoming further internally reflected upon exit, or will be further refracted upon re-entry into the water. This type of scattering is predominantly in the forward direction, both within small angles of the beam axis (due to refraction) and large angles (due to reflection).

2.4.2 Absorption

The atoms of all elements have unique physical properties resulting from their electronic structure. An atom receiving a quantum of light becomes excited (raised to a higher energetic state). This resultant change is manifest as changes in the rotational and vibrational characteristics of the electronic energy structure in which it is "stored", being either immediately re-emitted or remaining, changing the structure of the atom.

The interaction of a photon of light with matter may initiate a changes in the chemical structure with a wide range of possible outcomes, depending upon the bandwidth of the prevailing light field and the chemical composition of the medium.

There are four possible outcomes of molecule - light field interaction resulting from photochemical interaction: absorption followed by re-emission, molecular destruction, molecular construction and energy transfer. It is generally considered that the breaking down of molecules (photodegradation) brings about detrimental effects, whereas initiation, propagation, cycloaddition are more constructive outcomes (Hill, 1983).

In remote sensing, the absorption and scattering by pure water (see figure 2.6) is a well defined quantity (Smith and Baker, 1978; Smith and Baker 1981; Buiteveld *et al.*, 1994; Pope and Fry, 1997). The selective absorption of light by pure water forms the background against which the optical significance of in-water constituents are assessed (Austin and Petzold, 1981, Mueller and Trees, 1997; Moore *et al.*, 1997). Buiteveld *et al.* (1994) have made measurements of the absorption and scattering properties of pure water, the resulting coefficients for which are summarised in figure 2.6.

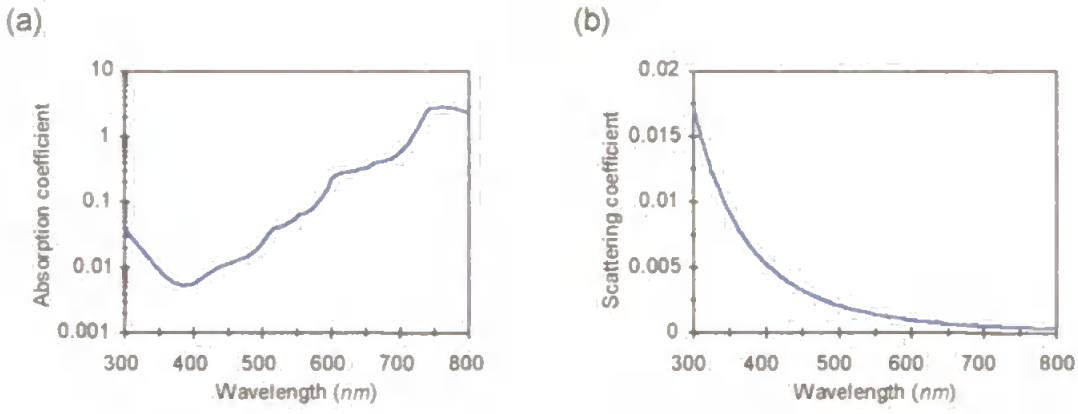

Figure 2.6. (a) Absorption and (b) scattering coefficients for pure water from 300-800*nm* as determined by Buiteveld *et al.* (1994). The units in each case are m^{-1}.

Other in-water characteristics relevant to this study are the absorption and scattering characteristics of (i) suspended particulate material (SPM) which may be either organic (phytoplankton, zooplankton) or inorganic (sediments) and (ii) dissolved organic material (DOM). In the case 1 environment the key optically significant fractions are the phytoplankton and their degradation products (Gordon and Morell, 1983). Figure 2.7 shows an example of the absorption spectrum of various fractions of a sample of water collected during field work carried out in the course of this research at a sampling station in the western English channel (site L4).

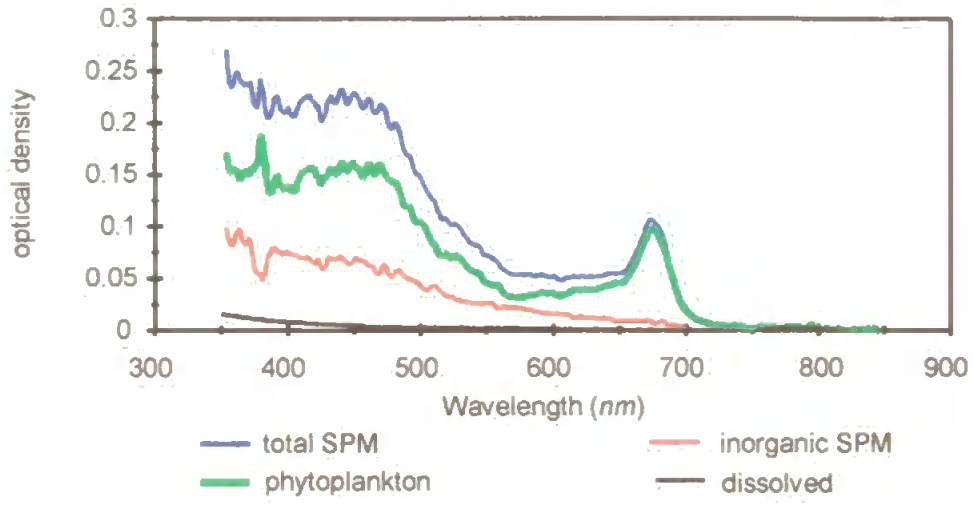

(b)

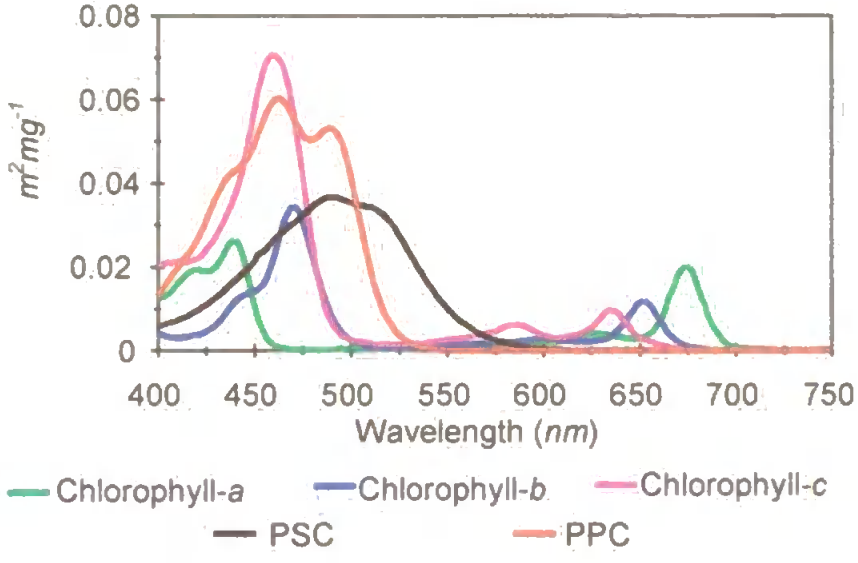

Figure 2.7. (a) An example of the absorption spectra of some constituents of a water sample collected at station L4 from a depth of 10*m* (1995, SDY 167). Data were determined from spectrophotometric analysis of a water sample concentrated on a Whatman GF/F filter pad (Mueller and Austin, 1995). DOM data were obtained from a sample filtered to 0.2μm (Kirk, 1980; Mueller and Austin, 1995). The biological fraction was removed using a hot methanol bath. Data were corrected to zero absorption at 750*nm*, but the path length amplification factor, β_L, had not been applied (Cleaveland and Weiderman, 1993). (b) 'Unpackaged' specific absorption coefficient spectra of some pigments identified in this study: chlorophylls *-a*, *-b* and *-c*, and the carotenoids grouped as photosynthetic (PSC) and photoprotective (PPC) types according to Bidigare *et al.*, (1990).

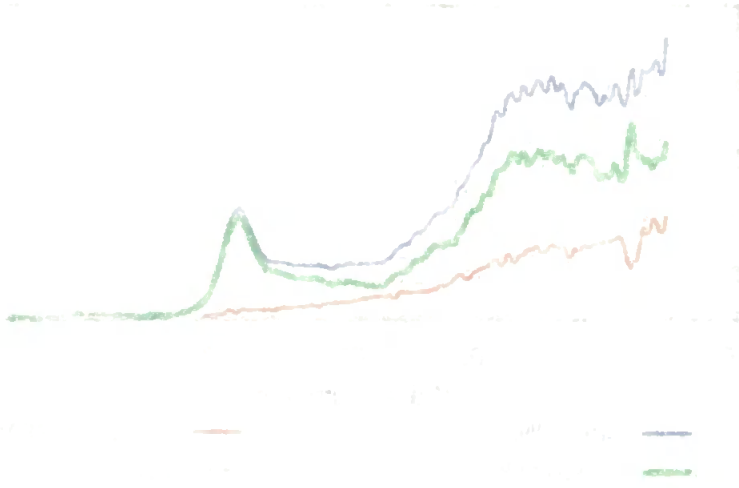

2.5 THE APPARENT OPTICAL PROPERTIES AND THEIR RELEVANCE TO REMOTE SENSING

Operational satellite oceanography is concerned with deriving key optical properties of the world's oceans by collecting radiometric measurements in-situ to enable the characterisation of the back-scattered light field as a function of the incident light and the in-water constituents of the surface waters. The signal received from a space borne radiometer includes skylight, the direct solar beam reflected from the surface as well as light back-scattered by the atmosphere (Kirk, 1994). The components of the signal are summarised in equation 2.16:

$$Es(\lambda) = T.Ew(\lambda) + T.Er(\lambda) + Ea(\lambda) \qquad (2.16)$$

where $Es(\lambda)$ is the total irradiance arriving at the detector, $T.Ew(\lambda)$ is the part of the emergent flux remaining after transmission, T, through the atmosphere. $T.Er(\lambda)$, similarly, is the portion of the reflected solar beam remaining. $Ea(\lambda)$ is the irradiant signal received by the sensor from light back-scattered by the atmosphere. Remote sensing radiometer systems typically view an irradiant atmospheric upwelling light field over a small angle (radiance) whereby E would be replaced by L in equation 2.16.

The unwanted effects are removed by a suite of corrective models such that the only remaining part of the received signal is that containing information about the surface waters, $Lw(\lambda, \theta, \phi)$, the emergent or water leaving flux. This flux is a function of the incident light field as well as the in-water constituents, the key feature that differentiates the apparent from the inherent optical properties. The

apparent properties are a function of the incident light field and the medium, whereas the inherent optical properties are of the medium only, regardless of the geometric distribution of the pervading light field.

The vertically emergent flux may be characterised by ship borne radiometric techniques in terms of remote sensing reflectance, $Rrs(\lambda)$, by measuring the downward irradiance, $Ed(\lambda,z)$ and the corresponding upwelling radiance, $Lu(\lambda,z,\theta,\phi)$, by profiled radiometry. $Rrs(\lambda)$, therefore, represents an integration of the optically significant in-water constituents and their absorbing and scattering properties. The apparent properties are often termed quasi-inherent optical properties as they remain broadly similar for any given water mass (seasonal variations accounted for) from one field work session to the next (Kirk, 1994).

As the incident irradiance (comprising skylight and the direct solar beam) penetrates the water column, the sub-surface light field retains some characteristics of its angular structure (the geometry of which is further complicated by light field perturbations due to waves at the interface). As the processes of scattering and absorption, which are wavelength dependent, further modify the light field, the spectral characteristics and the angular structure are changed until only isotropic blue green ($\approx$490*nm*-510*nm*) light remains.

2.5.1 The diffuse attenuation coefficient

The diffuse attenuation coefficient, $Kd(\lambda)$, is a measure of the rate of diminution of the downwelling irradiant light field by the water column and the in-water constituents as it propagates through the water column. The properties of the light field throughout the water column depend upon the nature of the incident light field, the interface effects,

the absorption and scattering characteristics of the in-water constituents and their concentration (as well as vertical variability), and the water depth. Equation 2.17 illustrates that the variability in the absorption of irradiant light by water may be expressed in terms of the additive effects of the absorbing fractions present therein:

$$Kd(\lambda) = Kd(\lambda,W) + Kd(\lambda,Y) + Kd(\lambda,SPM) + Kd(\lambda,C) \qquad (m^{-1}) \qquad (2.17)$$

where $Kd(\lambda)$ is the total diffuse attenuation coefficient for vertically downward irradiance, $Kd(\lambda,W)$ denotes the $Kd(\lambda)$ for pure water, $Kd(\lambda,Y)$ for dissolved organic material (DOM), $Kd(\lambda,C)$ for phytoplankton pigments and $Kd(\lambda,SPM)$ for suspended particulate material other than phytoplankton related material (Kirk ,1994).

The absorption model approach to accounting for the component partial $Kd(\lambda)$ values will hold true only if scattering is considered to be low enough to be insignificant. A photon scattered within an irradiant light field is not lost from it but follows a longer path length through it, with the consequence that it has an increased chance of absorption. Scattering will become significant in waters containing a high concentration of mineral particles of low intrinsic colour, when the assumption that relative rates of absorption are proportional to the partial vertical attenuation coefficients will be in error (Kirk, 1994). High levels of scattering may also be seen in waters where there are bloom conditions of coccolithophores, especially those containing high numbers of detached coccoliths suspended in the water (Balch *et al.*, 1991; Kirk, 1994; Van Den Hoek *et al.*, 1995).

$Kd(\lambda,z)$ is measured with either a scalar (2π) or vector downwelling irradiance radiometer. In this study a vector cosine collector was used, with a common Teflon Lambertian diffuser serving the 6 downwelling detectors (described in section 4.1). The attenuation of light in the sea follows a model of exponential decay as described by the Beer-Lambert law of diffuse attenuation, (Pilgrim, 1987; Pilgrim and Aiken 1989; Gordon,1989; Kirk, 1994), summarised in equation 2.18.

$$Ed(\lambda,z) = Ed(\lambda,0^-)\cdot e^{-Kd(\lambda)\cdot z} \qquad (2.18)$$

where $Ed(\lambda,z)$ is the measured vertical irradiance at wavelength, λ, and depth, z, $Ed(\lambda,0^-)$ is the irradiance at an infinitesimal distance below, and normal to, the surface, and $Kd(\lambda)$ is the diffuse attenuation coefficient.

Because the vertical attenuation of irradiance is a function of the prevailing light field, its value will be affected by solar elevation, cloud cover and sea state. The processing protocols for profile data are discussed in chapter 5 and serve to minimise measurement errors.

2.5.2 The variation of $Kd(\lambda)$ measurement with sun angle

In case 1 waters where scattering is low, $Kd(\lambda)$ varies in accordance with the absorption coefficient and zenith angle, θ, of the refracted solar beam just below the surface (equation 2.19) and relates to the increased path length (compared to the vertical case) that the photons travel, and hence their increased likelihood of being absorbed. The result is increased values of $Kd(\lambda)$ being derived from profiling as the zenith angle of the sun increases.

$$Kd(\lambda) = \frac{a(\lambda)}{\cos\theta} \tag{2.19}$$

The SeaWiFS satellite follows a sun synchronous polar orbiting pattern, so potential errors in the measurement of *Kd(λ)* introduced by changing sun zenith angle are minimised by scheduling all measurements of the in-water light field to coincide as closely with solar noon as logistics allow. The sun zenith angle during the sampling carried out in three field work sessions are shown in figure 2.8.

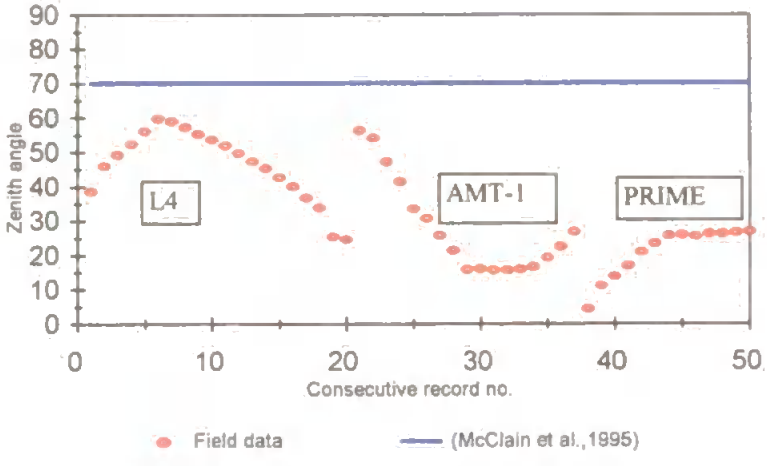

Figure 2.8. Sun zenith angle calculated for each field work sampling time and location. Also the cut-off (blue line) above which work should not be attempted. Consecutive record no. relates sequentially to the field sampling occasions during the campaigns as illustrated.

The blue line represents the flag for solar zenith angle of 70° suggested by McClain *et al.* (1995) which translates to a sub-surface angle of 45° (using equation 2.7). The rationale for this cut off was to limit uncertainty in radiometric atmospheric correction due to the extended path length at high solar zenith angles, as well as the high level of Fresnel reflectance which starts to increase rapidly at

this angle (70°), thus limiting the amount of light entering the water as well as increasing the optical path length between the water surface and the radiometer. These factors lead to erroneously high levels of Kd(λ) calculated from profiled radiometer data, and hence useful work should not be attempted. It can be seen from figure 2.8 that the work carried out during this study was at all times within this value.

2.5.3 The upward beam attenuation coefficient

Upwelling radiance is isotropic at shallow depths as the back-scattered light field is independent of the geometric distribution of the incident light. The upwelling light field is characterised using the same methodology as the downwelling light field, but from the $Lu(\lambda,z)$ profile (θ,ϕ are no longer required in the notation as the propagation is vertical) from which $Lu(\lambda,0^-)$ and $KL(\lambda)$ are derived by regression analyses. The term $KL(\lambda)$ is used to denote the upward beam attenuation coefficient as the measurement taken as $Lu(\lambda,z)$ by the PRR-600 is actually the upwelling component of $Eu(\lambda, z)$ measured over a small field of view looking vertically down. The upwelling radiance sensor is then viewing $Eu(\lambda, z)$ as described by equation 2.20:

$$Lu(\lambda,z) = Eu(\lambda,z) \cdot d\omega \qquad (2.20)$$

where dω is the field of view of the upwelling sensor. $Lu(\lambda,z)$ data were collected simultaneously with $Ed(\lambda,z)$.

As with the downwelling irradiance data, upwelling radiances are extrapolated to just below the surface ($z=0^-$) by least squares regression analyses, yielding in each case an average $Kd(\lambda)$ value representative of the profiled depth.

2.5.4 Water leaving radiance

The water leaving radiance measured by an above surface radiometer is the portion of light rays being emitted by the water surface after refraction pointing in the direction of the sensor, i.e. leaving the water within the instantaneous field of view (IFOV) of the sensor. The intensity of the water leaving radiance over the measured narrow bands relate to the intensity of a corresponding satellite image pixel once atmospherically corrected for that wavelength. During this study the measurement of $L_W(\lambda,0^-)$ was derived from the PRR-600 radiometer upwelling sensor measurements. In order to extrapolate this value through the surface, consideration has to be given to the effect of refraction on the emergent flux. The propagation of $Lu(\lambda,0^-)$ through the water-to-air interface to $Lw(\lambda,0^+)$ is carried out in the following manner, summarised in equation 2.21 (Mueller and Austin, 1995):

$$Lw(\lambda) = Lu(\lambda,0^-) \cdot \frac{1-\rho(\lambda,\theta)}{n_w^2} \qquad (2.21)$$

where n_w is the refractive index of sea water and ρ is the Fresnel reflectance of the water-air interface (0.02% at normal incidence). Equation 2.21 reduces to

$$Lw(\lambda,0^+) = Lu(\lambda,0^-)\cdot\frac{1}{n_w^2}$$

hence

$$Lw(\lambda,0^+ = Lu(\lambda,0^-)\cdot\frac{1}{1.34^2}$$

and so

$$Lw(\lambda,0^+) = Lu(\lambda,0^-)\cdot 0.5569 \qquad (2.22)$$

i.e. the emergent flux in any wavelength will be 55.7% as intense as it was at an infinitesimal distance below the surface, as the upwelling light field diverges due to refraction when passing through water-air boundary.

2.5.5 Normalised water leaving radiance

Water leaving radiance may be used as a direct measurement of ocean colour, but to standardise the radiometric input for in-water algorithms, and allow the comparison of different bio-optical data sets, it is necessary to normalise the measured *Lw(λ)*. One method of achieving this is to derive the normalised water leaving radiance, that is the equivalent value that would be derived if the sun were at the zenith, at the mean earth-sun distance, with all atmospheric effects removed. This process is summarised in equation 2.23 (Mueller and Austin, 1995).

$$Lwn(\lambda) = Lw(\lambda)\cdot\frac{\bar{F}o(\lambda)}{Es(\lambda,0^+)} \qquad (2.23)$$

where $\bar{F}o(\lambda)$ is the mean extra terrestrial irradiance, $Es(\lambda,0^+)$ is measured by a surface mounted radiometer conforming to the same specifications as the sub-surface unit , with logged measurements incorporated into the data stream being collected from the in-water profiler.

In this study $Es(\lambda,0^+)$ was only logged during AMT-1 as a result of additional instrumentation being deployed in tandem with the PRR-600 (see chapter 4). During the other programmes (the L4 survey and PRIME cruise) only in-water measurements of the light field were collected. The decision was therefore taken to use the remote sensing reflectance as the radiometric input into the algorithms, as described in the following sub-section.

2.5.6 Remote sensing reflectance

The remote sensing reflectance is a measure of the back-scattered light viewed over a small angle, radiance , $Lu(\lambda,z)$, as a function of the downwelling incident irradiance, $Ed(\lambda,z)$, (Kirk, 1994; Moore *et al.*, 1997):

$$Rrs(\lambda,0^+) = \frac{Lw(\lambda,0^+)}{Ed(\lambda,0^+)} \qquad (2.24)$$

For the purposes of algorithm development, $Rrs(\lambda.0^-)$ the values of $Lu(\lambda,z0^-)$ and $Ed(\lambda,z0^+)$ were calculated by extrapolation to a point an infinitesimal depth below the surface (0^-) which, derived from a line of best fit, represents a practical integration of the light field - water column interaction over the useable profiled depth (see chapter 5).

Because band ratio algorithms are employed in this study, extrapolation of $Rrs(\lambda)$ through the surface is not required as $Rrs(\lambda_i)$ and $Rrs(\lambda_j)$ are close so the interface effects are only weakly dependent upon wavelength (Aiken *et al.*, 1995). It will be noted that equation 2.25 will yield units for $Rrs(\lambda)$ of sr^{-1}, and that this will cancel out in the band ratio algorithm as $Rrs(\lambda_i)/ Rrs(\lambda_j)$.

2.5.7 THE DIFFERENCE BETWEEN USING $Lu(\lambda)$, $Lwn(\lambda)$ OR $Rrs(\lambda)$ AS THE RADIOMETRIC INPUT INTO ALGORITHMS

The previous sections (2.54, 2.55 and 2.56) detail three commonly used mathematical expressions of ocean colour. During the developmental stages of semi-analytical remote sensing algorithm generation, the inputs (light field and in-water constituent data) must be representative of those that will be required when operational, *i.e.* must emulate the characteristic optical signature of the waters resulting from the its biogeochemical contents. Past studies have used various inputs, table 2.2 details the results of some of these studies.

Table 2.2 Sample of $Kd(\lambda)$ algorithms generated by other investigators.

Investigators	$Kd(\lambda)$ (m^{-1})	band ratio radiometric input:	A	B	R^2(%)	Kw (m^{-1})
Austin and Petzold, (1981)	$Kd(490)$ $Kd(520)$	$Lu(\lambda,z,\theta,\phi)$	0.088 0.066	-1.491 -1.398	90.1 99.5	0.022 0.044 Smith and Baker (1978)
Moore *et al.* (1997)	$Kd(490)$	$Rrs(\lambda,0^-)$	0.129	-1.337	n/a	0.0192 Pope and Fry (1997)
Mueller and Trees, (1997)	$Kd(490)$	$Lwn(\lambda,z,\theta,\phi)$	0.1	-1.3	90.0	0.022 Smith and Baker (1978)

The relationship between *Lu(i:j)* will describe the variability in back scatter of the water at the two wavelengths, *i* and *j* (assuming no spectral dependence of the downwelling light field due to the interface effects). This measurement, however, although representative of the colour of the ocean as it would be seen above the surface at that instant, requires further information about the nature of the incident irradiance to be included in the measurement for comparisons to be made with data collected at different sites. From section 2.5.4, equation 2.21, it may be seen that there is a robust mathematical relationship relating the subsurface upwelling radiance with the above surface water leaving radiance. Once established, the water leaving radiance, *Lw(i:j)*, may be normalised to the incident irradiance to derive the reflectance. It is this value of 'what returns as a function of what goes in' which is used for the generation of algorithms as such data may be related to the similar optical parameter sensed remotely. *Lwn(λ)* and *Rrs(λ)* are both expressions of reflectance, *Lwn(λ)* is a function of the water leaving radiance normalised to an idealised incident irradiance (discussed in section 2.5.4); *Rrs(λ)* is a function of the water leaving radiance normalised to the downwelling incident irradiance above the sea surface at the time of profiling.

From equations 2.23 and 2.24 it may be seen that the difference between *Lwn(i:j)* and *Rrs(i:j)* is $\bar{F}o(i) / \bar{F}o(j)$ which amounts numerically to $198.5 \mu W\, cm^{-2} nm^{-1} / 190.0 \mu W\, cm^{-2} nm^{-1} = 1.045$ where i=443*nm* and j =555*nm* (Greg and Carder, 1990). If converting an algorithm that uses *Lwn(i:j)* to use *Rrs(i:j)*, the ratio derived above will have the effect of changing the value of the empirical constraints of a two-band ratio algorithm of the form $x=A[R(i:j)]^B$ where the revised $A = A[\bar{F}o\,(i:j)]^B$.

2.6 AN EXAMPLE OF WATER COLOUR CHARACTERISTICS DERIVED FROM THE MEASUREMENT OF THE APPARENT OPTICAL PROPERTIES

Figure 2.9 illustrates an example of data, derived from a processed PRR-600 profile, and shows the relationship between the light arriving at the outer edge of the atmosphere (Greg and Carder, 1990), the corresponding irradiant light intensity measured just below the water surface, $Ed(\lambda,0^-)$, and the corresponding emergent flux also measured just below the surface, $Lu(\lambda,0^-)$.

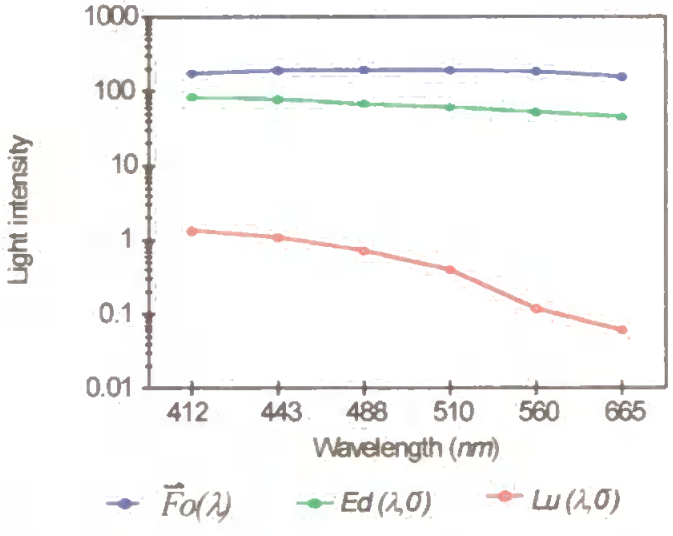

Figure 2.9 Values over the SeaWiFS bands for $Lu(\lambda,0^+)$ derived from profile measurements. Also displayed are corresponding $Ed(\lambda,0^+)$ data and $\bar{F}o(\lambda)$ (the extraterrestrial solar constant). The units for $Ed(\lambda,z)$ and $\bar{F}o(\lambda)$ are $\mu W\,cm^{-2}nm^{-1}$ and for $Lu(\lambda,z)$ and are $\mu W\,cm^{-1}nm^{-2}sr^{-1}$.

The difference between the top curves, from $\bar{F}o(\lambda)$ to $Ed(\lambda,0^+)$, are due to the attenuation of the incident beam as it propagates through the atmosphere and the sea surface.

2.7 THE OPTICAL DEPTH

From Beer-Lambert's law (equation 2.18) it can be seen that the diminution of irradiance is controlled by e^{-x}, where $-x$ is the exponent, $Kd(\lambda) \cdot z$. This is the geometric distance times the diffuse attenuation coefficient $Kd(\lambda)$, this is termed the optical depth, $\gamma(\lambda)$. This which describes the depth to which a certain diminution of irradiance will result for a given physical depth (Kirk, 1994) as detailed in equation 2.25:

$$\gamma(\lambda) = Kd(\lambda).z \qquad (2.25)$$

e.g. at 4m, and a $Kd(490)$ of 0.026m^{-1}: $\gamma(\lambda)$ = 0.026 x 4 = 0.104.

Significant optical depths are those employed by workers involved in studies of primary productivity, where knowledge of light level depths to characterise the waters under study may be obtained from ζ=2.3, where $Ed(\lambda,z) = 0.1 \times Ed(\lambda,0^-)$ and ζ=4.6, where $Ed(\lambda,z) = 0.01 \times Ed(\lambda,0^-)$.

2.8 THE DIFFUSE ATTENUATION LENGTH

An often used assessment of the relationship between the attenuation of the underwater light field and $Kd(\lambda)$ is the use of the attenuation length, $\pounds_k(\lambda)$, which is $1/Kd(\lambda)$. For instance if $Kd(490)$ is calculated from the measured profile as $0.026m^{-1}$, then 1 attenuation length = 1/0.026 = 38.5*m*. The diminution of irradiance over $\pounds_k(\lambda)=1$ may be seen from equation 2.26:

$$Ed(\lambda,z) = Ed(0) \times \exp[-Kd(\lambda) \cdot 1/Kd(\lambda)] \quad (2.26)$$

which is e^{-1} or 37%.

The diffuse attenuation length is the depth above which 90% of the back-scattered irradiance emanates, and so is considered to be the depth to which a remote sensor receives information relating to the optical properties of the waters. The diffuse attenuation length describes a diminution of irradiance regardless of physical depth.

2.9 THE BASIS OF THE BAND RATIO APPROACH FOR THE DEVELOPMENT OF ALGORITHMS DESIGNED TO DERIVE THE CONCENTRATION OF IN-WATER CONSTITUENTS FROM OCEAN COLOUR

The flux emergent from the water surface is a function of the downwelling light field, the interface effects and the inherent optical properties. Band ratio algorithms work on the principle that a variable to be retrieved (e.g. the [CHL-*a*], [SPM] and/or $Kd(\lambda)$) is empirically related to the intensity of the upwelling light field in one or more wavebands. In this manner an analytical approach to the

determination of optical properties is used to propose the form of the algorithm, while empirical relationships are used to determine the numerical coefficients (Aiken *et al.*, 1995; Moore *et al.*, 1997).

The radiometric input used in this study is the *Rrs* at two wavelengths *i* and *j*. The value of $Rrs(\lambda)$ for any given wavelength is determined by the downwelling light field, the interface effects and the inherent optical properties. $Rrs(\lambda,0^+)$, may therefore be expressed analytically as

$$Rrs(\lambda,0^+) = \frac{(1-\rho)(1-\tilde{\rho})\cdot R(\lambda,0^-)}{Q.n_w^2(1-r\cdot R(\lambda,0^-))} \qquad (2.27)$$

where n_w is the refractive index of sea water, $R(\lambda,0^-)$ is the irradiance reflectance an infinitesimal distance below the sea surface, ρ is the Fresnel reflectance at normal incidence and is 0.02 for the visible spectrum, $\tilde{\rho}$ is the Fresnel reflectance for sun and sky irradiance which ranges from 0.021 for a nadir sun angle to 0.064 for a solar zenith angle of 60°, and for totally diffuse skylight has a value of 0.066, giving a mean value of 0.043. The *r* term is the water to air reflectance for totally diffuse irradiance and is 0.48, Q is the underwater irradiance-to-radiance ratio ($Eu(\lambda)/Lu(\lambda)$), which is only weakly dependent upon wavelength. This would be π for a Lambertian reflector, but from the work of Kirk (1994) may be closer to 5. The $(1-\rho)(1-\tilde{\rho})n_w^{-2}$ term accounts for the effect of the air/sea interface and shows a weak relationship with wavelength, varying with the refractive index of water. The $(1-r\cdot R(\lambda,0^-))$ term can be ignored in case one waters where $R(\lambda,0^-)$ has a maximum value of 0.08-0.1.

Assuming the interface term is constant, the ratio of remote sensing reflectances at wavelengths *i* and *j* is expressed as

$$Rrs(i:j,0^+) = \frac{R(\lambda i,0^-)\cdot Q(\lambda j)}{R(\lambda j,0^-)\cdot Q(\lambda i)} \tag{2.28}$$

where *Rrs(i:j)* is shorthand for the ratio $Rrs(\lambda i)/Rrs(\lambda j)$.

As *Q* has a very weak dependence on wavelength over this range (Aiken *et al.*, 1995) the main determinand of the radiance ratio is the irradiance reflectance, $R(\lambda)$, which may be expressed as

$$R(\lambda) = G(\mu_0,\lambda)\left[\frac{b_b(\lambda)}{a(\lambda)+b_b(\lambda)}\right] \tag{2.29}$$

where the $G(\mu_0,\lambda)$ term represents the wavelength dependence of *R* on the cosine of the refracted solar beam just below the surface. The back-scattering, $b_b(\lambda)$, and absorption, $a(\lambda)$, coefficients (m^{-1}) are the inherent optical properties and are the sum of the optical properties of pure sea water and the optically active in-water constituents.

By the contemporaneous collection of the remote sensing reflectance using profiling radiometry and in-water measurements of downwelling irradiance and upwelling radiance, the analytically derived form of the algorithm may be constrained by the empirically derived numerical coefficients determined from analysis of field data.

3. REMOTE SENSING ALGORITHMS

In chapter 2 the analytical basis to the band ratio approach to algorithm development was introduced. The algorithms presented in this section are designed to calculate two products from upwelling radiances derived from a satellite image, or modelled from profiled radiometry. The products are (i) the diffuse attenuation coefficient, *Kd*(490) (m^{-1}), see section 3.1, and (ii) the surface mixed layer pigment concentration in terms of chlorophyll-*a* ($mg\ m^{-3}$), see section 3.2.

3.1 ALGORITHMS FOR THE DERIVATION OF THE DIFFUSE ATTENUATION COEFFICIENT

Since the derivation of water leaving radiances had become routinely available over large spatial scales from CZCS ocean colour satellite imagery, a method existed for the derivation of optical properties of the surface waters of the world's oceans, to estimate the nature and scale of variability across the globe.
A highly robust relationship relating the upwelling light field with the diffuse attenuation coefficient was presented by Austin and Petzold (1981) as part of the Nimbus Experiment Team (NET) CZCS ground truthing campaign. The form of the relationship is shown in equation 3.1:

$$Kd(\lambda_1) = A\left[\frac{Lu(\lambda i)}{Lu(\lambda j)}\right]^B + Kw(\lambda_1) \qquad (3.1)$$

where $Kd(\lambda_1)$ is the diffuse attenuation coefficient at the required wavelength and $Kw(\lambda_1)$ is the diffuse attenuation coefficient of the purest water at that wavelength. λ_i and λ_j are the wavelengths of the optical measurements that are significantly affected by the water property under consideration, and form the radiometric input into the model. The algorithm is constrained by the empirically derived constants, *A* and *B*, which are determined by naperian log-log regression of the $Kd(\lambda_1)$-$Kw(\lambda_1)$ ratio against corresponding light-field measurements.

The radiometric input into the Austin and Petzold (1981) algorithm was the ratio of measured upwelling radiance *Lu(i:j)*, where *i* was 443*nm* and *j* was 550*nm* from a data set consisting of 88 points. Two algorithms were developed to determine *Kd*(490) and *Kd*(520), as illustrated in equations 3.2 and 3.3 respectively.

$$Kd(490) = 0.0883\left[\frac{Lu(443)}{Lu(550)}\right]^{-1.491} + 0.022 \qquad (3.2)$$

$$Kd(520) = 0.0663\left[\frac{Lu(443)}{Lu(550)}\right]^{-1.398} + 0.044 \qquad (3.3)$$

where the values of *Kw*(490) and *Kw*(520) were those determined by Smith and Baker (1978).

This technique has since been re-evaluated by Moore *et al.* (1997) and Mueller and Trees (1997), in support of the NASA-SeaWiFS programme.

3.1.1 The SeaWiFS pre-launch *Kd*(490) algorithm (Mueller and Trees, 1997)

In the early stages of the SeaWiFS project, equation 3.2, was officially adopted as the pre-launch algorithm for the derivation of *Kd*(490). Consideration was then given to the effect upon the retrieval of optical properties using the standardised radiometric input proposed by the SeaWiFS community, normalised water leaving radiance, *Lwn(λ)*. Also considered was the potential effect upon the algorithm performance of the wavelength shift from detection of upwelling radiances over a 20*nm* band centred at 550*nm* to a 10*nm* band centred at 555*nm*. A new algorithm was therefore generated, following the same form as equation 3.2, using a data set of 242 measurements collected during cruises in the Arabian sea, one cruise in the Gulf of California and the First Atlantic Meridional Transect. A linear regression of the relationship between ln[*Kd*(490))-*Kw*(490)] and ln[*Lwn(i:j)*] yielded:

$$Kd(490) = 0.1\left[\frac{Lwn(443)}{Lwn(555)}\right]^{-1.3} + 0.022 \qquad (3.4)$$

where *Kw*(490) is the value determined by Smith and Baker (1978). This algorithm has been recommended to the scientific community as the definitive method of determining *Kd*(490) from scenes imaged by SeaWiFS.

3.1.2 The SeaWiFS *Kd*(490) algorithm (Moore *et al.*,1997)

During the analysis of data from the Atlantic Meridional Transect cruise series, equation 3.4 was re-worked to take advantage of advances in the determination of the diffuse attenuation coefficient for pure water by Pope and Fry (1997). The modification is included in equation 3.5.

$$Kd(490) = 0.129\left[\frac{Rrs(443)}{Rrs(555)}\right]^{-1.337} + 0.01922 \qquad (3.5)$$

where *Kw(*490*)* is the value determined by Pope and Fry, (1997). It was reported by Moore *et al.* (1997) that the incorporation of this new value for *Kw(*490*)* resulted in the linearity of the relationship between ln[*Rrs(i:j)*] and ln[$Kd(\lambda_1)$-$Kw(\lambda_1)$], (where λ_i was 443*nm*, λ_j was 555*nm* and λ_1 was 490*nm*), at low values of *Kd(*490*)*.

3.2 THE PIGMENT ALGORITHMS

The two band ratio pigment algorithms presented here are of the classic type by Clark (1981), that arose from the CZCS validation and calibration effort, and a more recent algorithm by Moore *et al.* (1997), based on work undertaken by Aiken *et al.* (1995), which proposed a refined model that generated an algorithm employing a hyperbolic analytical fit to the relationship between the light field band ratio and the CHL-*a* concentration.

A remote sensing system senses back scattered light over a translucent layer which raises the issue of what constitutes the surface pigment concentration in stratified waters which leads to vertical variability in the phytoplankton concentration. Clark (1981) investigated the effect upon the concentration of chlorophyll-*a* and concluded that no statistically significant difference existed between the surface chlorophyll-*a* concentration and a value derived from the application of an optical weighting function calculated from the pigment profile for a data set containing 55 profiles. The uncertainty in the determination of pigment concentrations by high performance liquid chromatography (HPLC – see chapter 6) is ±20% (Latasa *et al.*, 1996) which would indicate that the variability in the pigment concentration used for algorithm development due to the measurement technique can far exceed variability due to sub-surface stratification.

3.2.1 The CZCS pigment algorithm (Clark, 1981)

This algorithm (equation 3.6) was developed for case 1 waters and retrieves the combined concentration ($mg\ m^{-3}$) of CHL-*a* and CHL-*a* like pigments from CZCS imagery using the ratio of the irradiance reflectances measured at 440*nm* and 550*nm*. The rationale for choosing these wavelengths relates to the absorption characteristics of CHL-*a*, which has a maximum absorption at 443*nm* and a minimum close to 550*nm* (Hall and Rao, 1981; Jeffrey *et al.*, 1997).

$$(\text{CHL-}a + \text{phaeophytin-}a) = 1.32\left[\frac{R(440)}{R(550)}\right]^{-1.42} \qquad (3.6)$$

where $R(\lambda,0^+)$ is the irradiance reflectance, *Eu/Ed*. The constants are empirically derived by log-log regression. The PRR-600 does not directly measure $Eu(\lambda)$, so Q, the theoretical ratio of $Eu(\lambda)$ to $Lu(\lambda)$ was taken as π to convert $Lu(\lambda,0^-)$ to $Eu(\lambda,0^-)$, which formed the radiometric input into the model.

3.2.2 The CZCS-type SeaWiFS global pigment algorithm (Aiken *et al.*, 1995; Moore *et. al.*, 1997)

This case 1 CHL-*a* algorithm is derived from investigations undertaken upon pre-launch SeaWiFS bio-optical data collected during calibration and validation exercises, as well as the extensive use of climatological data bases. The algorithm constraints were then re-calculated by Moore *et al.* (1997) where the relationship was re-analysed to accept $Rrs(\lambda,0^-)$ as the radiometric input. This work resulted in equation 3.7.

$$\text{CHL-}a = \left[\frac{\left(Rrs(\lambda i)\,/\,Rrs(\lambda_2)\right) - C}{C.(A_1 - A_2).\left(Rrs(\lambda j)\,/\,Rrs(\lambda_2)\right)}\right]^B \qquad (3.7)$$

The final parameters for the curve fit (to the empirical relationship) were A_1 = 0·764, A_2 = 32·29, B = 0·88, C = 19.63 where $Rrs(\lambda_i)$, $Rrs(\lambda_j)$ are the remote sensing reflectances, $Lu(\lambda,0^-)/Ed(\lambda,0^-)$, at 443*nm* and 555*nm* respectively.

The results of the application of the algorithms presented here to the radiometry carried out during this work may be found in the data analysis section (chapter 8), where comparisons are made with contemporaneous in-situ data.

4. OPTICAL METHODOLOGY

The following section details the protocols that were followed during preparation for, and execution of, the field radiometry. The Biospherical Instruments Inc. Profiling and Reflectance Radiometer (PRR-600) was purchased in advance of the launch of SeaWiFS to undertake satellite calibration and validation work. The instrument was supplied by the manufacturers for this purpose, which meant that it had to meet the challenging specifications contained in the Ocean Optics Protocols for SeaWiFS validation, volume 5 (Mueller and Austin, 1992) and the revision that constituted volume 25 of the same series (Mueller and Austin, 1995).

Because of the complex nature of the measurement of light, and the need to account for and minimise all potential errors, the instrument was subjected to on-going characterisation to ensure that the most appropriate method of deployment was executed from all the platforms used.

During AMT-1 the ocean colour measurement programme was undertaken in collaboration with NASA personnel using a specialised deployment technique which allowed the simultaneous collection of data from two discrete radiometer systems: the PRR-600 and the Canadian Satlantic SeaWiFS profiling radiometer. A full description of the methodology was presented in the AMT-1 cruise report, Robins *et al.*, (1996).

4.1 THE PRR-600

The PRR-600 is a purpose built SeaWiFS band profiling radiometer which measures downwelling irradiance, $Ed(\lambda,z)$ and upwelling radiance $Lu(\lambda,z)$. Figure 4.1 shows the major features of the underwater module and table 1 the operational specifications.

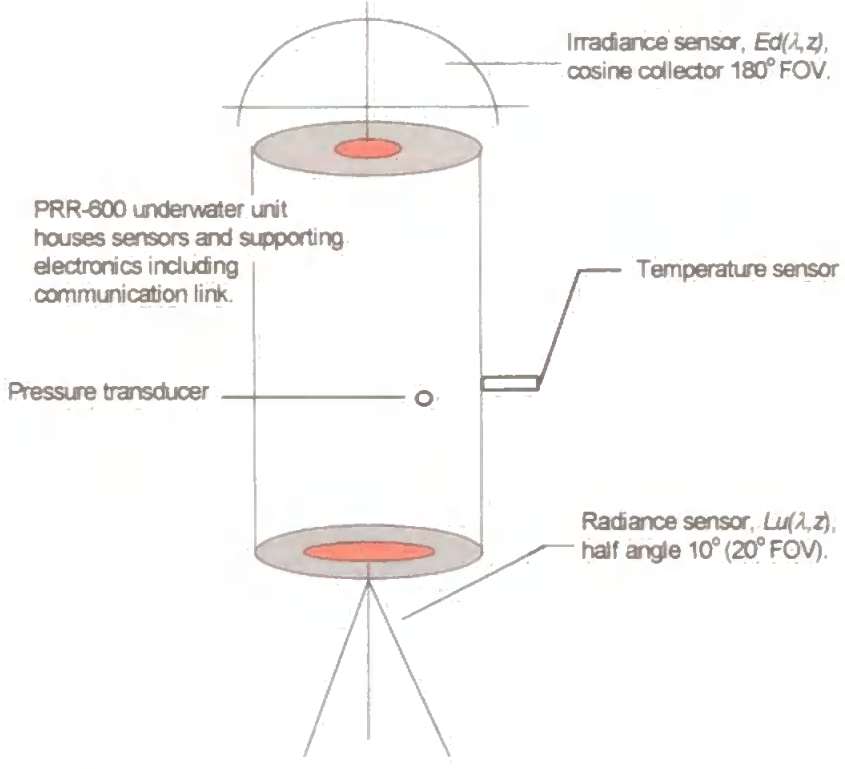

Figure 4.1 Schematic of the Biospherical Instruments Inc. PRR-600 underwater unit.

The unit is of robust construction, capable of withstanding 26 bar within its margin of safety. Data collection is via analogue to digital converter (housed in the underwater unit) and then RS422 interface (for communication cable lengths in excess of 50*m*). The digitised signal is then converted to RS232 for transfer from a

battery or mains powered deck box to a personal computer (PC). Management of the instrument is by a sophisticated disk operating system (DOS) driven package of programmes provided by the manufacturers, which includes a high level user interface. During deployment, selected calibrated data are available in real time either by channel or as a graphical representation.

Table 4.1 Summary of the PRR-600 operational specifications.

$\lambda(nm)$	TAG	CH	General notes (see also appendix 2).
Ed(412)	0	1	Downwelling irradiance sensor, $Ed(\lambda,z)$.
Ed(443)	0	2	Units: $\mu W\,cm^{-2}nm^{-1}$
Ed(488)	0	3	Field of view: 180° (cosine collector).
Ed(510)	0	4	
Ed(560)	0	5	
Ed(665)	0	6	
PAR	0	7	Units: $\mu Ecm^{-2}sec^{-1}nm^{-1}$. This measurement represents an integration of the energy sensed over 400*nm* -700*nm*.
Ed(GND)	0	8	Irradiance sensor Ground
Temp.	0	9	Platinum resistance thermometer. Units: °C.
Depth	0	10	Piezo electric pressure transducer; range 0*m* - 200*m*.
Lu(412)	1	1	Upwelling radiance sensor, $Lu(\lambda,z,\theta,\phi)$.
Lu(443)	1	2	Units: $\mu W\,cm^{-2}nm^{-1}sr^{-1}$
Lu(488)	1	3	Field of view: 10° half angle in water.
Lu(510)	1	4	
Lu(560)	1	5	
Lu(665)	1	6	
Lu(683)	1	7	
Lu(GND)	1	8	Radiance sensor ground

4.1.1 Downwelling irradiance sensor

The physical basis of the cosine collector is the Lambertian diffuser (figure 4.2). This is a material that effectively diffuses an incident light beam or field (be it collimated, diffuse or both) by the nature of the microstructure of the material and the intense scattering effect it has on the light propagating through it.

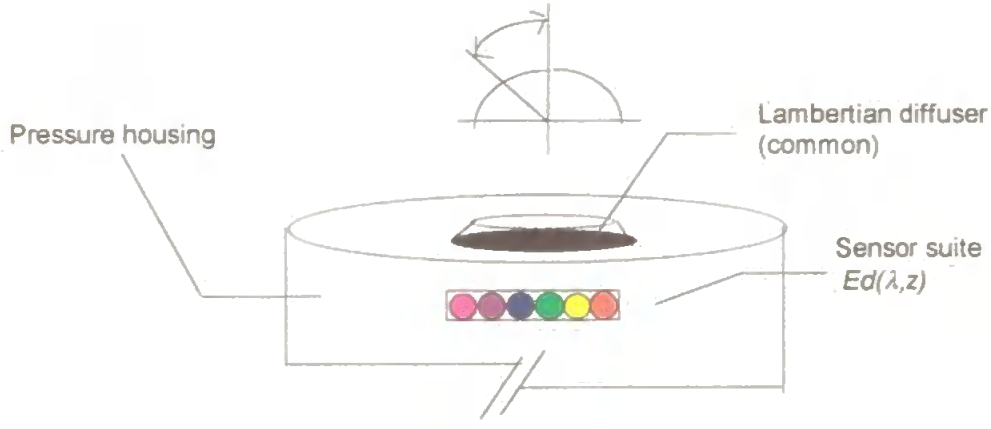

Figure 4.2 The PRR-600 downwelling irradiance cosine collector.

Typical materials used to achieve full incident light field diffusion are opal glass or teflon; the latter is used in the PRR-600. The instrument response changes in accordance with the angle of incidence of the light arriving at the face of the diffuser (described by the zenith, θ, angle). The photodiode response is inversely proportional to the zenith angle, i.e. the measured irradiant light will vary by the cosine of this angle.

4.1.2 Upwelling radiance sensor

In order to simulate ocean colour as it would be viewed by satellite, the sensor is required to view the upwelling irradiance over a small solid angle as illustrated in figure 4.3.

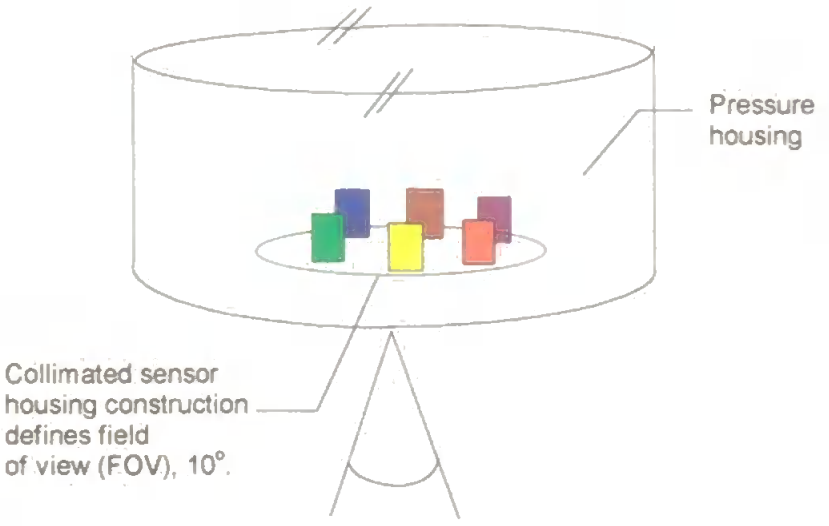

Figure 4.3. The PRR-600 upwelling radiance sensor head, $Lu(\lambda,z)$.

4.1.3 Instrument calibration

The calibration of light sensors is an evolving branch of research into marine optics, and consequently the accurate calibration of an instrument such as the PRR-600 was for the most part left to the manufacturer and personnel at the National Institute for Standards and Technology (NIST) with further characterisation (such as field of view, FOV, and spectral analyses) carried out at PML by the author.

The PRR-600 was initially calibrated by the manufacturers prior to purchase in 1993. The instrument subsequently developed a fault in its $Lu(443)$ channel and was returned for repair and re-calibration prior to the commencement of the fieldwork.

After extensive use in parallel near shore optical oceanographic research programmes, the PRR-600 was deployed during AMT-1. After deployment the instrument was sent to NIST for further calibration.

4.1.3(i) PRR-600 Calibration history

Programmed calibrations were carried out at the following times (full intensity calibrations are in italic):

Cal.1: At Biospherical Instruments Inc. post manufacture 1993

Cal.2: At Biospherical instruments Inc. December 1994

Cal.3: At PML during July 1995

Cal.4: At NIST post AMT-1, December 1995

Cal.5: At PML August 1996

Cal.6: At PML August 1997

4.1.3(ii) Downwelling irradiance sensor calibration

To calibrate the irradiance sensor the instrument was mounted such that the $Ed(\lambda)$ head viewed a stable light source at a series of fixed distances; care was taken that all additional light was excluded from the working area. Net voltage readings were calculated for the instrument and the standard reference photodiode at each incremental distance from the light source. If the standard SeaWiFS lamp was used (as was the case at NIST and PML) then a reference photodiode was not

required as the output of the standard SeaWiFS lamp was precisely known, provided the correct power management protocols were observed.

Two stages of processing established the linearity of the instrument response, enabling a calibration curve of volts per irradiance unit to be established. By applying these data to the voltage readings derived from optical profiles in the field, absolute irradiance values were obtained for each instrument scan. Linearity checks were carried out at PML, the details of which are given in section 4.1.6.

4.1.3(iii) Upwelling radiance sensor calibration

The upwelling light field in natural waters is diffuse so in order to calibrate a sensor designed to make such a measurement this light field must be re-created using a standard lamp viewed via a diffuse reflector.

There are two methods of calibrating a radiance sensor (i) by transferring the calibration via an integrating sphere from an irradiance sensor, in effect measuring irradiance, then calculating what would be sensed of that same light field when viewed over a small angle or (ii) by placing a Lambertian plaque at a fixed point in front of the light source, and arranging that the radiometer views it at as narrow an angle as possible; in this way the incident irradiance is transferred to the radiometer, modified by the inherent reflectance efficiency of the plaque. The linearity check is made possible by altering the distance between the radiometer and the plaque. It was not possible to do this at PML due to the fixed geometry of the apparatus and the wide field of view in air of the sensor head. For this reason the calibration supplied by the manufacturers and NIST was used.

4.1.4 Spectral characteristics of the instrument

Full spectral analyses were carried out for each channel to assess the out of band blocking efficiency from 300*nm* to 800*nm*, with more detailed characterisation in the region of specified band pass. These analyses enabled the calculation of the Full Half Wave Maximum value, FHWM, for each sensor (the spectral bandwidth at 50% of the response).

The location of the monochromator grating was checked using a 632*nm* helium-neon LASER. The LASER output is by definition monochromatic and there was a perfect correspondence between the LASER and the wavelength indicated by the monochromator. Once the spectral analyses were complete, the response of the reference photodiode to the monochromator lamp was measured to determine the relative response of the PRR-600 at each wavelength. It can be seen from figures 4.4 and 4.5 that the response in the blue end of the spectrum (at 412*nm* and 443*nm*) produced an inconclusive normalised function due to the very low output from the monochromator light source in this range.

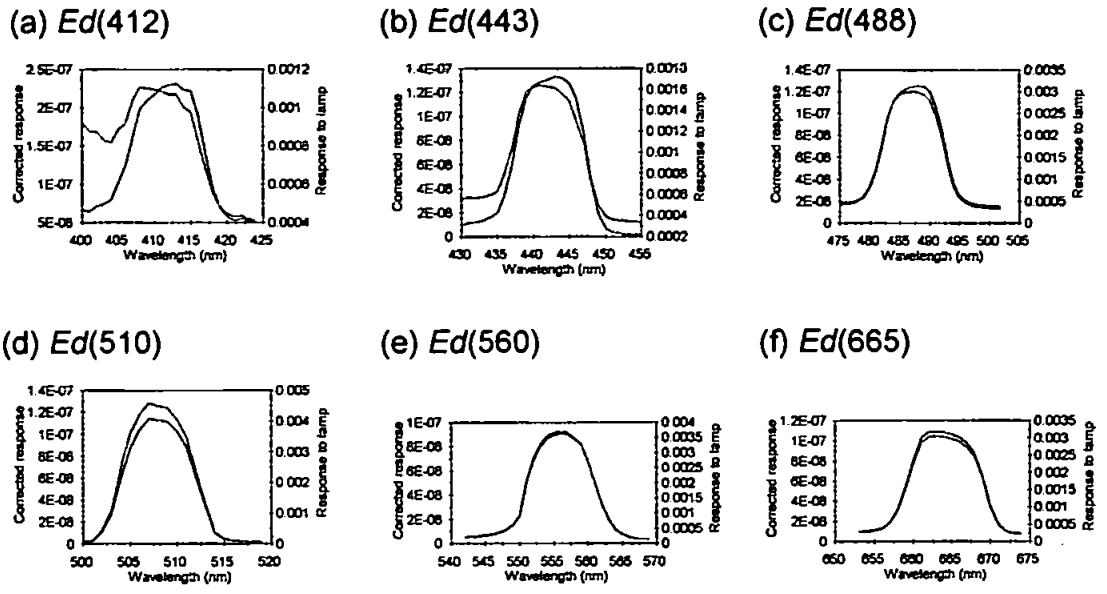

Figure 4.4. Spectral response of the PRR-600 downwelling irradiance sensors. The blue line is the instrument response to the monochromator light source at each wavelength, the green line is the response corrected for the variable lamp output.

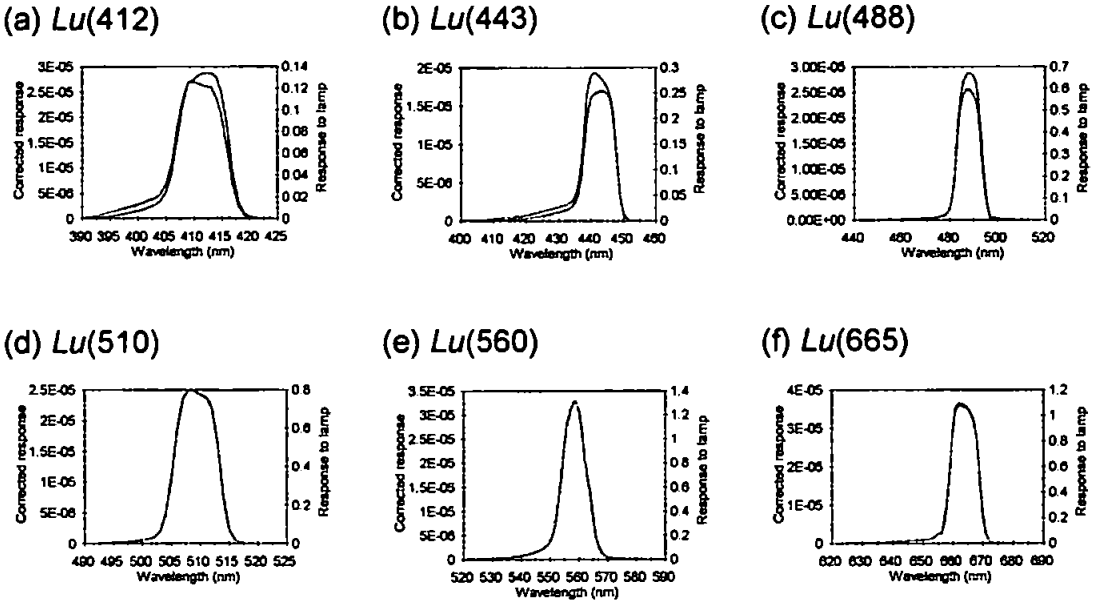

Figure 4.5. Spectral response of upwelling radiance sensors. The blue line is the instrument response to the monochromator light source at each wavelength, the green line is the response corrected for the variable lamp output.

Table 4.2. PRR-600 spectral analysis.

Band *(nm)*	Band centre *(nm)*	FHWM - Start λ*(nm)* and end λ*(nm)*	FHWM *(nm)*
Ed(412)	413	405-418	13
Ed(443)	443	437.5-447.5	10
Ed(488)	488	482-492	10
Ed(510)	507	504-512	8
Ed(560)	556.5	551-561	10
Ed(665)	663	659-669	10
Lu(412)	412	407-416	9
Lu(443)	443	438-448	10
Lu(488)	488.5	483-493.5	10.5
Lu(510)	508	505-513	8
Lu(560)	559	554-563	9
Lu(665)	662	659-669	10

It can be seen from table 4.2 that the spectral response of the PRR-600 matches very closely the manufacturers specifications, although the 560*nm* irradiance sensor was -3.5*nm* from its specification and -2.5*nm* from the corresponding upwelling sensor.

4.1.5 Instrument responsivity, snr and resolution

In order to be effective in the field the PRR-600 had to meet certain minimum specifications for responsivity, signal to noise and resolution, (Mueller and Austin, 1995).

4.1.5(i) Responsivity

Table 4.3 shows the PRR-600 band-set and how it compares with those of the SeaWiFS sensor. It can be seen that the green *(560nm)* channel did not conform to the protocols set out by Mueller and Austin (1995), which stipulate the selection of bands to within ±1*nm* for 443*nm* and 410*nm* channels, and ±2*nm* for all other spectral bands (with the centre wavelength known to 0.2*nm*). The reason for this is

that the 560*nm* band was removed from the specifications after the PRR-600 was constructed (Mueller and Austin, 1992; Mueller and Austin, 1995).

Table 4.3, PRR-600 spectral sensitivity (Mueller and Austin, 1995; Biospherical Instruments Inc., 1995).

Band	**SeaWiFS Wavelengths (FWHM- *nm*, and centre λ).**		**SeaWiFS bands recommended by Mueller and Austin, 1995 for in water radiometers.**	**PRR-600 bands (centre λ)**	**SeaWiFS offset**
1	402-422	(412)	412	412	0
2	433-453	(443)	443, 435	443	0
3	480-500	(490)	490	488	-2
4	500-520	(510)	510	510	0
5	545-565	(555)	555	560	+5
6	660-680	(670)	665, 683	665	0
7	745-785	(765)	-	-	
8	845-885	(865)	-	-	

The instrument was supplied by the manufacturers to meet the SeaWiFS protocols with regard sensitivity, giving an $Ed(\lambda,z)$ saturation value of 200$\mu W\, cm^{-2} nm^{-1}$ over all wavelengths (Mueller and Austin, 1995).

Saturation of upwelling radiances, $Lu(\lambda,z)$, in case 1 waters were expected to vary slightly across the spectrum from $7.5\mu W\,cm^{-2}nm^{-1}sr^{-1}$ at $410nm$ to $24\mu W\,cm^{-2}nm^{-1}sr^{-1}$ at $488nm$ and $8\mu W\,cm^{-2}nm^{-1}sr^{-1}$ at $665nm$. These case 1 saturation values are based on estimates of the expected reflectance in case 1 waters: 12.5% at $410nm$, 7.5% at $488nm$, and 0.5% at $670nm$ (Mueller and Austin, 1995).

4.1.5(ii) Signal to noise ratio, snr

Mueller and Austin (1995) suggest that the *A* to *D* converter must enable digital resolution to ≤ 0.5% of the light field reading to maintain a better than 100:1 snr. To maintain 1% accuracy in calibration it is necessary to digitally resolve 0.1% of the radiance produced by the laboratory standards, e.g. the NIST $1000W$ standard lamp. The PRR-600 *A* to *D* converter is specified as a bi-polar 12 bit unit with sufficient resolution to satisfy the protocols.

4.1.6 Instrument linearity and stability

During operational use the instrument was checked for (i) linearity of response and (ii) stability of that response in the field when deployed in regimes of widely varying temperature.

4.1.6(i) Linearity check

A linearity check of the instrument was attempted against the standard SeaWiFS lamp on two occasions. Data shown in figure 4.6, and table 4.4 were collected during analysis of the response of the irradiance sensor, and show a high degree of stability over the range of measurement possible at the PML calibration facility. These data were modified by the inverse square law for irradiance to normalise the response to the changing light field with distance from the calibration source. The inverse square law for irradiance states that:

$$E(\lambda) \propto \frac{1}{X^2} \tag{4.1}$$

where $E(\lambda)$ is a value determined for irradiance and X is the distance from the source at which the measurement was taken. From equation 4.2 it can be seen that, assuming that the response of the instrument is linear:

$$E(\lambda) = k \cdot \left(\frac{1}{X^2}\right) \quad \text{and hence} \quad k = E(\lambda) \cdot X^2 \tag{4.2}$$

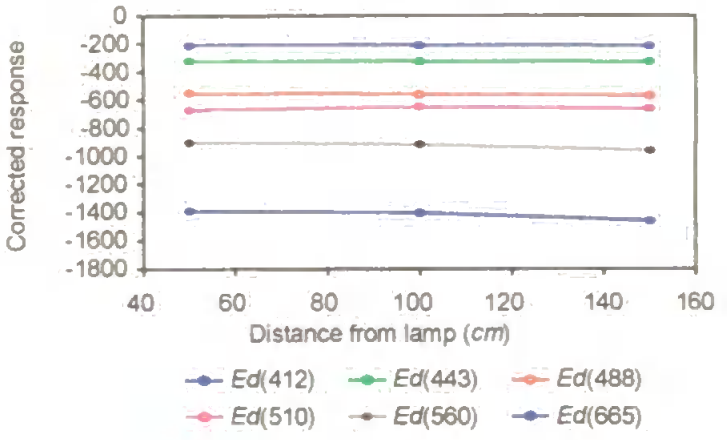

Figure 4.6. $Ed(\lambda)$ sensor linearity check.

The allowable uncertainty in linearity of the sensor and/or supporting electronics is 0.1% of any reading, within the normal operating range of the instrument (Mueller and Austin, 1995).

Table 4.4. Summary of $Ed(\lambda)$ sensor linearity analysis.

Irradiance sensor (*nm*)	***Ed*(412)**	***Ed*(443)**	***Ed*(488)**	***Ed*(510)**	***Ed*(560)**	***Ed*(665)**
Mean response (*V*)	-212.29	-323.69	-560.54	-661.5	-926.78	-1418
avg. deviation from mean	3.49	3.68	7.47	8.25	22.5	28.66
% deviation from mean	1.64%	1.13%	1.27%	1.24%	2.73%	2.03%

The data presented above demonstrate that the PRR-600 greatly exceeds this figure in all the irradiance sensors. It was not possible to carry out this analysis for the upwelling radiance sensor due to the wide field of view in air (see section

4.1.3(iii)). After consideration it was determied that the optical facility employed in this experiment, which is under continual development, lacked sufficient sensitivity to undertake such a characterization and as such the analyses must be considered experimental.

4.1.6(ii) Stability of the instrument dark offsets during the field campaigns

As is the case with any electronic circuit, the efficiency of operation depends upon the operating temperature, i.e. the cooler the circuit, the more efficiently it will operate. The thermal environment in which optical sensors are deployed differs widely and the sensor design needs to accommodate this. Figure 4.7 illustrates the voltages that were derived from the PRR-600 when all light was excluded (instrument dark readings) prior to immersion during the fieldwork that took place during 1995. As a matter of routine, dark voltages were collected by continuing data collection with the protective caps on the radiometer post profiling, when the instrument had reached thermal equilibrium with the surrounding water. Data in figure 4.7(a) show how the dark offsets varied with the ambient temperature prior to immersion, illustrated in figure 4.7(b) and (d). Figure 4.7(c) shows in more detail the variation in instrument dark offset for the *Ed*(510) channel. These data, as they were collected on the deployment platform deck, represent extremes of operating temperature and, if uncorrected, could give rise to erroneous measurements of $Ed(\lambda)$ and $Lu(\lambda)$.

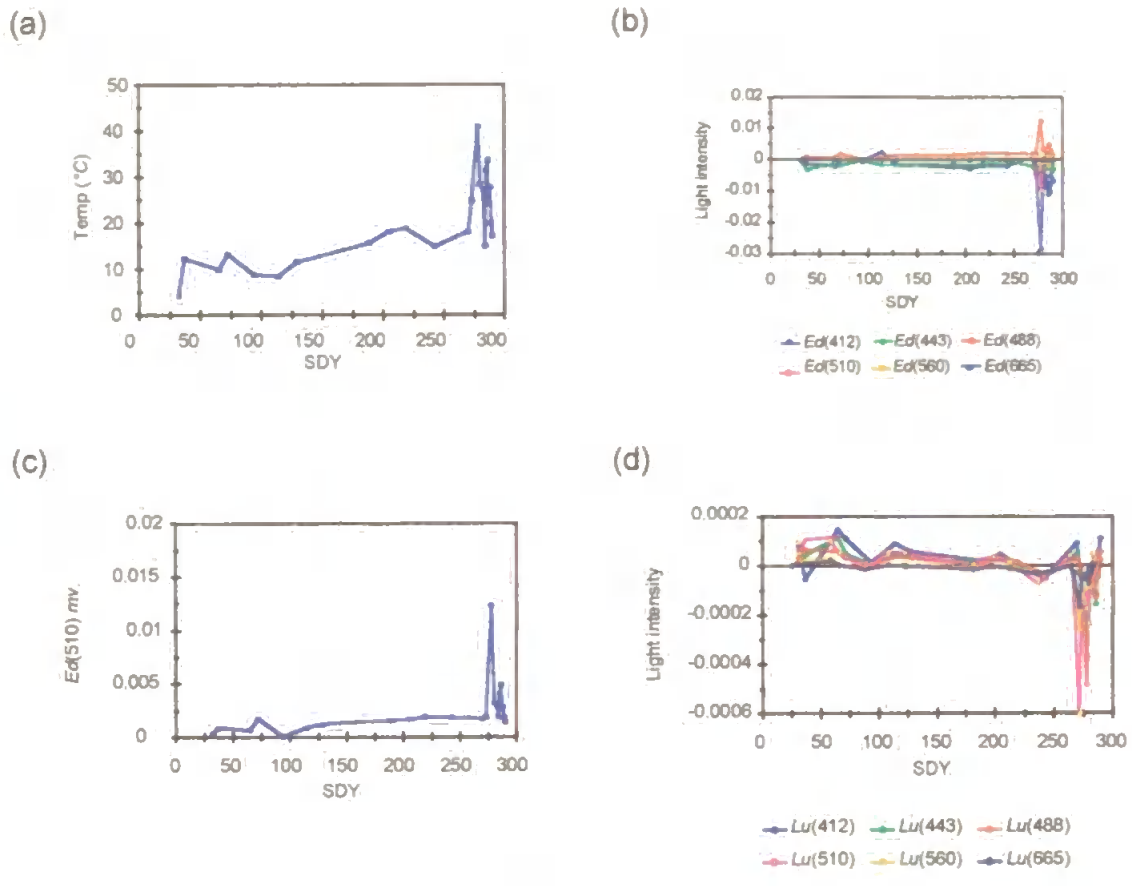

Figure 4.7. 1995 fieldwork dark offset variations (for the L4 study and AMT-1): (a) dark offset temperatures (b) irradiance sensor dark readings ($\mu W\ cm^{-2} nm^{-1}$) (c) *Ed*(510) dark readings ($\mu W\ cm^{-2} nm^{-1}$) (d) $Lu(\lambda)$ dark readings ($\mu W\ cm^{-2} nm^{-1} sr^{-1}$).

Table 4.5. Analysis of the PRR-600 dark offsets.

1995 Fieldwork (SDY)	Instrument dark, *Ed*(510) (Volts)	Temperature offset (Volts)	Irradiance unit value of offset ($\mu W\ cm^{-2} nm^{-1}$)	% of $\vec{E}_o$ (510)= 188.41 ($\mu W\ cm^{-2} nm^{-1}$)
32	0.00068	0.03309	0.00124	0.0007%
219	0.00068	0.05994	0.00226	0.0012%
273	0.00068	0.06304	0.00238	0.0013%
284	0.00068	0.03428	0.00128	0.0007%
289	0.00068	0.05724	0.00216	0.0011%

It can be seen from table 4.5 that the offset in absolute calibrated units is below the 0.1% uncertainty level specified by the SeaWiFS protocols (Mueller and Austin, 1995) for the sub-sample of data taken from the 1995 fieldwork campaign, even with the highly variable range of pre-immersion temperatures encountered. It must be remembered that where there is a change in temperature with depth encountered while profiling (which is usually the case) the dark offset will change correspondingly during profiling. It is therefore concluded that the PRR-600 is not significantly affected by the ambient water temperature within the range encountered during this study.

4.1.6(iii) Calibration stability

The stability of the absolute radiometric measurements between fieldwork sessions depended upon the long term effects of ageing on the instrument's detector system, particularly the filters. Frequent calibration was therefore essential to establish the stability characteristics of the instrument to validate the optical data collection.

Table 4.6 details the calibrations carried out during 1995 and 1996

Table 4.6 PRR-600 Stability between Biospherical Instruments Inc. calibration carried out December 1994, and NIST calibration December 1995. These data are represented as % drift between the calibration sessions.
*Units are $\mu W\ cm^{-2}nm^{-1}$ for irradiance and $\mu W\ cm^{-2}nm^{-1}sr^{-1}$ for radiance.

Sensor module	**Calibration by Biospherical Instruments 12/29/1994 Cal. factor (v/unit*)**	**Calibration by NIST 10/12/1995 Cal.factor (v/unit*)**	**% deviation between calibrations**
Ed(412)	0.030259	0.029184	-3.55
Ed(443)	0.030709	0.029809	-2.93
Ed(488)	0.032488	0.032624	0.42
Ed(510)	0.0321598	0.031227	-2.90
Ed(560)	0.033089	0.031693	-4.21
Ed(665)	0.033188	0.031954	-3.72
Lu(412)	0.637654	0.606	-4.96
Lu(443)	0.631975	0.6088	-3.67
Lu(488)	1.185165	1.15367	-2.65
Lu(510)	0.675182	0.6496	-3.79
Lu(560)	1.582458	1.55917	-1.53
Lu(665)	1.87536	1.67995	7.64

It may be seen that the red channel, *Lu*(665), showed the highest drift between calibration sessions during this period and was excluded from further use until investigation and repair could be undertaken. This procedure serves to both track the drift of the sensors and provide data to update the calibration coefficient files used to derive the absolute radiometric values from the instrument.

4.1.7 Instrument sampling resolution

For instruments using array sensors (such as the PRR-600) resolution will depend upon the profiling and scan rates. In general 5 or more samples should be taken over all logged channels per meter, sampled to within 10 milliseconds at each depth. The sampling rate specified by Biospherical Instruments Inc. for the PRR-600 is 2-3Hz, which equates to 8 to 12 scans per meter at a typical deployment rate of 0.25ms^{-1}, meeting the protocol requirement.

4.1.8 Sensor angular response characteristics

Data in figure 4.8 show field of view, FOV, data collected to test the instrument specification against the protocols. The tests were carried out at the PML calibration facility using a lamp with a stable power source and an indexing head arranged such that the instrument could be rotated, generating a series of different viewing angles.

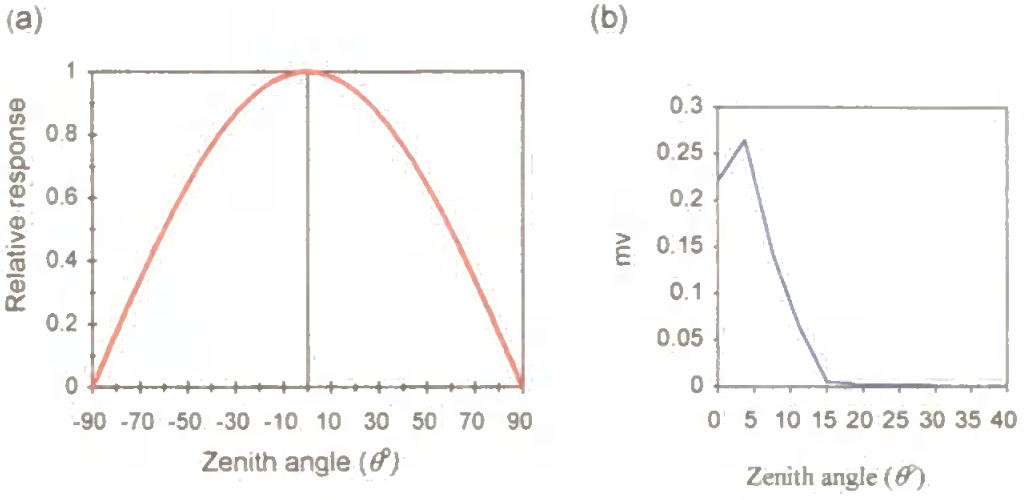

Figure 4.8. FOV analyses for (a) *Ed*(488) sensor (b) the *Lu*(488) sensor. Data are signal output (*mv*) measured as the sensors were oriented over the range of angles shown, and are modified for the immersion coefficient.

Data collected during the exercise were corrected for the immersion coefficient [where $Ed(490,0^-) = 0.796 * Ed(490,0^+)$] to account for the differing instrument viewing angles arising as the measurements were carried out in air.

4.1.9 Instrument operating depth

The protocols dictate that the radiometer must operate to 200*m* (the lower photic zone), measured to a resolution of 0.5*m* with an accuracy of 0.2*m* over bands 1-4 (Mueller and Austin, 1995).

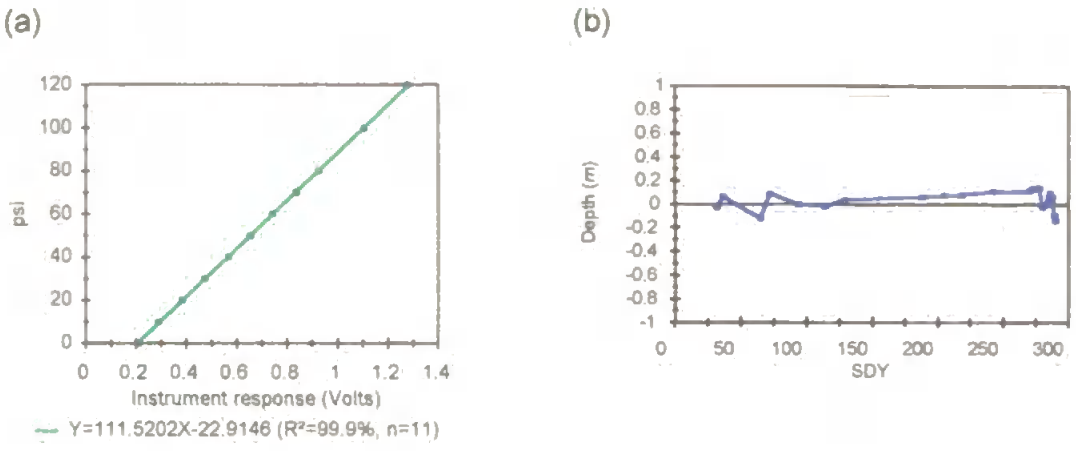

Figure 4.9 (a) pressure sensor calibration and (b) the variability of pressure transducer readings at the surface (converted to depth) during the 1995 fieldwork. The pressurising manifold used was calibrated in pounds per square inch, psi.

Data in figure 4.9 show the characterisation that was carried out on the PRR-600 depth sensor and show the instrument to be linearly stable within the range of operating pressures encountered in the field. Also illustrated (figure 4.9(b)) are the changes in zero offset at the surface that resulting from variability in the ambient atmospheric pressure at the time of sampling. The profile data are corrected for this value (to set the instrument pressure gauge zero offset) during data processing. During the 1995 field campaign, for example, when extensive measurements were taken over wide temporal and spatial scales, the variability measured by the pressure transducer translated to a maximum offset of $\pm 0.18m$.

4.1.10 Temperature sensor characterisation

Raw voltage data were collected from the PRR-600 sensor package coincident with thermometer readings. Data in figure 4.10 show a high level of stability within the temperature range of the waters sampled during this work.

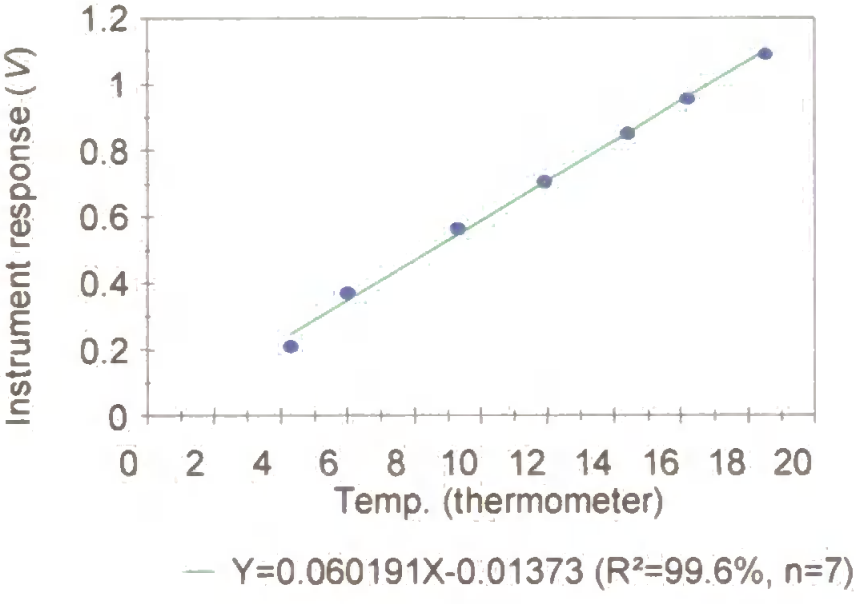

Figure 4.10. Temperature sensor calibration.

4.2 SUB-SURFACE PERTURBATIONS OF THE UNDERWATER LIGHT FIELD BY THE MEASUREMENT PLATFORM

Mueller and Austin (1995) stipulate that the measurement of in-situ optical data is to be achieved with an uncertainty of <5%. The following section details some suggestions from the protocols and how this was this was achieved.

4.2.1 Ship shadow avoidance

When profiling from a ship it is not possible to fully avoid the deployment platform from influencing the optical measurements. Assuming the ships hull is of an appropriate sub-water line colour (e.g. matt black) the major obstacle to accurate measurement is the ship's shadow. Figure 4.11 shows the generalised deployment strategy used to combat this effect. For all the sampling undertaken during this work the radiometers were deployed over the starboard quarter, normal to the centre-line of the vessel. In each case telescopic cranes were used to locate a pulley block at the maximum possible extension, with the radiometer cables run from a separate winch located slightly forward on deck. It often proved difficult to achieve the ideal conditions depicted in figure 4.11 without the ship running over the cable or coming around and shadowing the instrument during the cast.

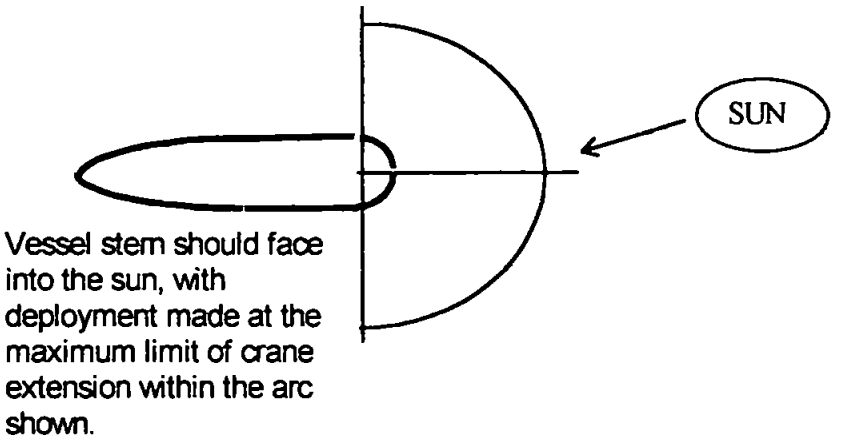

Figure 4.11. Deployment orientation of the relative positions of the platform, crane and sun.

The success of data collection during difficult conditions depended upon the effectiveness of the technicians and crew and the prevailing weather. Casts were aborted often, or used to generate data for analysis of ship shadow effects.

4.2.2 Protocols for avoiding in-water light field perturbations due to the deployment platform

Mueller and Austin (1995) suggest that the radiometers should be deployed a certain distance away from the ship to minimise optical perturbations to the sub-surface light field from the vessel superstructure. Avoidance of this effect can be characterised in terms of attenuation length, $1/Kd(\lambda)$. Figure 4.12 outlines these considerations:

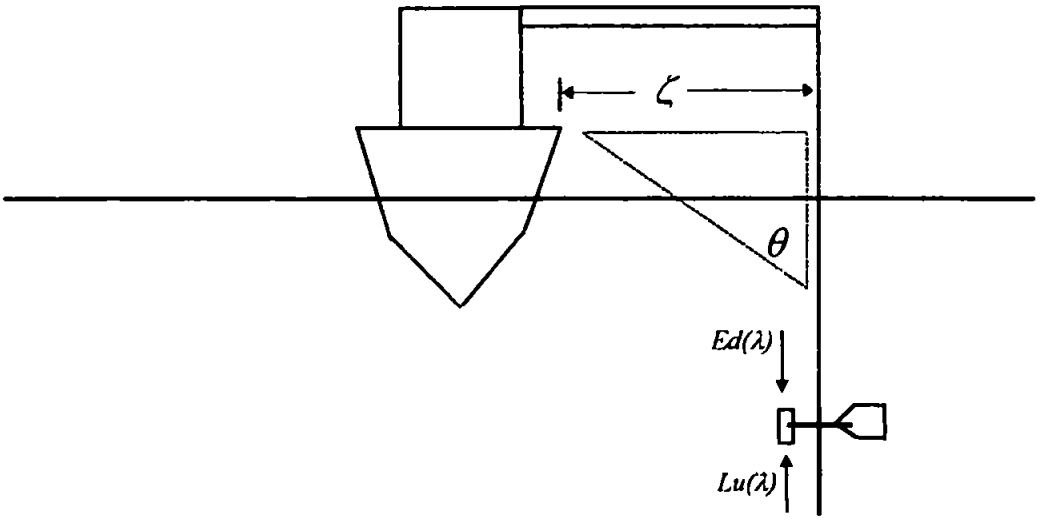

Figure 4.12. The protocol regarding the avoidance of ship structure perturbations to the underwater light field.

For measurements of $Ed(\lambda)$ the calculation to describe ζ is as follows:

$$\zeta = \frac{\sin(48.4^\circ)}{Kd(\lambda)} \qquad (4.3)$$

where 48.4° is the critical angle, θ_c, for Snell's window. For upwelling radiance the measurement distance should be no less than 1.5/*KL* (where *KL* is the diffuse attenuation coefficient for upwelling irradiance measured over a small angle). These distances should be increased if the instrument is deployed off the beam of the vessel, although may be reduced if working in overcast conditions. As a matter of routine the deployment cranes were used to their maximum extension. Table 4.7 details sample deployments from each field

program to show a comparison of the actual values of ζ achieved, compared to the distances that were required by the protocols, equation 4.3.

Table 4.7. A comparison of radiometer deployment crane extension distances in the field, and those suggested by Mueller and Austin (1995).

Field sample	$Kd(490nm)$ (m^{-1})	$K_L(490nm)$ (m^{-1})	ζEd (m)	ζLu (m)	Max. crane extension available (m)
AMT-1					11.5
AP272A	0.02796	0.03847	35.8	39	
AP280A	0.03574	0.06342	21	23.7	
AP290A	0.06444	0.05642	11.6	26.6	
L4					4
P950206A	0.2506	0.18297	3	8	
P950628A	0.07246	0.16759	10	9	
P950724A	0.29151	0.29361	3	5	
PRIME					10.5
P960711A	0.04128	0.07843	18	19	
P960714A	0.02854	0.03683	26	40.7	
P960717A	0.02237	0.04862	33	30.8	

It can be seen that the protocols were met on very few occasions, hence perturbed shallow profile data were removed prior to further analyses (as outlined in chapter 5).

4.2.3 Stability and control of the instrument attitude during sampling (tilting and surging)

As discussed in chapter 2, profiling radiometers are constructed such that they measure the appropriate upwelling and downwelling component of the light field (depending upon the type of sensor). Deviations from the vertical during measurement produce tilt errors resulting in under-reading (by $\cos\theta$) of $Ed(\lambda)$ and a corresponding much smaller error in the measurements of the $Lu(\lambda)$. For this reason Mueller and Austin (1995) set a limit of 10° from the vertical

beyond which data to be used for SeaWiFS calibration and validation are to be discarded.

When embarking upon this study it quickly became clear that the PRR-600 and its deployment system supplied by the manufacturers could easily become unstable, leading to a hysteresis effect as the instrument 'surged' in the water column. Examples of this effect are shown in figure 4.13.

An improved deployment technique was designed and constructed to be both inherently stable and minimise any shading of the radiometers from the revised frame. The Biospherical Instruments Inc. system and the new variant are shown in figure 4.14.

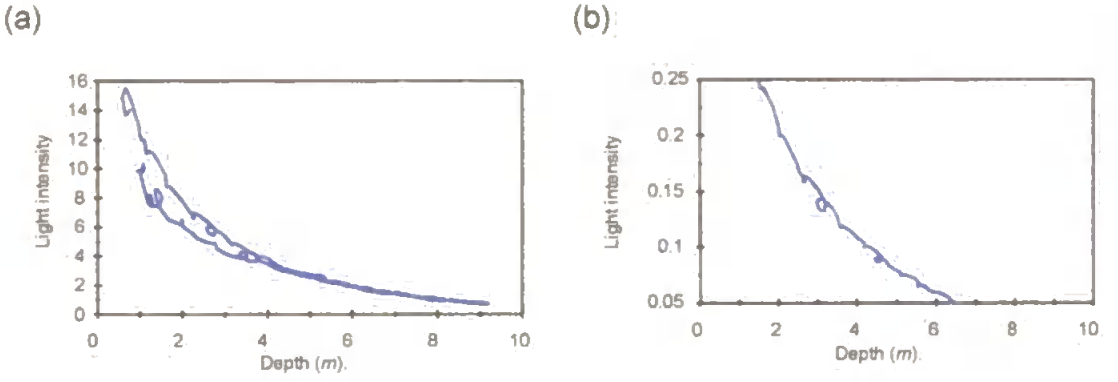

Figure 4.13. Shallow profile data collected using the PRR-600. The hysteresis is due to tilt and surge of the radiometer during profiling. Data are from (a) the *Ed*(510) sensor down and upcast ($\mu W\, cm^{-2} nm^{-1}$) and (b) the corresponding *Lu*(510) downcast ($\mu W\, cm^{-2} nm^{-1} sr^{-1}$).

The solution was to develop a deployment system that would allow the instrument to be suspended from the winch wire with an weight of non reflective colour ($\approx 40kg$) tethered below it. A vane was added to reduce the likelihood of the communications lead becoming entangled with the deployment warp, a particular problem when significant current shear is present. The sensor package was located on the extremity of the frame to remove the rig from its field of view.

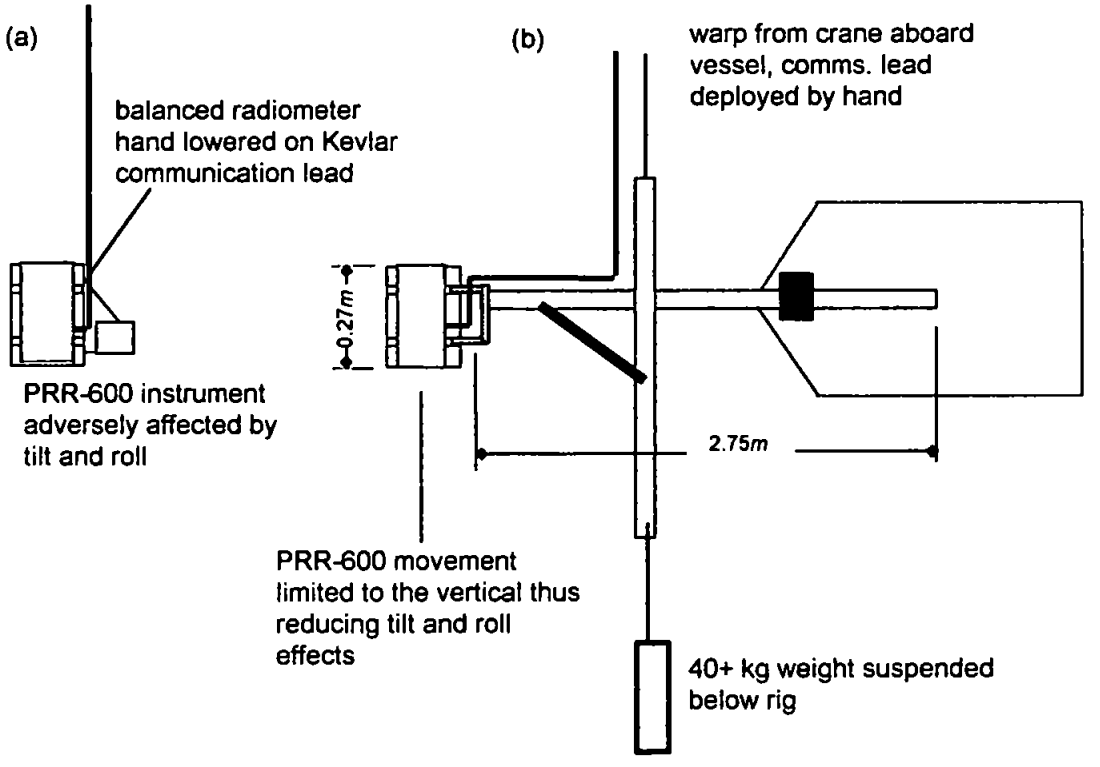

Fig. 4.14. (a) the manufacturer's deployment system, and (b) the new method developed for this study.

Figure 4.15 shows the method of deployment used from *RV Squilla* during the L4 study and *RRS Discovery* during PRIME.

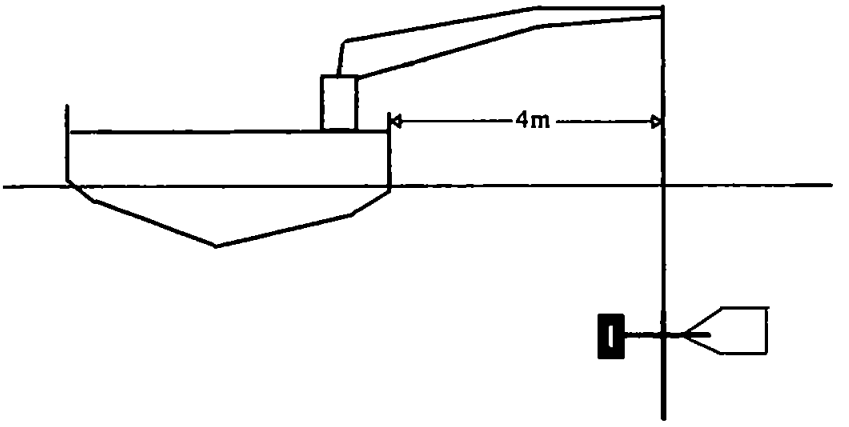

Fig 4.15 The deployment technique used to collect radiometric data from *RV Squilla*.

4.2.3(i) Sea trial of improved system

The performance of the revised deployment system was assessed in March 1995 from *RV Squilla*, with 0.75-1*m* of swell and stable overcast meteorological conditions. The crane was used to its maximum extension of 4*m*. The casts were made as similar as possible, with the sensor held just below the surface for 2 minutes prior to the start of each cast, before being lowered in 5*m* increments, with a stop for 1 minute at each depth increment of 5*m*. Data in figure 4.16 show the results of the study and represent the fluctuations in light field due to the sum of surging and surface wave effects, illustrating the improved stability of the modified system. It may be seen that

the regression analyses carried out for the two deployment techniques indicate a significant increase in the depth dependent variance of the light intensity measurements collected with depth, improving from to 98.4% for *Ed(510nm)*.

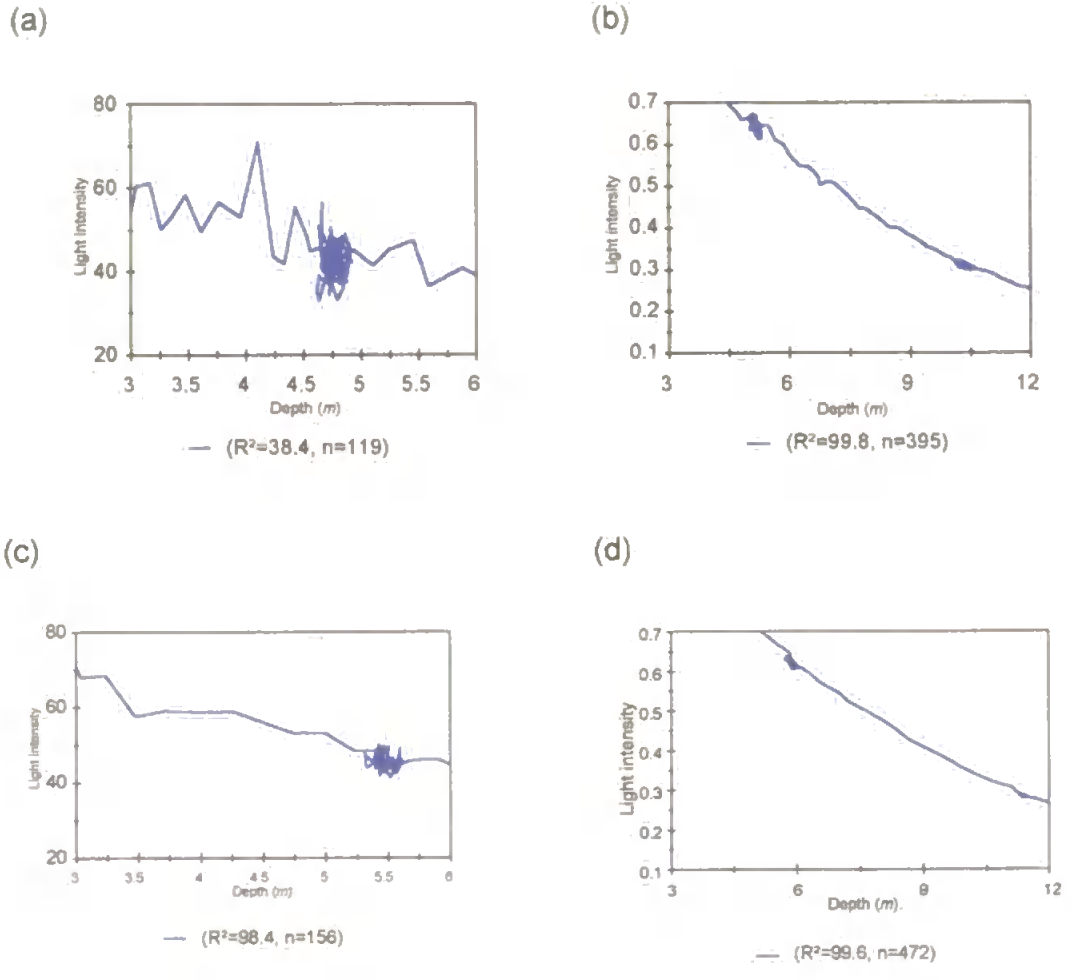

Figure 4.16. Data collected using (a) the PRR-600 *Ed*(510) and (b) the *Lu*(510) channels using the manufacturer's deployment system (as shown in figure 4.14a). (c) and (d) are the profiles obtained at the same location as in (a) and (b), but 30 minutes later and using the modified deployment frame, (4.14b). The units for irradiance are $\mu W\, cm^{-2} nm^{-1}$, and radiance $\mu W\, cm^{-2} nm^{-1} sr^{-1}$. Also shown are the degrees of variance describing the stability of the readings obtained from *dln*(*Ed*)/*dz* and *dln*(*Lu*)/*dz* respectively.

The good correspondence in the upwelling radiance data result from the inherently stable nature of the upwelling light field. The central issue is that

much of the data shown in figure 4.16(a) and (b) were collected while the sensor was not in the vertical plane, whereas a greater portion of the data collected using the modified technique falls within a narrower limit, illustrated in figure 4.16(c) and (d), with reduced instability. Data in figure 4.17 show tilt and roll measurements collected during the second AMT (using a dual plane inclinometer mounted on the frame) showing the orientation during a typical deployment.

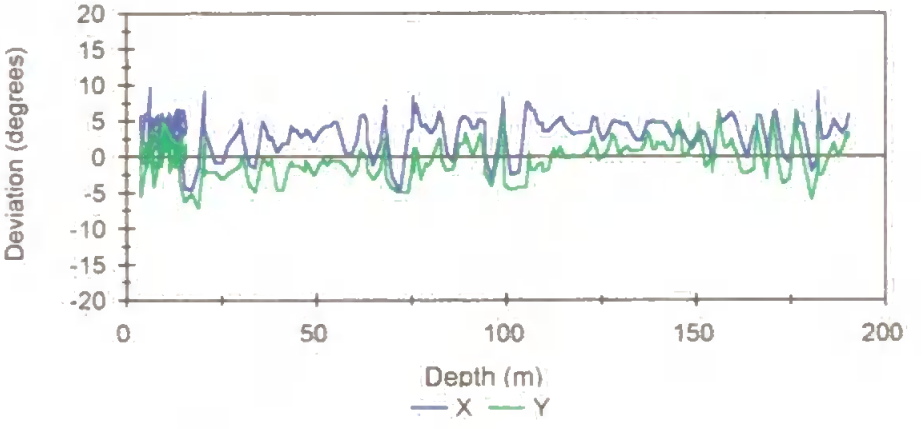

Figure 4.17. Tilt (Y) and roll (X) data collected from a typical profile up-cast during AMT-2 (SDY 122, 1996). Data were binned at 0.2m intervals.

It can be seen that the deployment technique developed ensures that the radiometer collected data from within the 10° limit stipulated by Mueller and Austin (1995).

4.2.4. The radiometer deployment technique used during AMT-1

During sampling at the L4 site and during PRIME, the deployment rig shown in figure 4.14(b) proved to be highly effective. In preparation for the AMT-1 a variation of the design was constructed using the same criteria, but able to carry two discrete radiometer systems, with up-the-wire communications and data transfer (Robins *et al.*, 1996). The rig that was constructed is illustrated in figure 4.18 and was successfully deployed to 220*m* (the initial design system has a capability of 90*m*, the limitation being the length of the communications lead).

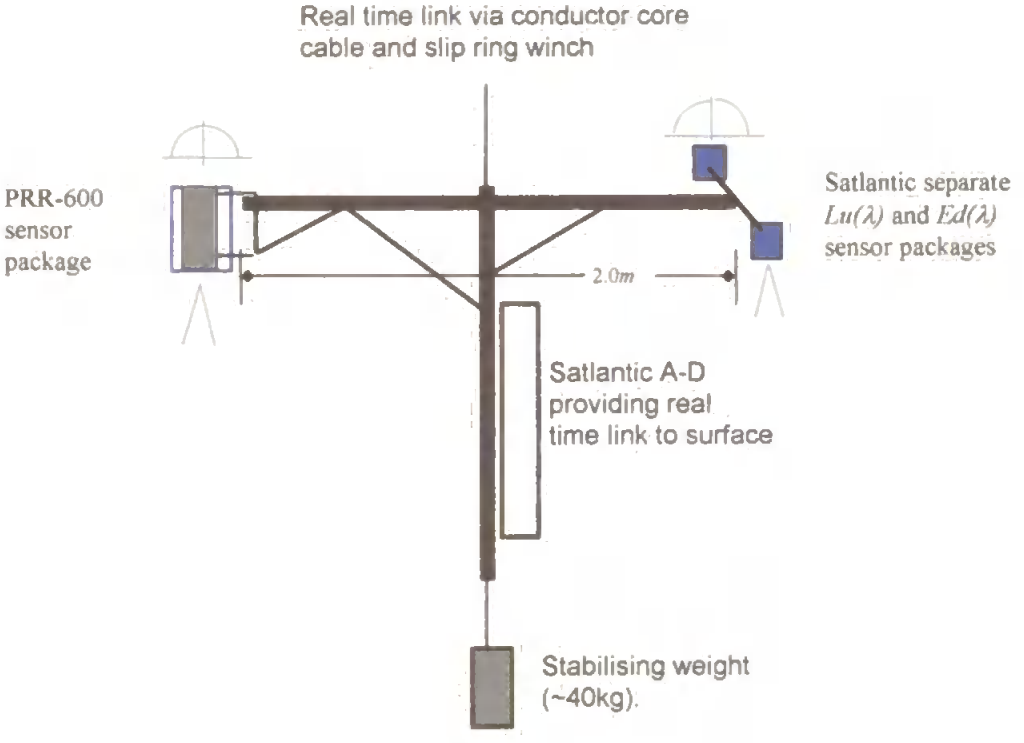

Figure 4.18. The deployment system used for optics data collection during AMT-1.

The system was more susceptible to rotation due to current shear than the system illustrated in figure 4.14, the reason being that the vane was removed to accommodate the second set of radiometers.

This system of deployment was successfully used during subsequent AMT cruises (usually with only the Satlantic radiometer system fitted), updated to incorporate a beam transmissometer, a downwelling scalar PAR sensor and a CTD-F sensor package fitted with a tilt and roll module. Figure 4.19 illustrates the layout of the radiometer deployment technique used during AMT-1 from *RRS James Clark Ross*.

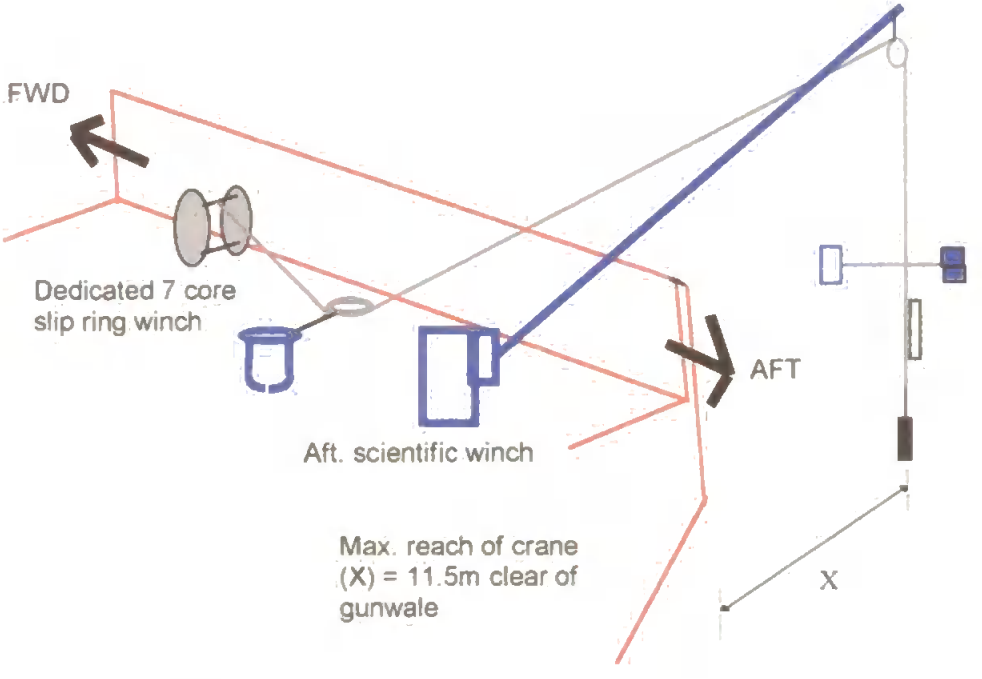

Figure 4.19. Deployment of optical the profiler during AMT-1.

5. OPTICAL DATA PROCESSING AND STATISTICAL ANALYSIS METHODOLOGY

In this section the techniques used to process and quality control the optical data sets generated during this study are discussed. Also detailed are the statistical methodologies employed to assess the performance of the algorithms presented in chapter 8.

5.1 OPTICAL DATA PROCESSING METHODOLOGY

The objective of the optical data analyses was to construct a processing procedure that could be applied to profiles from all fieldwork with a minimum level of subjectivity. To this end the work was undertaken using the Quattro Pro PC spreadsheet programming language V. 5 (Borland International Inc., 1993), allowing an interactive element to the processing at key stages, to be combined with procedural consistency.

Initially, $Ed(\lambda)$ and $Lu(\lambda)$ data were plotted against depth. Napieran log - light intensity transformed data were then plotted, to conform to the straight line relationship in accordance with Beer Lambert's law (Pilgrim and Aiken, 1989; Gordon, 1989). The plots were then examined for deviations from this relationship, which indicated one of three possible effects: (i) that the light field had been affected by stratified in-water constituents, *e.g.* the bio-physical variability often associated with a thermocline (see figure 5.1), or (ii) that the input of incident irradiance, $Ed(\lambda,0^{+})$, was not a constant value due to atmospheric effects such as

cloud perturbations, (see figure 5.2), or (iii) that the sub-surface light field had become perturbed by the ship's shadow (see figure 5.3) or wave effects at the air-sea interface (see figures 5.4 and 5.5).

Before any further processing took place, these potential errors had to be quantified and their effect removed. This frequently resulted in a cast being rejected as unusable.

5.1.1 Removal of in-water effects

The accuracy of $Rrs(\lambda,0^-)$ values derived from the profile data was dependent upon obtaining the correct measurement of the radiometric quantities logged at each depth. It would not be correct to suppose that there was no fine scale physical inhomogeneity in the mixed layer, so the $Kd(\lambda)$ value calculated from the radiometry represents a practical integration incorporating any fine scale structure. Data collected in the vicinity of relatively large scale features such as a thermocline must be removed as the spectral distribution of these data will not necessarily be representative of the surface. Figure 5.1 shows a comparison of an $R(443,0^-)$ and corresponding temperature profile. These data illustrate a common problem with the use of light profiling techniques, especially in regions where there is a shallow thermocline, as the only portion of the light profile that is representative of the upper mixed layer in figure 5.1 is the top $20m$. Below this depth the thermocline and associated biological activity (the presence of which is assessed from the vertical chlorophyll-*a* fluorescence data obtained from the CTD-F casts also carried out on station) introduces variability in measurement. This leads to the spectral

intensity of the light field changing which results in erroneous assessment of the diminution with depth and hence the derived ocean colour measurement.

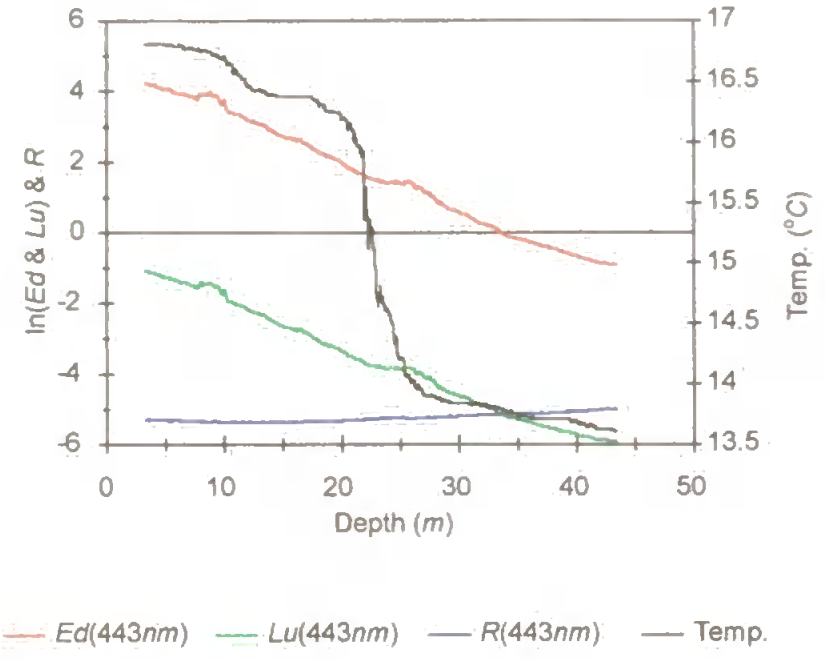

Figure 5.1. Changes in the underwater light field associated with the temperature profile at 443*nm*. The data displayed here were obtained by profiling and show the downwelling irradiance and upwelling radiance and corresponding reflectance (in natural log space). In addition to the optical measurements temperature and chlorophyll fluorescence are shown.

It can be seen that the reflectance ratio increases below the thermocline indicating either a lowering in the rate of attenuation of $Lu(\lambda)$ and/or a rise in the attenuation of $Ed(\lambda)$. On this basis the region of the cast shown in figure 5.1, the section below 15-20*m* would be rejected for the purpose of the surface layer $Kd(\lambda)$ derivation by least squares regression analysis. It may be seen that two shoulders are visible in the profile data which are due to atmospheric effects (see section 5.1.2). Note that these effects are cancelled out when the data are considered in terms of reflectance.

5.1.2 Removal of perturbations in the incident skylight, $Ed(\lambda,0^{+})$

The second potential effect that may cause irregularities to sub-surface measurement of the light profile is variation in the incident light field.

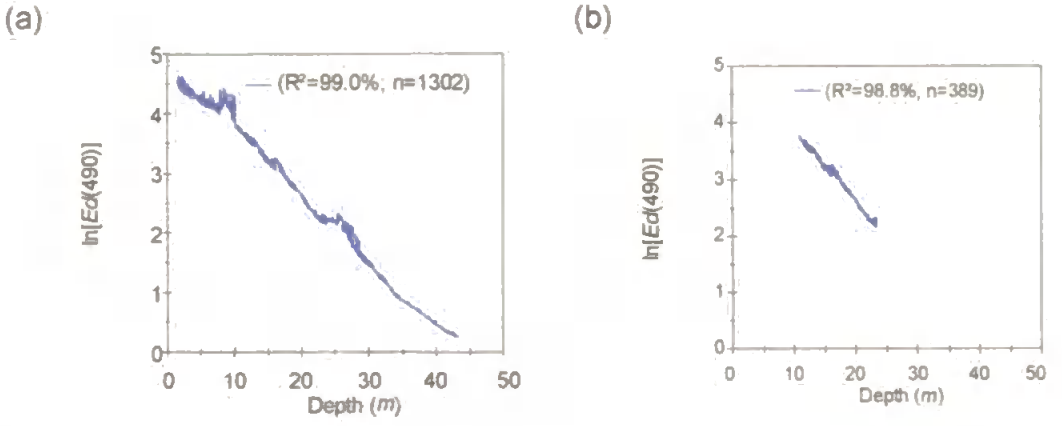

Figure 5.2. The change in measured *Ed(490nm)* with depth during a cast where the illumination conditions were affected by changing cloud thickness and/or type. These perturbed data were removed from the cast prior to further analyses. Plot (a) illustrates the raw data and (b) the same profile with the data affected by changing incident irradiance removed. The units of irradiance in this instance are $\mu W\, cm^{-2} nm^{-1}$.

There are two distinct shoulders, one at 9*m* and another at 25*m* visible in the data which are the result of decreasing incident irradiance during profiling (due to factors such as thinning cloud) increasing the subsurface measured intensities logged during these periods. These data are removed prior to further analyses, as shown in, figure 5.2(b). Data below 30m deviate from the straight line relationship possibly due to the detection of further meteorological perturbations or due to structural changes in the water column and are hence also discarded.

5.1.3 Ship shadow and wave effects

At shallow depths the integrity of the data can be seriously compromised by sub-surface perturbations in the underwater light field by not only the deployment platform but also the air/water interface.

5.1.3 (i) Ship shadow effects

Ship shadow effects show up in the surface of the ln[$Ed(\lambda,z)$] profile with depth. The effect is manifest as a non-linear portion of the curve with lower radiometric values over the affected depth as shown in figure 5.3. These data are removed prior to further analyses.

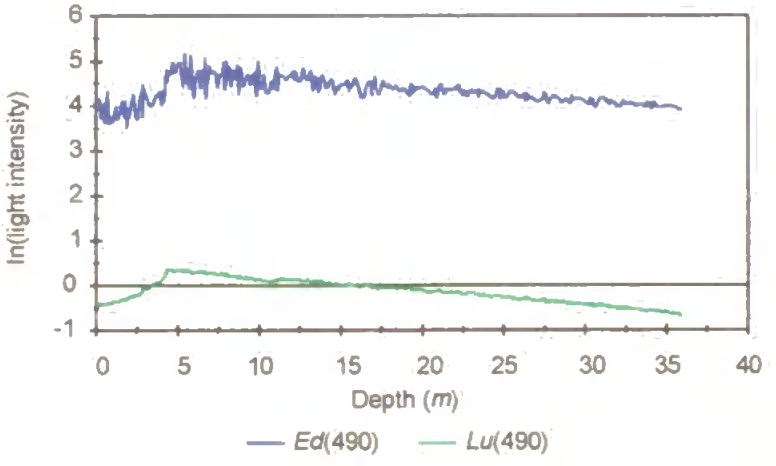

Figure 5.3. An example of the effect of ship's shadow on the sub-surface optical profile. The low light levels were apparent in the data from the top 5 meters, which are affected by the ship. The units of irradiance are $\mu W\,cm^{-2}nm^{-1}$ and of radiance are $\mu W\,cm^{-2}nm^{-1}sr^{-1}$.

5.1.3 (ii) Refraction effects of the incident downwelling light field at the air/sea interface

Near surface perturbations of the light field have a profound effect upon shallow measurements made by profiling radiometers due to refraction patterns caused by surface waves. Data in figure 5.4 show *Ed*(490*nm*) measurements collected at shallow depths, and the wide variation in the readings typically obtained. These data are routinely rejected from the profile to a depth of 2-5*m* in deep oceanic regions, and 0.5-2*m* when working inshore, depending upon the depth of the thermocline and the stability of the incident light field and/or water turbidity.

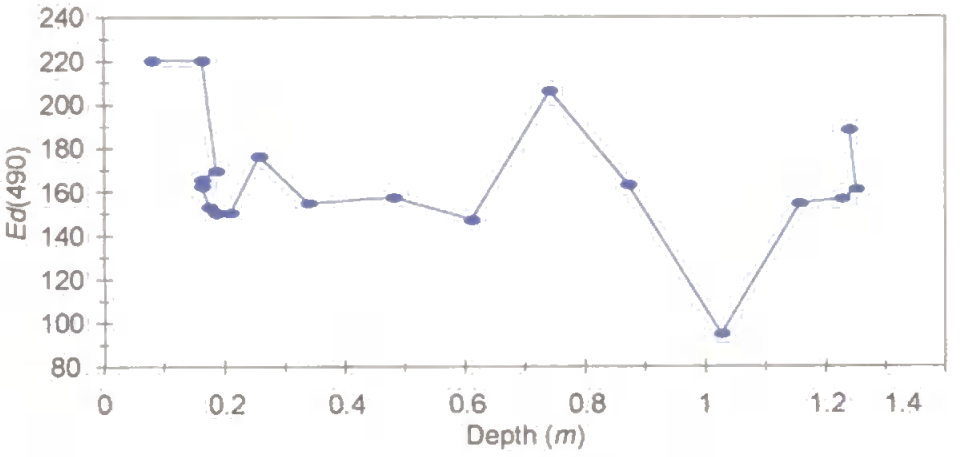

Figure 5.4 The variation in measured *Ed*(490*nm*) below the surface. These data are either averaged or removed from the data set prior to further processing. The units of irradiance are $\mu W\, cm^{-2} nm^{-1}$.

To examine this effect further a time series of data were collected with the radiometer deployed below the surface to a depth of 1*m* for 2 minutes, followed by a further 2

minutes suspended above the sea surface. This process was repeated four times. Figure 5.5 presents a section of the time series of data obtained and demonstrates the air/water interface effect upon the incident irradiance. The sea conditions were clear oceanic waters, no wind, no swell and surface waves of 5-10*cm* height.

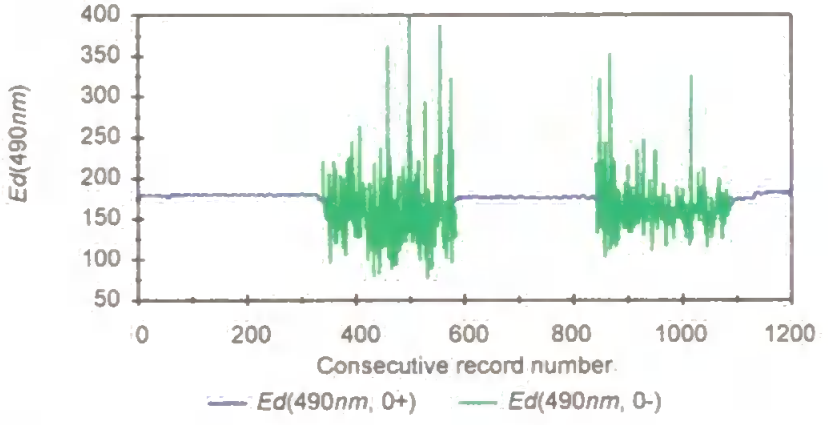

Fig 5.5. *Ed*(490) data collected above and below the air sea interface. The above surface measurements were adjusted for the immersion coefficient, which for the PRR-600 at 490*nm*, is $Ed(0^-) = 0.796 \cdot Ed(0^+)$. The units of irradiance are $\mu W\ cm^{-2} nm^{-1}$.

If large amounts of data are removed then the cast is may have to be rejected, except in very turbid waters where an isotropic light field (purely diffuse) may prevail at shallow depths.

Once the optical profile data had been subjected to the rigorous pre-processing quality control procedures detailed here, further processing stages were carried out for each up and downwelling channel. From equation 2.19 in chapter 2, it was shown that the vertically downward attenuation of irradiance may be described by:

$$Ed(\lambda,z) = Ed(\lambda,0^-)\exp[-Kd(\lambda)\cdot z] \quad (5.1)$$

By plotting ln[*Ed(λ,z)*] against depth, *z*, and performing least squares regression analyses, equation 5.1 may therefore be solved for *Kd(λ)* and *Ed(λ,0⁻)* as shown in equation 5.2.

$$\ln[Ed(\lambda,z)] = \frac{d\ln Ed(\lambda,z)}{dz}\cdot z + \ln[Ed(\lambda,0^-)] \quad (5.2)$$

where $\frac{d\ln Ed(\lambda,z)}{dz}$ = *Kd*.

The upwelling radiance, *Lu(λ,z)*, profile data were similarly treated to derive values for $K_L(\lambda)$ and correspondingly *Lu(λ,0⁻)*. It may be noted from figure 5.6 that there is a strong similarity between the attenuation coefficients, *Kd(λ)* and $K_L(\lambda)$ derived from profiled measurements using the *Ed(λ) and Lu(λ)* sensors respectively.

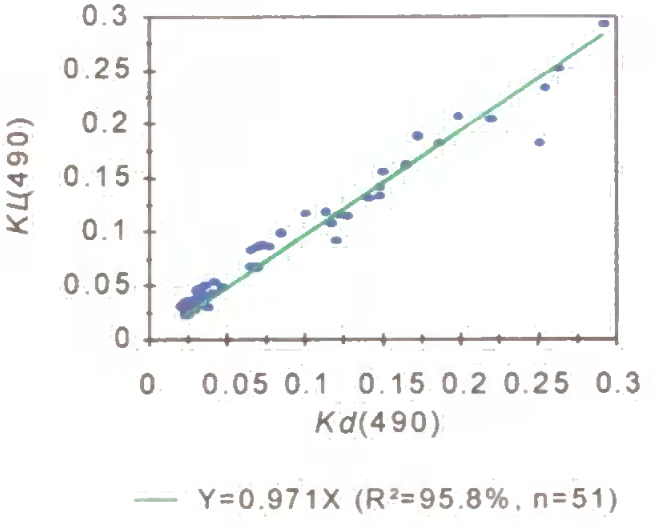

Figure 5.6. Illustration of the relationship between $K_L(490)$ and *Kd*(490) for the amalgamated data set comprised of the L4, AMT-1 and PRIME data.

5.2. STATISTICAL METHODOLIGIES

The statistical and descriptive methodologies used in chapter 8 to describe the observations presented in chapter 7 are presented here.

5.2.1 Departures from normality

The following terms, in conjunction with the Kolmogorov-Smirnov two sample test (see section 5.2.4), are used to describe structured deviations, where present, from the normal case of the error frequency distribution. Equations are not given for their derivation as this is considered beyond the scope of this description. Their calculation was undertaken using subroutines provided with the Quattro-pro spreadsheet, (Borland International Inc., 1993).

5.2.2(i) Skewness (assymmetry)

Skewness is apparent in a distribution in which the mean and median are not of the same value, i.e. that one side of the curve is drawn out more than the other. The conventional sample statistic for measuring skewness is denoted g1. Curves may be either drawn out to the left, negative g1, or right , positive g1 (Sokal and Rohlf, 1995).

5.2.2(ii) Kurtosis

Kurtosis describes the proportion of items found in the tails in relation to those in the shoulders compared to the 'bell' shaped normal distribution.

The conventional sample statistic for measuring Kurtosis is denoted g2. A negative g2 indicates platykurtosis (fewer items at the centre but more at the tails than a normal case) and a positive g2 indicates leptokurtosis (more items at its centre than at the tails) (Sokal and Rohlf, 1995).

5.2.3 Asessment of the deviation from the normal distribution case using the Kolmogorov-Smirnov two sample test (Sokal and Rohlf, 1995)

The null hypothesis of the Kolmogorov-Smirnov two sample test is that the two samples are distributed identically, thus the test is sensitive to location, dispersion, skewness and kurtosis. It is based on the unsigned differences between the relative cumulative frequency distributions of the two samples. The critical value is calculated using equations 5.3 and 5.4.

The example given in table 5.1 uses the comparison between two algorithms, designed to retrieve $Kd(490nm)$; one, A1, developed from other work equation 3.5 (Moore *et al.*, 1997) and the other, A2, developed in this work, equation 8.2. These relationships were both applied to the remote sensing reflectance data collected during AMT-1, (further discussed in section 8.1.2).

Analytical procedure :

1. Tabulate the cumulative frequency (*F1* and *F2*) of the error distributions for algorithms A1 and A2,
2. Compute relative cumulative frequencies by dividing *F* through by *n* in each case,
3. Compute the values for the absolute difference between the relative cumulative frequency columns, *d*,
4. Find the largest value of *d*,
5. Where ***D*** is the termed the maximum unsigned difference, this value is in turn multiplied by the product of $n_1 n_2$ to normalise the values.

Table 5.1. Worked example of the Kolmogorov-Smirnov two sample test.

Bin	**A1**	***F1*** (n_1=20)	**A2**	***F2*** (n_2=20)			
					$\frac{F1}{n_1}$	$\frac{F2}{n_2}$	$d = \left\lvert \frac{F1}{n_1} - \frac{F2}{n_2} \right\rvert$
-0.6	0	0	0	0	0.0000	0.0000	0.0000
-0.52	0	0	1	1	0.0000	0.0500	0.0500
-0.44	0	0	1	2	0.0000	0.1000	0.1000
-0.36	0	0	0	2	0.0000	0.1000	0.1000
-0.28	2	2	3	5	0.1000	0.2500	**0.1500 *D***
-0.2	3	5	0	5	0.2500	0.2500	0.0000
-0.12	2	7	3	8	0.3500	0.4000	0.0500
-0.04	5	12	4	12	0.6000	0.6000	0.0000
0.040	2	14	4	16	0.7000	0.8000	0.1000
0.12	3	17	4	20	0.8500	1.0000	0.1500
0.2	3	20	0	20	1.0000	1.0000	0.0000

The critical value for this statistic can either be found from tables or may be calculated using equations 5.3 and 5.4.

$$D\alpha = K\alpha \sqrt{\frac{n1 + n3}{n_1 n_2}} \tag{5.3}$$

where $K\alpha = \sqrt{\frac{1}{2}\left[-\ln\left(\frac{\alpha}{2}\right)\right]}$ (5.4)

where α denotes the probability level that the populations are distributed identically, *e.g.* p=0.05. In this case the critical value was calculated to be 8.589. By comparing this to $n_1 n_2 D\alpha$, where a value of 0.15*20*20 = 60 was obtained, due to the magnitude of the critical value (which is considerably smaller) the null hypothesis that the error distributions are the same and hence will contain samples from the same population must be rejected. Had the critical value been greater than $n_1 n_2 D\alpha$, then the null hypothesis must be accepted (at the p=0.05 level).

5.2.4 Accuracy and precision

The terms accuracy and precision are employed in the context of this work to describe the manner in which an algorithm may mathematically retrieve an in-water property from upwelling radiances as a function of the location and spread of the peaks and troughs when data are viewed as either along cruise track or time plots. Simple graphical examples are given in figure 5.7.

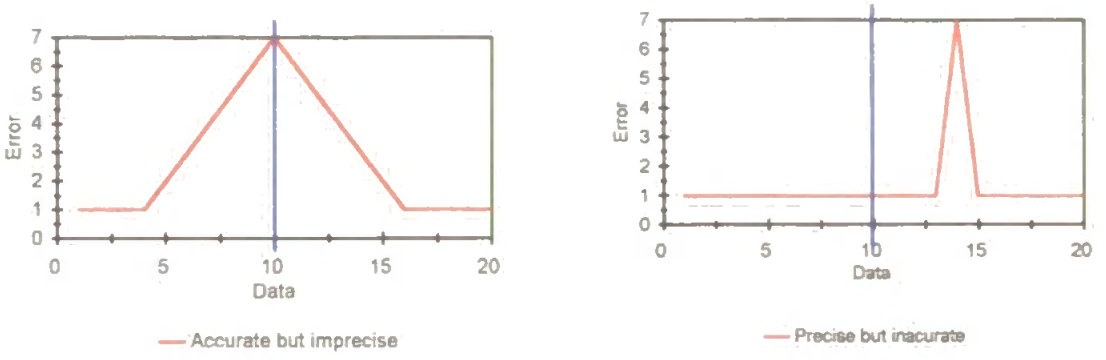

Figure 5.7. The concept of accuracy and precision as applied to this work.

6. PIGMENTS DETERMINED BY HIGH PERFORMANCE LIQUID CHROMATOGRAPHY (HPLC)

In this chapter the major classes of phytoplankton pigments identifiable by HPLC are introduced, as well as the methodology employed in the collection of the water samples and their subsequent laboratory analyses.

6.1 THE RANGE OF PIGMENTS PRESENT IN PHYTOPLANKTON

The biological sampling rationale was to establish the concentrations of the chlorophyll and carotenoid components of the pigment assemblage present at the time of the contemporaneous optical casts. There are three classes of pigment in phytoplankton: (i) the chlorophylls, (ii) the carotenoids and (iii) the phycobilins (Hall and Rao, 1981; Rowan, 1989; Kirk, 1994; Jeffrey *et al.*, 1997). The third group was not identified by the HPLC analysis undertaken during this study, so are beyond the scope of this work.

6.1.1 The chlorophylls

CHL-*a* (a bluish-green colour) is the principle ubiquitous photosynthetic pigment of all higher green plants and algae and exists in two forms in natural populations of phytoplankton: CHL-*a* and divinyl chlorophyll-*a* (DV-*a*) (Jeffrey *et al.*, 1997). During the fieldwork these two pigments were identified as observations of DV-*a* in the oligotrophic waters indicating the presence of prochlorophytes (Suzuki and Handa, 1995)

Figure 6.1(a) shows the proportion of the total observed CHL-*a* that was found to be DV-*a* during AMT-1. These data are further discussed in chapter 7.

(a)

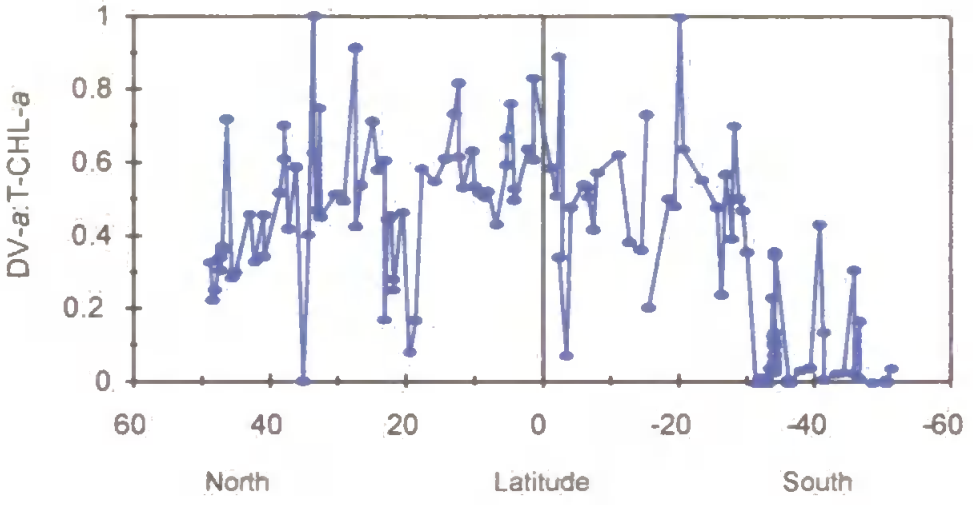

(b)

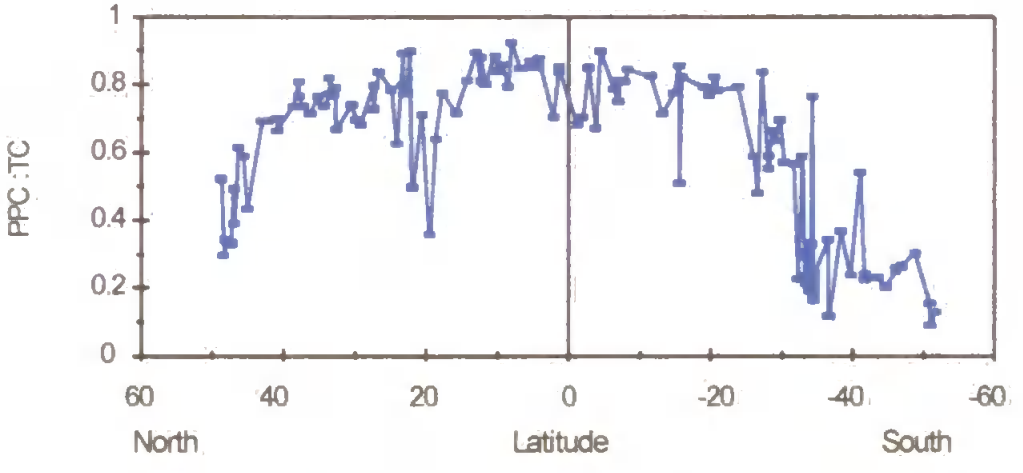

Figure 6.1. Pigment data collected during AMT-1 showing (a) the change in the ratio of DV-*a* as a proportion of the T-CHL-*a* along the cruise track, and (b) the variability in photoprotective carotenoids (PPC) as a proportion of the total carotenoid (TC) assemblage.

There are additional chlorophylls (*b* and *c*) that co-exist with CHL-*a* in certain photosynthesising plants, e.g. CHL-*b* occurs in red algae (Rhodophyta), CHL-*c* occurs in

diatoms and brown algae (Heterokontophyta),

6.1.2 The carotenoids

The carotenoids are a diverse yellow and orange class of pigments found in all photosynthesising cells. They are usually either hydrocarbons (carotenes) or oxygenated hydro-carbons (carotenols or xanthophylls). They have triple banded absorption spectra between 400*nm* to 550*nm*, and are found in the chloroplast lamellae in close proximity to the chlorophylls. There are two broad sub-groups: the photosynthetic carotenoids which include fucoxanthin, hexanoyloxyfucoxanthin, butanoyloxyfucoxanthin, prasinoxanthin, beta-carotein; and the photoprotective carotenoids which include diadinoxanthin, alloxanthin, zeaxanthin, lutein). The colour of these pigments are usually masked by the intense green of CHL-*a*, although in autumn they are seen as leaf yellowing in terrestrial plants as the CHL-*a* and phycobilins break down first and are washed out (the latter being water soluble).

Photosynthetic carotenoids assist in the photosynthetic process by absorbing photons in regions of the spectrum that CHL-*a* does not and passing captured energy to the reaction centres in the photosynthetic pathway. Photoprotective carotenoids, however, are used to combat the potentially lethal effects of high levels in incident irradiance on aquatic algal populations. In such conditions the photoprotective pigments as a proportion of the total will be higher, changing the colour of the cell and acting as a short-wave light filter (Kirk, 1994). An example of variability within the carotenoid component of the pigment assemblage is illustrated in figure 6.1(b), where the PPC observed during AMT-1 make

up varying proportions of the total carotenoid concentrations observed. This PPC variability is accompanied by corresponding changes in the PSC concentration observed.

6.2 PIGMENTS IDENTIFIED BY THE HPLC ANALYSIS

Data in table 6.1 detail some of the key pigments that may be determined for which standards are readily available (Jeffrey *et al.*, 1997).

Table 6.1 HPLC pigments grouped according to Bidigare *et al.* (1990).

Pigment (common name).	**Chemical formula (colour)**	**Taxonomic indicator for**	**Use by plant**
		Chlorophylls	
Chlorophyll-*a*	$C_{55}H_{72}N_4O_5Mg$ (blue-green)	Present in all green algae.	Principle photosynthetic pigment. Usually dominant, but the relative concentration varies widely (Kirk, 1994).
Divinyl chloro -phyll-*a*	$C_{55}H_{70}N_4O_5Mg$ (green)	Prochlorophytes	Becomes present in greater quantities in the oligotrophic regions (Suzuki and Handa, 1995).
Chlorophyll-*b*	$C_{55}H_{70}N_4O_6Mg$ (olive/emerald-green)	Prasinophytes, chlorophytes, prochlorophytes.	Photosynthetic accessory pigment, usually present in green algae (Vernon and Seeley, 1966).
Chlorophyll-c_1	$C_{35}H_{30}N_4O_5Mg$ (Light olive-green)	Brown algae, diatoms, dinoflagellates.	Photosynthetic accessory pigment found in green and brown algae, important in the prymnesiophyte *Emiliania huxlei* (Vernon and Seely, 1966).

Table 6.1 continued			
Phaeopigments			
Chlorophyllide-*a*	$C_{35}H_{34}N_4O_5Mg$ (blue-green)		Degradation product of chlorophyll-*a*.
Phaeophorbide-*a*	$C_{35}H_{36}N_4O_5$ (yellow-grey)		Degradation product of chlorophyll-*a*.
Phaeophytin-*b*	$C_{35}H_{36}N_4O_5$ (yellow-grey)		Degradation product of chlorophyll-*b*.
Carotenoids			
Internal standard			
Canthaxanthin	$C_{40}H_{52}O_2$ (red)	Cyanobacteria (Van Den Hoek *et al.*, 1995). Trace pigment in some blue-green algae, diatoms (Jeffrey *et al.*, 1997).	Very rare occurrence in the wild makes it suitable for use as an internal standard.
Photoprotective carotenoids			
Diadinoxanthin	$C_{40}H_{54}O_3$ (yellow)	Diatoms, prymnesiophytes dinoflagellates, (Kirk, 1994; Jeffrey *et al.*, 1997).	Photoprotective carotenoid
Alloxanthin	$C_{42}H_{58}O_6$ (yellow-orange)	Cryptomonads (Jeffrey *et al.*,1997)	Photoprotective carotenoid
Zeaxanthin	$C_{49}H_{56}O_2$ (yellow-orange)	Rhodophyta, chlorophytes (Kirk, 1994), prochlorophytes cyanobacteria (Jeffrey *et al.*, 1997).	Photoprotective carotenoid
Lutein	$C_{40}H_{56}O_2$ (yellow)	Chlorophyta, rhodophyta (Kirk, 1994; Jeffrey *et al.*, 1997)	Photoprotective carotenoid
Beta Carotein	$C_{40}H_{56}$ (yellow-orange)	All marine algae except cryptophyta, (Kirk, 1994).	Photosynthetic carotenoid
Photosynthetic carotenoids			
19'-Hexanoyloxy -fucoxanthin	$C_{48}H_{68}O_8$ (orange)	Prymnesiophytes and some dinoflagellates (Jeffrey *et al.*, 1997).	Photosynthetic carotenoid
19'-Butanoyloxy -fucoxanthin	$C_{46}H_{64}O_8$ (yellow-orange)	Chrysophytes e.g. *Pelagococcus*, some prymnesiophytes with traces in *Emiliania huxlei* (Jeffrey *et al.*, 1997).	Photosynthetic carotenoid
Fucoxanthin	$C_{42}H_{58}O_6$ (orange)	Diatoms (Kirk, 1994; (Jeffrey *et al.*, 1997). Brown sea weeds, some dinoflagellates (Jeffrey *et al.*, 1997).	Photosynthetic carotenoid
Prasinoxanthin	$C_{40}H_{56}O_4$ (deep pink)	Prasinophytes (Jeffrey et al.,1997)	Photosynthetic carotenoid
Peridinin	$C_{39}H_{50}O_7$ (brick red)	Photosynthetic dinoflagellates, except those containing endosymbionts (Jeffrey *et al.*, 1997).	Photosynthetic carotenoid

6.3 WATER SAMPLING, FILTRATION AND STORAGE

The procedures that were used to derive measurements of the chlorophyll and carotenoid components of the phytoplankton pigment assemblage, from water sample collection and storage to analysis by high performance liquid chromatography, HPLC, are presented in this section.

The goals for filtration were to minimise contamination and particle degradation, maximise retention, and concentrate an adequate amount of particles on the filters for accurate measurements to be derived by HPLC (Mueller and Austin, 1995).

6.3.1 Water collection

The water sampling strategy inevitably varied considerably from platform to platform, but the rationale remained the same. The objective was to collect water as close to the time of the optical cast as possible, filter the sample and preserve it in liquid nitrogen (LN_2) for subsequent laboratory analysis. The time between sampling and LN_2 preservation was kept to a minimum, with a repeatable sampling pattern being established and executed throughout all fieldwork.

6.3.1(i) Sampling at station L4

Samples were collected using Niskin bottles at a depth of 1*m* using the crane fitted to the starboard after quarter of *RV Squilla* (see figure 4.15). As the survey progressed a four bottle string was used during the summer of the sampling to extend the measurement suite below the surface, thus allowing the targeting of water column structure to be variability identified by temperature and/or chlorophyll fluorescence profiles. The bottle depths were targeted from an assessment of the temperature profile (see figure 6.2). Historical data from prior PML work were used as a guide to sampling, (Holligan and Harbour, 1977).

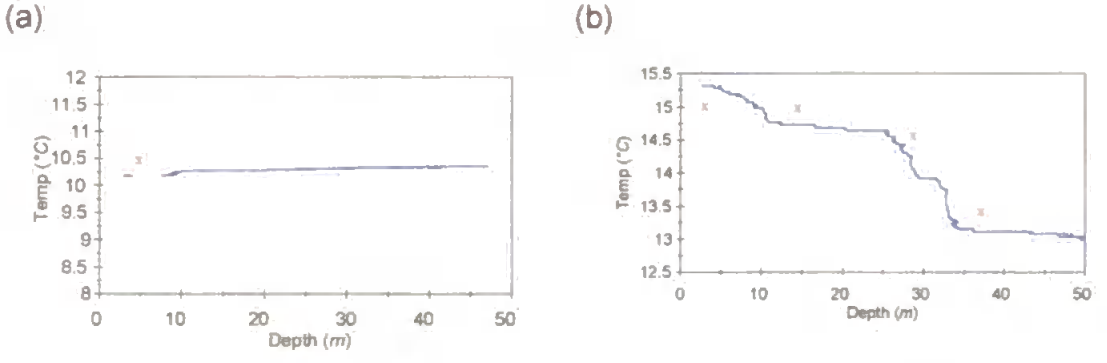

Figure 6.2. Typical L4 site temperature data collected during 1995 sampling where (a) illustrates winter conditions (SDY 30) and (b) early summer conditions, (SDY 179) at station L4. The red crosses overlaid on the plots indicate the sample bottle depths targeted from these temperature data.

Samples were collected on the same day each week, weather and logistics permitting. Filtration was carried out immediately after the samples were drawn from the bottles using the positive pressure filtration system described in section 6.3.2(i).

6.3.1(ii) Sampling during AMT-1 and PRIME

The CTD bottle water sampling system used on board *RRS James Clark Ross* during AMT-1 and *RRS Discovery* during PRIME varied only in the method of sample targeting.

During the AMT-1 daily sampling stations, two CTD rosette mounted Niskin bottles were used to sample at each main depth (which were the same at each station), and one bottle at two extra depths (determined during the CTD downcast). Typical CTD casts were to a depth of 200*m* (see figure 6.3). In addition to the bottle samples collected at the profile site, additional samples were collected from the uncontaminated sea water supply at a depth of 7*m* while underway. Two litre samples from the first five depths were filtered and stored in LN_2 at each optics profiling site. The sampling resolution depended upon information collected on station from profiled radiometric measurements of photosynthetic available radiation (PAR) and temperature structure derived from an undulating oceanographic recorder (UOR), which was lowered vertically down to 100*m* upon arrival on station to obtain a quick look CTD-F cast (the profiling CTD/bottle rosette on board *James Clark Ross* had no fluorometer fitted during AMT-1 to determine the vertical chlorophyll structure).

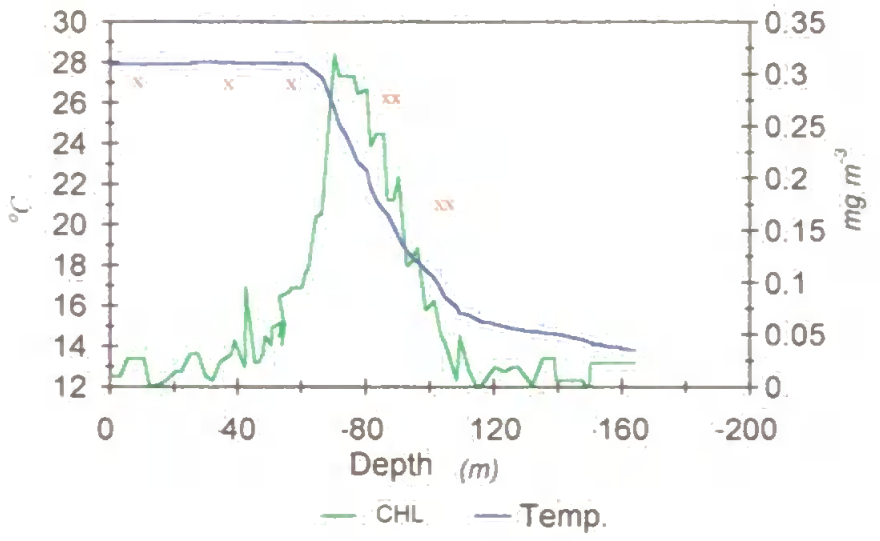

Figure 6.3. AMT-1 UOR derived chlorophyll fluorescence (CHL) and temperature (Temp.) data. The red crosses overlaid indicate the depths at which sample bottles were fired.

The CTD rosette used 12 * 20 litre Niskin bottles deployed from a dedicated winch located slightly aft on the starboard side of the vessel. Sub-samples were siphoned into the 2 litre bottles ready for filtration. Similar sampling protocols were followed during PRIME sampling, with two litre water samples collected from each bottle from each CTD-F cast during the cruise programme.

6.3.2 Filtration

Whatman GF/F filters were used as specified by Mueller and Austin (1995). The GF/F filter has a finely woven glass fibre microstructure (see figure 6.4a), with a nominal pore size of 0.7μm, around which the size retention is normally distributed. Also shown, figure 6.4(b), is an electron microscope scan of a 0.2μm Nucleopore membrane filter, (of the type used to examine the absorption spectrum of the DOM fraction illustrated in figure 2.7).

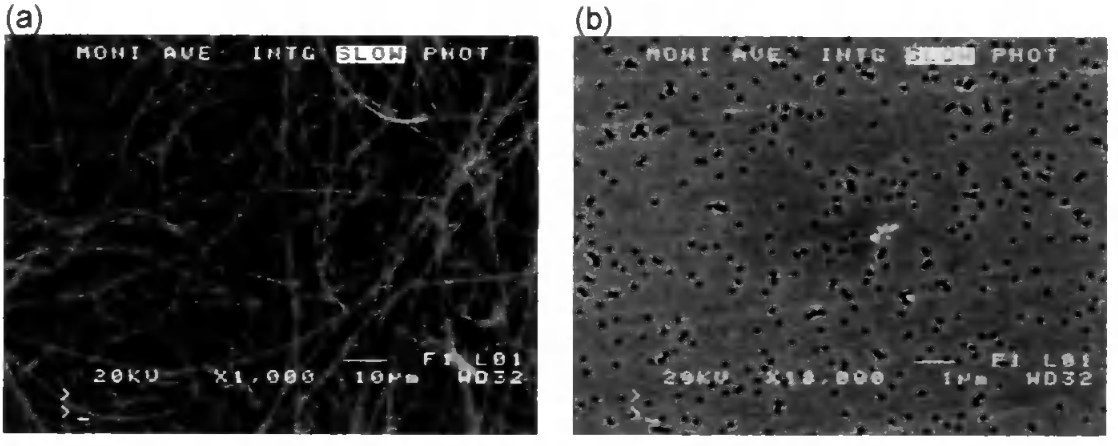

Figure 6.4. Scanning electron micrograph of (a) a Whatman GF/F (0.7μm) glass fibre filter pad and (b) a 0.2μm Nulceopore membrane filter. Images generated courtesy of the University of Plymouth Electron Microscopy Unit.

6.3.2(i) Positive pressure filtration system

The water samples were filtered as soon as was practicable after collection using a purpose built low positive pressure filtration system (figure 6.5). The system design brief was to produce a portable, robust, efficient and easy to use apparatus that would not contaminate the sample and would cause minimum sample degradation during filtration.

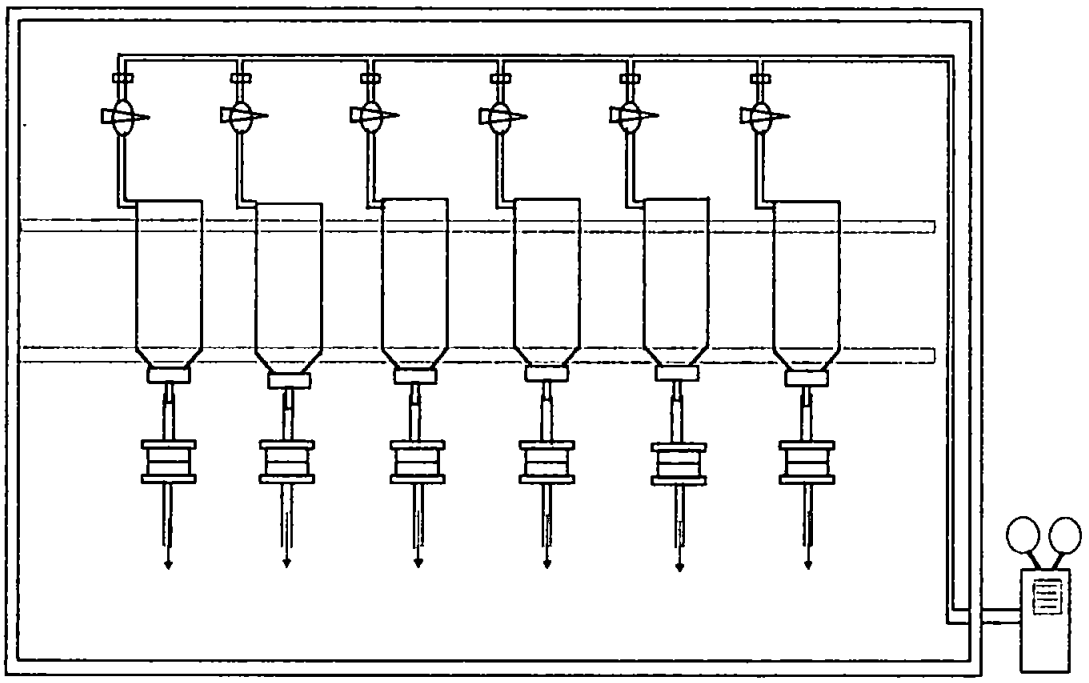

Figure 6.5. One half of the water filtration system used throughout the fieldwork showing the bottles, pressurising manifold and 25*mm* filter housings.

Modifications to the filter housings and a possible design for an automated filtration and storage system are discussed in appendix 2.

6.3.2(ii) Filtration rig components

The filtration rig used Tygon R3603 tubing with a specification that was non-contaminating as well as providing a good grip over the operational pressure ranges of 0-15 psi. The filter housing quick release connectors were made from Polypropylene and stainless steel, preventing fluid flow upon disconnection. The Nalgene 'T' section joints were made of polypropylene, as were the non-return valves. The Gelman Sciences 25*mm* filter housings were made of Teflon with a stainless steel filter support. The Nalgene sample bottles were of non-contaminating polypropylene construction (to DIN 13316 and 168) which were available in 0.5*l*, 1*l* and 2*l* capacities, sharing a common lid size enabling ease of switching between sample volumes. The bottles were suitable for the field temperatures encountered which ranged between 4-32°*C*, with minimal losses due to shattering. The sample bottles were fitted straight onto the positive pressure filtration rig, where up to 12 samples could be filtered simultaneously or the system used in two discrete sections of 6.

Pressure was applied using a standard oil-less Millipore twin manifold pump with pressure taken from what is usually the 'exhaust' port, this was kept to a minimum during filtration to minimise phytoplankton cell disruption during filtration.

6.3.2(iii) Filtration procedure

The following section outlines the filtration protocols that were observed from water collection to sample storage in liquid nitrogen. While the filtration time may increase in waters containing relatively high levels of suspended particulate material, the process was typically completed in 10-15 minutes.

(a) The primed cryo-flask (see section 6.1.3) and set of marked vials were to hand to enable the filters to be frozen immediately they were transferred from the housings.

(b) The rig was set up with Whatman 25*mm* GF/F filters prior to sampling to save time. If more than 12 samples were to be taken at any one filtration session then bottles were re-primed with new filters as they became available.

(c) The pump operating pressure and the integrity of all unions were checked for leaks.

(d) The two litre sample containers were brim-filled from the CTD bottles (to set the sample volume) and the lids screwed down. The bottles were then inverted and placed upon the racks (the non-return valves and snap connectors preventing the sample being spilt during transfer).

(e) The bottles were connected to the pressurising manifold and the filter housings. Pressure was applied to the sample by adjustment of the pump regulator and the isolation switch, which would often require a raised pressure to break the surface tension of the water across the filter pad before reducing the pressure once flow was established. The filtrate was either left to drain or could be captured for further analyses.

(f) As the filters became blocked the regulator valve was adjusted to increase the pressure slightly. Should it not have proven possible to filter the entire sample, the unfiltered volume was measured and subtracted from the whole and/or smaller bottles were used for future samples before the increased sample volumes were once again appropriate.

(g) As the sample bottles emptied, the isolation valves were shut, with the regulator valve being opened as necessary to blow off the excess pressure.

(h) Upon completion of filtering (by which time the valves were shut) the regulator was opened completely.

(i) The snap connectors that linked the filters to the waste pipe-work were released to allow clear access to the filter housings, which were then unscrewed to allow access to the filters; these were then removed using flat faced forceps.

(j) The filter papers were carefully placed in the cryo-vials which were immediately stored in liquid nitrogen. All the filtration rig components were then rinsed in clean fresh water ready for re-use.

6.3.3 Cryogenic preservation and transportation

In order to arrest sample degradation once filtered the marked cryo-vials were immediately stored in LN_2 at -196°C until analysis. Logistical arrangements were made during each fieldwork session to ensure that this was possible.

6.4 PIGMENT PROCESSING BY HPLC

In this study the derivation of pigment concentrations by HPLC was undertaken using routine analysis techniques by trained technicians. In this way the operation was employed as a 'black box' process employing the methodology of Wright *et al.*,(1991), the focus of this work being the chromatogram analysis.

Pigment samples were processed at two sites on similar systems: (i) Plymouth Marine Laboratories (PML) under the guidance of Dr. Ray Barlow; and (ii) at the Centre for Hydro-optics and Remote Sensing (CHORS) under the guidance of Dr. Charles Trees.

The HPLC chromatograms were recorded as a scaled deflection against time as determined by the optical detectors (typically at 443*nm*-455*nm* absorbance and/or 670*nm* fluorescence). The area under the curve of the chromatogram is proportional to the concentration of the separated pigment as it passes through the detector, the identification of which was made on the basis of retention time, Rt (the time taken for the compound to reach the detector from the injection of the sample into the column) and by periodic comparison of the component peaks with a library of absorption spectra obtained from known standards.

6.4.1 Running the samples through the CHORS HPLC

The samples were taken from the nitrogen and dissolved in 100% acetone for a minimum of 15 hours and kept in the dark at -20°C. The samples were then centrifuged for 5 minutes before a sub-sample (600μl) was placed in the HPLC auto sampler vial. The vials were then placed in the racks, with the temperature control of the tray set to -1°C to inhibit sample degradation during analyses (a run of 48 samples takes about 24 hours).

An internal standard solution of canthaxanthin was used at CHORS, which is found only rarely in wild populations of cyanophyta, heterokontophyta, haptophyta and dynophyta (Van Den Hoek *et al.*, 1995) and was added to the extracting solvent to account for any changes in volume by using the identified concentration to normalise all the subsequently resolved pigments. Since canthaxanthin is a carotenoid, its fluorescence spectrum would not offset any accompanying fluorometric analyses, (see section 6.4).

Pigments were separated by an ODS-2 column using a three solvent system at a flow rate of 1$ml\ min^{-1}$. A sample run took 25 minutes with the pigment peaks being detected by two absorption detectors; a Thermal-Separation Products (TSP) UV2000 measuring absorption at 436*nm* and 450*nm*, and a TSP Spectra Focus scanning detector measuring 32 channels from 396*nm* to 524*nm*. In addition a Spectrasystem FL 3000 scanning fluorescence detector was used to detect and quantify degradation products. Although CHL-*a* and DV-*a* co-elute on this column, their absorption characteristics vary at 436*nm* and 450*nm*. Their separation was achieved by the

CHORS system employing the di-chromatic equation technique (Latasa *et al.*, 1996). It was therefore possible to account for the divinyl chlorophyll-*a* component by monitoring changes in the ratio as a function of changes in the divinyl chlorophyll-*a* (Dv-*a*) percentage of the total Chlorophyll-*a* (Chl-*a*) concentration.

6.4.2 Running the samples through the PML HPLC

The same methodology was used for sample preparation and analyses as described for the CHORS HPLC analyse in the last section, but employing different hardware. The system used was a Shimadzu HPLC with dual LC-6A pumps and an SPD-6AV spectrophotometric absorption detector and RF-535 fluorescence detector with an SCL-6B controller. The type of system employed was capable of resolving CHL-*a* and dv CHL-*a* directly (Barlow *et al.*, 1997), see figure 6.7.

6.5 Calibration of the fluorometer used during the AMT-1 along track sampling

The following section describes the calibration procedure that was undertaken prior to AMT-1, (which was then re-calibrated at the end of AMT-2). The concentration of the chlorophyll-*a* standard was determined spectrophotometrically from the measured extinction coefficients (Vernon and Seely, 1966) prior to adding 2 drops of 0.1N hydrochloric acid (HCL) for data collection post acidification, as shown in table 6.2 and equations 6.1 and 6.2. Data were corrected for the optical density, $[\log_{10}(1/T)]$, at 750*nm*.

As any absorption in evidence at this wavelength was an artifact of the optical characteristics of the spectrophotometer as chlorophyll-*a* is optically inactive in this spectral region.

Table 6.2. Absorption characteristics of the standard chlorophyll-*a*.

Wavelength (*nm*)	Reading, (optical density)	Reading corrected for absorption. at 750*nm*, (optical density)
630	0.156	0.099
645	0.188	0.131
665	0.742	0.685
750	0.057	
Post acidification		
665	0.449	0.391
750	0.057	

$$\text{Chlorophyll-}a = \left[11.63(A_{665}) - 0.14(A_{630}) - 1.31(A_{645})\right] \times \frac{10}{5} \times 100 \quad (g\ m^{-3}) \qquad (6.1)$$

where the constant, 10/5, accounts for the use of a 5*cm* rather than the 1*cm* cuvet used to generate the relationship.

$$\text{Chlorophyll-}a = 26.7(A_{665a} - A_{665b}) \times \frac{10}{5} \times 100 \qquad (g\ m^{-3}) \qquad (6.2)$$

From these data the concentration of the standard was calculated to be 1.645 *mg* m^{-3}. Data in table 6.3 show the range of standard concentrations that were generated to calibrate the fluorometer.

Table 6.3 Sample standard dilution.

Dilution of standard sample	Concentration $g\ m^{-3}$
1.0	1.563
0.8	1.251
0.6	0.938
0.4	0.623
0.2	0.313
0.1	0.157

Examination of these standards in the fluorometer gave the results listed in table 6.4. Fa was derived for each standard concentration using equation 6.3.

$$Chlorophyll-a = (Rb - Ra) * \frac{Vomume\ \ extracted}{Volume\ \ filtered} * Fa \qquad (mg\ m^{-3}) \qquad (6.3)$$

where Rb is the reading before acidification, and Ra the reading after.

Table 6.4. The calculation of Fa from the range of standard dilutions.

Dil.	Con.	Rb	Ra	Diff. Ra	Rb/Ra	Fa
1.0	1.645	1.8	1.08	0.72	1.66	2.171
0.8	1.316	1.48	0.85	0.63	1.741	1.985
0.6	0..987	1.12	0.689	0.431	1.626	2.176
0.4	0.623	0.51	0.32	0.19	1.59	3.291
0.2	0..249	0.44	0.24	0.2	1.83	0.782
0.1	0.165	0.2	0.12	0.08	1.67	1.954
					AVG.Fa	2.0597

From table 6.4 it can be seen that the average value of Fa, the calibration factor, was determined to be 2.06 for the fixed optical configuration of the fluorometer.

6.6 FLUOROMETRIC CHLOROPHYLL-*a* ANALYSES

During the AMT-1 cruise, fluorometric analyses of water samples were carried out *in-vitro* in tandem with the collection of HPLC samples for storeage. During the cruise, samples were collected at approximately two hourly intervals, and were extracted in 10*mls* of 90% HPLC grade acetone in the dark at -20°*C*. These samples were then analysed one day in arrears to derive the concentration of CHL-*a* and phaeophytin-*a* (Yentsch and Menzel, 1963). Data in figure 6.6 show the resultant CHL-*a* data generated from the along cruise track measurements.

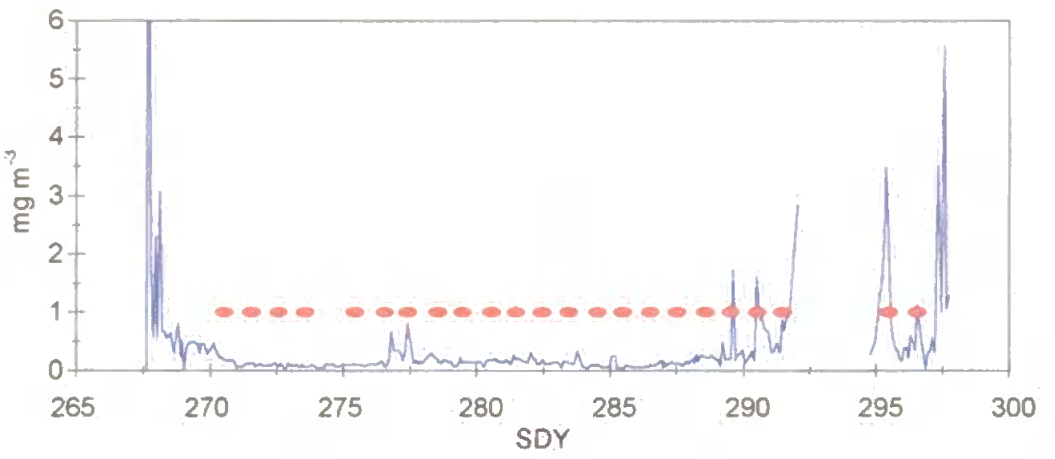

Figure 6.6. Underway fluorescence data collected during AMT-1. The red dots correspond with the times (SDY) of the daily CTD casts and do not relate to the Y-axis.

These data give an indication of along track variability in phytoplankton biomass.

6.7 PIGMENT DATA PROCESSING METHODOLOGY

The chromatograms produced for each pigment sample contain the peaks and associated areas for each compound separated by the system. Figure 6.7 shows a typical chromatogram of the type routinely identified in oceanic water samples. Also shown are some algal groups commonly associated with these pigments. The chromatograms were recorded and then re-analysed prior to transfer of the peak areas, residence times and calibration factors to a spreadsheet, to enable the concentration of each pigment identified to be calculated.

6.7.1 HPLC calibration data

The peak areas obtained from the HPLC were converted to concentrations by the application of the calibration factors obtained from HPLC analysis of pure pigment samples of known concentration (from spectrophotometric determination). Table 6.5 and

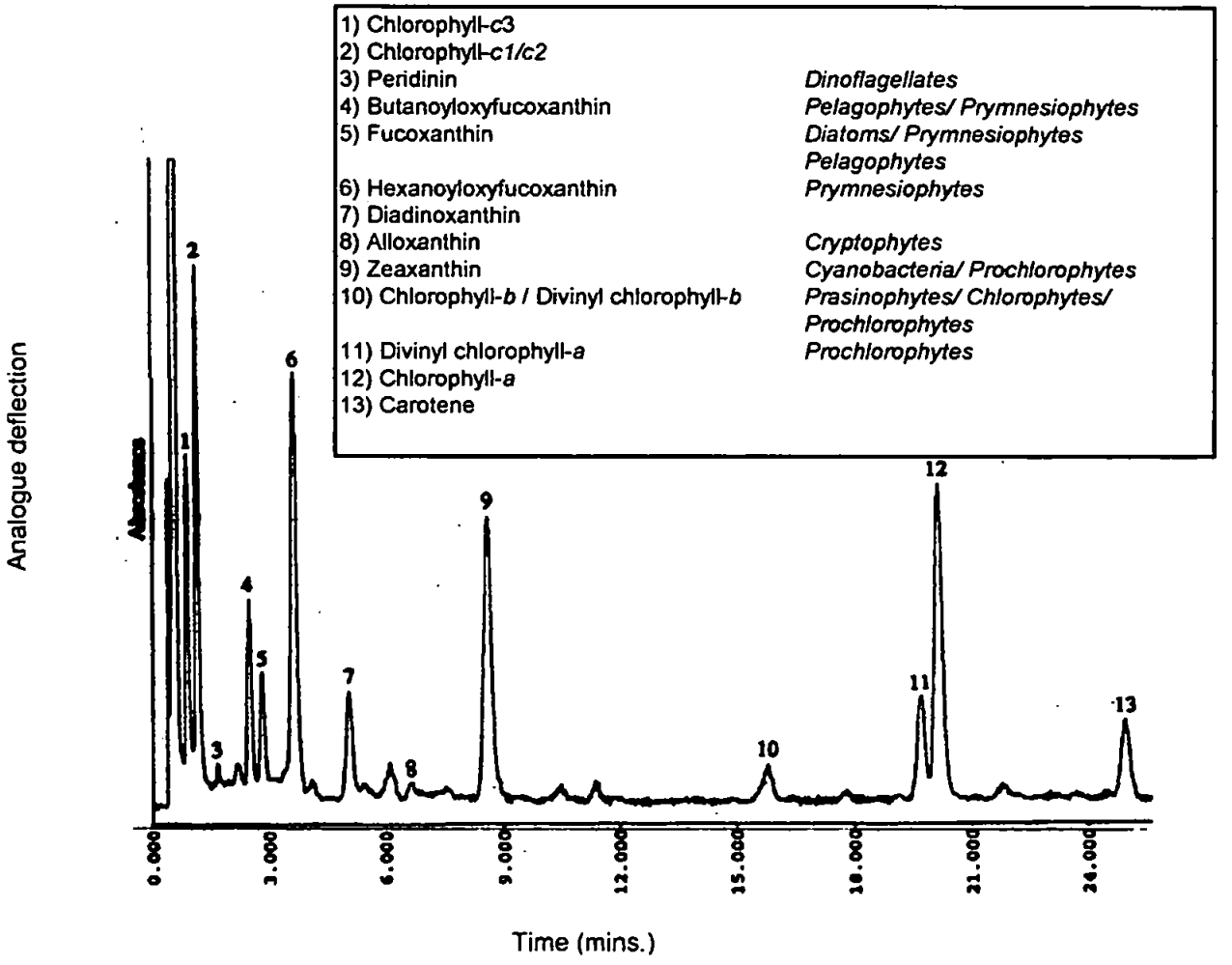

Figure 6.7. Typical chromatogram produced by HPLC analysis.

and 6.6 respectively show the calibration data (as well as retention times) that were determined at CHORS and PML prior to the commencement of this study. The calibration data were obtained by running standards through the configured HPLC system, and the instrument analogue response is thus calibrated.

Table 6.5 Calibration data applied to the CHORS HPLC.

Identified pigment	Detector wavelength (*nm*)	Retention factor (Rf).	Retention time, mins. (Rt).
canthazanthin (internal standard)	450	********	********
chlorophyll-*c*	450	0.00125	6.4
peridinin	450	********	7.8 - 8
butanoyloxyfucoxanthin	450	0.0012	8.4
fucoxanthin	450	0.00296	8.9
hexanoyloxyfucoxanthin	450	0.00124	9.5
prasinoxanthin	450	0.00136	10.8
diadinoxanthin	450	0.00117	13.1
alloxanthin	450	0.000823	14.7
lutein	450	0.00131	16.9
zeaxanthin	450	0.00131	16.9
chlorophyll-*b*	450	0.00199	20
chlorophyll-*a*	436	0.0027	21.234
chlorophyll-*a*	450	*********	21.234
phaeophorbide-*a*	450	*********	>10 <14
phaeophytin-*a*	450	0.8476	24.5
phaeophytin-*b*	450	0.04535	23.1

Table 6.6 Calibration data applied to the PML HPLC.

Pigment identified	Detector wavelength (*nm*)	Retention factor (Rf)	Retention time (Rt) (mins).
chlorophyll-*c3*	440	00.239	0.9
chlorophyll-*c2*	440	1.969	1.23
peridinin	440	4.64	2.02
butanoyloxyfucoxanthin	440	6.902	3.63
fucoxanthin	440	7.0523	3.92
prasinoxanthin	440	6.353	4.84
hexanoyloxyfucoxanthin	440	5.572	5.14
diadinoxanthin	440	11.784	6.95
alloxanthin	440	10.455	9.19
zeaxanthin	440	9.569	11.3
lutiein	440	13.954	11.51
chlorophyll-*b*	440	2.916	19.62
divinyl chlorophyll-*a*	440	4.097	23.4
chlorophyll-*a*	440	3.19	23.82
alpha-carotein	440	10.665	28.86
beta-carotein	440	6.043	28.91
phaeophorbide-*a1*	670	8.391	3.186
phaeophorbide-*a2*	670	11.556	3.879
phaeophorbide-*a3*	670	11.556	4.257
chlorophyll-*a*	670	3.897	23.9
phaeophytin *a1*	670	6.378	29.21
phaeophytin *a2*	670	8.033	30.772

6.7.2 Conversion of HPLC chromatogram output to pigment concentrations

The method of deriving pigment concentrations from the HPLC data differed between the two sites: (i) the equation used to derive pigment concentrations from the CHORS system was as follows (equation 6.4):

$$Conc. = (Rf \cdot peak\ \ area) \cdot \frac{vol.\ \ extract\ \ (ml)}{vol.\ \ filtered\ \ (l)} \cdot\ 0{\cdot}001\ \cdot \left(\frac{10830}{Cantha.\ \ response} \right)\ \ (mg\ m^{-3}) \qquad (6.4)$$

where Rf is the calibration coefficient for that pigment, volume extracted is the volume of 90% acetone (contaminated with canthaxanthin) in which the filter pad is immersed during pigment extraction, and 10830 is the average canthaxanthin signal (peak area) obtained from analysis of the extraction acetone/canthaxanthin mixture. This value was used to correct the identified pigment concentrations from each sample run, accounting for extract volume changes due to factors such as evaporation during handling.

(ii) The algorithm used for the PML system: equation 6.5 was used to derive pigment concentrations from the PML data.

$$Conc. = \left[\frac{\left(\frac{Area}{Rf} \right) \cdot 6 \cdot volume\ \ of\ \ extract\,(ml)}{0{\cdot}3\ \cdot\ volume\ \ filtered\,(l)} \right] \cdot 1000^{-1} \qquad (mg\ m^{-3}) \qquad (6.5)$$

where the constants, 6 and 0.3, account for the sample dilution during analyses.

7. RESULTS

The following section presents a summary and description of the observations made during the fieldwork.

7.1(i) Temperature structure observed at station L4 during the 1995 sampling programme

Temperature data are illustrated in figure 7.1 for 1995 which were collected using a PML built sensor package. These data show that a weak thermocline persisted up to SDY 72, intensifying up to SDY 226 with stratification then decreasing as the water column became increasingly mixed throughout the remainder of the year due to steadily decreasing diel patterns of radiative forcing, and increased surface mixing due to wind. These data correspond with the pigment analyses presented in figure 7.3(ii), where differences were observed in the phytoplankton assemblage during the onset of water column stratification, and in section 8.3.2 the seasonally variable physical structure of the water column is discussed and related to the performance of remote sensing algorithms designed to retrieve chlorophyll-*a* from remote sensed ocean colour.

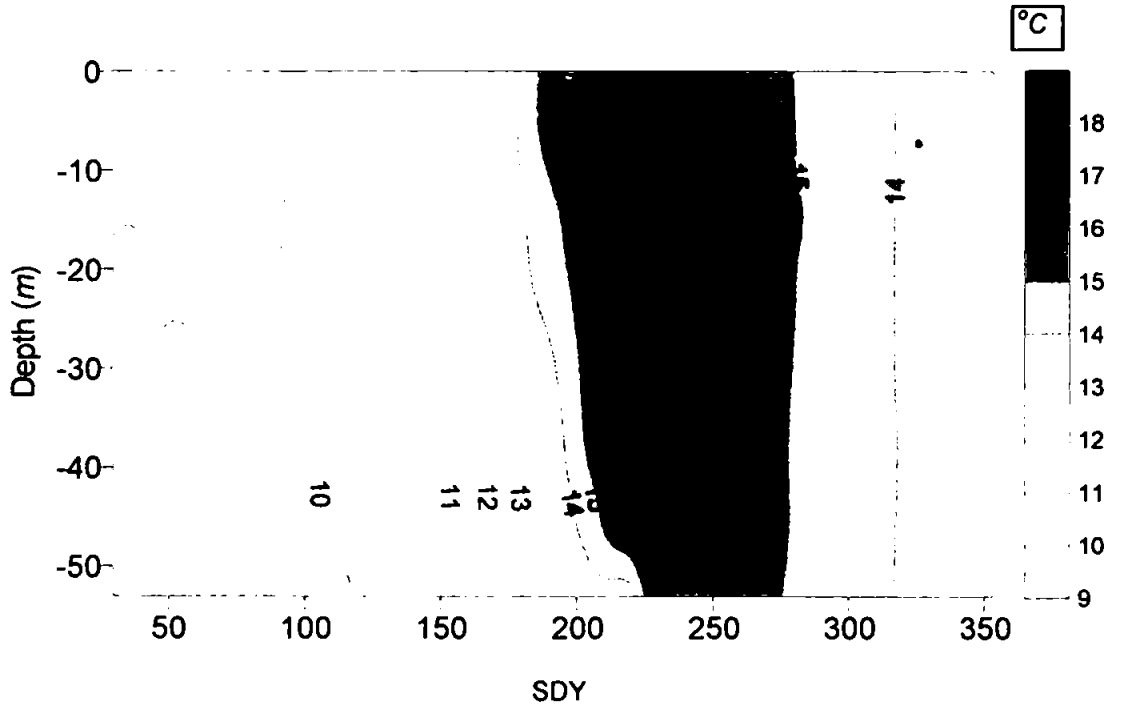

Figure 7.1. 1995 station L4 temperature data from the CTD-F sensor package deployed at the L4 site.

7.1(ii) Temperature structure observed along the AMT-1 cruise track

The thermal structure of the water column was characterised along track using a temperature sensor on board an undulating oceanographic recorder, UOR (Aiken, 1985; Aiken and Bellan, 1990). These data complemented the daily station vertical sampling where a suite of profiling instruments were deployed (Robins *et al.*, 1996). These included CTD, $Lu(\lambda)$, $Ed(\lambda)$ with the addition of a 12 bottle (120 litre total) water sampling rosette. Data in figure 7.2 illustrate the vertical temperature structure to 200*m* measured using the CTD on station. The data follow the cruise track (see figure 1.3), so do not represent a true latitudinal section; and because data were collected daily, only variability at a scale of >250 nautical miles was

resolved. The data show a strong thermocline in evidence at the start of sampling in the western approaches at 47.0°*N*, intensifying towards the 23.3°*N* sampling site, the maximum extent of which was not resolved as sampling was only to 200*m*. The depth of the thermocline increased from 20.0°*N* to the equator but over only the top 40 -175*m*, deepening to a maximum below 200*m* at about 15°*S*.

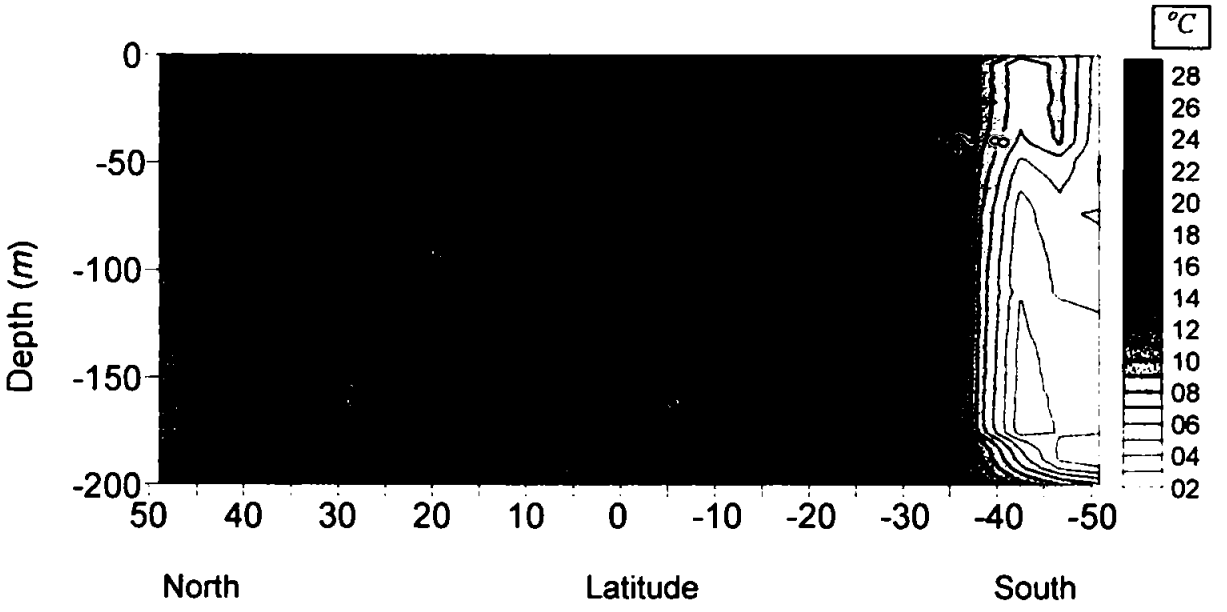

Figure 7.2 Contoured Temperature profile data collected at each daily station stop along the AMT-1 cruise track.

The depth of the thermocline diminished sharply by 30.0°*S*, giving way to cooler mixed surface waters to 200*m* from 35.0°*S* to 40.0°*S*, with a weak thermocline observed from 40.0°*S* to 52.0°*S*.

These data provide a general understanding of the background physical structure that broadly correlates with the changing biological regimes apparent in the corresponding phytoplankton pigment analysis presented in section 7.3(iv).

7.1(iii) Temperature structure observed along the PRIME cruise track

Data in figure 7.3 show the vertical temperature structure down to 80*m* from the start of the cruise at 59.4°*N* to the most southerly extent of the track at 37.2°*N*. A weak thermocline existed at 59.0°*N* to a depth of 25 -30*m*. From 57.5 – 51.0°*N* the temperature of the surface waters became warmer as the survey progressed southwards, intensifying the thermocline, as indicated by the closely stacked isotherms, down to a depth of 20 - 30*m* from 51.0 - 43.0°*N* and deepening to 50 - 60*m* from 41.0°*N* to 37.0°*N*.

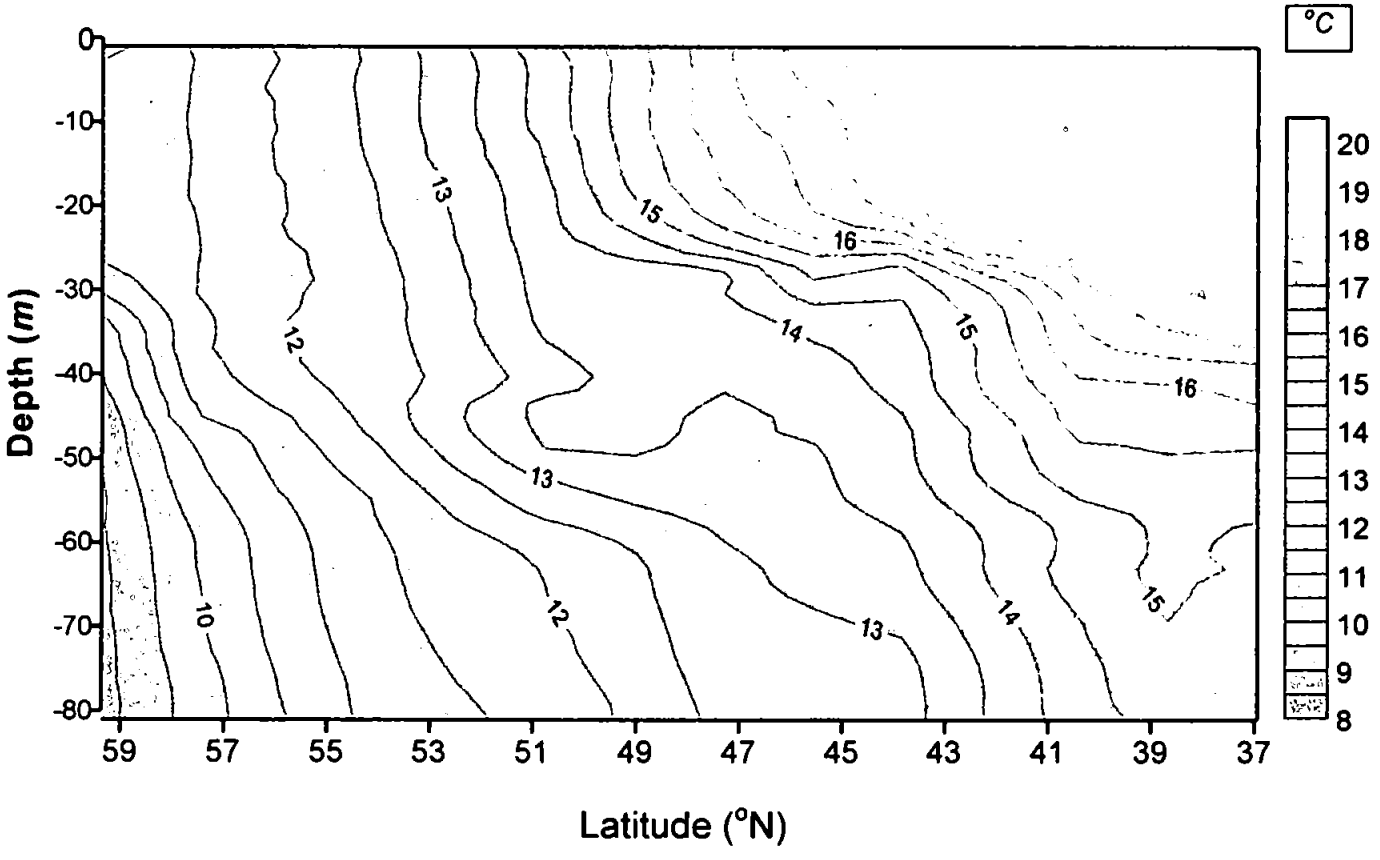

Figure 7.3 CTD cast temperature structure data collected during the transect south from 59.415°*N* to 37.175°*N* during the PRIME cruise. The latitude scale does not correspond with the absolute values of the sampling site locations due to the interpolation and display properties of the contouring package used.

These data helped provide a general understanding of the along track variability of the associated optical, see section 7.2, and biological, see section 7.3(iv) observations (Westbrook *et al.*, 1999).

7.2 OPTICAL CHARACTERISTIC DETERMINATION FROM FIELD RADIOMETRY

It would not be appropriate to display here the vast number of optical data that were generated during this study. The core data products that form the radiometric input to the models investigated are the remote sensing reflectances, calculated just below the surface, $Rrs(\lambda,0^-)$, the observed values of which are displayed in figures 7.4, 7.5 and 7.6 for the three field programmes. Accompanying these data are the corresponding measured diffuse attenuation coefficients, $Kd(\lambda)$. For reference, in each case the chlorophyll-*a* concentration (derived from the HPLC analysis) is also displayed.

The L4 data set included measurements collected using the *Lu*(665*nm*) channel that was subsequently found to be faulty (due to excessive drift between calibrations, see section 4.16; data subsequently collected using this channel were excluded from analyses). Data in figure 7.4(a) show a downward trend in the measured $Rrs(\lambda)$ values as the sampling progressed. 7.4(b) illustrates the corresponding $Kd(\lambda)$ data which showed a trend towards increasing water clarity throughout the period of the study (from the winter through to the summer 1995).

Figure 7.5 illustrates the $Rrs(\lambda)$ and $Kd(\lambda)$ data observed during AMT-1. In Figure

7.5(a) shows that from the start of the cruise at 47.0°*N* the *Rrs(λ)* values ranged from 0.009sr^{-1} at 412*nm* to 0.003sr^{-1} at 560*nm*. The *Rrs*(412*nm*), *Rrs*(443*nm*), and to a lesser extent, the *Rrs*(490*nm*) data show values increasing through 40°*N* to 30°*N* . Observations in these three channels were then reduced at the 19.5°*N* site, corresponding with a rise in the measured *Rrs*(560*nm*). Between 19.5°*N* and the equator further peaks were observed at 412*nm*, 443*nm* and 490*nm*, a pattern repeated between the equator and 19.6°*S*. Between 30.2°*S* and 46.0°*S* the spectral *Rrs(λ)* intensity was reduced. Data in figure 7.5(b) show *Kd(λ)* data derived from radiometric measurements collected at the daily station sampling sites. As with the *Rrs(λ)* data, the *Kd(λ)* measurements also show a spectral variability which characterise the along track variability. Throughout the study the 412*nm*, 443*nm* and 490*nm* *Kd(λ)* data were observed to be similar.

At the start of the optical data collection programme in the western approaches the *Kd(λ)* data follow a downward trend to 23.3°*N*, where the observed values then rose sharply (particularly at 412*nm* and 443*nm*) through 19.5°*N* before becoming reduced at 9.2°*N*, where the data were relatively stable through to 19.6°*S*, before rising along the rest of the track to 47.0°*S*, the final station of the study where optical data were collected.

Figure 7.6 illustrates a summary of the optical data in terms of *Rrs(λ)* and *Kd(λ)* observations made during PRIME. Data in figure 7.6(a) show the *Rrs(λ)* variability observed in the waters at the start of the cruise track (59.4°*N* 20.0°*W*) where there was little observed spectral dependency through to 46.0°*N* at which point the 412*nm*, 443*nm* and 490*nm* wavelength data intensified. This was accompanied by a reduction in the intensity of the corresponding 510*nm* and 560*nm* channels. The *Kd(λ)* data shown in figure 7.6(b) show corresponding spectral variability in the 412*nm* and 443*nm* wavelengths from 49.5°*N* to 42.9°*N*, whereas data collected from 42.1°*N* to

36.7°*N* show greater variation at 560*nm*.

(a)

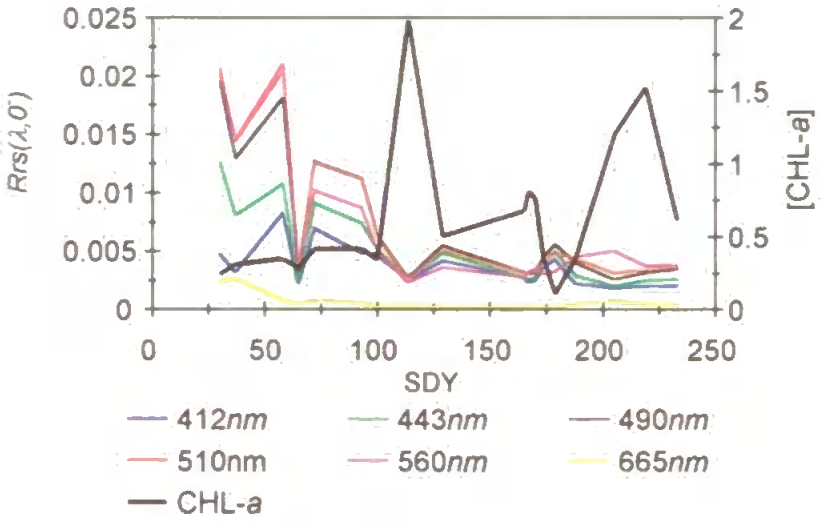

(b)

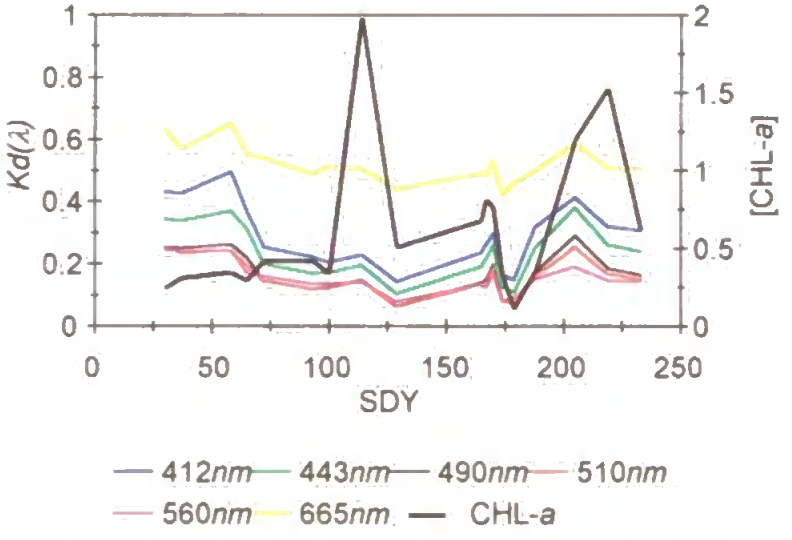

Figure 7.4. (a) *Rrs(λ,0⁻)* against time (SDY) and (b) the corresponding *Kd(λ)* values derived from analyses of radiometric profiles carried out during the L4 study. The December 1995 calibration of the PRR-600 identified the *Ed*(665) channel as becoming unstable (see chapter 4); these data were excluded from work carried out from the beginning of AMT-1 onwards. The units for *Rrs(λ)* are sr^{-1}; *Kd*(λ): m^{-1}, and $mg\ m^{-3}$ for Chlorophyll-*a* (CHL-*a*).

(a)

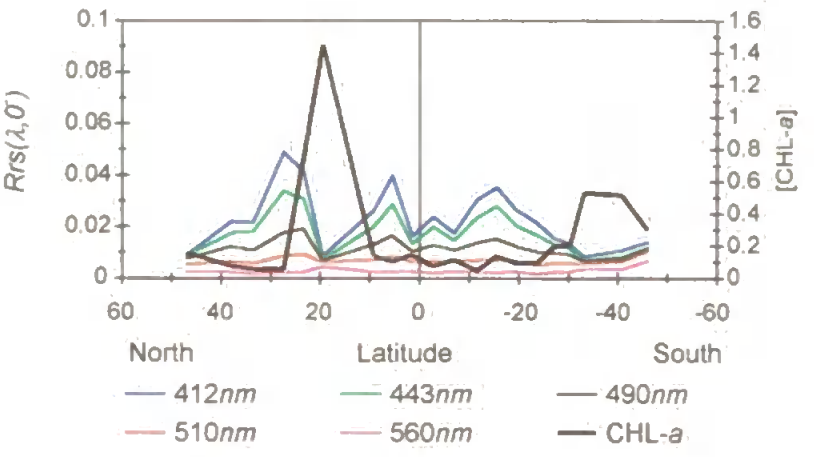

(b)

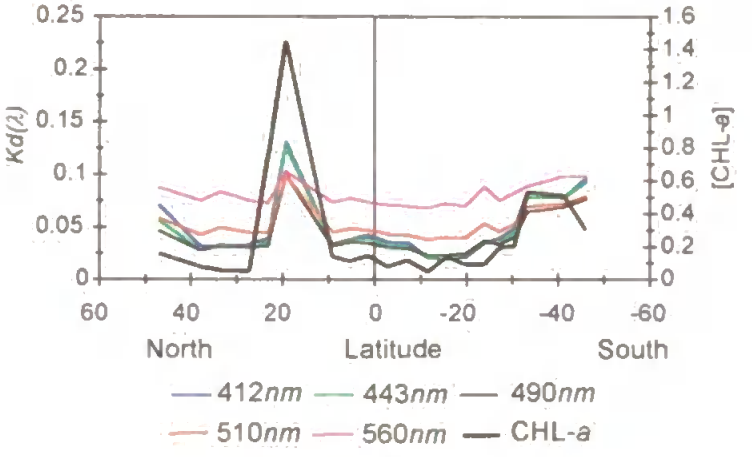

Figure 7.5. (a) *Rrs(λ,0⁻)* against latitude and (b) the corresponding *Kd(λ)* values derived from analyses of radiometric profiles carried out during AMT-1. The units for *Rrs(λ)* are sr^{-1}; *Kd(λ)*: m^{-1}, and $mg\ m^{-3}$ for Chlorophyll-*a* (CHL-*a*).

(a)

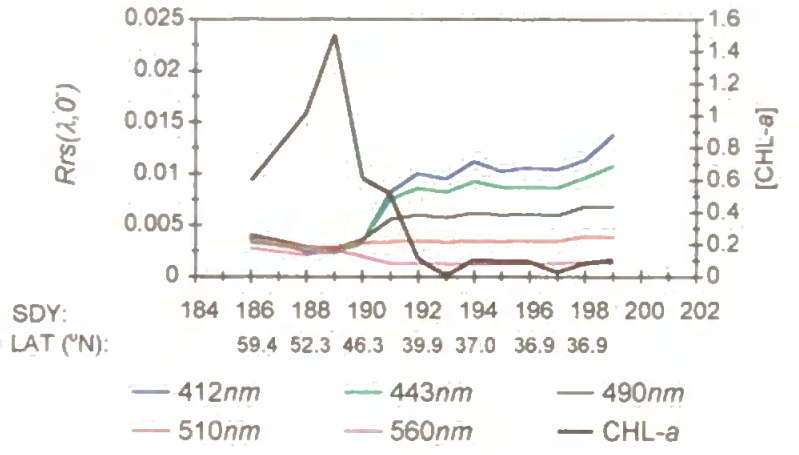

(b)

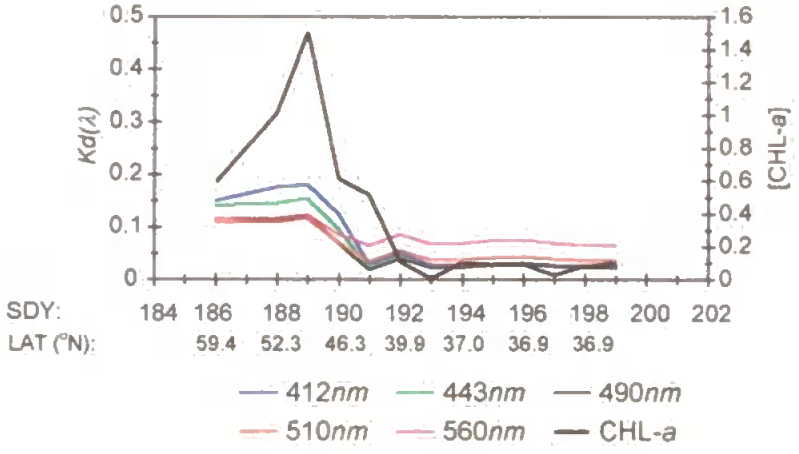

Figure 7.6. (a) *Rrs(λ,0⁻)* against time (SDY) and the corresponding latitudinal position of the sampling site and (b) the corresponding *Kd(λ)* values derived from analyses of radiometric profiles carried out during the PRIME study. The units for *Rrs(λ)* are sr^{-1}; *Kd*(λ): m^{-1}, and $mg\ m^{-3}$ for Chlorophyll-*a* (CHL-*a*).

7.3 PIGMENT CONCENTRATIONS DERIVED BY HPLC

The pigment data presented here, together with the optical characteristics of the water itself and those substances dissolved in it, represent the sum of the driving influences on the optical signature of the surface waters at each sampling site. In order to generate a data set incorporating a range of conditions (both to provide the basis for calculating algorithm empirical constraints and to enable effective testing of the established pigment-light field relationships) sampling over a range of phytoplankton concentrations was required. In addition to the variation in concentration, variability in the composition of the pigment assemblage from site to site (in space and time) was also observed, arising from either spatial or seasonally changing phytoplankton species' dynamics. Aspects of the pigment data analyses were considered in two ways: (i) as a compilation of all three data sets (figure 7.7) and (ii) as data derived from each fieldwork programme (figures 7.8, 7.10 and 7.12); a summary of the ratios of certain key pigment groups determined by regression analysis of these data may be found in table 7.2, and comparisons with other work in table 7.3.

The pigment groups were discussed in section 6, with a summary presented in table 6.1. A list of those that could have been determined by the analyses (i.e. for which pure pigment standards had been obtained), had they been present, may be found in section 6.7.1, tables 6.5 and 6.6 (Jeffrey *et al.*, 1997). The combined data set data set consists of 18 data derived from the L4 study, 20 from AMT-1 and 13 from PRIME. The data are either single surface samples or are an average of data derived from those observations made in the first *Kd*(490*nm*) optical depth (see section 6.3.1), (Clark, 1981).

In this section the pigment data are first treated as an amalgamated data set and then in two ways for each of the 3 individual sampling programmes: firstly as a study of the inter-pigment ratios between the observed groups and secondly as a study of how the presence of a pigment or variability of its ratio with other pigments present, may be used to infer the corresponding presence of a range of phytoplankton groups. These data illustrate the variability in biological regime achieved when undertaking the fieldwork, although care must be taken as biomass and relative pigment concentration can be misleading due to inter-species cell size variability. This technique requires validation by the taxonomic identification of phytoplankton samples by microscopy, which is beyond the scope of this work.

7.3(i) Pigment relationships derived from all fieldwork

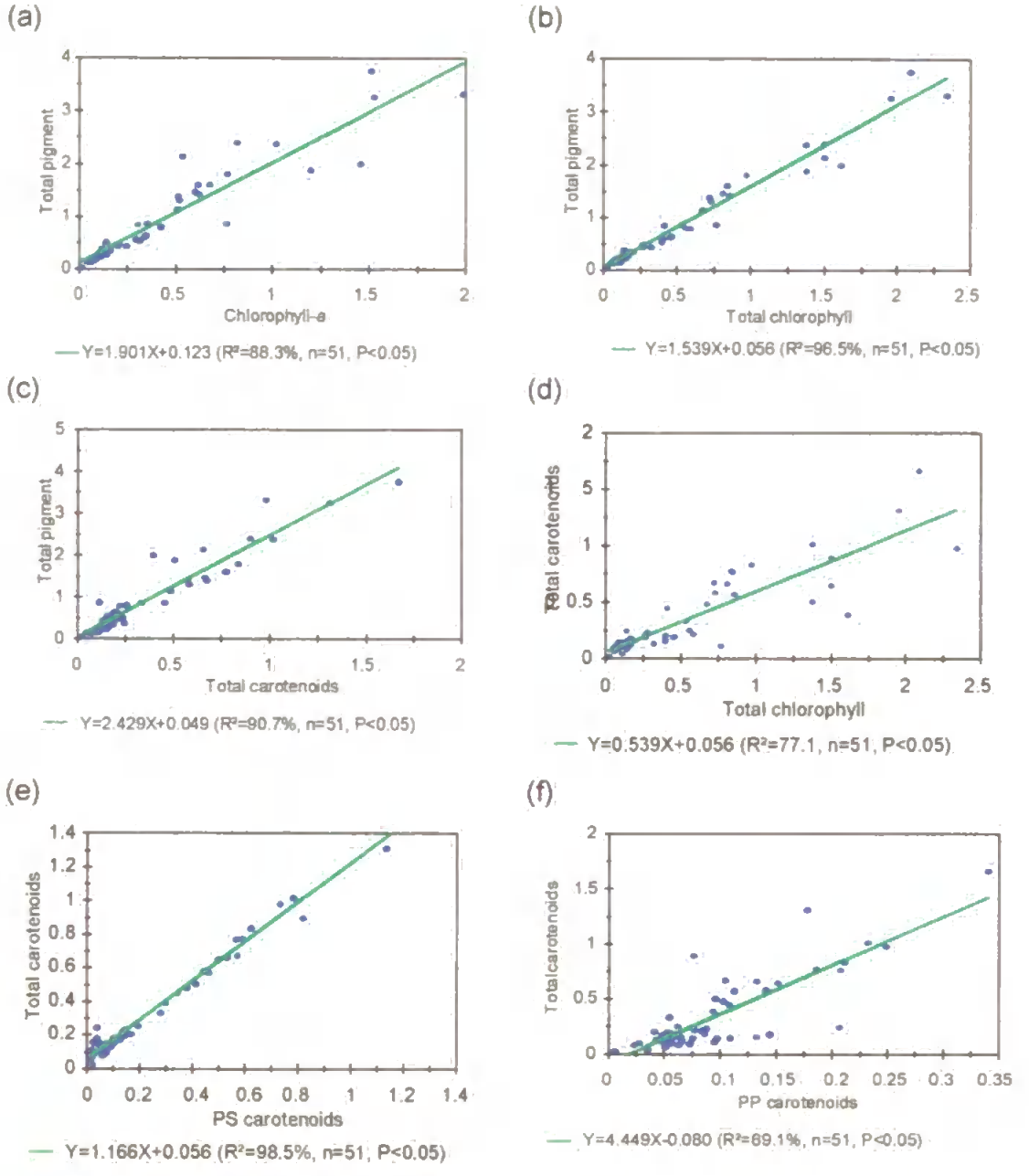

Figure 7.7. Regression analyses of some key pigments derived from an amalgamation of the L4, AMT-1 and PRIME data sets: (a) chlorophyll-*a* to total pigment, (b) total chlorophyll to total pigment, (c) total carotenoids to total pigment, (d) total carotenoids to total chlorophyll, (e) photosynthetic carotenoids to total carotenoids, (f) photoprotective carotenoids to total carotenoids. The units of all pigment concentrations are *mg* m^{-3}.

Data in figure 7.7 show the total chlorophyll (T-PIG) to total pigment (T-CHL) ratio. Observations were described by a high degree of the variance explained, R^2=96.5%, as was the case with the T-PIG:total carotenoid (TC) ratio at R^2=90.7%. Within these fractions, however, lesser degrees of covariance were evident from the lower variances observed between other groups. For example: the T-PIG:CHL-*a* relationship had a lower R^2 of 88.3%, indicating that the relatively poor covariance shown in figure 7.7(a) was due mainly to variability within the [CHL-*a*], a factor less significant when the CHL group were considered as a whole. Data in figure 7.7(c) show regression analyses of the T-PIG:TC (R^2=90.7%) and (d) TC:T-CHL (R^2=77.1%), the relatively low variance in each case being due to the variability in the CHL (mostly CHL-*a* as discussed above) and TC (mostly the photoprotective carotenoid, PPC, fraction), as can be seen from the high degree of variance explained in the TC as a function of the photosynthetic carotenoid fraction (PSC) at 98.5% (figure 7.7(e)). It may be seen, however, from figure 7.7(f), that the TC were large compared to the PPC (4.45 fold on average). The scales of variability of these observations is further discussed in a global context at the end of section 7.3(iv).

7.3(ii) Pigment relationships derived from the L4 study data

When considered in isolation, the L4 pigment data set showed a similar pattern of inter-pigment relationships to the combined data shown in figure 7.7, although the T-PIG:T-CHL relationship, figure 7.8(b), displayed a lower variance of 89.7% than the corresponding value derived from the combined data set. Data in figure 7.8(c) show the well correlated total pigment concentration (R^2=94.4%) observed as a proportion of the carotenoid concentration, albeit a larger fraction than that

determined from the amalgamated data set (from 2.42 to 2.77). The TC correlate well as a function of the PSC, with a variance of 98.5% so the T-PIG:TC relationship is not, therefore, significantly reduced by the PPC variability, which also covaries with the TC with an R^2 value of 69.2%.

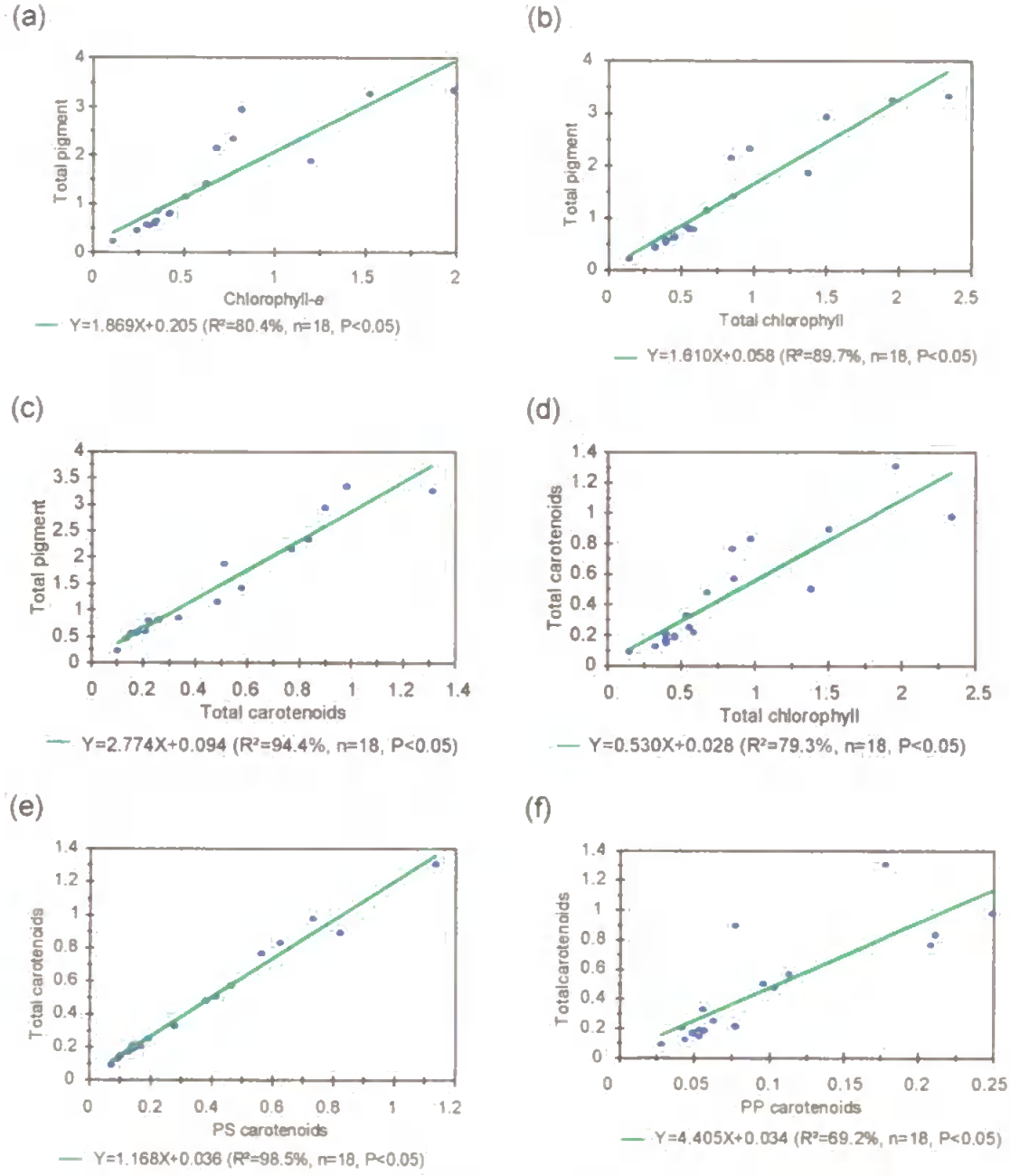

Figure 7.8 Regression analyses of the key pigments derived from the L4 study: (a) chlorophyll-*a* to total pigments, (b) total chlorophyll to total pigment, (c) total carotenoids to total pigments, (d) total carotenoids to total chlorophyll, (e) photosynthetic carotenoids to total carotenoids,
(f) photoprotective carotenoids to total carotenoids. The units of all pigment concentrations are *mg* m^{-3}.

In chapter 6, section 6.5, the sequential structure of a typical HPLC chromatogram, and some key pigments that could be identified from the technique, were illustrated. To re-cap, table 7.1 presents a summary of these data (first introduced in table 6.1):

Table 7.1. Some key pigments identifiable by HPLC, and the classes of phytoplankton to which they typically relate.

Pigment name (abbreviations used in the following discussion)	**Pigment type: PSC=photosynthetic carotenoid, PPC= photoprotetive carotenoid**	**Taxonomic indicator for: (Jeffrey *et al.*, 1997)**
Peridinin (PER)	PSC	• Dinoflagellates
Butanoyloxyfucoxanthin (BUT)	PSC	• Pelagophytes • Prymnesiophytes
Fucoxanthin (FUCO)	PSC	• Diatoms • Prymnesiophytes • Pelagophytes
Hexanoyloxyfucoxanthin (HEX)	PSC	• Prymnesiophytes
Alloxanthin (ALLO)	PPC	• Cryptophytes
Zeaxanthin (ZEA)	PPC	• Cyanobacteria • Prochlorophytes
Chlorophyll-*b* (CHL-*b*) Divinyl chlorophyll-*b* (DV-*b*)	Chlorophyll	• Prasinophytes • Chlorophytes • Prochlorophytes
Divinyl chlorophyll-*a* (DV-*a*)	Chlorophyll	• Prochlorophytes

As is the case with the distribution of terrestrial and freshwater plants, it is also true that at a given marine sampling site there will be a range of algal species represented but, within these groups will be organisms which are typically found in a range of physical environments and are thus broadly indicative of the dominant features of the phytoplankton population dynamics that can be expected to prevail from one sampling site to the next.

With regard the major groups detailed in table 7.1, dinoflagellates are usually the most numerous of the phytoplankton in stratified, nutrient poor tropical and subtropical waters (Holligan and Harbour, 1977; Lalli and Parsons 1997). Prymnesiophytes are important members of the phytoplankton from the tropical to sub-polar Atlantic, although some species (e.g. *Emiliania Huxleyi*) may thrive in neritic zones (Balch *et al.*, 1991). Diatoms are found in all waters, especially the nutrient rich temperate coastal waters and are a strong feature in upwelling zones (Lalli and Parsons, 1997). Cyanobacteria and prochlorophytes are present in the oligotrophic nutrient depleted oceanic gyres (Barlow *et al.*, 1993; Kirk, 1994; Van Den Hoek, 1995).

Figure 7.9 illustrates a time plot (SDY) of the relative proportions (by normalising to [Chl-*a*]) of the pigment concentrations observed during the L4 seasonal study.

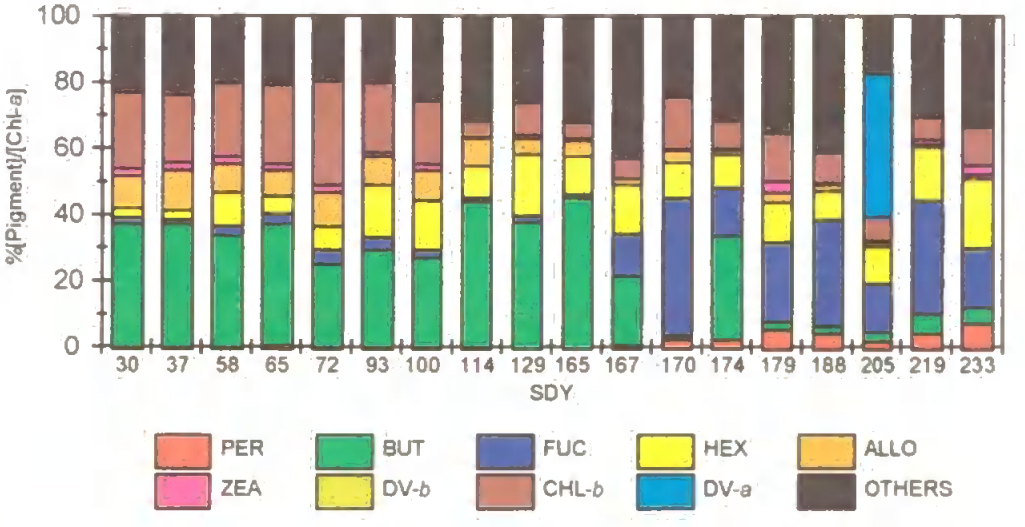

Figure 7.9. Some key pigment groups identified from the L4 study data set, expressed as a percentage of the [total pigment], normalised to the [CHL-*a*]. For key to pigments see table 7.1.

It can be seen from figure 7.9 that the observations may be separated into two sections: (i) up to SDY 165 and (ii) SDY 167 to 233. Although the overall pigment concentration was low (<0.5 *mg* m^3 of CHL-*a* from figure 7.4), during the first section the relatively high BUT and HEX concentrations suggested the presence in the phytoplankton population of prymnesiophytes. The pigment markers for this group continued to be present after SDY 167, but their relative importance within the overall pigment assemblage was reduced. Post SDY 167 FUCO became more important, whereas BUT became much reduced in relative importance indicating greater proportion of diatoms were present.

The occurrence of PER post SDY 165 indicated the presence of dinoflagellates. A single instance of DV-*a* was observed at SDY 205, indicating the presence of prochlorophytes, organisms more usually associated with the nutrient depleted oceanic gyres. This pattern broadly agrees with data presented by Holligan and Harbour (1977), who carried out a study of the phytoplankton population dynamics at a station close to L4: E1, during 1975 and 1976. They found that diatoms were abundant through May (SDY 120-150) in the surface waters, and then sub-surface, with dinoflagellates dominant in the thermocline from June to August (SDY 151-242), and diatoms once again becoming abundant as the thermocline eroded during September (SDY 244-273). The pigment data presented in figure 7.9, although a limited time series, show diatoms persisted in the surface waters through the full period of the study in conjunction with the increasing concentration of PER from SDY 167.

Prior to SDY 165 the pigments that were observed, but are not displayed in figure 7.9, were dominated by chlorophyll *-c1/-c2* (between 0.1 and 34.8%) an accessory pigment found in diatoms (Vernon and Seely, 1966). Post SDY 165 the dominance was by beta carotein at values ranging between 2.1 and 8.5% of the total

normalised pigment. This pigment is present in all marine algae except cryptophytes (Jeffrey *et al.*, 1997).

7.3(iii) Pigment relationships derived from the AMT-1 study data

The AMT-1 pigment data illustrated in figure 7.10 broadly followed a similar pattern of relationships as found in the amalgamated data set, figure 7.7, although the pigment fraction represented a lower proportion of the T-CHL on average at 1.30, down from the value of 1.54 shown in figure 7.7(b). The data displayed generally lower variances throughout the observed pigment groups. The T-PIG:TC relationship, figure 7.10(c), showed a relatively low degree of variance explained at 72.0%, which may be explained by data in figure 7.10(d) where the co-variance between the carotenoid assemblage and the T-CHL were described by an R^2 value of 51.3%, although the exclusion of three outliers (circled) improved this to 89.1%. Further variability is apparent in figure 7.10(e) where, although still high at 94.8%, the variance explained in the PSC:TC ratio was reduced from the higher value displayed in figure 7.7(e) of 98.5%.

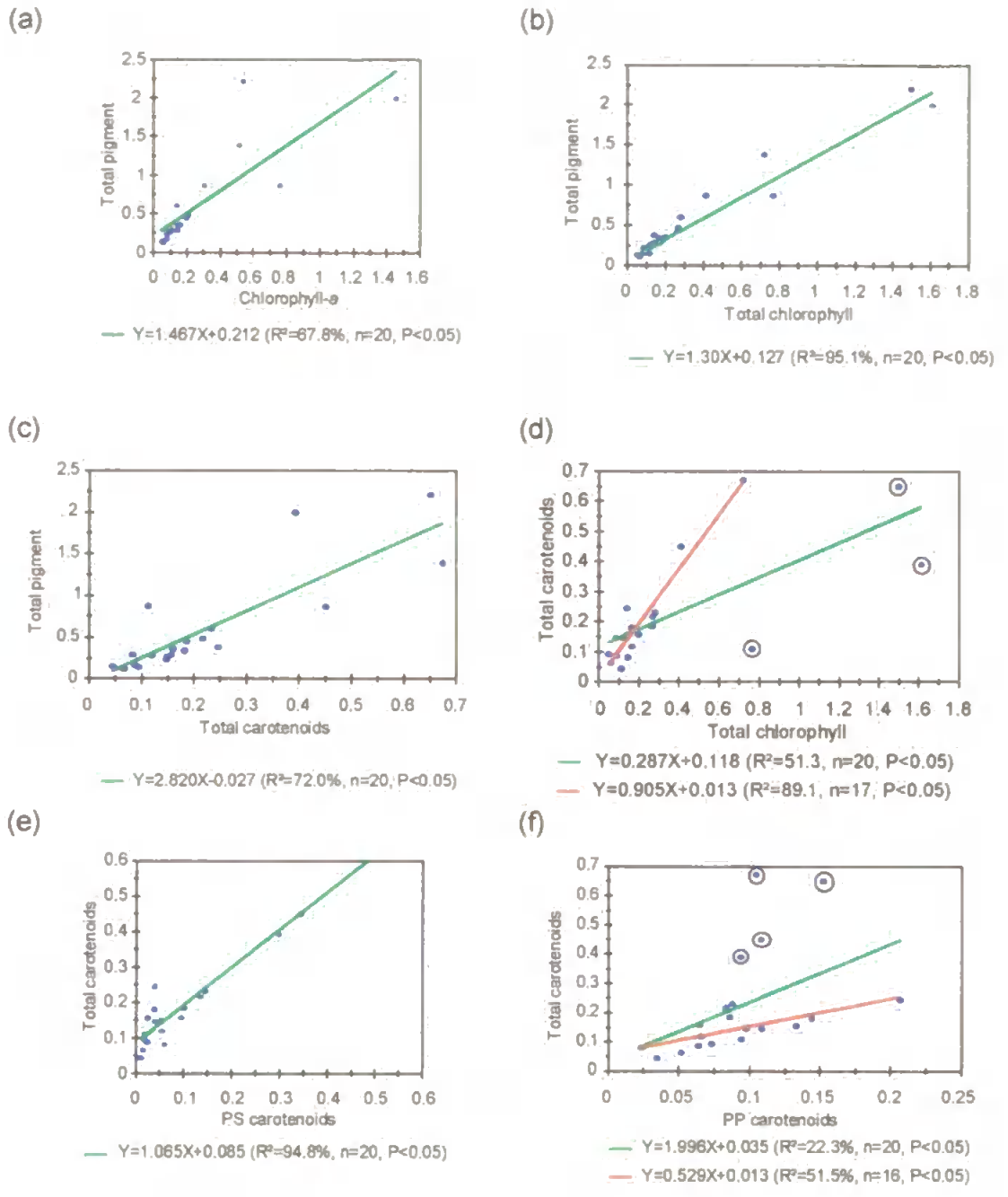

Figure 7.10 Regression analyses of the key pigments derived from the AMT-1 study: (a) chlorophyll-*a* to total pigments, (b) total chlorophyll to total pigment, (c) total carotenoids to total pigment, (d) total carotenoids to total chlorophyll, (e) photosynthetic carotenoids to total carotenoids, (f) photoprotective carotenoids to total carotenoids. The units for concentration of all pigments are $mg\ m^{-3}$.

Data in figure 7.10(f) show a poor PPC:TC relationship. The spread in these data, as was the case with the TC:T-CHL data in figure 7.10(d), showed improvement with the variance explained from 59.3% to 89.1% by exclusion of four points (circled). These data therefore indicated a change in the pigment assemblage had taken place during the sampling, altering the average TC:PPC relationship from TC=1.996 x (PPC)+0.035 to TC=0.529 x (PPC)+0.013. In the case of 7.10(d) the three 'outliers' (circled) are positioned at the latitude 23.3°*N* and 19.5°*N* sampling sites in tendrils flowing offshore associated with the upwelling of nutrient rich water off the coast of Mauritania, and a site on the approach to South America at 33.2°*S*. In the case of 7.10(f) the circled data were collected from the Latitude 9.5°*N*, once again in the region associated with the West African

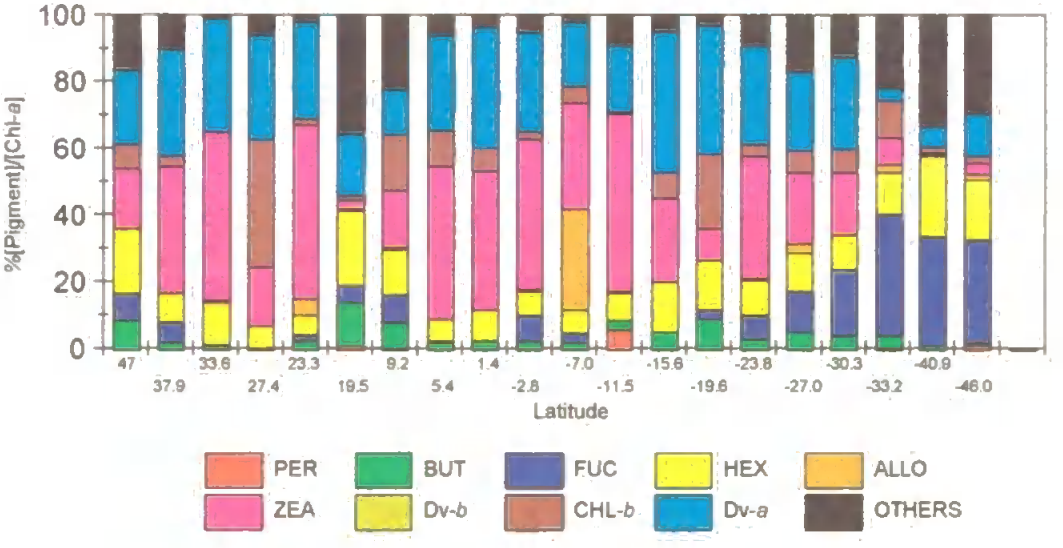

Figure 7.11. Some key pigment groups identified from the AMT-1 data set plotted against latitude. Data are presented as a percentage of the [total pigment], normalised to [CHL-*a*]. For key to pigments see table 7.1.

Mauritanian upwelling zone, and three sites 33.2°*S*, 40.9°*S* and 46.0°*S*, the latter two being in the Falklands current. These observations are therefore distinct from the remaining data which were collected in the oligotrophic north and south Atlantic.

The along track AMT-1 pigment data illustrated in figure 7.11 show several key taxonomic markers were observed during the programme. At 47.0°*N*, present in the phytoplankton population were prochlorophytes, indicated by the DV-*a* and ZEA. The presence of HEX and BUT indicated that prymnesiophytes were present, with FUCO indicating the presence of diatoms.

On this basis it may be seen that the prochlorophytes dominated the observations through the 37.9°*N* and 33.6°*N* sampling sites. By 23.3°*N* the population became once again dominated by prochlorophytes and cyanobacteria. The prymnesiophytes that were in evidence at 47.0°*N*, and to a lesser extent at 37.9°*N*, were also observed through 23.3°*N*, before decreasing once again at 5.40°*N*. At 19.5°*N* the incidence of cyanobacteria and prochlorophytes became reduced in favour of prymnesiophytes with further evidence provided by the observation of HEX at a relatively higher concentration. At this site the high relative concentration of FUCO indicated diatoms were also in evidence, dropping off by 1.4°*N*, with continued observations of HEX and BUT dominated in relative concentration by DV-*a* and ZEA. This pattern continued through to 19.6°*S* where FUCO began to increase in relative importance. A notable exception was the observation of PER at 11.5°*S*, a marker for dinoflagellates. Beyond 27°*S* the cyanobacteria and prochlorophytes gave way in relative importance to observations of diatoms and a low proportion of prymnesiophytes, shown by the low relative concentrations of BUT.

The observed pigments unaccounted for in figure 7.11 were mostly chlorophyll *-c1/-c2* from a minimum value of 0.5% to a maximum of 21.7% at 33.2°S, probably in a diatom bloom where high levels of fucoxanthin were observed and were increasing. Diadinoxanthin ranging between 0.08% to 12% (present in diatoms, prymnesiophytes and dinoflagellates) was also observed (Kirk, 1994; Jeffrey *et al.*, 1997), with small quantities of prasinoxanthin ranging from between 0.04 to 3.8%, a phototsynthetic carotenoid present in prasinophytes (Jeffrey et al., 1997) also in evidence.

7.3(iv) Pigment relationships derived from the PRIME data

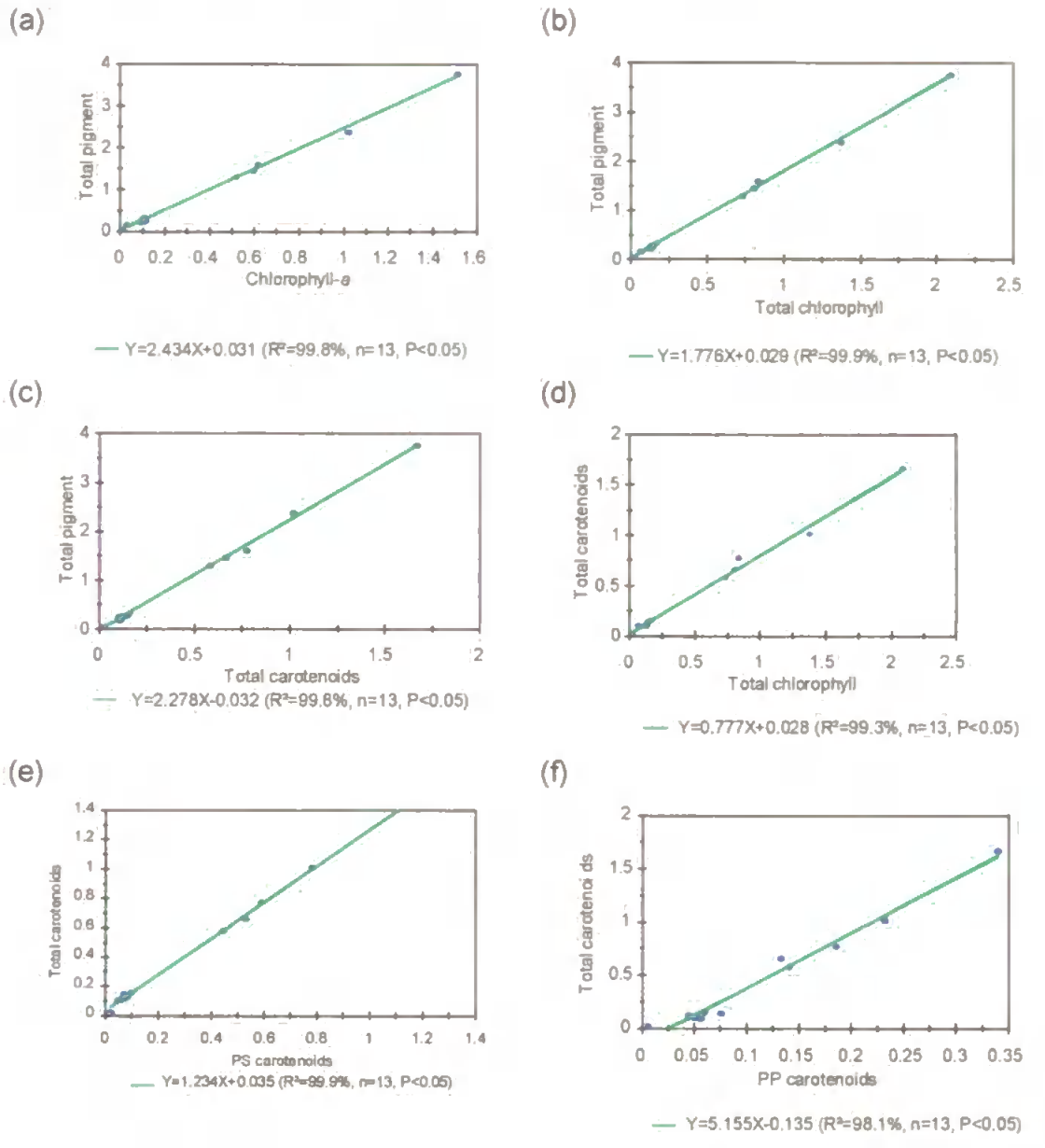

Figure 7.12. Regression analyses of the key pigments derived from the PRIME study: (a) chlorophyll-*a* to total pigments, (b) total chlorophyll to total pigment, (c) total carotenoids to total pigments, (d) total carotenoids to total chlorophyll, (e) photosynthetic carotenoids to total carotenoids, (f) photoprotective carotenoids to total carotenoids. The units of all pigment concentrations are *mg* m^{-3}.

The PRIME cruise data showed strong correlations between the concentrations of the observed groups, where in each variances determined by regression analyses were found to be in excess of 98.1%. The reason for these data displaying such consistent inter-pigment ratios was the limited diversity of biological regimes sampled and the high quality of the subsequent HPLC analysis. The T-PIG:CHL-*a* and T-PIG:T-CHL ratios shown in figure 7.12(a) and (b) respectively were higher than the values derived from the amalgamated data set, the converse being the case with the carotenoid fraction which, on average, formed a lower proportion of the T-PIG. The average PSC:TC ratio was slightly lower than the value determined for the whole data set, whereas the PPC formed a greater proportion of the TC.

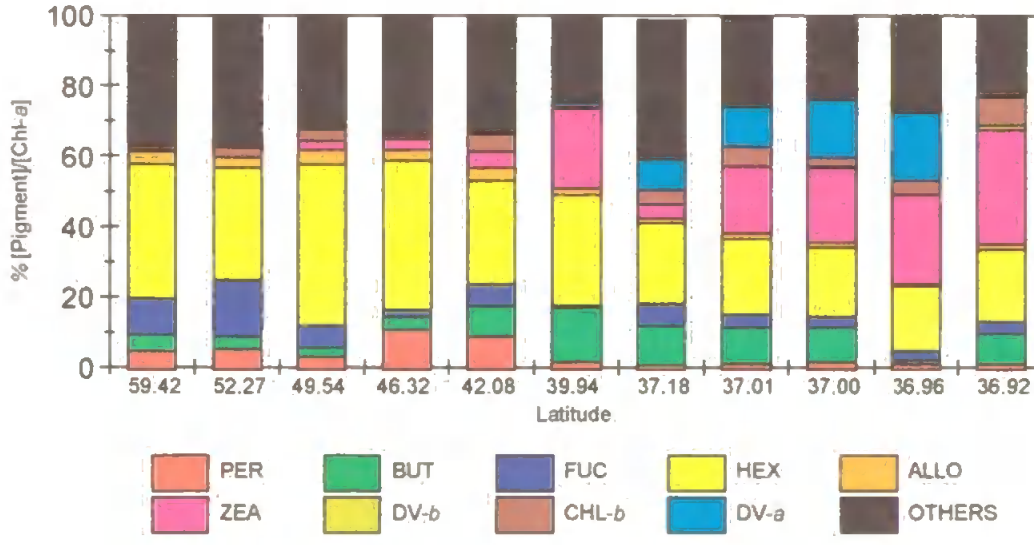

Figure 7.13. Some key pigment groups identified from the PRIME study expressed as a percentage of the [total pigment], normalised to [chlorophyll-a]. For key to pigments see table 7.1.

Data in figure 7.13 show the pigment assemblage variability observed, with HEX and BUT indicating that prymnesiophytes were present, and diatoms indicated to be present from the observations of FUCO. PER was also observed, which is

indicative of dinoflagellates. A notable change was observed at the 49.54°*N* site with the presence of ZEA, indicating that cyanobacteria and / or prochlorophytes were present. This pattern continued to 42.1°*N* where DV-*a* was also observed, further evidence that prochlorophytes were dominant between these two groups. At 39.9°*N* the ZEA concentration was relatively strong compared to the DV-*a* concentration, indicating that cyanobacteria could be the dominant feature between these two groups, with prochlorophytes less numerous. Data collected in the region of 37.0°*N* at the PRIME lagrangian study site, from 37.1°*N* to 36.9°*N*, show variability in the observations made with increasing incidence of cyanobacteria and prochlorophytes, which may not have been detected at the last station due to the absence of DV-*a*. The relative importance of prymnesiophytes is seen to be low from the 39.94°*N* sampling site onwards. The remainder of the observed pigment distribution is dominated by beta carotein (between 0.1 and 5.4%) and chlorophyll-*c* to the north of the front with normalised concentrations ranging between 0.1 and 9%,

A summary of data derived from linear regression analyses of the pigment data sets presented here is detailed in table 7.2. In the case of the AMT-1 data, there were displayed more than one potential linear relationship was displayed for: (i) the TC compared with T-CHL, figure 7.10(d), and (ii) the PPC compared with the TC, figure 7.10(f). When the higher concentration values were removed (3 and 4 data respectively) a change in these inter-pigment relationships was apparent between these groups representing a consistent and structured alteration in the species diversity of the algal biomass sampled. In table 7.2 the regressions derived from the lower numbers of data are given in bold.

The pigment data presented here broadly fall within the ratio ranges reported by Aiken *et al.* (1995) who carried out a study of HPLC pigment data from a wide diversity of biogeochemical provinces. Their findings are summarised in table 7.3, and it will be noted that some regressions required inversion for comparison to be possible.

Table 7.2 HPLC pigment data analysis summary.

Pigment ratio	ALL DATA	L4	AMT-1	PRIME
CHL-*a*: T-PIG	1.901	1.869	2.820	2.430
T-CHL:T-PIG	1.539	1.610	1.300	1.776
TC:T-PIG	2.429	2.774	2.820	2.278
TC:T-CHL	0.539	0.530	0.287 (20obs.) **0.905 (17 obs.)**	0.777
PSC:TC	1.166	1.168	1.065	1.234
PPC:TC	4.449	4.405	1.996 (20 obs.) **0.529 (16 obs.)**	5.155

It may be seen that the fieldwork data presented here fall within the ratio extremes of the various groups determined by this previous work. Comparing in more detail: the CHL-*a*:T-PIG data derived here are all within 90% of the global mean reported by Aiken *et al.* (1995) at 0.464, corresponding with the North East Atlantic (NEAT) Biogeochemical Ocean Flux study (BOFS) data at 0.422. The CHL-*b*:T-PIG data observed during this work match closely that reported (0.042), at an average value of 0.057. There is significant spread within the data, with the L4 study mean value of 0.083 corresponding with the value of 0.085 determined from data collected in the Greenland Iceland Norweigan (GIN) seas, whereas the AMT-1 value of 0.061 most closely corresponds to a value of 0.066 determined for the Georges Bank area. The PRIME data yield a low value of 0.025 which corresponds closely to the values reported for NEAT of 0.016-0.024. The average CHL-*c*:T-PIG ratio determined here at 0.086 is higher than the figure of 0.077 reported by Aiken *et al.* (1995), driven by the values from all the fieldwork being generally close to the

mean, except the PRIME data, which exhibited a high value for this relationship of 0.124, comparing closely with the value reported from the NEAT data of 0.134. The L4 and AMT-1 data are described by similar values of 0.067 and 0.061 respectively conforming closest to data reported in the literature from the Georges Bank area.

Table 7.3. Ratio values between some pigment groups from the study by Aiken *et al.* (1995).

Cruise	CHL-*a*:T-PIG	CHL-*b*:T-PIG	Chl-*c*:T-PIG	PSC:T-PIG	PPC:T-PIG	TC: CHL-*a*
L4 mean, (this work).	0.429	0.083	0.067	0.223	0.087	0.645
AMT-1 mean, (this work).	0.462	0.061	0.061	0.184	0.257	1.206
PRIME mean, (this work).	0.409	0.025	0.124	0.312	0.171	1.200
All fieldwork mean, (this work).	0.464	0.057	0.086	0.249	0.175	1.017
Global minimum (Aiken *et al.*, 1995)	0.367	0.006	0.020	0.186	0.043	0.522
Global maximum (Aiken *et al.*, 1995)	0.544	0.085	0.154	0.377	0.249	1.129
Global mean (Aiken *et al.*, 1995)	0.475	0.042	0.077	0.276	0.128	0.814

The TC:CHL-*a* data show that, on average, the pigment assemblage was dominated by the TC fraction, exceeding the concentration of the observed T-CHL with a mean value for all fieldwork of 1.017. A breakdown of the sampling included in this study shows that at the L4 site a low value was determined of 0.645, corresponding closely to the Georges Bank data (0.665), where AMT-1 and PRIME observations of 1.206 and 1.200 respectively more closely compare with data from the GIN seas, where a value of 0.129 was reported.

Within the TC data, the PSC:T-PIG values derived here produced a mean of 0.249, corresponding closely with the global value of 0.276 reported by Aiken *et al.* (1995). There was variability within the data, however, from 0.223 for the L4 study to 0.184 for AMT-1 and 0.312 for the PRIME data. The PPC:T-PIG data displayed

similar variability with a mean value of 0.175 made up of 0.087 from the L4 study, 0.257 for AMT-1 (exceeding the global maximum of 0.249) and 0.171 for PRIME.

It is apparent that the ratios determined from the pigment data generated by this study fall largely within the extremes of data reported in the literature (comprehensively summarised in Aiken *et al.* (1995)).

The pigment data resulting from this study therefore withstand rigorous quality control and provide a suitable basis for comparison with the contemporaneous measurements of ocean colour and the assessment of the SeaWiFS algorithm, and others, discussed in chapter 3 and applied to these data in chapter 8.

8. DATA ANALYSIS

In this section the results presented in chapter 7 are analysed and discussed. For clarity: the term 'general' applies to the algorithm generated from the amalgamated data set, as opposed to the term 'local' which refers to the algorithms derived from each of the three component data sets.

8.1 GENERATION OF GENERAL ALGORITHMS TO RETRIEVE *Kd*(490*nm*) FROM SeaWiFS SATELLITE IMAGERY

The diffuse attenuation coefficient, $Kd(\lambda)$, at 490*nm* is a core data product from CZCS imagery, and more recently the SeaWiFS project, (Austin and Petzold, 1981; Mueller and Trees, 1997) as it is closely relates the optical properties of oceanic waters to the SPM and associated CDOM, or in case 1 water describes the 'bio-optical state' (Smith and Baker, 1978). At each depth the spectral characteristics of ocean waters have a maximum downwelling irradiant intensity at a wavelength, $Ed(\lambda, z_{max})$, determined by the minimum corresponding value of $Kd(\lambda)$ which, in case 1 waters is 490*nm* for CHL-*a* concentrations ranging from $0.01 mg\ m^{-3}$ to $1.0 mg\ m^{-3}$ (Smith and Baker, 1978).

Austin and Petzold (1981) developed the methodology whereby *Kd*(490*nm*) may be derived from the blue (443*nm*) and green (550*nm*) ratio of water leaving radiances measured by the CZCS. This methodology is to be used here, applying ocean colour data collected during the field work using the PRR-600 radiometer.

The algorithm accounts for the sum of the partial contributions to $Kd(\lambda)$ of the diffuse attenuation coefficient of the water and the in-water constituents which,

from section 1 (figure 1.1), are DOM and SPM (inorganic and organic). There are, by definition, only phytoplankton and an amount of dissolved organic material associated with the standing algal crop in the dissolved fraction present in the open ocean marine environment, except in the special case of a dominance in the phytoplanton of coccolithophores where the SPM will contain a significant quantity of calcium carbonate which is secreted externally by the algae (Balch et al., 1991; Kirk, 1994). Figure 8.1 illustrates the relationship between the *Kd*(490*nm*) attributable to in-water constituents (accounting for diffuse attenuation by the water itself, *Kw*) and the coincident ocean colour measurements in terms of *Rrs(443:560, 0⁻)* made over the three fieldwork programmes (*Kdm* was calculated according to the procedure outlined in section 2.5.1, equation 2.17).

Kd = exp[c] * $Rrs(i{:}j, 0^-)^m$ + Kw, the final form of which was:

$$Kd(\lambda) = A\left(\frac{Rrs(\lambda i,0^-)}{Rrs(\lambda j,0^-)}\right)^B + Kw(\lambda) \qquad (m^{-1}) \qquad (8.1)$$

where, in this case, A= exp[c] = exp[-2.273] = 0.103

and B= m = -1.148

The algorithm generated from this study for the derivation of *Kd*(490*nm*) from water leaving radiances measured using the SeaWiFS methodology was therefore:

$$Kd(490) = 0.103\left[\frac{Rrs(443)}{Rrs(560)}\right]^{-1.148} + 0.0192 \qquad (m^{-1}) \qquad (8.2)$$

(a)

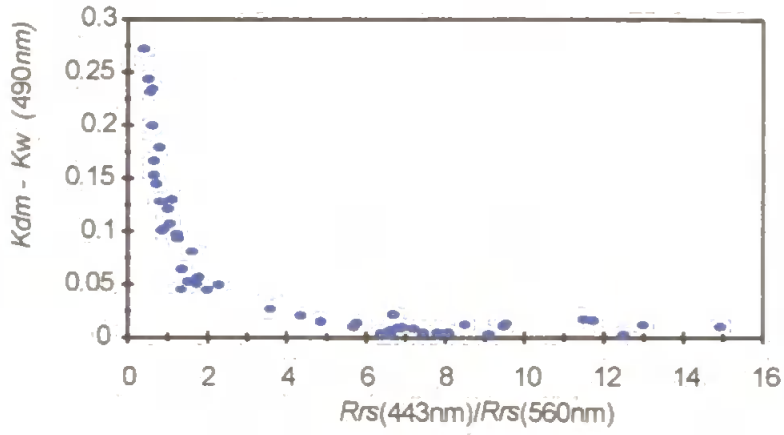

(b)

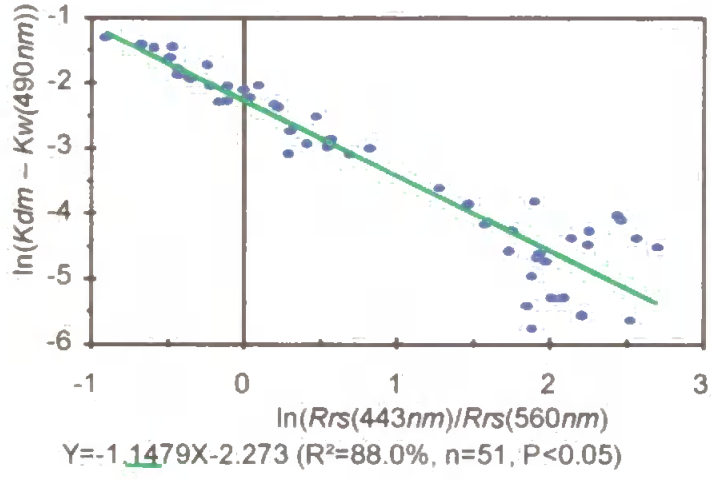

Figure 8.1. Comparison of the measured $Kd(\lambda)$, $(Kdm - Kw)$, and $Rrs(443{:}560, 0^-)$ where (a) shows the original data and (b) illustrates the naperian log transformed data. The units for $Kd(\lambda)$ and Kw are m^{-1}.

The least squares regression analysis illustrated in figure 8.1(b) yields

Y=-1.148X-2.273, from which:

$$\ln[Kd\text{-}Kw] = \ln[Rrs(i{:}j, 0^-)^m] + c$$

$$Kd\text{-}Kw = (Rrs(i{:}j, 0^-))^m \times exp[c]$$

There are two steps to assessing the effectiveness with which the empirical constants derived by regression analyses constrain equation 8.2: by comparison with the source data and with algorithms generated from different data.
The *Kd*(490*nm*) data are discussed in more detail in section 8.1.2, where a comparison is made with the algorithm of Moore *et. al.* (1997), equation 3.5.

Table 8.1 contains a summary of comparisons between the general algorithm and its source data, divided into the individual research programmes (the figure references indicate the corresponding graphical representations of these relationships). It may be seen that there is a variability in the precision on average between the algorithms which is driven by the different empirical constraints with which the measured values may be retrieved from the corresponding algorithms, even when the degree of variance explained between the measured and retrieved values is consistently high.
These data illustrate the diversity within the measurements collected during this study, and the problem faced by workers attempting to apply general algorithms to water leaving radiances measured at a specific site. This is further discussed in section 8.1.2.

Table 8.1 General algorithm regression and error analysis (comparison with source data), where *Kdc=m x Kdm+c.*

Figure no.	Comparison with source data from field program	*m (=B)*	*c*	R^2 (%)	Average error (%)= $\left[\frac{\sum((measured-retrieved)/measured)}{n}\right]*100$
8.2	L4	0.729	0.036	86.2	12.65
8.3	AMT-1	0.807	0.005	91.3	14.42
8.4	PRIME	0.907	0.007	94.7	19.34

8.1.2 Comparison of the *Kd*(490*nm*) field measurements with the Moore *et al.* (1997) algorithm

A comparison was made between the algorithm based upon data collected during the fieldwork (equation 8.2) and an algorithm derived from parallel work undertaken to retrieve *Kd*(490*nm*) values from measured remote sensing reflectances in SeaWiFS bands 2, 443*nm,* and 5, 555*nm.* In chapter 3 it was pointed out that Moore *et al.* (1997) generated equation 3.5 to derive *Kd*(490*nm*). To re-cap:

$$Kd(490) = 0.129\left[\frac{Rrs(443nm)}{Rrs(555nm)}\right]^{-1.337} + 0.0192 \qquad (m^{-1}) \qquad (8.3)$$

Because this algorithm was generated from a data set not included in this study, the relationship serves as an inter-comparison with the *Ed*(490*nm*) measurements collected during the fieldwork from which *Kd*(490*nm*) were determined. Data in figure 8.2, 8.3 and 8.4 show the results of comparisons made for each programme. It can be seen that equation 8.3 overestimates *Kd*(490*nm*) from the radiometry collected at station L4, as *Kdm=Kdc* x 0.775+0.096, compared to the AMT-1 data set as *Kdm=Kdc* x 0.973+0.004 and PRIME as *Kdm=Kdc* x 0.985-0.002, illustrating an inherent effect when combining data sets to create generally applicable algorithms. The empirical constants derived have a smoothing effect on the data, the extent of which depends upon the diversity of the water types from which the algorithm source data were collected. When data from fieldwork covering a limited number of bio-optical regimes are used to generate an algorithm, the bias inherent

in the relationship will be towards those conditions (e.g. in the case of $Kd(\lambda)$ algorithms relatively clear or turbid waters) in which the measurements were undertaken. In the case of the *Kd*(490*nm*) retrievals presented here, such an algorithm produces erroneously high values from the radiometric data collected from a bio-physical regime of relatively high turbidity. This effect is apparent in figure 8.2(b), where regression analysis applied to the L4 study data shows a bias as the measured *Kd*(490*nm*) value (*Kdm*) is about 77.5% of the magnitude of the corresponding value calculated from equation 8.3. Figures 8.3(b) and 8.4(b) show a ratio close to 1:1 relationship in each case as the AMT-1 and PRIME data were collected in waters where the *Kd*(490*nm*) values matched closely the waters from which the empirical constraints driving equation 8.3 were determined. These data provide procedural validation for the radiometric quality control techniques employed in the analysis of the data presented here (see chapters 2, 4 and 5).

(a)

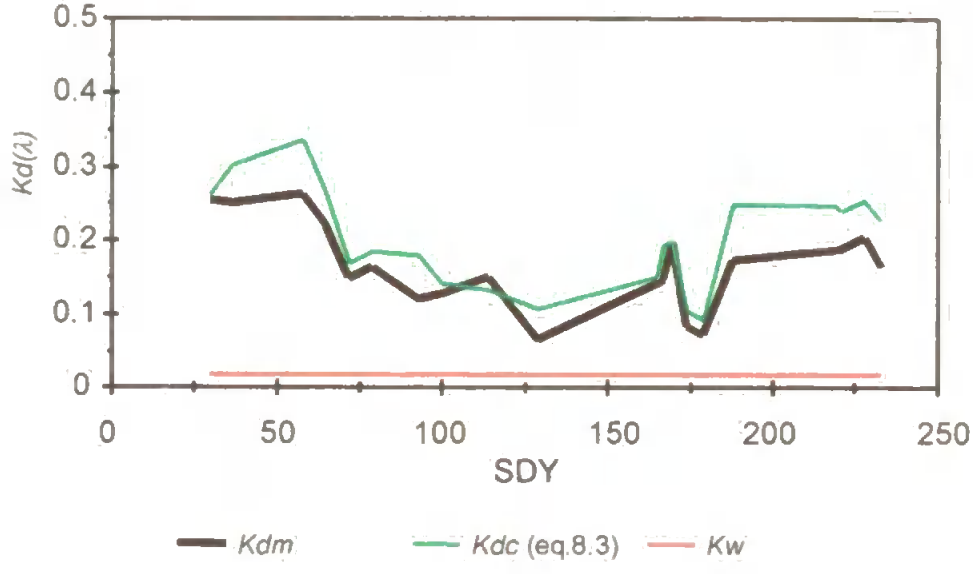

(b)

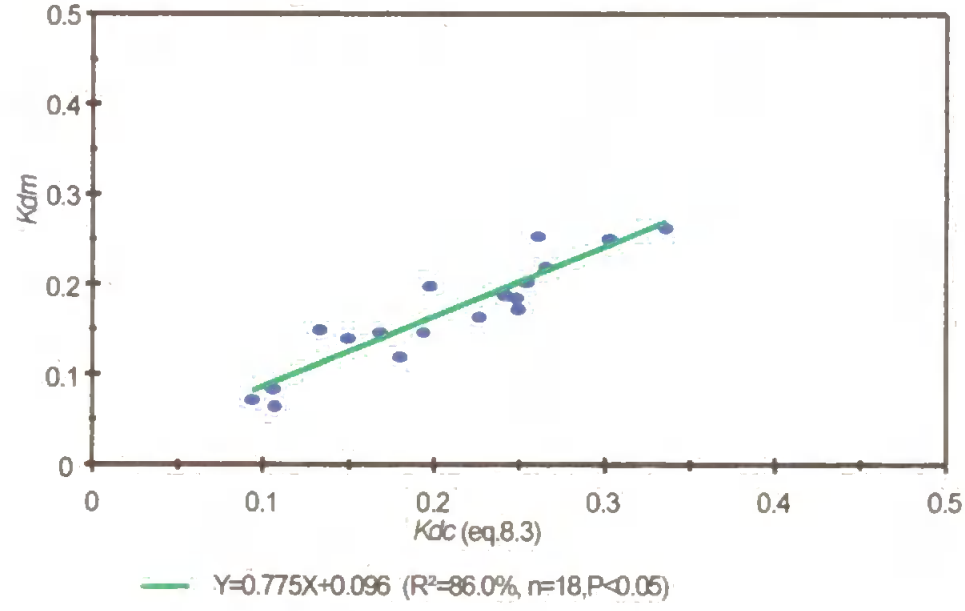

Figure 8.2 Comparison of the measured L4 *Kd(490nm)* data against the calculated *Kd(490nm)* using equation 8.3 to test the *Kd(490nm)* derived from the *Ed*(490, *z*) profile values measured during the fieldwork sessions, denoted here by *Kdm*. The units of *Kd(λ)* are m^{-1}.

(a)

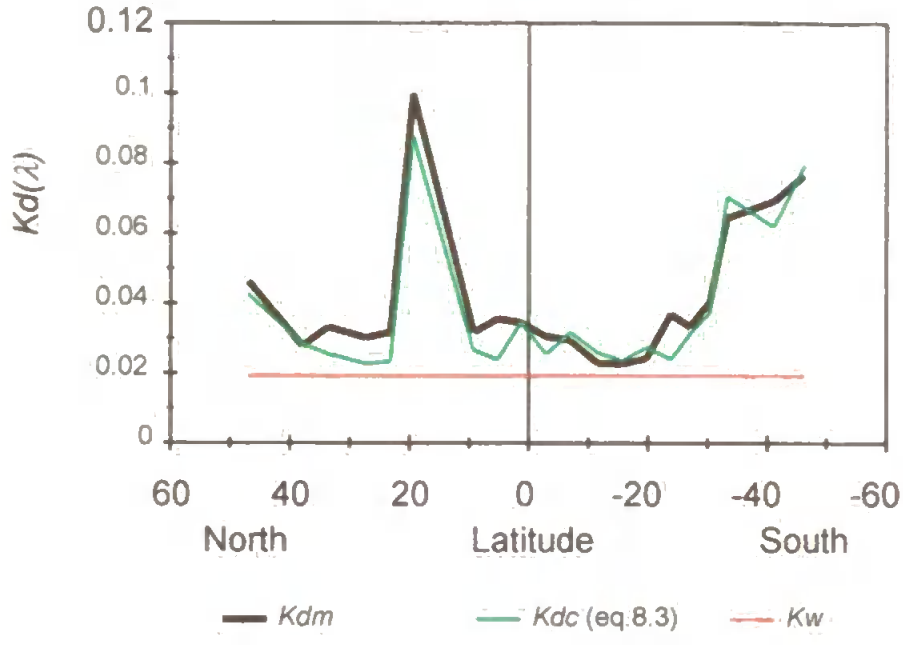

(b)

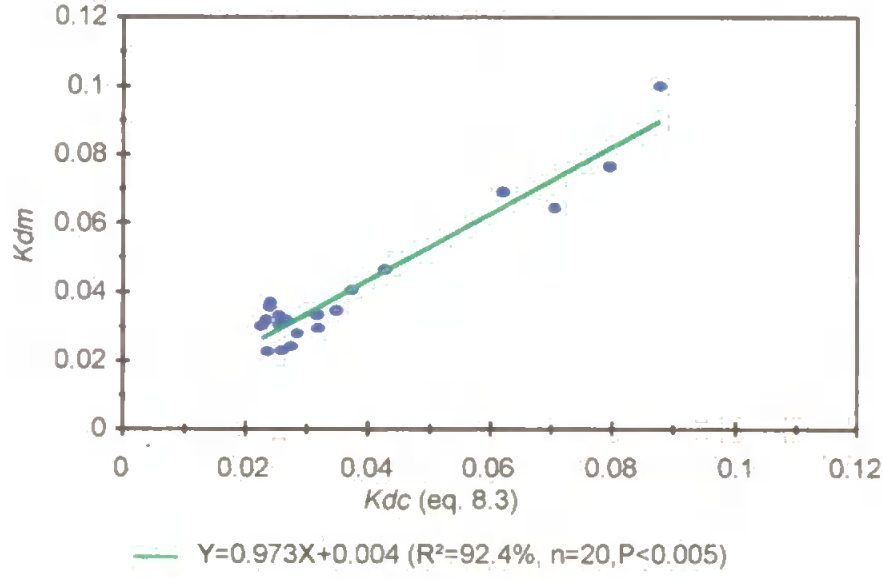

Figure 8.3 Comparison of the measured AMT-1 *Kd(490nm)* data against the calculated *Kd(490nm)* using equation 8.3 to test the *Kd(490nm)* derived from the *Ed*(490, *z*) profile values measured during the fieldwork sessions, denoted here by *Kdm*. The units of *Kd(λ)* are m^{-1}.

(a)

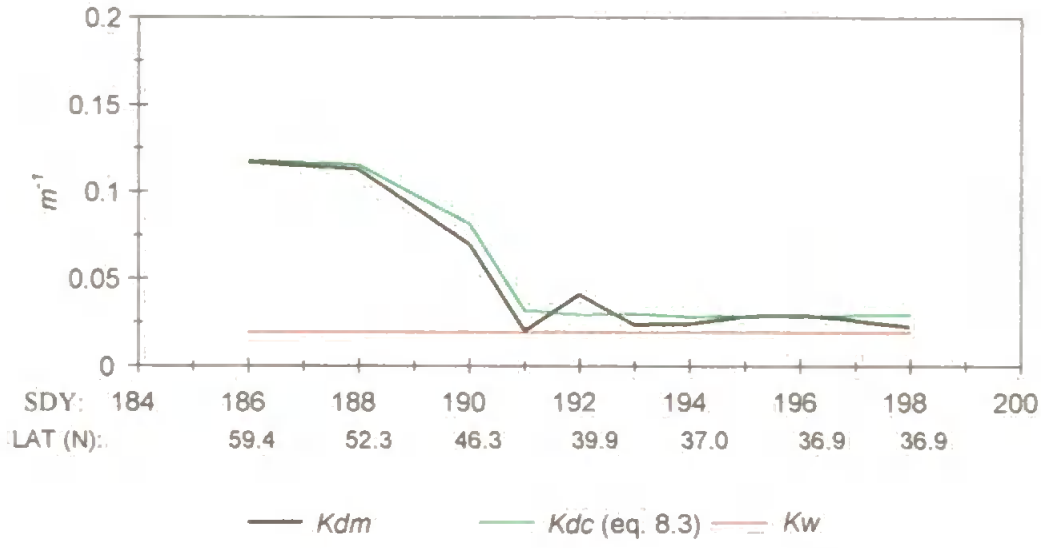

(b)

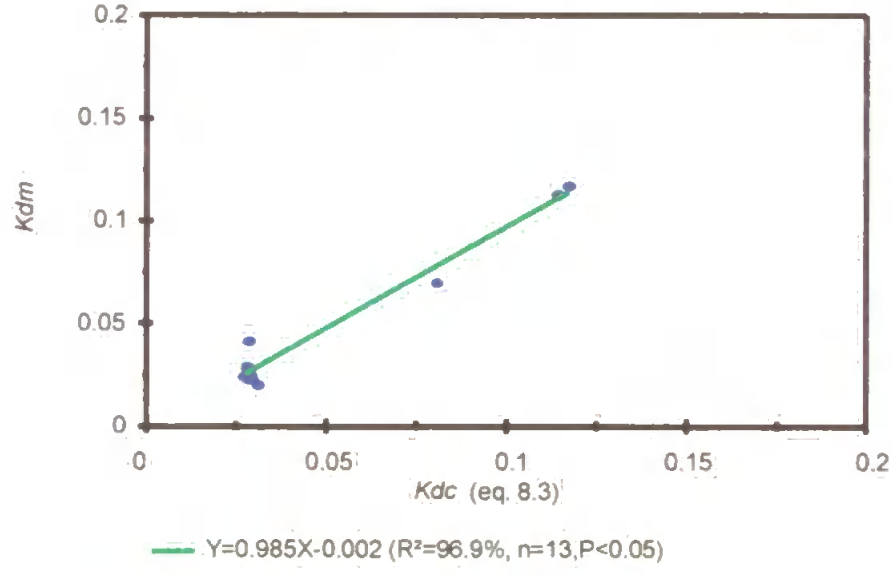

Figure 8.4 Comparison of the measured PRIME *Kd(490nm)* data against the calculated *Kd(490nm)* using equation 8.3 to test the *Kd(490nm)* derived from the *Ed*(490, *z*) profile values measured during the fieldwork sessions, denoted here by *Kdm*. The units of *Kd(λ)* are m^{-1}.

Figure 8.5 shows the results of a comparison made between the two algorithms (equations 8.2 and 8.3) applied to the amalgamated data set. Figure 8.5(a), illustrates the effectiveness with which equation 8.2 retrieves data from all three field campaigns, with a close to 1:1 relationship of Kdm=1.044 x Kdc and a variance explained of 95.7%. It can be seen from figure 8.5(b) that equation 8.3 is biased by the relatively high $Kd(\lambda)$ data to over estimate and produce a relationship of Kdm=0.797 x Kdc, with 93.4% of the variance explained. Using the Kolmogorov-Smirnov two sample test, the frequency distribution of the errors in retrieval for each algorithm was found to be significantly different at the p=0.05 level, where $n_1n_2D_{(0.05)}$ = 450 for a critical value of 13.581, so the null hypothesis that the distributions are the same is rejected. The g1 and g2 statistics indicate that the two distributions do, however, have similar characteristics, with the values for skewness indicating equation 8.2 to be less positively biased than equation 8.3, but displaying a greater degree of platykurtosis. This pattern of skewed error distribution is further apparent if the performance of equations 8.2 and 8.3 are compared when applied to the optical observations made during each of the individual field works.

Figure 8.6, 8.7 and 8.8 illustrate the relationship between equation 8.2 and 8.3, with the data sets broken down into retrieved $Kd(490nm)$ values from the L4, AMT-1 and PRIME studies respectively. From figure 8.6 it is once again apparent that equation 8.3 is overestimating $Kd(490nm)$ when compared to values computed from equation 8.2. For to the L4 data set where the error distributions were found to be significantly different at the p=0.05 level, where $n_1n_2D_{(0.05)}$= 220 for a critical value of 8.589. The g1 and g2 statistics indicate that data derived from equation

8.2 has a more positively skewed error distribution than that from equation 8.3, and displays much more leptokurtosis.

The same applies to the error distributions for data derived from AMT-1 and PRIME, shown in figures 8.7 where $n_1n_2D_{(0.05)}$= 60 for a critical value of 8.589 and 8.8 $n_1n_2D_{(0.05)}$= 12 for a critical value of 6.653 respectively. This indicates both error distributions to be significantly different at the p=0.05 level, though to a lesser degree in the case of AMT-1 and PRIME as the radiometric data more closely conform to the empirical limits constraining equation 8.3 due to the dominance in the source data used to derive equation 8.2 of observations made in the deep oceanic Atlantic in these programmes. In the case of figure 8.7 (AMT-1 data) the g1 value indicates the distribution of errors to be similarly structured in the degree of skewness, but equation 8.3 displays much more negative platykurtosis than equation 8.2. The PRIME data error distributions show the errors not to be skewed in the case of equation 8.2, with the g2 value indicating equation 8.2 to display high leptokurtosis and 8.3 high platykurtosis.

(a) This work, equation 8.2

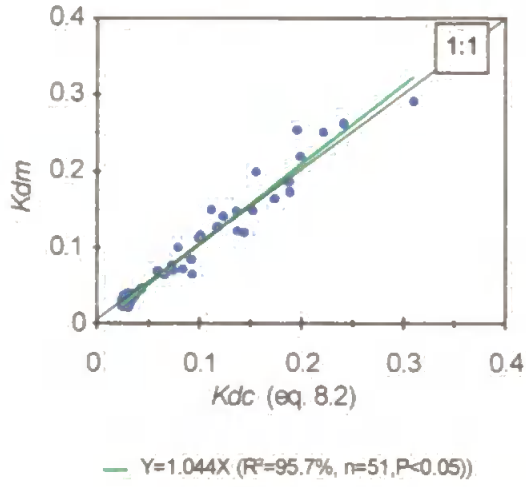

(b) Moore *et al.* (1997), equation 8.3

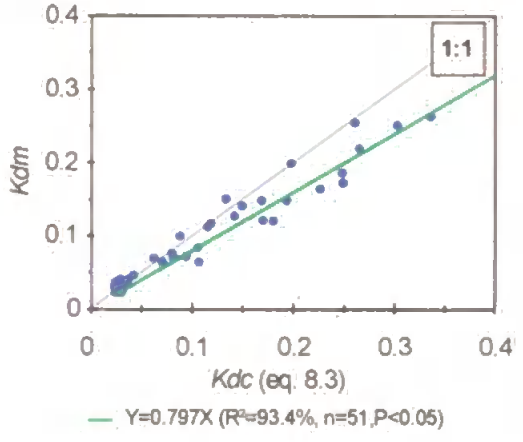

(c) Error frequency distribution

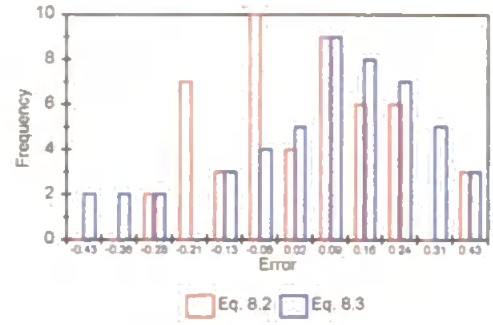

Eq. 8.2: g1= 0.305; g2= -1.041
Eq. 8.3: g1= 0.46; g2= -0.608

Figure 8.5 Comparison of the values of *Kd(490nm)* derived by profiling the PRR-600 *Ed(490nm)*, and the corresponding values retrieved from This work, equation 8.2; (b) Moore *et al.* (1997), equation 8.3. (c) Error frequency distribution. The units for *Kd(λ)* are m^{-1}.

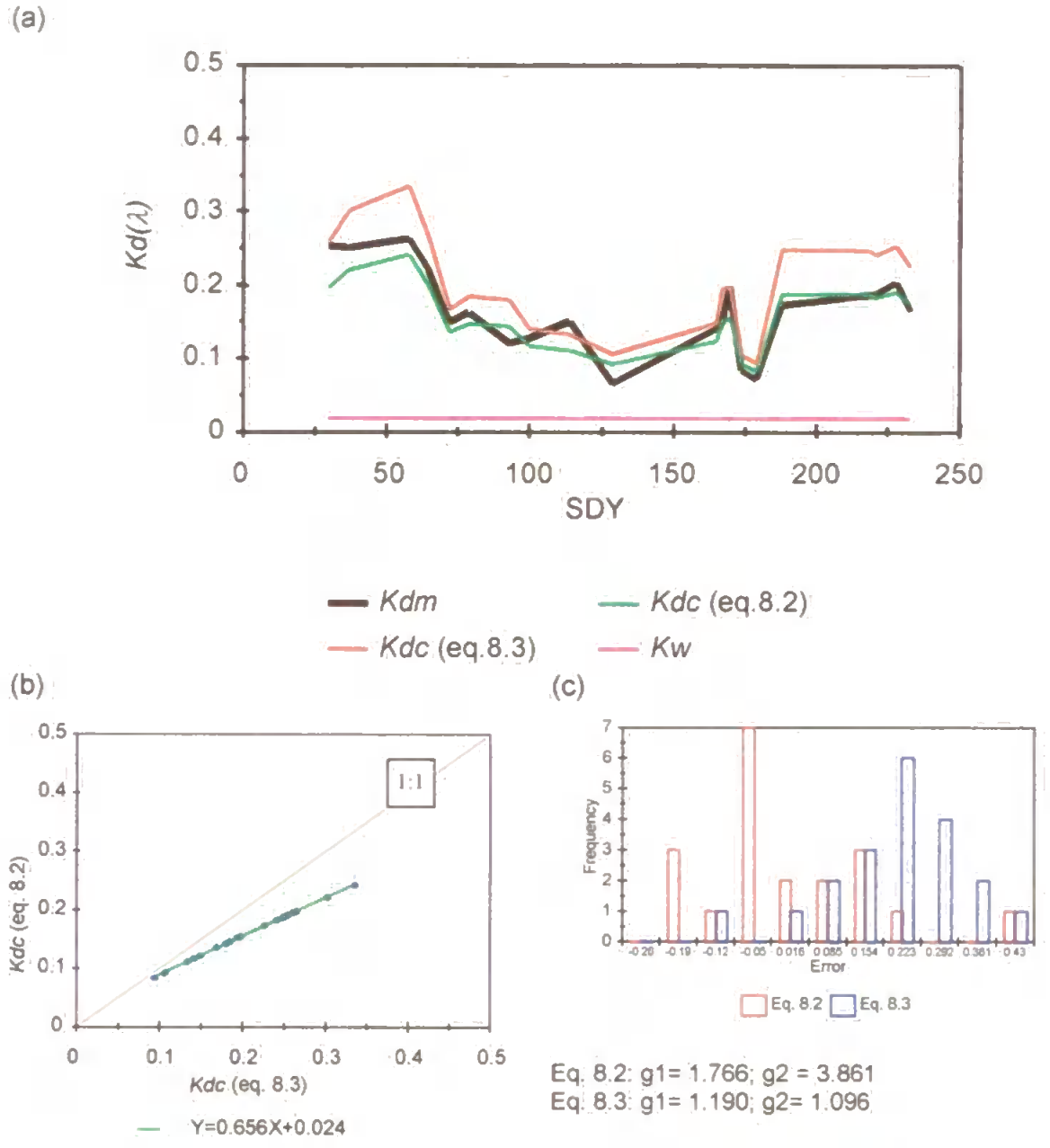

Figure 8.6 (a) Comparison and (b) regression analysis of the retrieved values of *Kd(490nm)* from equations 8.2 (*Kdc(490nm)* this work) and 8.3 (*Kdc(490nm)* Moore *et al.*, (1997)) for the L4 data set. The units for *Kd(λ)* are m^{-1}. (c) shows a histogram of the frequency distribution of the errors.

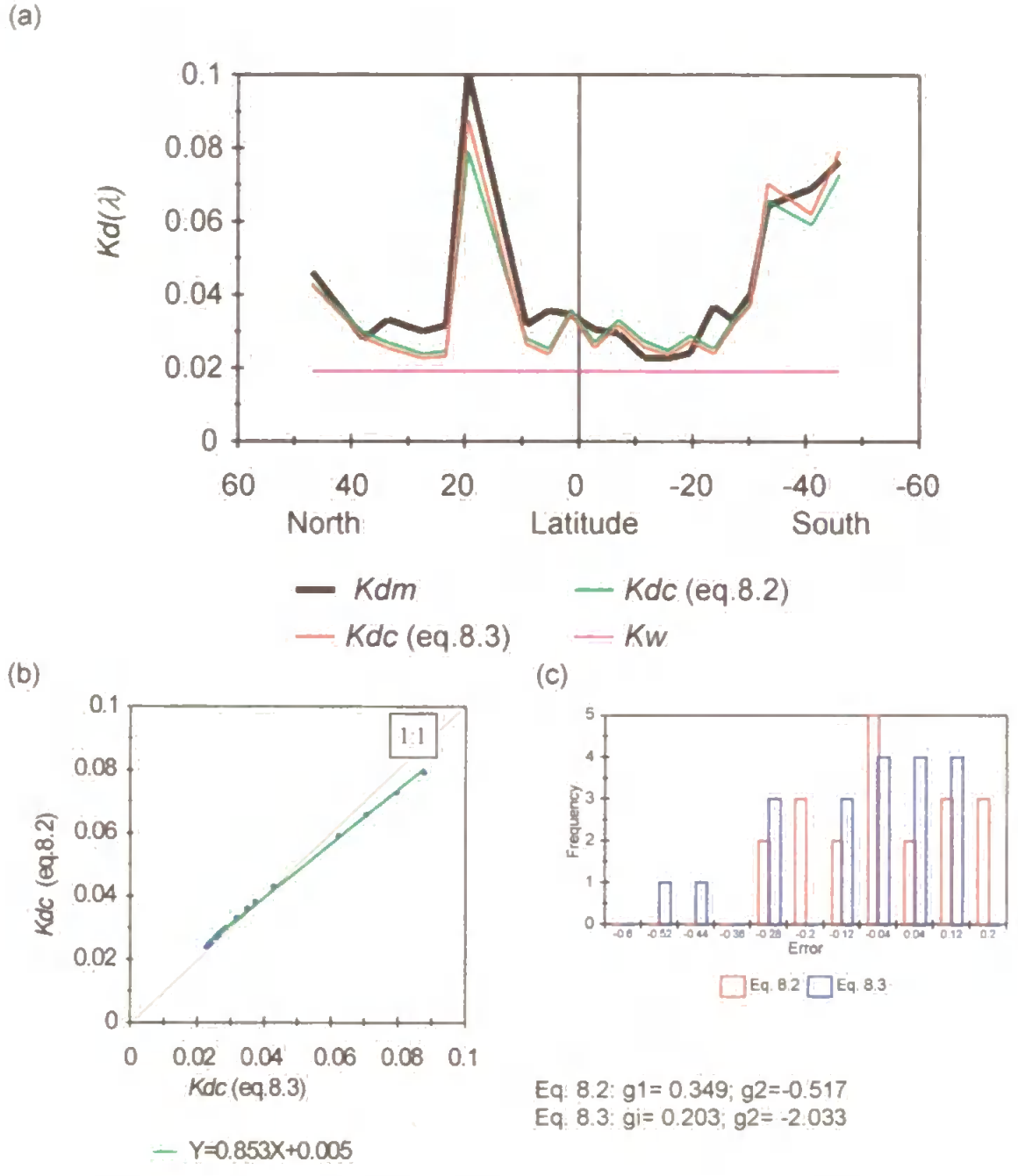

Figure 8.7 (a) Comparison and (b) regression analysis of the retrieved values of *Kd(490nm)* from equations 8.2 (*Kdc(490nm)* this work) and 8.3 (*Kdc(490nm)* Moore *et al.*, (1997)) for the AMT-1 data set. The units for $Kd(\lambda)$ are m^{-1}. (c) shows a histogram of the frequency distribution of the errors.

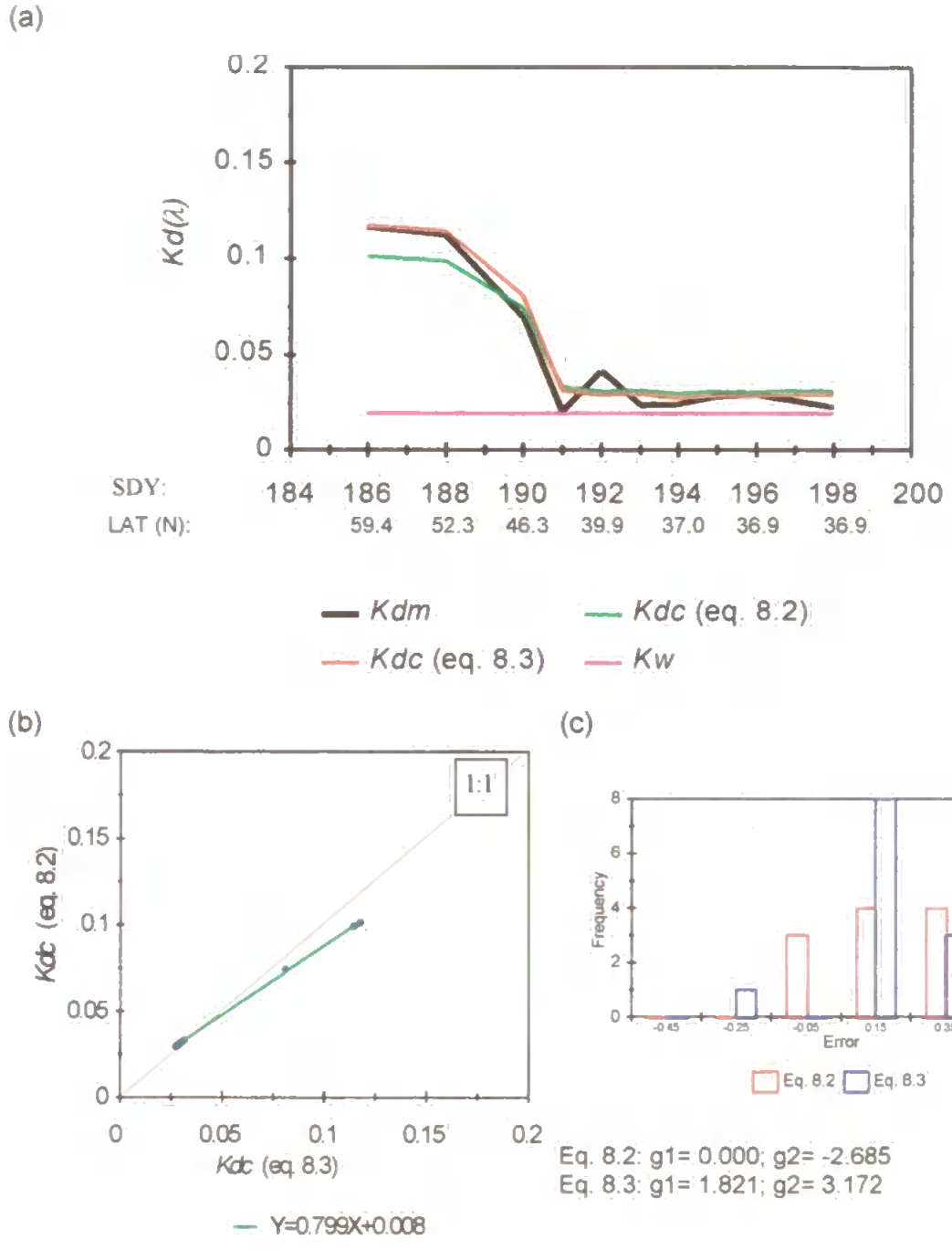

Figure 8.8 (a) Comparison and (b) regression analysis of the retrieved values of *Kd*(490*nm*) from equations 8.2 (*Kdc*(490*nm*) this work) and 8.3 (*Kdc*(*490nm*) Moore *et al.*, (1997)) for the PRIME data set. The units for $Kd(\lambda)$ are m^{-1}. (c) shows a histogram of the frequency distribution of the errors.

This analysis illustrates that the general algorithm yields error values which, rather than being normally distributed about a zero mean, are structured becoming evident when comparing the measured and retrieved variables. Also that the pattern of these errors is related to the magnitude of the empirical algorithm constraints. This is especially evident when the algorithms are applied to the radiometric data from the three field sampling programmes.

8.2 FIELDWORK SITE SPECIFIC *Kd(λ)* ALGORITHMS

Up to now the optical data sets generated from the observations made during the three field campaigns have been considered in their entirety, and the effectiveness of this approach to the retrieval of *Kd(490nm)* from the radiometry has been discussed. Further investigations were made to ascertain how fieldwork specific algorithms would perform when compared with the general approach. A summary of the algorithms of the form illustrated in equation 8.1 were generated using the same procedure outlined in section 8.1, and are presented in table 8.2.

Table 8.2 A summary of the *Kd(490nm)* algorithm constants, *A* and *B*, generated from the individual field observations.

Field session	λ (nm)	A	B	R^2 (%)	n	p
L4	490	0.101	-1.318	85.7	18	<0.05
AMT-1	490	0.088	-0.964	64.7	20	<0.05
PRIME	490	0.1219	-1.337	91.2	13	<0.05

Figures 8.9, 8.10 and 8.11 illustrate comparisons of the general and fieldwork specific *Kd*(490*nm*) algorithms presented in table 8.2.

In figure 8.9 it can be seen that up to *Kd*(490*nm*)=0.15m^{-1}, the *Kdc*(490*nm*) derived from the general algorithm underestimates the value of *Kdc*(490*nm*) from the L4 specific variant. Above 0.15m^{-1} the algorithm overestimates. The g1 and g2 values derived from the frequency distribution of the error shows the general algorithm to be slightly more skewed in the general case than the local algorithm. In the case of kurtosis, however, the general algorithm displays leptokurtosis and the local variant

(a)

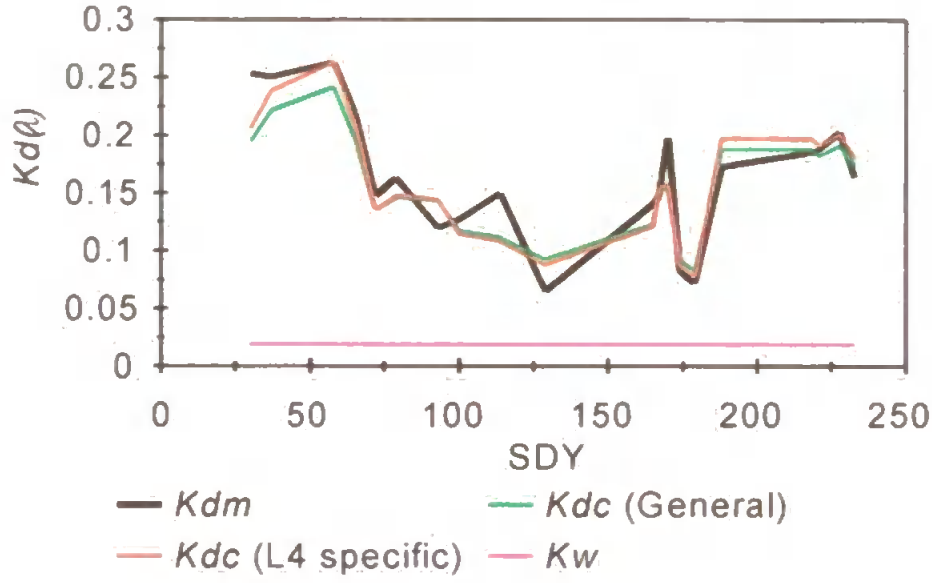

(b)

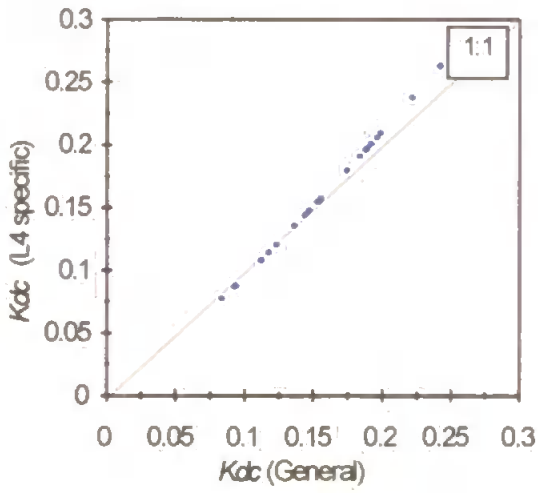

(c)

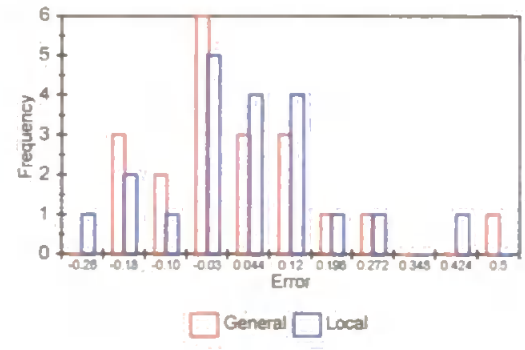

General:- g1 = 1.157, g2 = 1.437
Local:- g1 = 0.916, g2 = -0.578

Figure 8.9 (a, b) comparison of the general *Kd(490nm)* algorithm (equation 8.2) with the L4 fieldwork specific variant shown in table 8.4. Also shown are the values for absorption at 490*nm* by pure water. *Kdm* represents the *Kd(490nm)* derived from profiles of *Ed(490nm)*, *Kdc* represents the value of *Kd(490nm)* derived from the algorithms. The units for $Kd(\lambda)$ and $Kw(\lambda)$ are m^{-1}. (c) shows a histogram of the frequency distribution of the errors.

(a)

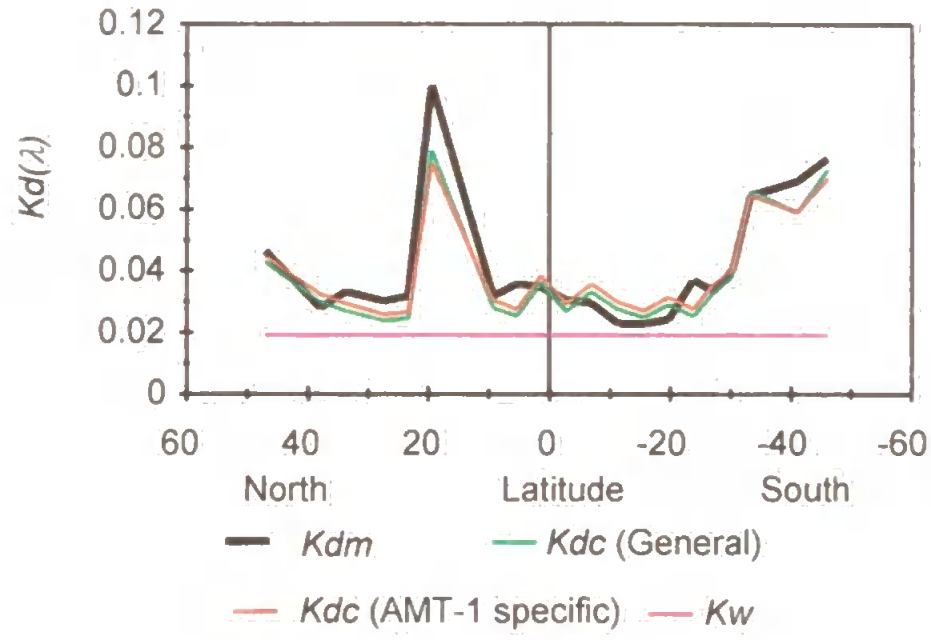

(b)

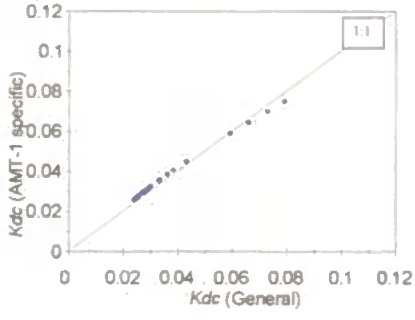

(c)

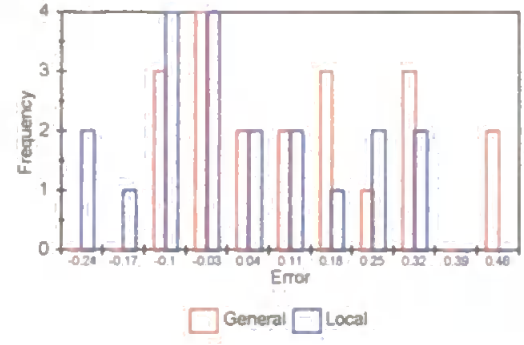

General:- g1 = -0.143, g2 = -1.231
Local:- g1 = 0.401, g2 = -0.154

Figure 8.10 (a, b) comparison of the general *Kd(490nm)* algorithm (equation 8.2) with the AMT-1 fieldwork specific variant shown in table 8.4. Also shown are the values for absorption at 490*nm* by pure water. *Kdm* represents the *Kd(490nm)* derived from profiles of *Ed(490nm)*, *Kdc* represents the value of *Kd(490nm)* derived from the algorithms. The units of $Kd(\lambda)$ and $Kw(\lambda)$ are m^{-1}. (c) shows a histogram of the frequency distribution of the errors.

(a)

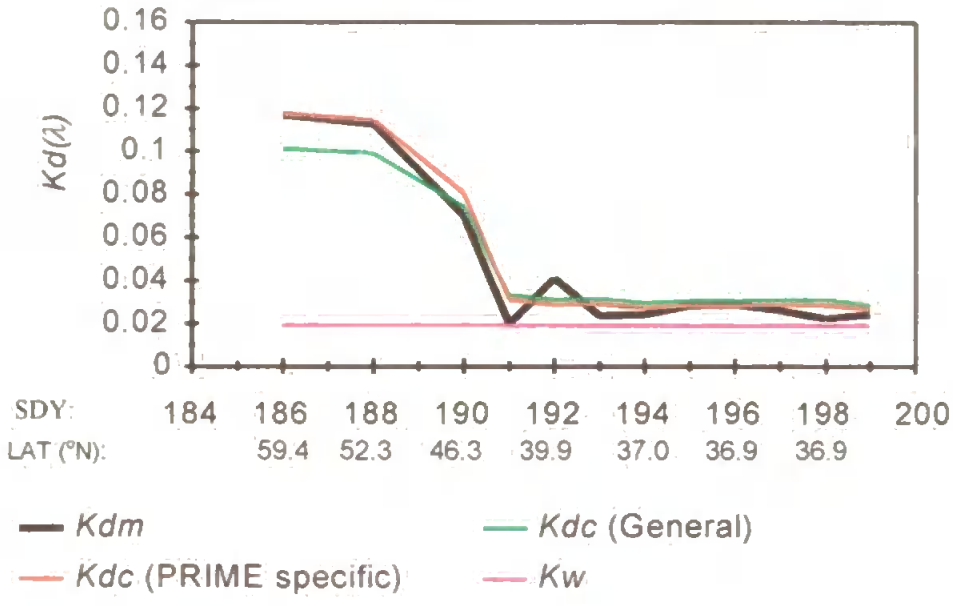

(b)

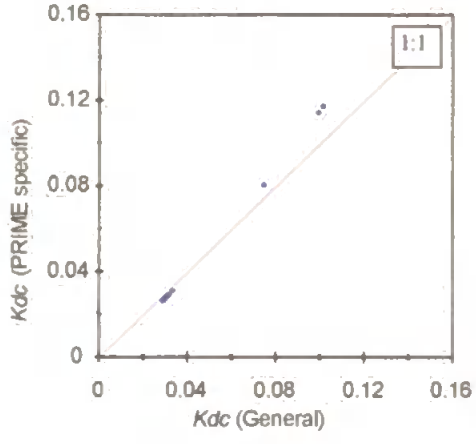

(c)

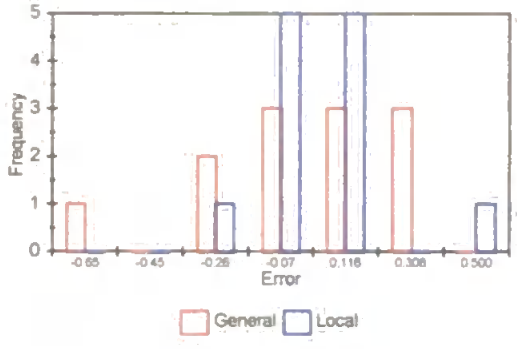

General:- g1 = -0.359, g2 = -2.089
Local:- g1 = 1.072, g2 = -0.986

Figure 8.11 (a, b) comparison of the general *Kd(490nm)* algorithm (equation 8.2) with the PRIME fieldwork specific variant shown in table 8.4. Also shown are the values for absorption at 490*nm* by pure water. *Kdm* represents the *Kd(490nm)* derived from profiles of *Ed(490nm)*, *Kdc* represents the value of *Kd(490nm)* derived from the algorithms. The units for $Kd(\lambda)$ and $Kw(\lambda)$ are m^{-1}. (c) shows a histogram of the frequency distribution of the errors.

displays platykurtosis. The L4 data when applied to the two algorithms indicate the retrieval errors from the general and locally derived variants to be from significantly different distributions, at the p=0.05 level, as $n_1n_2D_{(0.05)}$ yields a critical value of 8.589 with a derived value of 40.

In figure 8.10 it may be seen that the AMT-1 general algorithm slightly underestimates $Kd(490nm)$ up to a value of $0.04m^{-1}$, starting then to overestimate above $0.06m^{-1}$. The AMT data $n_1n_2D_{(0.05)}$ yields a critical value of 8.589 with a derived value of 80.

The two algorithms, when applied to the PRIME data (the results of which are illustrated in figure 8.11), show that for estimations of $Kd(490nm)$ over $0.04m^{-1}$ the general algorithm underestimates when compared to data calculated using the PRIME specific variant as, from figure 8.11(a), it may be seen that when applied to the more turbid waters the general algorithm underestimates, when compared to the local algorithm. Statistical analysis of the PRIME data yields an $n_1n_2D_{(0.05)}$ value of 24, and a critical value of 6.653. The algorithms display different g1 but similar g2 patens, with the general algorithms displaying negative skewness (-0.359) and platykurtosis (-2.089), while the local algorithms displaying positive skewness (1.072) and varying degrees of platykurtosis, greater in the case of the PRIME local algorithm (-0.996).

The algorithm modifications presented in this section result from analyses of the measured underwater light field at each station. The difference in the work carried out here from the original Austin and Petzold (1981) approach is the value assigned to the empirical constants, A and B in equation 1, and the form of the radiometric input, which determines and constrains the relationship between the measured light field ratio and the retrieved $Kd(\lambda)$. In terms of the frequency

distribution of the errors, the algorithms are all significantly different at the p=0.05 level; with the exception of the PRIME specific algorithm, the field sampling specific algorithms perform with increased precision over the source data than the general relationship determined from the full data set. In all cases the distribution of errors in retrieval by the local relationships follow different patterns of skewness about the mean when compared to the general case, such that the algorithms perform operationally in a significantly different manner.

8.3 RETRIEVAL OF CHLOROPHYLL-*a* CONCENTRATION FROM PROFILED RADIOMETRY

The following section details the results of the application of the pigment algorithms developed by (i) Clark (1981), equation 3.6, and (ii) Moore *et al.*, (1997), equation 3.7, to the radiometric data. These data were then compared with the HPLC derived CHL-*a* concentrations.

8.3.1 The CZCS CHL-*a* (pigment) algorithm (Clark, 1981)

The algorithm generated from the CZCS survey (equation 3.6) was applied to the radiometric data collected during each programme, the results of which are illustrated in figure 8.12. During the L4 study, from figure 8.12(a), it can be seen that there is a low percentage of variance explained, of 13.5%, between the measured chlorophyll-*a* concentration (CHL-*a*) and the values retrieved from the

algorithm, although the plots follow a more similar pattern after SDY 125, an effect that corresponds with the measured CHL-*a* values plotted concurrently with the $Kd(\lambda)$ data displayed in figure 7.4.

Figure 8.13 shows a much improved retrieval of CHL-*a* from the *in-situ* radiometry collected during AMT-1, when compared to the HPLC measurements, although a consistent under-estimation is apparent from the data where: retrieved CHL-*a* =0.325 x (HPLC CHL-*a*)+0.025 described by a variance of 52.8%. A second relationship was identified by considering the high measured [CHL-*a*] at the 23.3°*N* and 19.5°*N* sampling sites (circled), yielding an improved degree of variance explained (R^2=71.9%) with these data excluded. Data in figure 8.14 show that the retrieval characteristics of equation 3.6, when applied to the PRIME data, resolve l the corresponding CHL-*a* data collected (R^2=88.5%) well, notably the data from the sites in the high biomass waters north of the 39.9°*N* sampling site, however it underestimates in the relatively low biomass waters to the south of this station.

(a)

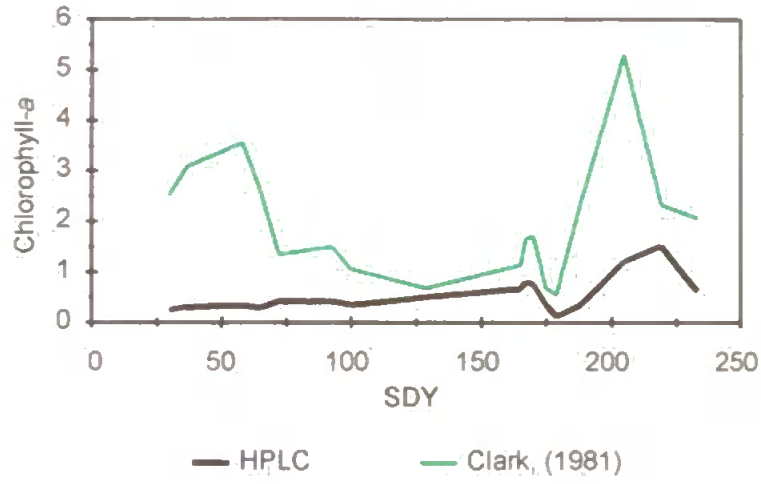

(b)

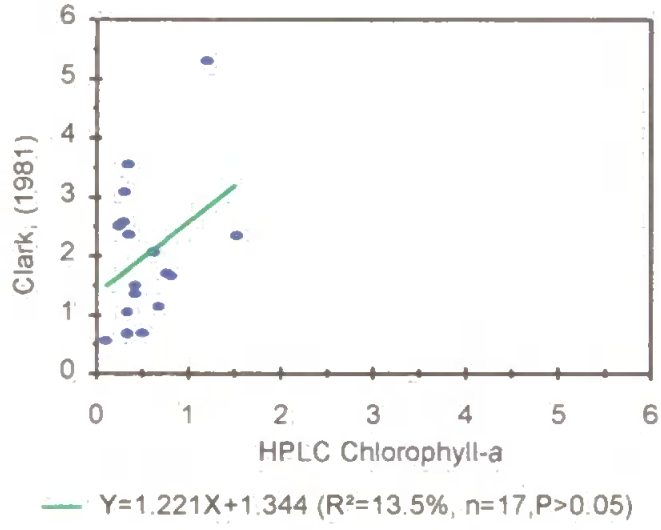

Figure 8.12 The CZCS pigment algorithm (equation 3.6) applied to the L4 data, showing both the phase similarity of the data and regression analyses between the measured and retrieved concentrations. The CHL-*a* concentration is in units of *mg* m^{-3}.

(a)

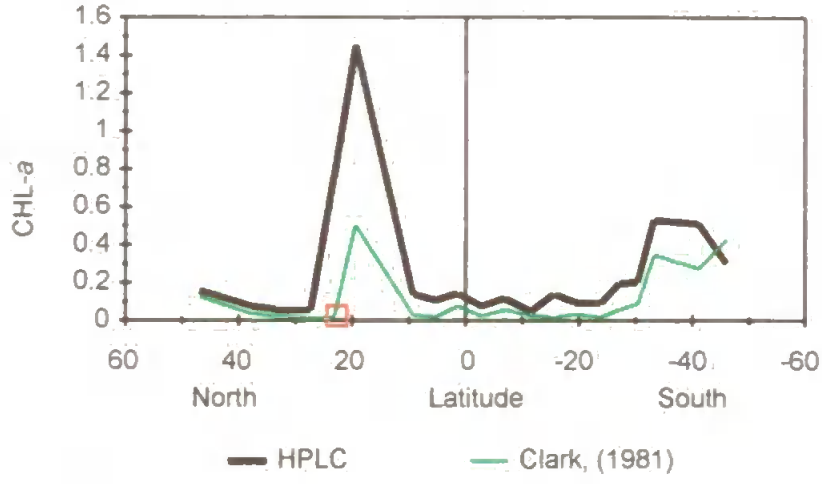

(b)

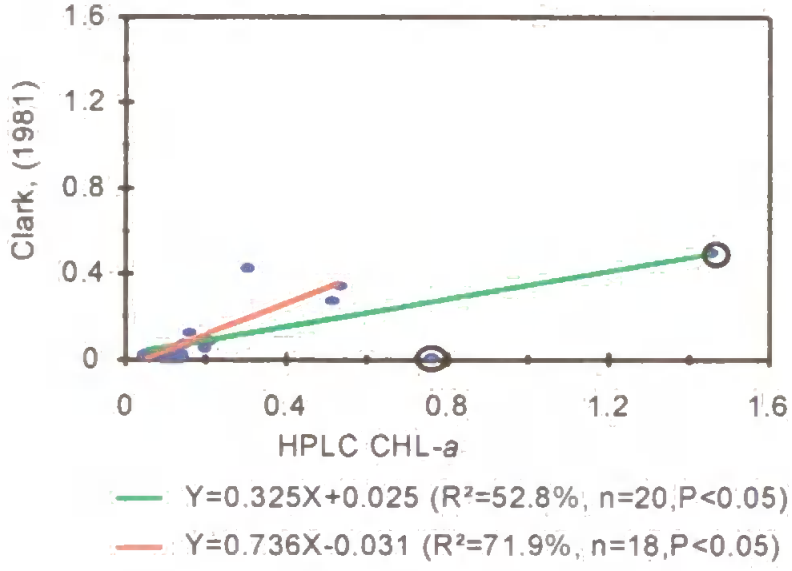

Figure 8.13 The CZCS pigment algorithm (equation 3.6) applied to the AMT-1 data, showing both the phase similarity of the data and regression analyses between the measured and retrieved concentrations. The low value red circled in (b) corresponds with the red boxed data point in (a). The CHL-*a* concentration is in units of $mg\ m^{-3}$.

(a)

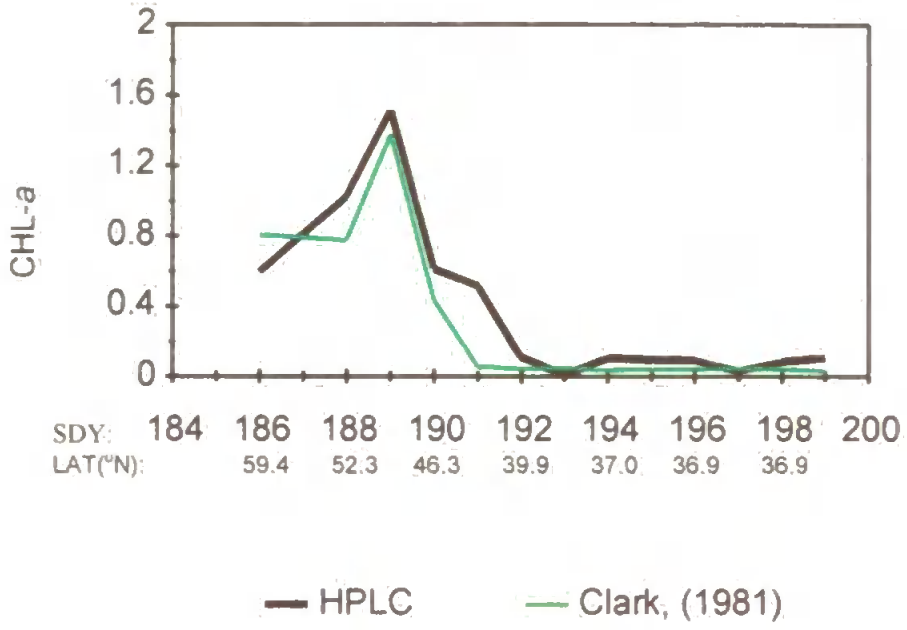

(b)

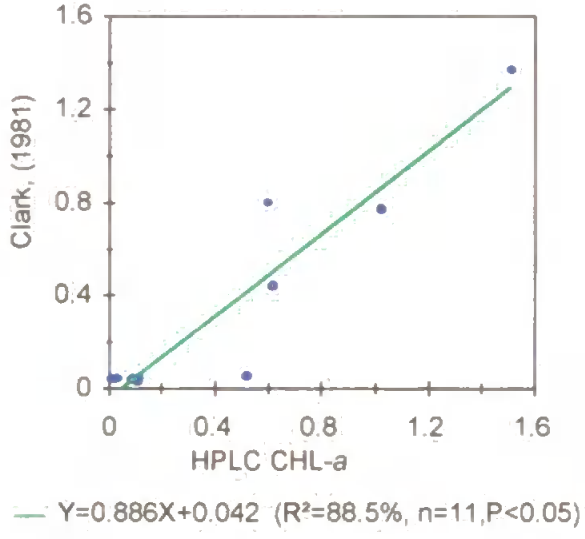

Figure 8.14 The CZCS pigment algorithm (equation 3.6) applied to the PRIME data, showing both the phase similarity of the data and regression analyses between measured and retrieved concentrations. The CHL-*a* concentration is in units of *mg* m^{-3}.

8.3.2 The CZCS-type SeaWiFS pigment algorithm (Moore *et al.*, 1997)

The performance of the SeaWiFS-CZCS type algorithm, equation 3.7, was very similar to the CZCS algorithm presented in section 8.3.1. CHL-*a* data retrieved from the radiometry compare poorly in the L4 coastal study, figure 8.15(a), displaying the same large errors evident in figure 8.12(a), with the phase similarly of the observations persisting beyond SDY 125 as was the case with the CZCS algorithm (see figure 8.12).

The AMT-1 data, figure 8.16, show good agreement between the retrieved and measured variables in the low concentration waters, accounting for 44.3% of the variance, underestimating significantly at the 23.3°*N* and 19.5°*N* sampling sites. These bias the regression analysis which was re-run excluding these data (red line) with an improvement in the R^2 value to 75.0% and corresponding improvement in the retrievals from: retrieved [CHL-*a*] = 0.405 x (HPLC CHL-*a*)+0.109 to: retrieved [CHL-*a*]= 1.088 x (HPLC CHL-*a*)+0.015. The changing biomass was clearly resolved by this algorithm, as was the case with the PRIME data, figure 8.17, retrieving accurate values and giving good agreement with the HPLC derived observations (R^2= 86.6%). It may be seen from figure 8.17(a) that for data collected at the sampling sites to the north of 39.9°*N* in the higher concentration waters, equation 3.7 produced low estimates of the true CHL-*a* concentration, whereas in the very low biomass waters south of this station this algorithm slightly over-estimated the measured values.

(a)

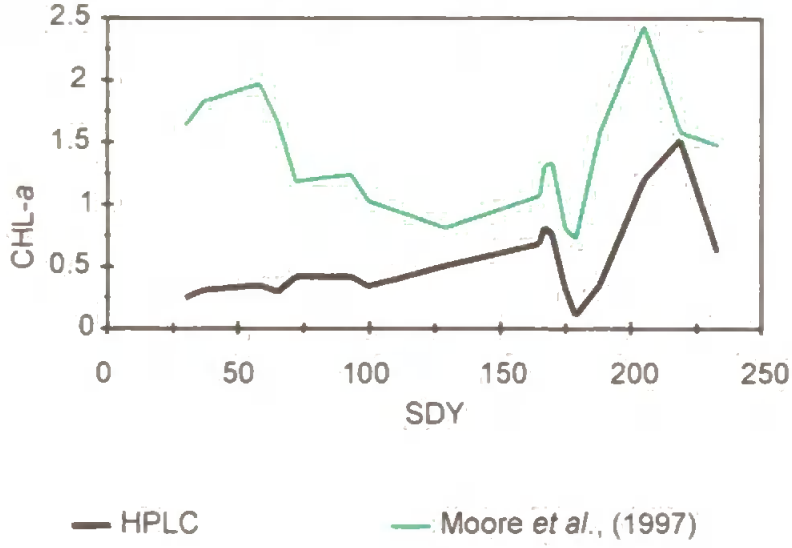

(b)

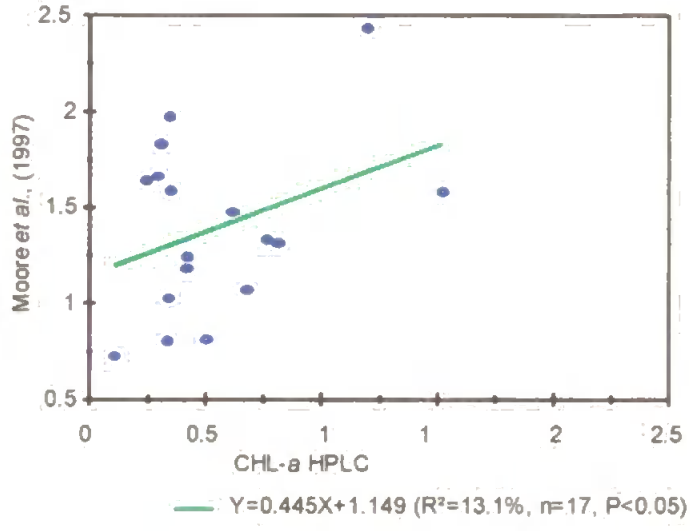

Figure 8.15 The CZCS-SeaWiFS type pigment algorithm, equation 3.7, applied to the L4 data, showing both the phase similarity of the data and regression analyses between the measured and retrieved concentrations. The CHL-*a* concentration is in units of $mg\ m^{-3}$.

(a)

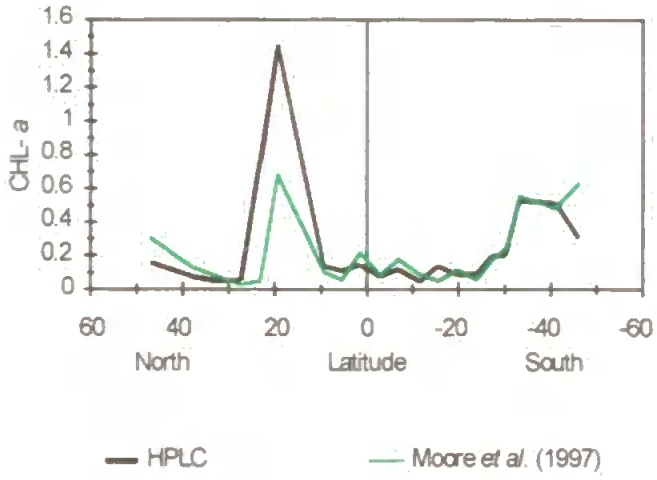

(b)

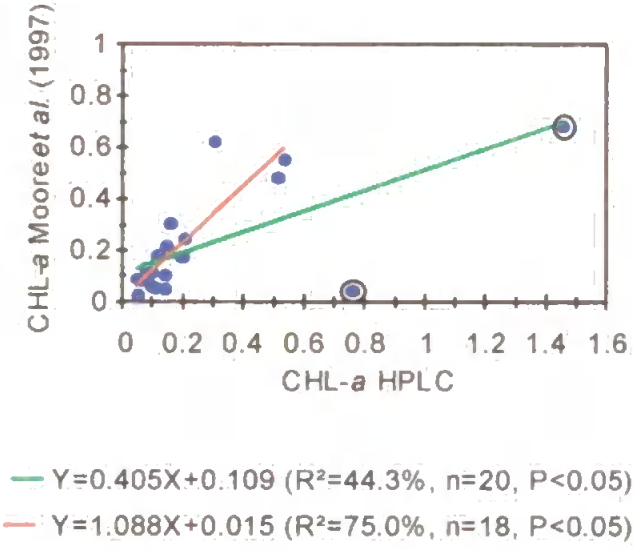

Figure 8.16 The CZCS-SeaWiFS type pigment algorithm, equation 3.7, applied to the AMT-1 data, showing both the phase similarity of the data and regression analyses between the measured and retrieved concentrations. The CHL-*a* concentration is in units of $mg\ m^{-3}$.

(a)

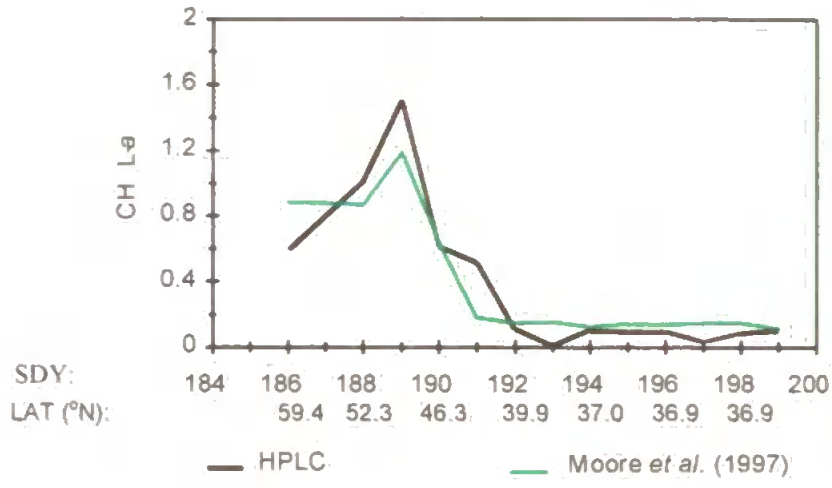

(b)

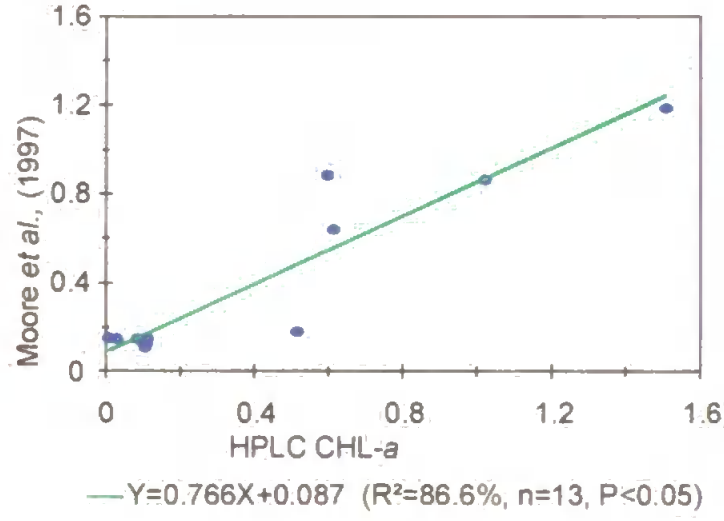

Figure 8.17 The CZCS-SeaWiFS type pigment algorithm, equation 3.7, applied to the PRIME data, showing both the phase similarity of the data and regression analyses between the measured and retrieved concentrations. The CHL-*a* concentration is in units of $mg\ m^{-3}$.

As discussed in chapter 1 (section 1.0) the field sites included here were chosen because it was considered that they were representative of the case 1

marine environment.

From figures 8.12(a) and 8.15(a) it can be seen that the L4 study represents a special case from the point of view of the retrieval of the CHL-*a* from both the pigment algorithms discussed in this section where although there were similarities between the measured and retrieved values with time, a low degree of the variance was explained at R^2= 13.5% (equation 3.6) and 13.1% (equation 3.7). As discussed earlier, the measured and retrieved data began to converge after SDY 125, where the peaks and troughs were better resolved by the algorithm derived data, even though the absolute values still varied significantly. Some insight into this phenomenon may be derived from the variability of the water column thermal structure illustrated in figure 7.1, when a thermocline began to build from about SDY 130, intensifying through SDY 175 to about SDY 260, at which time the thermocline became eroded. Station L4 is situated 6.5 nautical miles south of the Plymouth breakwater which marks the mouth of the estuary served by two major rivers, the Plym and the Tamar (fed by other tributaries), with additional seaward flow entering from the east via the river Yealm. Seasonal storm activity and the associated fresh water input can have an effect upon the suspended particulate fractions of the water column (Dyer, 1986) and the dissolved organic fraction (Carder *et.al.*, 1989; Kirk, 1994) which can have an effect upon the colour of the water and reduce the relative optical significance of the phytoplankton pigments in the blue end of the spectrum (as illustrated in figure 2.7). Weekly PML/MBA sampling of salinity at the L4 site was found to be erratic and inconclusive, but the effect seen in figure 8.12(a) and 8.15(a) during the early stages of sampling (SDY 30 to about SDY 125) of 1995 could be explained by the presence of high DOM

concentrations associated with terrestrial fresh water land runoff which has an exponentially increasing optical significance towards the shorter visible wavelengths (and into the UV) so competing directly for blue (443*nm*) light with CHL-*a*. Carder *et al.* (1989) have demonstrated that a DOM absorption coefficient of $0.005m^{-1}$ at 440*nm* can give rise to errors in the estimation of CHL-*a* derived from upwelling radiances of $0.1mg\ m^{-3}$. This hypothesis is consistent with the anomalous values produced by equations 3.6 and 3.7 in this instance and is further illustrated in figure 8.18 by spectrophotometric analysis of coincident 0.2 micron filtrate for absorption spectra (Westbrook, unpublished data), analysed in accordance with the protocol laid out in Mueller and Austin (1995).

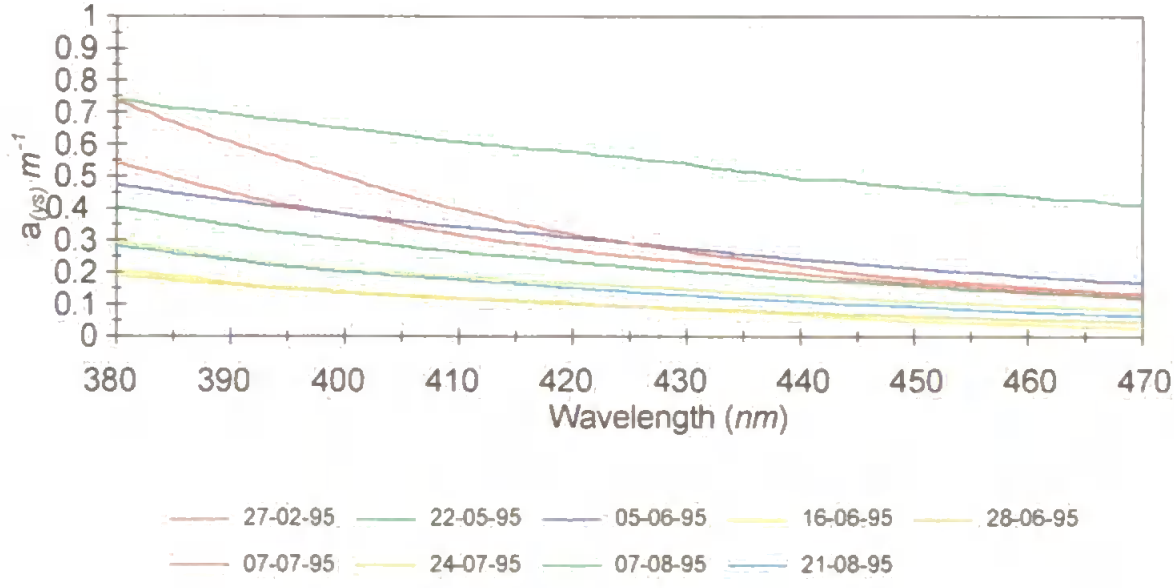

Figure 8.18 Detail of the absorption spectra of available samples from the 1995 L4 sampling campaign of the <0.2 micron fraction as determined by spectrophotometry. The legend refers to the sampling date.

Further research led by the author in the Plymouth area has resulted in the tentative establishment of a region specific link between the optical spectrum of the dissolved fraction (<0.2 micron) at the SeaWiFS band 1 wavelength and the associated carbon concentration as determined by total carbon analysis (Alvarez-Salgado and Miller, 1998. This was found to be $\mu M\ C\ l^{-1}$ = 1087 ($a_{(ys)}412nm$) + 137.5 (R^2=87.6%, n=8) and hence the range of total carbon concentrations represented by the $a_{(ys)}412nm$ data in figure 8.18 is 247 to 490 $\mu M\ C\ l^{-1}$ which compares with typical values of 80 $\mu M\ C\ l^{-1}$ which may be observed away from the coastal zone (Vodacek *et al.*, 1995) where only nominal influence is exerted by this fraction on the blue absorption (443*nm*; 490*nm*). These results are preliminary and further experiments to increase the number and diversity of the source data are required to refine the relationship and allow further algorithm development, particularly in the light of the high intercept value given above.

8.4 RETRIEVAL FROM RADIOMETRY OF THE CO-VARYING CAROTENOIDS ASSOCIATED WITH CHLOROPHYLL-*a* FROM THE RATIOS IDENTIFIED BY HPLC ANALYSIS

In this section an example of the retrieval of CHL-*a* and total carotenoid (TC) concentrations is presented which could in theory have been derived from SeaWiFS image scenes of the AMT-1 cruise track. Data in Figure 8.19 show the concentrations of these pigments as determined by HPLC. Figure 8.19(b) illustrates the regression analysis results carried out to determine the relationship between these two pigment groups, but with the outliers (circled) separated out. Included in both regressions were a low value inset in a square. The two outliers

relate to anomalous data shown in figure 7.10(d), where it may be seen that at the 23.3°*N* and 19.5°*N* sampling sites there was evidence of a change in the pigment assemblage (as discussed earlier). To simulate these data from the radiometry, the along track CHL-*a* concentration was calculated from the Moore *et al.* (1997) algorithm, equation 3.7, the retrieval characteristics of which were discussed in section 8.3.2. From figure 8.19(b) it was then established by regression that for 18 data points a relationship existed of [TC]=1.257 x [CHL-*a*]+0.002 (R^2=94.4%), whereas for the two data driving the second relationship (plus one anchoring data point near the origin) similar analysis indicated that: [TC]=0.222 x (CHL-*a*)+0.0273 (R^2=81.3%).

Figure 8.20(a) shows the retrieved CHL-*a* and TC concentrations derived from the above methodology for 18 data (green line) and for 3 data (red line). It may be seen that the corrected data more closely match the pattern of co-variance shown in figure 8.19(a). The corrected TC data compare poorly with the corresponding measured data, overestimating with a regression relationship of TC retrieved = 1.215 x (TC HPLC)+0.070 (R^2=67.6%), but the technique does demonstrate the link that may be exploited between the semi-analytical algorithm and local knowledge leading to possible improved estimations of accessory pigment distributions from satellite imagery.

(a)

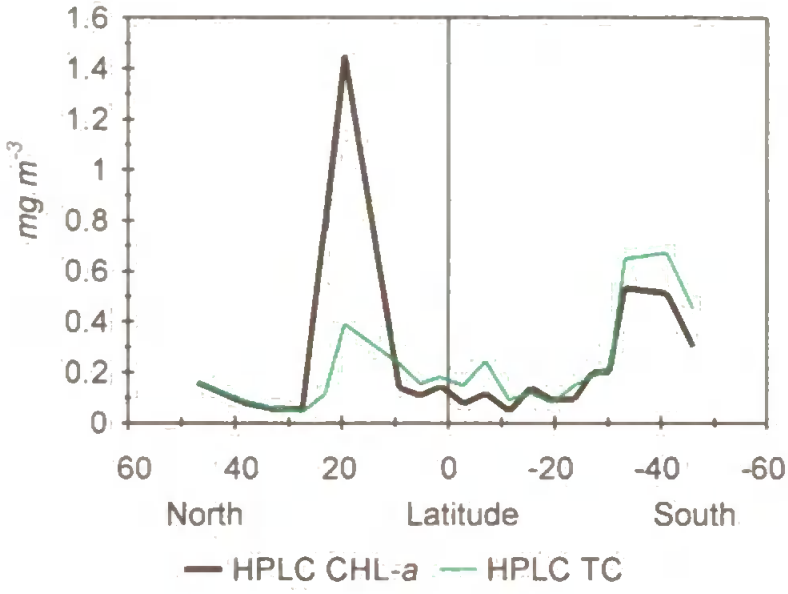

(b)

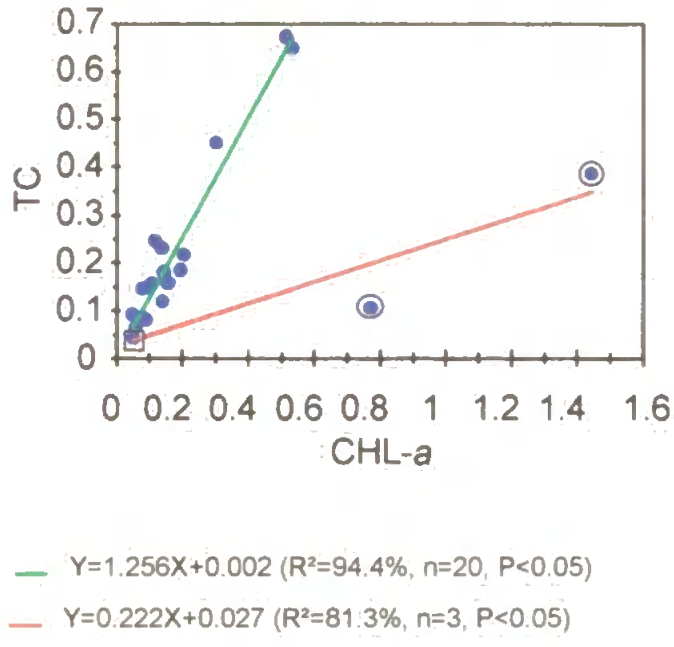

Figure 8.19 (a) AMT-1 CHL-*a* and TC data measured by HPLC and (b) regression analyses of TC:CHL-*a* for 20 data points, and for two outliers (plus 1 anchor data point). The pigment concentrations are in units of *mg* m^{-3}.

(a)

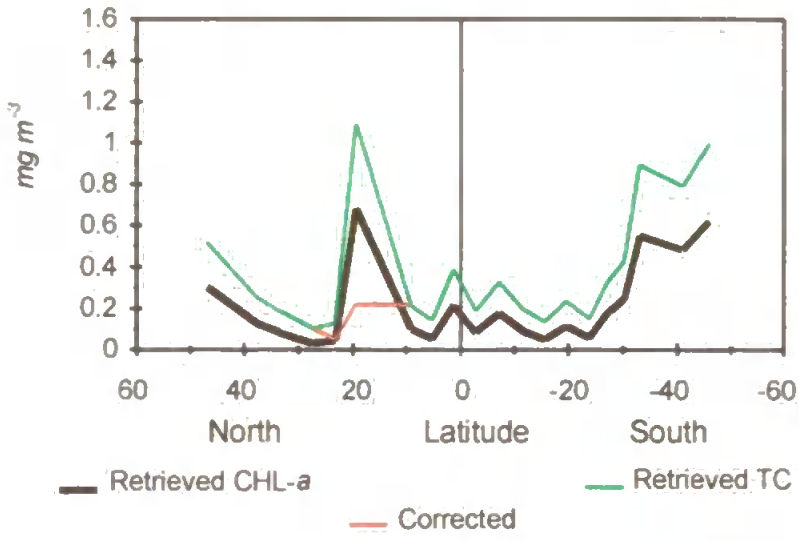

(b)

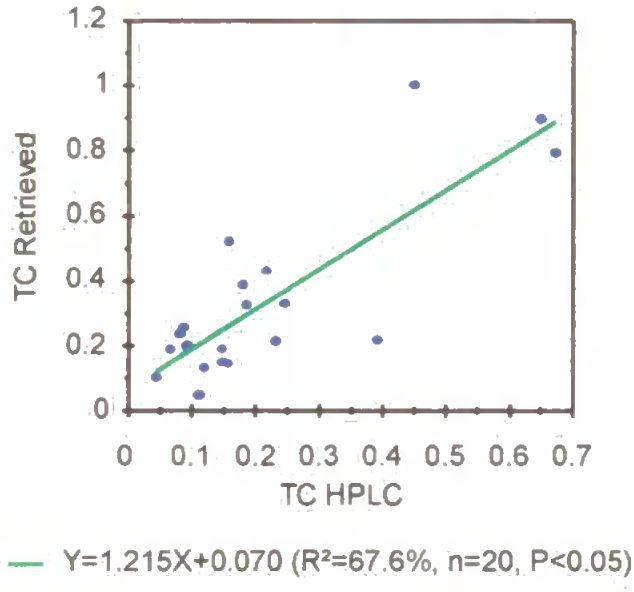

Figure 8.20 (a) AMT-1 CHL-*a* data retrieved from the radiometry by the algorithm (Moore *et al.*, 1997), equation 3.7, and TC from the relationship identified from the HPLC analyses by regression shown in figure 8.18(b). Also shown (b) is a regression analyses to compare the retrieved TC concentration against the corresponding HPLC TC. The pigment concentrations are in units of $mg\ m^{-3}$.

8.5 THE GENERATION OF ALGORITHMS TO RETRIEVE THE MAJOR PIGMENT GROUPS FROM UPWELLING RADIANCES

It may be seen from section 7.5 (table 7.3), where the results of the pigment analyses were presented and compared with previous work, that the observations made during this study follow accepted patterns of pigment assemblage co-variability (Aiken *et al.,* 1995). In the last section aspects of the co-variance identified were explored by utilising, as an example, the effectiveness with which the TC concentration may be derived from the relationship established between this group and CHL-*a*, which was in turn derived from upwelling radiances by the Moore *et al.* (1997) algorithm. In this section the relationship between the light field and the major pigment groups is explored directly.

Figure 8.21 illustrates the development of an algorithm designed to derive CHL-*a* from upwelling radiances determined at each sampling site during AMT-1. As has been the case in previous discussions, the regression analysis is driven by the high levels of CHL-*a* measured at the 23.3°*N* and 19.5°*N* sampling sites. Figure 8.21(a) shows a regression both including (green line) and excluding (red line) these data (circled).

Equation 8.4 is the algorithm resulting from the second regression analysis, where n=18, and R^2=71.7% in figure 8.21(a).

$$\text{CHL-}a = 0.702 \left[\frac{Rrs(443)}{Rrs(560)}\right]^{-0.914} \quad (mg\ m^{-3}) \qquad (8.4)$$

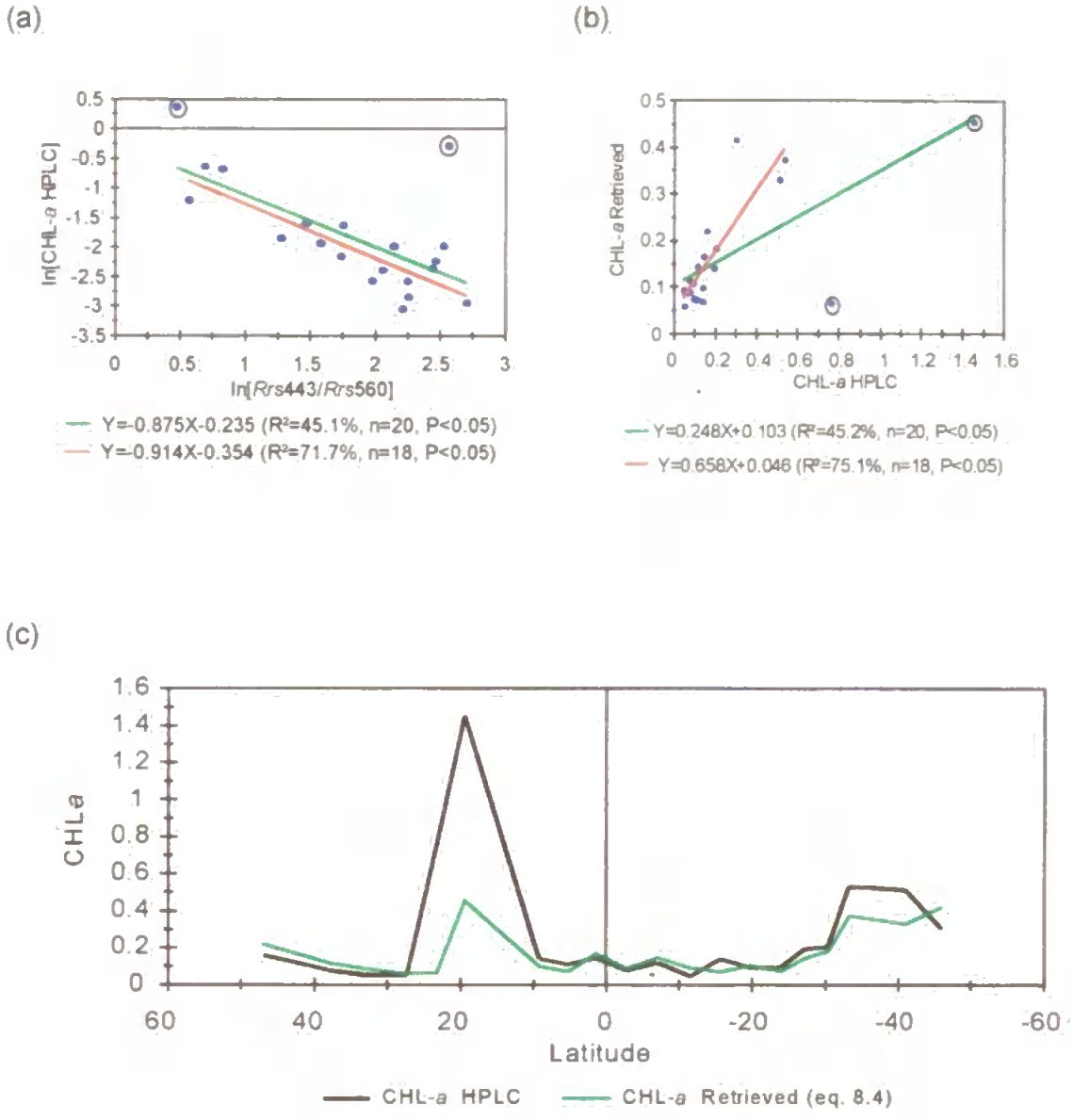

Figure 8.21 Development of an algorithm to derive the concentration of CHL-*a* from upwelling radiances where (a) illustrates the data from which the algorithm was generated, (b) presents a regression analysis of the retrieved against measured concentrations and (c) shows the same information as (b) but displayed as an along cruise track plot. The CHL-*a* concentration is in units of *mg* m^{-3}.

As in section 8.1, the empirical constraints were determined by Napieran log-log regression. The same techniques were then applied to some further components of the measured pigment data. The algorithms thus derived are detailed in table 8.3.

Table 8.3 Pigment algorithm summary. Key: T-CHL, T-CAR = total carotenoids, T- PSC = total photosynthetic carotenoids, T-PPC = total photoprotective carotenoids, T-PIG = total pigment.

Field work		Chl-*a*	T-CHL	T-CAR	T-PSC	T-PPC	T-PIG
Alldata	***A***	0.494	0.668	0.396	0.297	0.093	2.071
	B	-0.728	-0.723	-0.525	-0.841	-0.147	-0.705
	R^2 (%)	50.3	52.1	39.4	54.2	5.40	50.3
L4	***A***	0.449	0.765	0.783	0.254	0.079	0.938
	B	-0.421	-0.115	-0.025	-0.131	-0.045	-0.323
	R^2 (%)	4.6	4.9	0.3	0.3	0.06	0.026
AMT-1	***A***	0.702	1.189	0.795	0.866	0.132	2.028
	B	-0.914	-0.952	-0.855	-1.448	-0.252	-0.898
	R^2 (%)	71.7	46.6	69.1	73.0	12.5	57.4
PRIME	***A***	1.163	1.577	1.254	1.027	0.248	1.163
	B	-1.399	-1.344	-1.223	-1.402	-0.864	-1.399
	R^2 (%)	62.5	68.8	70.5	75.7	77.0	62.5

As the pigment data set had been demonstrated to contain a degree of co-variance, there should have been a broadly similar relationship between the ratios derived from the HPLC analyses and the corresponding ratios retrieved using the algorithms. Some comparisons are detailed in table 8.4.

Table 8.4 Comparison of pigment concentrations derived by HPLC and retrieved from the algorithms detailed in table 8.3.

Pigment ratio	From HPLC analysis	Retrieved from algorithm
TC:T-CHL	0.42	0.79
PSC:T-CHL	0.30	0.31
PPC:T-CHL	0.12	0.43

It may be seen from table 8.4 that there is a degree of similarity between the sample ratios determined from the measured and retrieved pigment data sets,

although the small number of data collected during this study, and the narrow range of the measurements make the pigment data unreliable in this context.

Data in Figure 8.22 shows the similarities that could be established between the pigment concentrations that were derived from the HPLC analysis of the water samples, and the same quantities derived from pigment component algorithms applied to the radiometry carried out coincident with sampling.

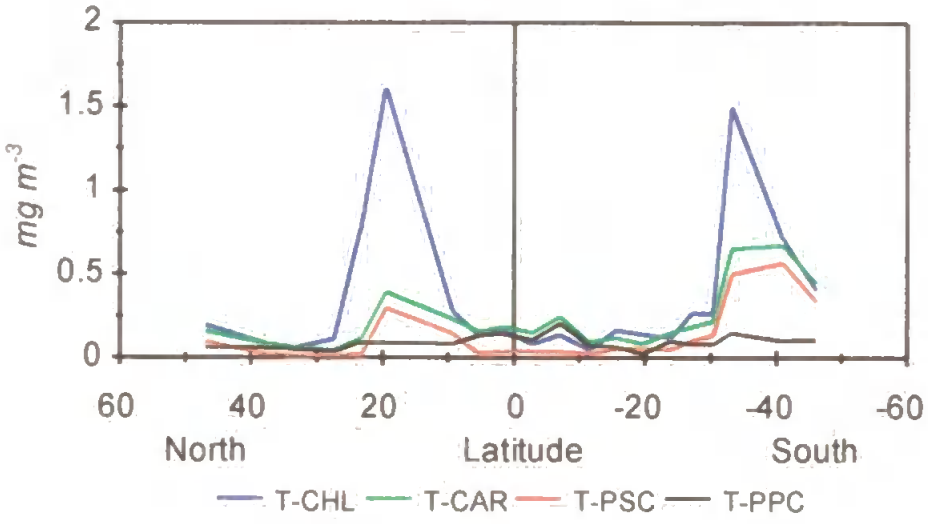

(a) Measured concentrations

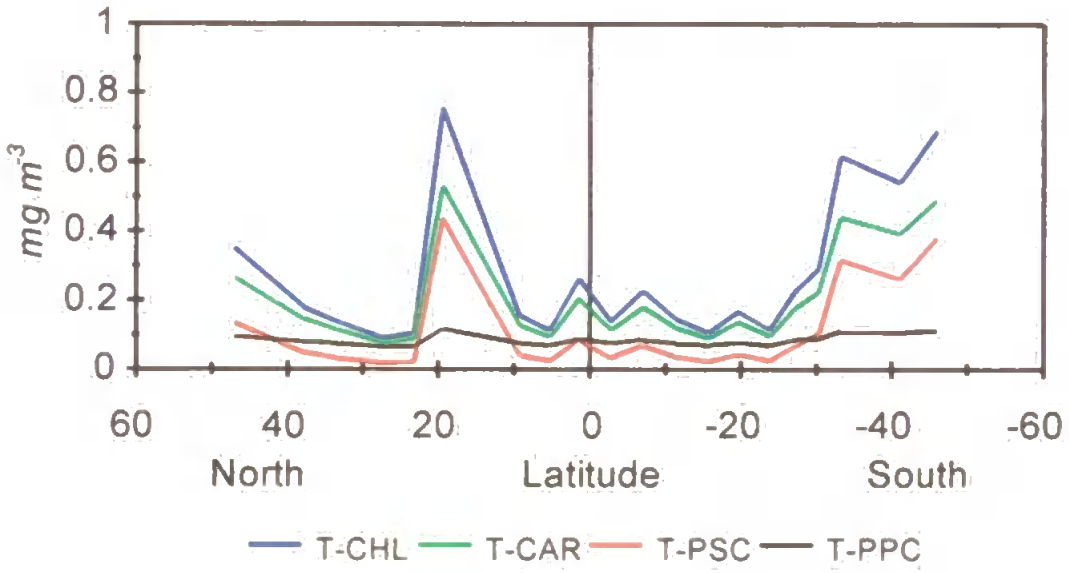

(b) Retrieved concentrations

Figure 8.22 Along track plot of values for (a) measured concentrations of the major pigment groups and (b) corresponding data determined from the algorithms detailed in table 8.5 as applied to the AMT-1 radiometric data set.

(a)

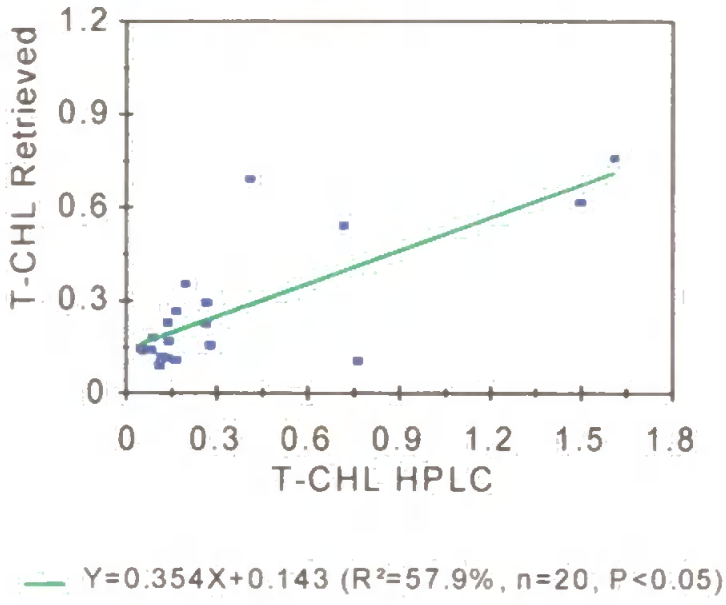

(b)

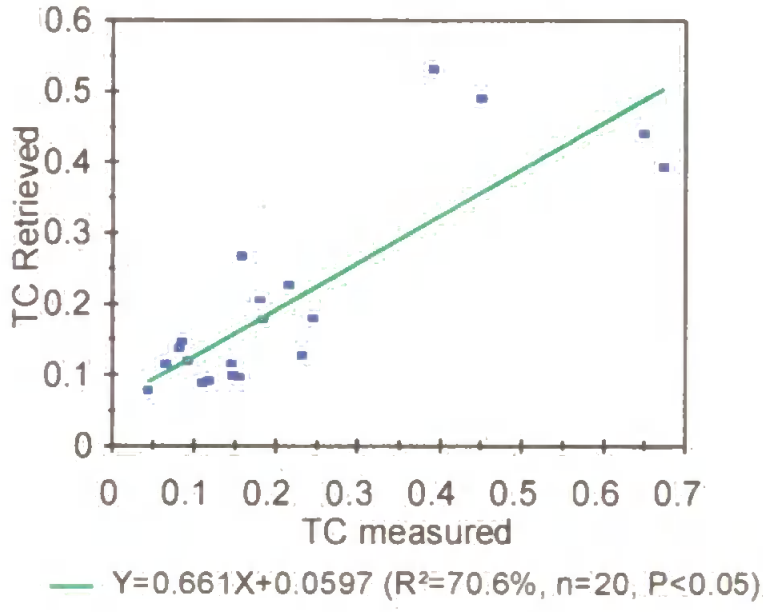

Figure 8.23 Regression analyses of (a) T-CHL (retrieved) v T-CHL (measured) and (b) T-CAR (retrieved) v T-CAR (measured). The pigment concentrations are in units of *mg* m^{-3}.

(a)

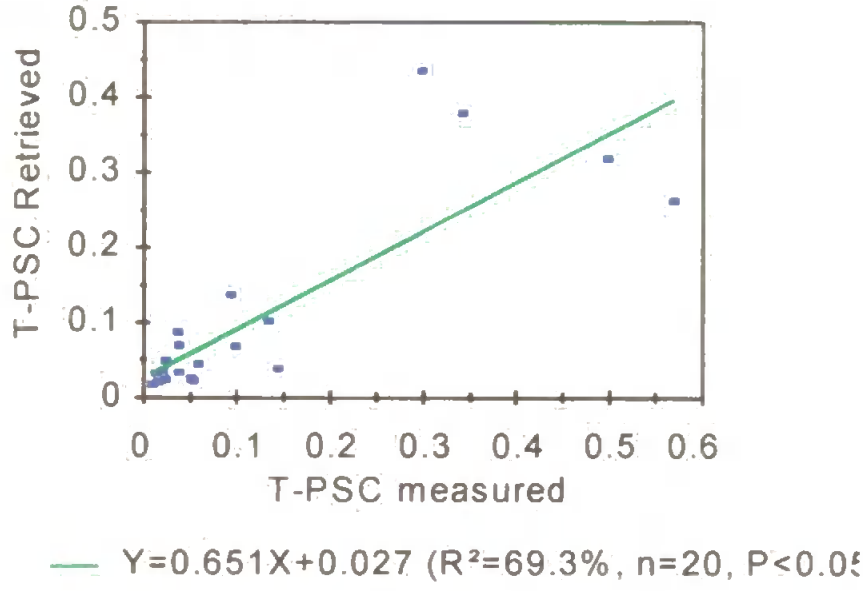

(b)

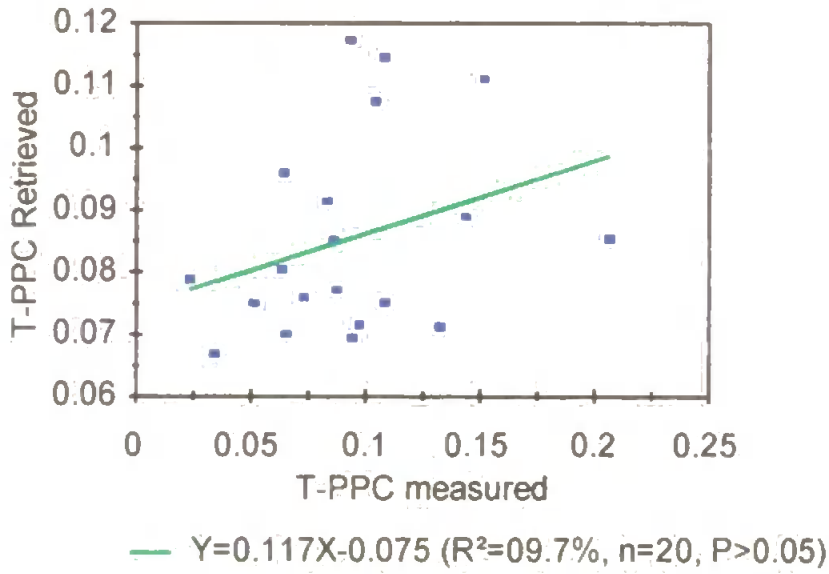

Figure 8.24 Regression analyses of (a) T-PSC(retrieved) v T-PSC(measured) and (b) T-PPC(retrieved) v T-PPC(measured). The pigment concentrations are in units of *mg* m^{-3}.

Data in figure 8.22 illustrate an example of the retrieved and measured T-CHL, TC, PSC and PPC concentrations derived by (a) HPLC and (b) the algorithms detailed in table 8.3. Regression analyses of these data are presented in figures 8.23 and 8.24, with an assessment of the average errors presented in table 8.5. On this basis it can be seen that the algorithms perform very poorly.

In this instance the use of algorithms to retrieve the carotenoid fractions from the ocean colour measurements yield broadly accurate but highly imprecise estimations. The use of semi-analytical algorithms to determine the concentration of accessory pigments will produce accurate results due to the predictable co-varying nature of the pigment assemblage, rather than their direct covariance with the light field measurements. The reasonable accuracy of the approach applied to these data mean that should this technique be applied to satellite derived measurements of general variability then the data may prove useful. The natural variability in the inter-pigment ratios observed between sampling sites, however, means that if precise determinations of the pigment assemblage are to be derived, then local knowledge must form part of the input into the model, or an alternative approach should be investigated.

Table 8.5 Errors in pigment retrieval (derived from the amalgamated data set).

Pigment assemblage component	**Average % error=** $\left[\frac{\sum\left(\frac{\lvert(HPLC\ \ value - retrieved\ \ value)\rvert}{HPLC\ \ value}\right)}{n}\right]*100$
CHL-*a*	80.929
T-CHL	71.129
T-CAR	71.291
T-PSC	87.977
T-PPC	71.751
T-PIG	146.433

It is concluded that the range of Chl-*a* encountered during data collection for this study ranged from 0.001 $mg\ m^{-3}$ to 1.98 $mg\ m^{-3}$ which was insufficient to generate any relationship that could improve upon the Moore *et al.* (1997) approach.

9. SUMMARY AND CONCLUSIONS

This chapter brings together the salient points from the results and subsequent data analysis, with some comment on the methodologies employed, followed by a summary of the findings.

9.1 *IN-SITU* DATA COLLECTION

The instruments employed to obtain the core measurements were 'off the shelf' technology. During the preparatory phases of the project consideration was given to the development of effective, but practical, solutions to the problems that would be encountered while undertaking field observations.

9.1.1 Radiometric measurements

The accuracy of the optical sampling was carried out to within the limits set for SeaWiFS calibration and validation exercises of 5% absolute and 1% relative radiometric accuracy (Hooker *et. al.*, 1992), traceable to the SeaWiFS calibrated standard lamp. Drift in the voltages output by the sensors incorporated into the PRR-600 was tracked by periodic calibration carried out by the manufacturers (Biospherical Instruments Inc.) and the USA National Institute of Standards and Technology (NIST), as detailed in chapter 4. The $Kd(\lambda)$ values derived from the *in-situ* radiometry were therefore taken to have met the required quality control objectives outlined in chapter 4 for the purpose of algorithm generation and for

making comparisons with the work of other investigators. Summary data were presented in section 7.2.

9.1.2 Phytoplankton pigment analyses

The pigment analyses brought together a spatially and temporally diverse suite of measurements which, for the purposes of interpretation, were treated both as individual data sets (applicable to the sampling programme) and as an amalgamation of all three data sets (applicable more generally), see section 7.3. Particularly notable were the data collected at the 23.3°*N* and 19.5°*N* sampling sites during AMT-1 (section 7.3(iii)). These sampling locations produced varied data in both the chlorophyll and carotenoid fractions as the phytoplankton population changed from domination by prochlorophytes (evident from the relatively high divinyl chlorophyll-*a* and zeaxanthin signal) to diatoms (from the fucoxanthin signal). As well as the broad quantification of the standing crop at basin scales, the detection and understanding of local features of this type using satellite imagery is important at the local scale. These data allow the assessment of the effect that the variability in the pigment assemblage has upon the optical characteristics of the water and hence algorithm performance.

The analyses presented in section 8.5 showed that the observations constituted too narrow a range of data (the chlorophyll-*a* concentration ranged from 0.01 to 1.99$mg\ m^{-3}$) for meaningful pigment algorithm generation from this work that could compare with or improve upon the work of Clark (1981) or Aiken *et al.* (1995). This conclusion is based upon the poor light field – pigment relationships summarised in section 8.5, table 8.3, and the error analysis detailed in table 8.5.

9.2 THE DEVELOPMENT OF ALGORITHMS FOR THE DERIVATION OF *Kd*(490*nm*) USING THE OPTICAL DATA COLLECTED DURING THE FIELD WORK

New algorithm empirical constraints were presented in section 8.1 as modifications to the *Kd*(490*nm*) algorithm for SeaWiFS based on analyses of the data sets collected during the field sampling. To re-cap, equation 9.1 shows the form of the general algorithm derived in section 8.1.

$$Kd(490) = 0.103 \left[\frac{Rrs(443)}{Rrs(560)}\right]^{-1.148} + 0.0192 \qquad (m^{-1}) \qquad (9.1)$$

The application of this algorithm assumes a vertically mixed ocean, as the calculations were based upon values determined from measurements of ocean colour representative of one diffuse attenuation length (see sections 2.4 and 5.1). These data may be related to the pigment concentration (in terms of chlorophyll-*a*, Smith and Baker 1978) and the penetration of PAR into the surface waters to give an estimate of the availability of the underwater light field to autotrophic organisms through the attenuation properties of the waters (Zaneveld *et al.*, 1993).
It can be seen from figure 2.7(b) (from the work by Bidigare *et al.* (1990)) that in case 1 waters, although phytoplankton are active absorbers in this region, the specific pigment absorption at 560*nm* is relatively low (ranging from 0.0009-0.0061m^2 mg^{-1}), driven by chlorophylls -*a*, -*b* and –*c* and the photosynthetic carotenoids. At 443*nm* the specific absorption is much higher (ranging from

0.0129 - to 0.0442m^2 mg^{-1}) due to chlorophylls -*a*, -*b* and -*c* and the total carotenoids (photoprotective and photosynthetic), all of which are more active absorbers at this shorter wavelength of light. The value of the light field reflectance band ratio will therefore not only be affected by changing biomass, but also relative differences in concentrations of each pigment assemblage component present at the optical profiling station. These factors are taken into account during the smoothing process that accompanies the derivation of the empirical constraints at the semi-analytical algorithm generation stage (see section 8.1). The algorithm(s) therefore are able to retrieve precisely only one value for the property determined, with the frequency distribution of the errors becoming significantly different within a certain range of variation, as the radiometric input deviates from the limits set by the constraints determined by the range of source data.

AMT-1 and PRIME provided a cross comparison between this study and a radiometric data set collected over a range of similar biological regimes. The variability in the accuracy of the mathematical retrievals illustrated that the algorithm generated here remains effective over a wide range of *Kd*(490*nm*), from that of close to pure water, 0.0200m^{-1} observed during AMT-1 and PRIME, to values as high as 0.2920m^{-1} measured during the L4 study.

In section 8.2 consideration was given to the generation of field site specific algorithms, where there were indications that greater degrees of precision were possible, even though the relationships were based on low numbers of local data, and hence potentially had a lower statistical significance. Rigorous assessment of the error distributions using a statistical test (see section 5.2) indicated that the general and local algorithms displayed significantly different performance characteristics at the p=0.05 level. This analysis demonstrates that it is not

appropriate to apply algorithms to remotely sensed observations of waters that significantly deviate from those observed during the collection of algorithm source data. New relationships must be produced if accuracy is to be maintained.

In summary: all the algorithms designed to retrieve $Kd(\lambda)$ discussed here are consistently accurate (in terms of location), regardless of the data set to which they were applied. In terms of precision (absolute error), however, they yield widely varying results. The numbers and diversity of the data used to constrain the relationships profoundly influence the result. For this reason it is not possible to derive 'global' $Kd(\lambda)$ values from a single algorithm which fully utilises the level of accuracy in radiometric input that is now available from SeaWiFS. Future effort should be focussed upon the generation of $Kd(\lambda)$ maps from satellite imagery, using a network of locally derived algorithms from continuing spatially and seasonally extensive ground truth data collection programmes. This would accurately represent the maximum possible range of variability, locally identified, over the biogeochemical regimes that make up the world's oceans. While this is not practical in the short term, the inclusion of a bio-optical component when designing programmes of research is becoming increasingly common, routinely producing comprehensive suites of observations at key locations.

9.3. COMPARISON OF STANDARD ALGORITHMS DESIGNED TO RETRIEVE CHLOROPHYLL-*a* WITH MEASURED VALUES DETERMINED BY HPLC

Algorithms designed to retrieve the chlorophyll-*a* concentration from upwelling radiances were compared with contemporaneous *in-situ* data, and their effectiveness assessed. The relationships established between the major components of the pigment assemblage were explored to assess which of the various groups, if any, could be retrieved from the radiometry (further discussed in section 9.5). The HPLC chlorophyll-*a* data were used to test the retrieval characteristics of the two established pigment algorithms discussed in chapter 3:

(i) the CZCS algorithm (section 8.3.1), and

(ii) the CZCS-type SeaWiFS pigment algorithm (see section 8.3.2).

Both the algorithms presented show a degree of correlation between the HPLC measurements of chlorophyll-*a* and the corresponding values retrieved from the radiometry during the AMT-1 and PRIME cruises, but a very poor correlation for data resulting from the L4 seasonal study. Evidence presented in section 8.3.2 (figure 8.18) indicates that this may be due to possible deviation from the case 1 oceanic environment at station L4 during the survey. Here the case 1 algorithms were found to be less effective in areas where it may be considered that there were additional non-phytoplankton related optically significant material. It is concluded that the CZCS algorithm still performed well, even when applied to radiometry where the green band used was +10*nm* from the original CZCS specification of 550*nm*, but tended to under-estimate in the oligotrophic regions, where the chlorophyll-*a* concentration was found to be very low, see figure 8.12. This could be due to the absence of phaeophytin-*a* data, the presence or otherwise

of which was not identified by the HPLC analysis. The retrieved values derived from the CZCS-type SeaWiFS algorithm for the chlorophyll-*a* concentration co-varied closely with the measured values in the low concentration areas traversed during AMT-1 and PRIME. These regions of the world's oceans, although relatively sparsely populated by photosynthetic algae, with chlorophyll-*a* concentrations generally below 1.5 $mg\ m^{-3}$ (Aiken *et al.*, 1995; Westbrook *et al.*, 1998; Westbrook *et al.*, 1999) are very large. The accurate determination of the phytoplankton biomass at low concentrations is therefore an important scientific objective to provide characteristic baseline values for surface algal biomass distributions which may be used in climate models (Houghton *et al.*, 1996). The AMT-1 light field and pigment data were included in the NASA SeaWiFS algorithm generation data base. Although algorithm performance must continually be assessed through periodic calibration and validation exercises, this can now be satisfactorily achieved using the NASA SeaWiFS chlorophyll-*a* case 1 algorithm.

9. 4. RETRIEVAL FROM RADIOMETRY OF MAJOR GROUPS OF PIGMENTS FROM THE INTER-PIGMENT RATIOS ESTABLISHED BY THE HPLC ANALYSIS

From the relationships established by the pigment analyses presented in section 7.3, it follows that the calculation of the chlorophyll-*a* concentration from pixel intensities isolated from an imaged SeaWiFS oceanic scene allows the subsequent determination of the concentration of the associated pigment groups that have been identified as co-varying with it from the HPLC pigment analysis. The example presented in section 8.4 (figures 8.18 and 8.19) illustrates the results of a

comparison between the measured and retrieved concentrations of the total observed carotenoids (TC) determined in this way. Regression analyses of these data indicated two distinct relationships. The use of both relationships when applied to the appropriate locations along the AMT-1 cruise track resulted in retrieved data more closely matching the measured values (as illustrated in figure 8.20).

This approach could be adopted in any region of the world oceans for which the seasonal and temporal variability of the pigment assemblage has been studied.

9. 5 THE RETRIEVAL OF COMPONENTS OF THE PIGMENT ASSEMBLAGE BY THE APPLICATION OF ALGORITHMS TO OCEAN COLOUR MEASUREMENTS

Semi-analytical algorithms were derived for chlorophyll-*a*, total chlorophyll, total carotenoids, total photosynthetic carotenoids, total photoprotective carotenoids and total pigment using the methodology illustrated in figure 8.21. A summary of the algorithms was given in table 8.3. It is concluded that the poor degree of variance explained in the regression analysis was due to the insufficient range of observed pigment concentrations for construction of any algorithms which, although enabling a degree of light field-pigment group covariance, the algorithms generally achieved very poor precision when compared with the values measured *in-situ*.

9.6 FUTURE WORK

The performance of all the algorithms discussed here must be tested against data derived from additional fieldwork to assess the spatial applicability of this work and any improvement in the resolution of in-water parameters discussed, when compared with data derived from the standard algorithms currently in use. This must be a continuing process of evolution within all research organisations using ocean colour remote sensing data products.

As discussed earlier, with the development of the pigment algorithm by Aiken *et al.* (1995) also presented by Moore *et al.* (1997), the derivation of the case 1 chlorophyll-*a* concentrations from upwelling radiances received by the space borne SeaWiFS is a technique that is providing data of acceptable quality over the narrow range of concentrations found in the open oceans (see figures 8.16 and 8.17). In these localities the empirical algorithm constraints reflect the diversity of a substantial source data set. Data retrieved from the ecologically and economically important near coastal case 2 environment is generally less well understood. Particularly, the DOM fraction has been widely reported as being a highly significant factor, contributing to errors in the retrieval of in-water parameters (Kirk, 1980; Tassan, 1988; Carder *et al.*, 1989; Aiken *et al.*, 1995). Together with the assessment of primary productivity and phytoplankton species diversity from satellite derived products, this area of work still constitutes a significant challenge for remote sensing scientists.

9.8 SUMMARY

This work assessed and applied the state of the art optical sampling techniques to enable the collection of high quality data from a range of sampling sites and deployment platforms and forms a practical reference to assist those undertaking such observations in the future. The application of these techniques resulted in a data set forming a high quality basis for the assessment of currently available algorithms designed to derive the optical properties discussed, as well as the presentation of new algorithm constraints for $Kd(490nm)$ derivation.

While all these algorithms, old and new, were proven applicable, it was shown that the precision with which $Kd(490nm)$ may be derived mathematically can be both spatially and / or seasonally restricted (Westbrook *et al.*, 1999). Limited success was reported in the use of 'locally' derived algorithms, which were compared with the 'general' variants, resulting in a significant difference in the performance between them being identified. These observations form the basis of the conclusion that empirical algorithm scaling is a vital consideration when including routinely available airborne or satellite $Kd(\lambda)$ data in programmes of research.

As a result of this work a further understanding of remote sensing algorithms has been achieved that needs to be considered by all workers in the field using such data in their day to day research. The form and empirical basis of all remote sensed data products needs careful consideration when either making comparisons with ground truth data or using such data products as a source of information directly.

To this end the remote sensing community should be prepared to publicise the equations used to generate data products with a reference accompanying imagery where the generation and development of the algorithm may be found, ensuring that only published algorithms be used. In this manner investigators wishing to employ these optical data may be able to assess the suitability of a product for their purposes and enable the research community to make full use of the high accuracy radiometric input (1% relative and 5% absolute) now routinely available to algorithms from SeaWiFS and the next generation of sensors either awaiting launch or under construction.

10. REFERENCES

Aiken J, (1985). The undulating Oceanographic Recorder Mark 2. A multirole oceaographic sampler for mapping and modelling the biophysical marine environment. In: Mapping Strategies in Chemical Oceanography. Zirino A., Ed. American Chemical Society, **209**, 315-332.

Aiken J. and Bellan I., (1990). "Optical Oceanography: an assessment of towed measurement". In: Light and Life in the Sea. Herring P.J., Campbell M., Whitfield M. and Maddock L., Eds. Cambridge University Press, 39-57.

Aiken J., Moore G.F., Holligan, P.M., (1992). Remote sensing of oceanic biology in relation to climate change, mini review. Journal of Phycology, **28**, 579-590.

Aiken, J., Moore G.F., Trees C.C., Hooker S.B. and Clark D.K., (1995). The SeaWiFS CZCS-type pigment algorithm. NASA Tech. Memo. 104566, Vol. 29, S.B. Hooker and E.R. Firestone, eds., NASA Goddard Space Flight Centre, Greenbelt, Maryland, 24pp.

Alvarez-Salgado, X.A. and Miller, A.E.J. (1998). Simultaneous determination of dissolved organic carbon and total dissolved nitrogen in seawater by high temperature catalytic oxidation: conditions for precise shipboard measurements. Marine Chemistry 62:325-333.

Asrar G., and Greenstone R., (1995). Mission to planet Earth/ Earth observing system (MTPE/EOS). NASA Goddard Space Flight Centre, Greenbelt, MD 20771.

Austin R.W. and Petzold T.J., (1981). The determination of the diffuse attenuation coefficient of sea water using the Coastal Zone Colour Scanner. In Oceanography from Space, Gower J.F.R., ed., (1981). Marine Science Volume 13, Proceedings of the COSPAR/SCOR/IUCRM symposium on Oceanography From Space. Plenum Press, 233 Spring Street, New York, 10013.

Balch W.M., Holligan P.M., Ackleson S.G., Voss K.J., (1991). Biological and optical properties of mesosclae coccolithophore blooms in the Gulf of Maine. Limnology and Oceanography, 36(4), 629-643.

Barlow R.G., Cummimgs D.G. and Gibb S.W., (1997). Improved resolution of mono- and divinyl chlorophylls *a* and *b* and zeaxanthin and lutein in phytoplankton extracts using reverse phase C-8 HPLC. Marine Ecology Progress Series, Vol. 161, pp. 303-307.

Barlow R.G., Mantours R.F.C, Gough M.A. and Fileman T.W., (1993). Pigment signitures of the phytoplankton composition in the northeastern Atlantic during the 1990 spring bloom. Deep Sea Research, Vol. 40, pp. 459-477.

Biospherical Instruments Inc., (1995). The PRR-600 Profiling Reflectance Radiometer users manual. Biospherical Instruments Inc., 5340 Riley Street, San Diego, CA 92110.

Bidigare R.R., Ondrusek M.E., Morrow J.H. and Kiefer D.A., (1990). *In-vivo* absorption properties of algal pigments. SPIE Vol. 1302, Ocean Optics X (1990), pp. 290-302.

Borland International Inc., (1993). Quattro Pro for Windows version 3, reference manual. Corporate headquarters, 1800 Green Hills Road, P.O. box 660001, Scotts Valley, CA 95067-0001.

Buiteveld H., Hakvoort J. H. M. and Donze M., (1994). The optical properties of pure water. International Society of Optical Engineers (SPIE), Vol. 2258 Ocean Optics XII, 174-184.

Carder, K.L., Steward R.G., Harvey G.R. and Ortner P.B., (1989). Marine humic and fulvic acids: their effects on remote sensing of ocean chlorophyll. Limnology and Oceanography, **34**, 68-81.

Clark D.K., (1981). Phytoplankton pigment algorithms for the NIMBUS-7 CZCS. In Oceanography from Space, Gower J.F.R., ed.,(1981). Marine Science Volume 13, Proceedings of the COSPAR/SCOR/IUCRM symposium on Oceanography From Space. Plenum Press, New York, 233 Spring Street, New York, 10013.

Cleveland J.S. and Weiderman A.D., (1993). Quantifying absorption by aquatic particles: a multiple scattering correction for glass fibre filters. Limnology and Oceanography **38**(6) 1321-1327.

Dyer K. R., (1986). Coastal and eastuarine sediment dynamics. John Wiley and Sons, Chichester, Sussex, England.

Gordon H. R., (1989). Can the Lambert-beer law be applied to the diffuse attenuation coefficient of ocean water. Limnology and Oceanography **34**(8) 1389-1409.

Gordon H.R. and Morel A., (1983). Remote assessment of ocean colour for interpretation of satellite visible imagery: A review. 114pp. Springer-Verlag, New York.

Greg W. W. and Carder K. L., (1990). A simple spectral solar irradiance model for cloudless marine atmospheres. Limnology and Oceanography, **35**(8) 1657-1675.

Hall D.O. and Rao K.K., (1981). Photosynthesis, third edition. Edward Arnold (Publishers) Limited, 41 Bedford Square, London, WC1 3DQ.

Hill R. (course manager), (1983). Photochemistry: light , chemical change and life. The open university press, Walton Hall, Milton Keynes.

Holligan P. M. and Harbour D., (1977). The vertical distribution and sucession of phytoplankton in the Western English Channel in 1975 and 1976. Journal of the Marine Biological Association, UK, **57**, 1075-1093.

Holligan P.M., Aarup T., Groom S.B., (1989). The North Sea satellite colour atlas. Continental Shelf Research, **9**,665-765.

Hooker S.B., Esaias W.E., Feldman G.C., Gregg W.W., McClain C.R., (1992). An Overview of SeaWiFS and Ocean Colour. NASA Tech. Memo. 104566, Vol.1, S.B. Hooker and E.R. Firestone, eds., NASA Goddard Space Flight Centre, Greenbelt, Maryland, 24pp.

Houghton J.T., Meira Filho L.G., Callander B.A., Harris N., Kattenberg A., and Maskell K., eds. (1996). Climate Change 1995, the science of climate change. Contribution of working group 1 to the second assessment report of the intergovernmental panel on climate change. The Press Syndicate of the University of Cambridge, The Pitt Building, Trumpington Street, Cambridge, CB2 IRP.

Ikeda M. and Dobson F.W., eds., (1995). Oceanographic applications of remote sensing. CRC press, New York.

Jeffrey S.W., Mantoura R.F.C., Wright S.W., eds., (1997). Monographs on Oceanographic methodology 10: Phytoplankton pigments in oceanography. United Nations Educational, Scientific and Cultural Organisation, Place de Fontenoy, 75700 Paris.

Jerlov N., (1968). Elsevier Oceanography Series, volume 5 - Optical oceanography. Elsevier Publishing Company, 335 Jan Van Galenstraat, P.O. Box 211, Amsterdam, The Netherlands.

Kirk J.T.O., (1980). Spectral absorption properties of natural waters: contribution of the soluble and particulate fractions to light absorption in some inland waters of South Eastern Australia. Australian Journal of Marine and Freshwater Research, **31**, 287-296.

Kirk, J.T.O., (1994). Light and photosynthesis in aquatic ecosystems, second edition. Cambridge University Press, The Pitt Building, Trumpington Street, Cambridge, CB2 1RP.

Lalli C.M. and Parsons T.R., (1993). Biological oceanography: an introduction. Pergamon. Elsevier Science Ltd., The Boulevard, Langford Lane, Kidlington, Oxford, OV5 1GB, UK. ISBN 0 08 041014 6

Lalli C.M. and Parsons T.R., (1997). Biological oceanography: an introduction, second eddition. Butterworth-Heineman. Linacre House, Jordan Hill, Oxford, OX2 8DP, UK. ISBN 0 7056 33840

Latasa M., Bidigaire R.R., Ondrusek M.E., Kennicutt M.C., (1996). HPLC analysis of algal pigments: a comparison exercise among laboratories and recommendations for improved analytical performance. Marine Chemistry, 51, 315-324.

Lavender S., Westbrook A.G., Aiken J., Pilgrim D.A., (1997). The derivation of water leaving radiances during PACE. proceedings of the Third International Remote Sensing Conference, Copenhagen, Denmark.

Lavender S., Westbrook A.G., Moore G.F., Bottrell H., (1996). Plymouth Atmospheric Correction Experiment (PACE), 23rd International Remote Sensing Society Conference, Reading, UK.

McClain R. C., Arrigo K., Esaias W. E., Darzi M., Patt F. S., Evans R. H., Brown J. W., Brown C. W., Barnes R. A. and Kumar K., (1995). SeaWiFS algorithms, part 1. NASA Tech. Memo. 104566, Vol.28. Hooker S.B. and Firestone E.R., eds., NASA Goddard Space Flight Centre, Greenbelt, Maryland, 38pp., plus colour plates.

McClain C.R., Cleave M.L., Feldman G.C., Gregg W.W. and Hooker S.B., (1998). Science Quality SeaWiFS Data for Global Biosphere Research. Sea Technology, reprint, 5pp.

Mobley, C.D., (1994). Light and water; radiative transfer in natural waters, Academic Press Limited, 24-28 Oval Road, London, NW1 7DX. ISBN 0-12-502750-8.

Moore G., Aiken J., Hooker S.B. and Rees N., (1997). Remote sensing of bio-optical provinces. 24th International Remote Sensing Conference, Reading, UK.

Morel, A. and Berthon, J.-F., (1989). Surface pigments, algal biomass profiles and potential production of the euphotic layer: Relationships re-investigated in view of remote-sensing applications. Limnology and Oceanography., **34** (8), 1545-1562.

Mueller J.L. and Austin R.W., (1992). Ocean optics Protocols for SeaWiFS validation. NASA Tech. Memo. 104566, Vol. 5, Hooker S.B. and Firestone E.R., eds., NASA Goddard Space Flight Centre, Greenbelt, Maryland, 43 pp.

Mueller J.L. and Austin R.W., (1995). Ocean optics Protocols for SeaWiFS validation, Revision 1. NASA Tech. Memo. 104566, Vol. 25, Hooker S.B. and Firestone E.R., eds., NASA Goddard Space Flight Centre, Greenbelt, Maryland, 67pp.

Mueller J.L. and Trees C.C., (1997). Revised SeaWiFS Pre-launch Algorithm for the Diffuse attenuation Coefficient *K*(490). In Yeh E., Barnes R. A., Darzi M., Kumar L., Early E. A., Johnson B. C., Mueller J.L., (1997). Case studies for SeaWiFS calibration and validation, Part 4. NASA Tech. Memo. 104566, Vol. 41, Hooker S.B. and Firestone E.R., eds., NASA Goddard Space Flight Centre, Greenbelt, Maryland, 35pp.

Pilgrim D. A., (1987). Measurement of the extinction coefficient in turbid estuarine waters. Continental Shelf Research Vol. **7**, 11/12 pp 1425-1428.

Pilgrim D.A, and Aiken J., (1989). Measurement of the diffuse optical attenuation coefficient. The Hydrographic Journal, **54**, 23-27.

Pond D., Harris R., Head R., Harbour D., (1996). Environmental and nutritional factors determining seasonal variability in the fecundity and egg viability of *Calanus helgolanicus* in coastal waters off Plymouth. Marine Ecology Progress Series, **143**, 45-63.

Pope R.M. and Fry E.S., (1997). Absorption spectrum (380-700*nm*) of pure water II. Integrating cavity measurements, Applied Optics, **36**(33), pp.8710-8723.

Robins D.B., Bale A.J., Moore G.F., Rees N. W., Hooker S.B., Gallienne C.P., Westbrook A.G., Maranon E., Spooner W.H. and Laney S.R., (1996). AMT-1 Cruise Report and Preliminary Results. NASA Tech. Memo. 104566, Vol. 35, Hooker S.B. and Firestone E.R., eds., NASA Goddard Space Flight Centre, Greenbelt, Maryland, 87 pp.

Robinson I.S., (1985). Satellite oceanography, an introduction for oceanographers and remote sensing scientists. Ellis Horwood series in Marine Science. Ellis Horwood Limited, Chichester, UK.

Rowan, K.S., (1989). Photosynthetic pigments of algae, Cambridge University Press.

Sathyendranath, S., Gouveia, A.D., Shetye, S.R., Ravindran, P. and Platt, T., (1991). Biological control of surface temperature in the Arabian Sea, *Nature* (London), **349**, 54-56.

Smith R.C. and Baker K.S., (1978). Optical classification of natural waters. Limnology and Oceanography, **23**, 260-267.

Smith R.C. and Baker K.S., (1981). Optical properties of the clearest natural waters (200-800nm). Applied Optics, **20**(2), pp.177-184.

Sokal R.R. and Rohlf J., (1995). Biometry, third Ed. W.H. Freeman and Company, USA.

Suzuki K. and Handa N., (1995). Distribution of the prochloropyte *prochlorococcus* in the Central Pacific Ocean as measured by HPLC. Journal of the American Society of Limnology and Oceanography, **40**(5), 983-989.

Tassan S., (1988). The effect of dissolved 'yellow substance' on the quantitative retrieval of chlorophyll and total suspended sediment concentrations from remote measurements of water colour. International Journal of Remote Sensing, **9**(4), pp. 787-797.

Van Den Hoek C., Mann D.G. and Jahns H.M., (1995). Algae an introduction to phycology. The press syndicate of the University of Cambridge. The Pitt Building, Trumpington, Cambridge, CB2 1RP.

Vernon L.P. and Seely G.R., (1966). The chlorophylls, physical, chemical and biological properties, Academic Press, New York.

Vodacek A., Hoge F.E., Swift N.S., Yungel J.K., Peltzer E.T., Blough N.V., (1994). The use of in situ and aibourne fluorescence measurements to determine UV absorption coefficients and DOC concentrations in surface waters. Limnology and Oceanography, 40(2), 411-415.

Watson A.J., Robinson C., Robinson J.E., Williams P.J. and Fasham J.R., (1991). Spatial variability in the sink for atmospheric carbon dioxide in the North Atlantic. Nature (London) **350**:50-3.

Westbrook A.G., Pinkerton M.P., Aiken J. and Pilgrim D.A., (1999). Simulated Performance of remote sensing ocean colour algorithms during the 1996 PRIME cruise. Deep Sea Research PRIME special issue, accepted.

Westbrook A. G., Aiken J. and Pilgrim D.A., (1998). Spatial variation in the performance of algorithms for the interpretation of remotely sensed measurements of ocean colour during the first Atlantic Meridional Transect (AMT-1). Applied Optics and Optoelectronics, Proceedings of the Applied Optics Divisional Conference of The Institute of Physics, Brighton (talk, paper bound in proceedings). 6pp.

Williamson P., (1990). Oceans, carbon and climate change, an introduction to the Joint Global Ocean Flux Study (JGOFS). Scientific Committee on Oceanic Research, Halifax, Canada. ISBN 0-9694959-0-0

Wright S.W., Jeffrey S.W, Mantoura R.F.C., Llewellyn C.A., Bjornland T., Repeta D. and Welschmeyer N., (1991). Improved HPLC method for the analysis of chlorophylls and carotenoids from marine phytoplankton. Marine Ecology Progress Series, **77**, 183-196.

Yentsch C.S. and Menzel D.W., (1963). A method for the determination of phytoplankton chlorophyll and phaeophytin fluorescence. Deep Sea Research. **10**, 221-231.

Zaneveld, J.R.V., Kitchen J.C. and Mueller J.L., (1993). Vertical structure of productivity and its vertical integration as derived from remotely sensed observations. Limnology and Oceanography, 38(7), 1384-1393.

Appendices

APPENDIX 1: ACRONYMS AND SYMBOLS

ACRONYMS

AMT	Atlantic Meridianal Transect
BOFS	Biogeochemical Ocean Flux Study
PRR-600	Biospherical Instruments Inc. Profiling and Reflectance Radiometer
RRS James Clark Ross	BAS Research Vessel
BAS	British Antarctic Survey
CDOM	Coloured Dissolved Organic Material
CHORS	Centre for Hydro-Optics and Remote Sensing
CZCS	Coastal Zone Colour Scanner
CASI	Compact Airborne Spectrographic Imager
CTD-F	Conductivity Temperature and Depth with Fluorometer
DOM	Dissolved Organic Material
FWHM	Full Half Wave Maximum
HPLC	High Performance Liquid Chromatography
IR	Infra Red
IFOV	Instantaneous Field Of View
LASER	Light Amplification of Stimulated Emitted Radiation
MBA	Marine Biological Association
NASA	National and Aeronautics Space Administration
NIST	National Institute of Standards and Technology
NERC	Natural Environment Research Council
NRA	National Rivers Authority (now the Environment Agency, EA)
RRS Discovery	NERC Research vessel
PAR	Photosynthetically Available Radiation
PACE	Plymouth Atmospheric Correction Experiment
PML	Plymouth Marine Laboratory
RV Squilla	PML Research vessel
L4	Sampling station SW off Plymouth, UK
SeaWiFS	Sea Viewing Wide Field of View Sensor

snr	Signal to noise ratio
SPM	Suspended Particulate Matter
SDY	Synchronous Day of the Year
UOR	Undulating Oceanographic Recorder
UoP	University of Plymouth
USA	United States of America
UV	Ultra Violet

SYMBOLS

a	Absorption coefficient
A	Attendance
ϕ	Azimuth angle
b_b	Back-scattering coefficient
c	Beam attenuation coefficient
C	Celsius
θ_c	Critical angle
z	Depth
$£_K$	Diffuse attenuation length
$Kd(\lambda)$	Diffuse attenuation coefficient (general case) at wavelength, λ
$Kdm(\lambda)$	Diffuse attenuation coefficient at wavelength, λ, derived from sub-surface profile measurements of $Ed(\lambda, z)$
$Kdc(\lambda)$	Diffuse attenuation coefficient at wavelength, λ, derived using algorithms applied to the upwelling light field ratio at two wavelengths, i and j
$Kw(\lambda)$	Diffuse attenuation coefficient (general case) of pure water at wavelength, λ
$Ed(\lambda,z)$	Downwelling monochromatic irradiance at depth z
b_f	Forward scattering
ρ	Fresnel reflectance
Hz	Hertz
$Ed(\lambda,0+)$	Incident solar Irradiance above the sea surface

$E(\lambda)$	Irradiance
$R(i:j)$	Irradiance band ratio reflectance
$\bar{F}o(\lambda)$	Mean extraterrestrial irradiance at the outer Earth's atmosphere
m	Meter
μ	Micro (10^{-6})
θ_n	Nadir zenith angle
nm	Nanometer (10^{-9} m)
$Lwn(\lambda)$	Normalised water leaving radiance (normal to the air/sea interface)
γ	Optical depth
r	Path length
β_L	Path length amplification factor
π	Pi
n	Quantum number
L	Radiance
F	Radiant energy
Φ	Radiant flux
I	Radiant intensity
n_a	Refractive index of air
n_w	Refractive index of water
$R(\lambda)$	Reflectance at wavelength, λ
$R_{RS}(\lambda)$	Remote sensing reflectance at wavelength, λ
$Rrs(i:j)$	Remote sensing reflectance band ratio
ψ	Scattering angle
b	Scattering coefficient
s	Seconds
ω	Solid angle
ζ	Suggested distance from platform for profiling radiometer deployment
0^+	The location of a quantity an infinitesimal distance above the sea surface
0^-	The location of a quantity an infinitesimal distance below the sea surface
t	Time

$Lu(\lambda,z,\theta,\phi)$	Upwelling monochromatic radiance at depth z, from direction (θ, ϕ)
R^2	Variance
$K_L(\lambda)$	Vertically upward diffuse attenuation coefficient at wavelength, λ
v	Volts
β	Volume scattering function
$Lw(\lambda)$	Water Leaving Radiance (normal to the air/sea interface)
λ	Wavelength
θ	Zenith angle

APPENDIX 2.

PROPOSED IMPOROVEMENTS TO THE APPARATUS USED DURING THE COURSE OF THIS STUDY

There were a number of areas encountered when undertaking this programme of research that can be improved upon as a result of the experience gained.

2.1 MODIFICATIONS TO THE PRR-600

There are a number of steps that need to be taken to upgrade the PRR-600 for it to match the specifications of newer state of the art radiometers.

(i) The PRR-600 needs to be returned to the manufacturers, Biospherical Instruments Inc. for upgrading and calibration. Particularly the issue of out of band blocking of the type of filters used in this instrument needs to be addressed.

(ii) A software programme is required to interface the PRR-600 with state of the art PML calibration facilities to allow full 0.2*nm* resolution spectral analyses to be carried out.

(iii) The construction of a mating collar is required to allow the instrument to be field calibrated using the NIST/NASA developed SeaWiFS Quality Monitor (SQM). NASA have indicated that they are prepared to undertake this if the PRR-600 were to be used for future SeaWiFS calibration and validation research.

(iv) For the PRR-600 to be included in future SeaWiFS calibration and validation exercises, a tilt and roll sensor must be fitted. The specification suggested by the SeaWiFS protocols (Mueller and Austin, 1995) that all radiometer data are flagged by tilt and roll will be strictly adhered to in future as such modules are now available at nominal cost.

(v) Although the derivation of the sub-surface remote sensing reflectance, $R_{RS}(\lambda,0^-)$, has been effectively calculated here, the derivation of normalised water leaving radiance, $L_{WN}(\lambda)$, requires the incident irradiance, $Ed(\lambda,0^+)$, to be logged either on deck or just below the surface, contemporaneously with data from the underwater unit. These data are an essential aid for the quality control and analysis of in-water radiometer profiles, and must also be flagged for tilt and roll of the deployment platform. 'Deck cells' are routinely supplied by the manufacturers. A beneficial modification to the standard deck cell would be the inclusion of an above surface pressure transducer to allow the correction of the underwater unit depth sensor to the ambient atmospheric pressure. Errors of up to 0.3m are possible over

the normal range of 30mb between typical high and low pressure systems that dominate the weather in the North East Atlantic.

2.2 CHARACTERISATION OF THE UNDERWATER OPTICAL SIGNATURE OF THE VESSEL

Future work should take into account suggestions by Mueller and Austin (1995) that experimental radiometric profiling be carried out at distances incrementally closer to the deployment platform edge to examine the range at which perturbations to the sub-surface light field become apparent in the measurements. This work should be carried out for each deployment platform in both bright sunshine and overcast skies.

2.3 SOFTWARE DEVELOPMENT

PML staff have developed a comprehensive suite of programs for the processing of radiometric data collected during extensive oceanic research. While the quality of the processing may be comparable to the work undertaken in this study using the Quattro-pro spreadsheet, the efficient use of computing power and the display capabilities provided by the Interactive Data Language, IDL, programme means it is rapidly becoming the standard throughout sections of the optical oceanographic community, and hence such a program is required for the processing and display of PRR-600 data. This would include potential for the automated inter-comparison of data streams derived from different radiometers deployed simultaneously.

2.4 IMPROVED METHODOLOGY FOR BIOLOGICAL SAMPLE COLLECTION

There is scope for improvements in the collection of water samples in the following areas:

2.4.1 FILTER HOUSING RE-DESIGN

There is a requirement to re-design the 25*mm* Gelman Sciences filter housings currently in use for two reasons: (a) the knurled body of the housings cut the operators hands during extended field sampling, especially in cold waters. The use of gloves is not practical due to the small size of the housings, and other operations such as the insertion of filters; (b) the filter housings leaked occasionally due to a poor design of the o-ring seat. An alternative design is presented in figure A2.1.

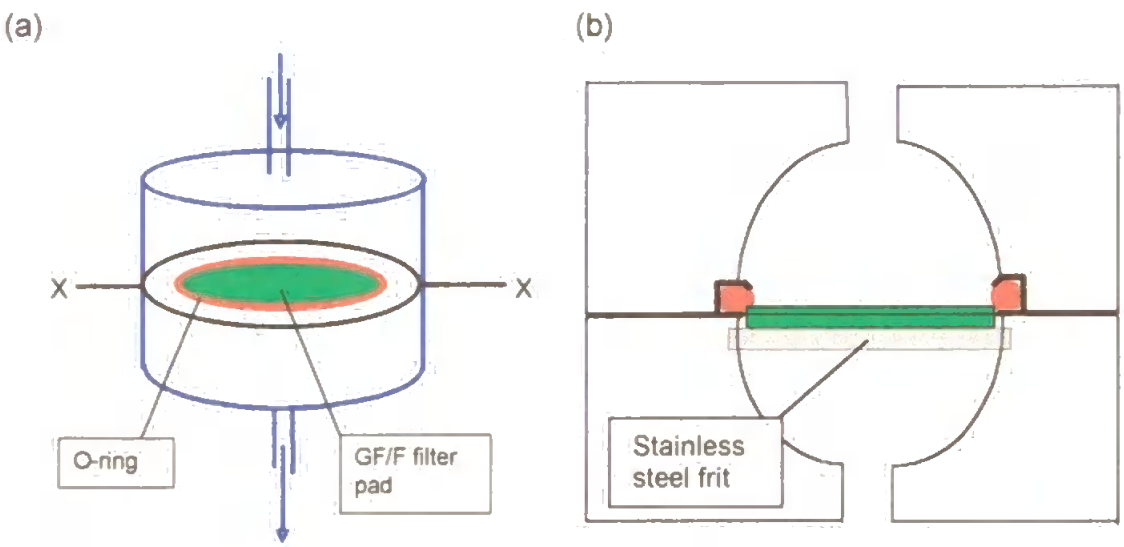

Figure A2.1. Proposed improved design for the standard Gelman Sciences 25mm filter housings, where (a) shows the general construction and (b) a detail in the vertical plane across X-X.

The main improvements that this design has over the existing system is the quality of the machining of the mating faces, and the location and design of the o-ring groove to prevent leakage. The housings would be easier to use due to increased size, with the two components clamped together by interlocking wedges located on the outer surface. This has the advantage of a small amount of travel when joining the halves together, and a greater torque being easy to apply due to the clamps being located at the maximum pitch circle diameter possible.

2.5 GENERAL FILTRATION SYSTEM IMPROVEMENTS

The system of using Nalgene bottles of various capacities, but which share the same dimension lid was very effective when it became necessary to vary the sample volume, particularly during the L4 study. There were, however, problems with leakage around the unions which require re-manufacture to an improved design. This work would will need to be one off as repeated attempts to purchase corrosion resistant components from specialist suppliers have been unsuccessful. The rebuilding of the racks is required to allow the use of 4l sample bottles for sampling in the oligotrophic zones.

2.6 DEVELOPMENT OF AN AUTOMATED WATER SAMPLING, FILTRATION AND LIQUID NITROGEN STORAGE SYSTEM

The filtration and storage of algal samples is a core component of satellite calibration and validation campaigns. These data are collected at discrete intervals 24 hours a day (where possible) depending upon the numbers and capabilities of the personnel involved. An automated system of along-track filtration would greatly simplify the sample collection procedure, allowing operators to devote time to increasing or consolidating the suite of measurements undertaken during the fieldwork. These could include ship borne HPLC analysis and/or measurements (e.g. DOM) that are best made as soon as possible after water collection due to the problems of sample degradation during storage. The system would also serve to remove errors in biological sampling by fatigued and/or inexperienced personnel, or from ships of opportunity.

Based on experience gained during this study, and a review of state of the art pump and valve technology, it is considered feasible to construct a fully automated sampling system that could store samples in liquid nitrogen. Figure A2.2 shows a schematic of how the system would operate.

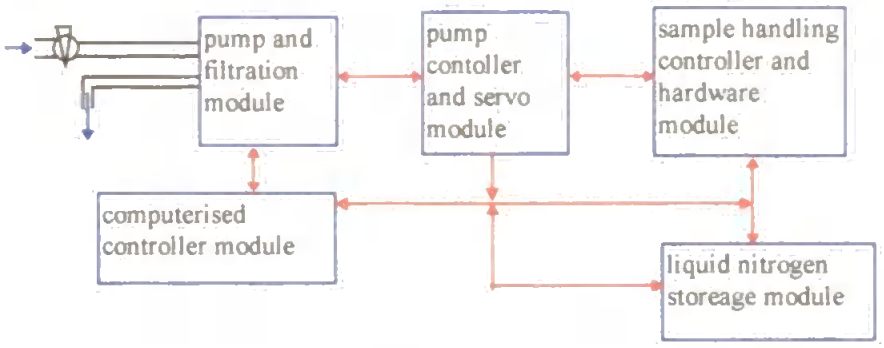

Figure A2.2 Proposed schematic of a fully automated water sampling and LN_2 portable storage facility.

The system would be modular (at least during the prototype phase of development) to minimise the dependency of component design upon the whole, and to allow easy inter-change ability and repair in the field. The sample handling components of the system would be constructed from general purpose plastics such as Teflon, with appropriate grades of stainless steel used for all fittings and machine parts.

Proposed filtration procedure:

A sample of sea water is introduced from the sampling platform uncontaminated supply into the filtration module where a filter pad is placed in the sampling chamber and retained by pneumatic pressure. By switching of the sample water and the introduction of positive pressure (or vacuum) from an air pump the sample is filtered, prior to a volume of 0.7μm filtered sea water being flushed through the reservoir to collect the residue. All valves and chambers are closed and the pneumatic pressure retaining the filter is released. The filter is transferred to the liquid nitrogen storage

module where it is sandwiched gently between two non contaminating fine teflon plates, retaining the filtered sample in a chamber above the surface of the LN_2 where the sample will quick freeze to -196°C. The entire process is servo controlled by CPU, which also logs the sample collection time. The CPU may also be interfaced with a standard DGPS to log the precise time and location from which the sample was collected. It is estimated that the construction of such a system would be time consuming due to the precision of manufacture required for the electro-mechanical components. Such a system would, however, improve the effectiveness with which underway sampling could be achieved.

2.7 FUTURE HPLC ANALYSES

The HPLC analysis was undertaken using the most sophisticated systems and techniques available at the sites where analyses were undertaken. Improvements to detectors and data collection software are on-going and should be incorporated into the analysis pathway as a matter of course. For future satellite calibration and validation work (where samples require freighting) the regulations regarding the transportation of liquid nitrogen and the interest shown by customs officials carry with them a high risk of sample thawing due to delays. Lab based HPLC analysis is acceptable when the cruise terminates in the country in which the laboratory analysis is to be carried out (or where the samples may be accompanied by scientific personnel), and where fresh supplies of LN_2 are available.

A minimum of three replicate samples should be collected unless the water budget absolutely forbids it, with representative samples being stored in separate shipping dewars in case of losses. Unpublished data collected by the author resulting from analysis of triplicate samples collected in waters off north west Scotland indicated errors in HPLC analysis using internal standard correction techniques may be as high as 20% hence triplicate analysis are preferable to ensure the reduction of these errors, particularly important in algorithm development.

In studies employing more than one HPLC, consideration should be given to increasing this level of replication to at least six for sampling sites from various biological regimes, to test the performance of the facilities when identifying different pigment assemblages.

APPENDIX 3:

PUBLICATIONS (either published or in press)

(In the interest of saving space, only sample publications and reports are included here).

Lavender S., Westbrook A.G., Aiken J. and Pilgrim D.A., (1997). The derivation of water leaving radiances during PACE. Proceedings of the third international remote sensing conference, Copenhagen, Denmark. 6pp.

Westbrook A. G., Aiken J. and Pilgrim D.A., (1998). Spatial variation in the performance of algorithms for the interpretation of remotely sensed measurements of ocean colour during the first Atlantic Meridianal Transect (AMT-1). Applied Optics and Optoelectronics, Proceedings of the Applied Optics Divisional Conference of the Institute of Physics, Brighton (talk, paper bound in proceedings).

Westbrook A.G., Pinkerton M.P., Aiken J. and Pilgrim D.A., (1999). Simulated performance of remote sensing ocean colour algorithms during the 1996 PRIME cruise. Deep Sea Research PRIME special issue, accepted.

PLYMOUTH ATMOSPHERIC CORRECTION EXPERIMENT (PACE)

S. Lavender[1], A. Westbrook[2], G. Moore[3] and H. Bottrell[4]

1. Manager, NERC Remote Sensing & GIS Unit, c/o Computing Service, University of Plymouth, Plymouth, Devon, PL4 8AA.
2. PhD Student, Institute of Marine Studies, University of Plymouth, Plymouth, Devon, PL4 8AA.
3. Researcher, Plymouth Marine Laboratory, Prospect Place, Plymouth, Devon, PL1 3DH
4. Researcher, Plymouth Marine Laboratory, Prospect Place, Plymouth, Devon, PL1 3DH

Abstract.

A description of PACE is presented, outlining the concept and measurement platforms as well as the instrumentation that was deployed in order to achieve atmospheric closure. Contemporaneous measurements of atmospheric and in-water constituents are combined with above / in-water optical data to correct / validate the optical imagery, which conforms to the NASA SeaWiFS band set, (Hooker *et al.*, 1992; Mueller *et. al.*, 1992). Preliminary results are presented, including a sample Compact Airborne Spectrographic Imager (CASI) image, to demonstrate the site suitability and variations in suspended sediment. The data will be processed to derive the following products: validation of Case 2 (sediment dominated water) atmospheric correction procedures; comparison of SeaWiFS / CASI imagery with ground truthing and atmospheric data; development / validation of remotely sensed algorithms to describe ocean colour.

Introduction.

This inter-agency project involved Natural Environment Research Council (NERC) and Environmental Agency (EA), formally the National Rivers Authority (NRA), CASI sensors mounted on light aircraft. The Meteorological Research flight (MRF), Plymouth Marine Laboratory (PML), University of Plymouth (UoP) and Andrew Wilson (RSADU Monks Wood) provided *in-situ* atmospheric / in-water measurements. Two operational periods of 2 weeks were set aside, with measurements from all platforms being achieved on 16 August 1995 when there were clear sky conditions.

The Plymouth sound area has been the focus of much attention, particularly from PML (e.g. Morris *et al.*, 1982; Holligan *et al.*, 1983) and UoP (e.g. Pilgrim and Millward, 1989; Fitzpatrick, 1990), with numerous optical and biogeochemical studies extending from the Plym and Tamar estuaries to beyond the Eddystone lighthouse (see Figure 1). With historical data as a background to the study, remote sensing applications may be assessed in conjunction to a wide variety of seabed and in-water parameters (Fitzpatrick, 1990).

Of particular importance is the weekly plankton survey that takes place at station L4, site of survey vessel 1 (SV1). This survey has continued from the original project, the Biogeochemical Ocean Flux Study (BOFS), and has been run by PML for some years. By using this site as a model for Case 1 oceanic water (in Summer) the project benefits from the depth of previous knowledge. Throughout 1995, the weekly surveys were increased to include optical characterization of ocean colour, with additional biological samples collected to undertake pigment determination by High Performance Liquid Chromatography (HPLC). This site also forms the location for a parallel but related project: the Plymouth Marine Bio-optical Data buoy (PlyMBODy), (Pinkerton, 1995).

Core scientific objective: Atmospheric closure

Atmospheric correction is a very important procedure for both aircraft and satellite sensors as only 5 to 10% of the signal originates from the water. It is not feasible to be constantly measuring all the atmospheric parameters necessary, so models have to make broad assumptions, particularly about aerosols.

The models calculate the water-leaving radiance from the signal received at the sensor, by dividing the atmosphere up into it's scattering and absorbing components. The main absorbers are ozone, water vapour and the gases, and the main scatterers are molecules and aerosols. The absorbers are quantified by their optical depths, which are calculated by multiplying the concentration by the absorption coefficient and scale height factor. Molecular scattering is quantified by the Rayleigh optical depth, which can be calculated to a reasonable accuracy using the surface pressure. The aerosol scattering and Rayleigh-aerosol interaction are much more complex and have been calculated by many different methods. All of these are based on assumptions about the aerosols, and so by measuring some of the aerosol parameters it will be possible to validate these assumptions.

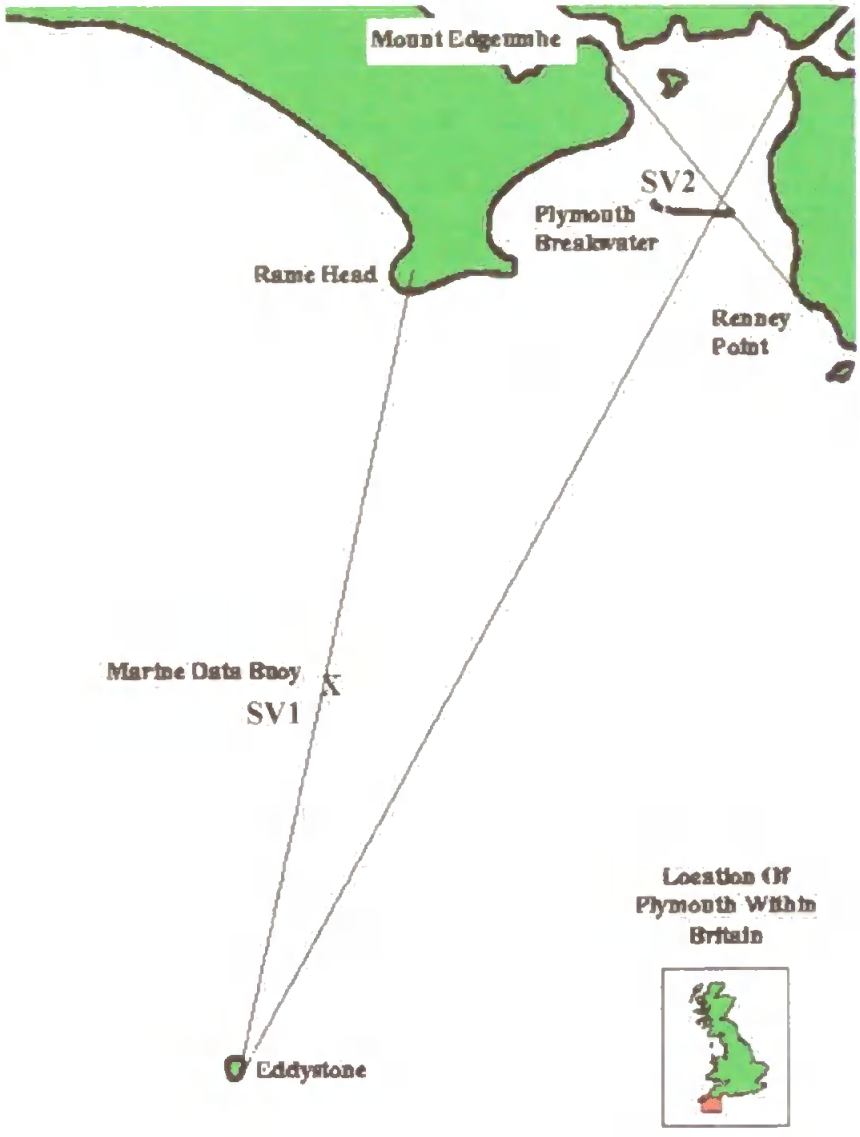

Figure 1: PACE Aircraft Flightlines and location of SV1 and SV2.

In Case 1 waters (dominated by photosynthetic pigments) where the optical properties of the water are smoothly varying and the aerosol contribution can be considered constant models have been reasonably successful. However, in the Case 2 waters (dominated by suspended sediment) which are present in the coastal zone the water parameters and aerosol properties exhibit large variations over small spatial scales. Consequently modified models need to be considered whereby the aerosol variations can be assumed and corrected for.

By flying the MRF concurrently with a multispectral aircraft radiometer and taking extensive ground truth measurements it would be possible to collect the meteorological data required for testing and modifying the atmospheric models. The vertical aerosol structure will be investigated (by flying at several heights in the boundary layer and one above) to see if the atmosphere can be treated, in models, as one or several distinct layers. The aircraft sensor will be flown at the same heights, allowing multi-height images to be corrected. This would provide a method by which the various models could be validated and compared over suspended sediment

laden waters. The measurements will also be applied to satellite data if there are suitable cloud free conditions.

Methodology.

The field campaign was split into four categories:

a) Remotely Sensed Imagery (CASI) collected by NERC and EA.

Both aircraft followed a loop of three flight lines around the Plymouth Sound area (see Figure 1), including both Case 1 and 2 water conditions. Overflights occurred at altitudes of 2000, 5000, and 10000 feet to investigate the vertical atmospheric structure. The two survey vessels were placed at the intersection of the two flightlines just inside the breakwater, and at the middle of the Eddystone flightline. This gave a validation point for each flightline

b) Meteorological measurements collected by MRF.

The MRF collected general atmospheric data, such as wind speed and humidity, plus more detailed aerosol measurements continuously over each flight line. Atmospheric parameters such as the total water content and ozone concentration will be used to determine water vapour absorption and investigate the contribution of tropospheric ozone to the total ozone optical depth. Measurements of the number densities of aerosol particles, aerosol light scattering and aerosol size spectrum can be used to calculate the aerosol scattering phase function.

The MRF was flown concurrently with a multispectral aircraft radiometer to provide measurements of the atmosphere, including information on the type, size and distribution of aerosols. This will be combined with ground truth measurements of the upwelling radiance to validate atmospheric correction models.

The survey area was mapped by a set of three flightlines, which were flown at three altitudes of 10000, 5000 and 2000 feet (same as airborne imagery).

c) Sun Photometry.

A sun photometer was deployed from a ground station at Rame Head which provided optical depths for input into the atmospheric correction scheme.

d) Shipborne radiometry and water and sampling.

Ground truthing was carried out at two sites:

SV1 (PML research vessel Squilla) surveyed the physical structure of the region, using an Undulating Oceanographic Recorder (UOR), throughout the day. The vessel was situated at station L4, some 6.5 nautical miles South-West of Plymouth between Rame Head and the Eddystone lighthouse (see Figure 1). A range of measurements were taken at this site:

a) Throughout the pre-flight survey and during the L4 station sampling, measurements of chlorophyll-*a* fluorescence, total suspended material (SPM), Optically significant Dissolved Organic Carbon (ODOC) and pigment determination by HPLC.

b) A series in-water optical profiles of downwelling and upwelling radiance, E_d and L_u, (412, 443, 488, 510, 555 & 635 nm) with temperature and depth, were collected throughout the overflight period using the Biospherical Instruments Profiling Reflectance Radiometer (PRR-600).

c) Water-leaving radiance (L_w) measurements to characterize the water surface colour and incident light field. This was achieved using two PML designed and calibrated spectrometers corrected for tilt and roll.

SV2 (PML research vessel Tamaris) was anchored at a site near the breakwater, underneath the intersection of the two Plymouth Sound flightlines (see Figure 1). This provided a Case 2 validation point and involved measurements of:

a) In-situ measurements of chlorophyll-*a* fluorescence, HPLC pigment analysis, SPM and ODOC.

b) Optical profiles using the Canadian Satlantic SeaWiFS profiling radiometer (E_d and L_u at 412, 443, 490, 510, 550 & 632 nm) during the overflights.

c) Measurements of L_w and E_d, using the NERC Equipment Pool for Field Spectroscopy (EPFS) Spectron SE-590.

Results.

The atmospheric and in-water information were position located to the airborne remote sensing imagery and atmospheric models have been adapted for use in sediment laden waters using the research that is currently being undertaken at PML. These models are based on a "bright" pixel atmospheric model (Moore *et al.*, 1996), which assumes there is water-leaving radiance in the near infrared (700 - 900 nm). This near infrared water-leaving radiance is caused by the SPM scattering the light and can also be used to derive SPM maps (Hudson *et al.*, 1994).

Figure 2 shows the variation in bottle sample derived SPM during the survey period. SV1 has consistently low SPM concentrations in keeping with the Case 1 nature of the water between Rame Head and Eddystone (Holligan and Harbour, 1977). SV2 has much higher SPM concentration, which vary tidally and describe the Case 2 situation within the Sound.

Figure 3 is a geometrically corrected CASI colour composite overlaid with a contour map of the Plymouth Sound bathymetry. The CASI image was geometrically corrected in Erdas/Imagine using Ground Control Points (GCPs) from the Geographical Information System (GIS) based contour map. The image (collected using an 80 degree Field Of View lens) had been previously roll corrected, during the EA calibration procedure, as can be seen from the undulating edge. A true colour composite has been produced from the original 14 waveband data, which displays the visible water colour.

a)

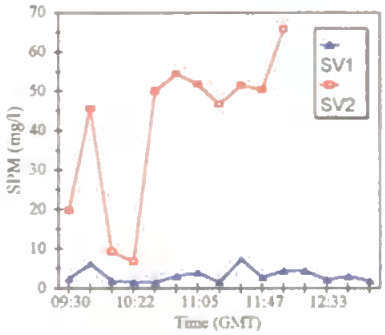

b)

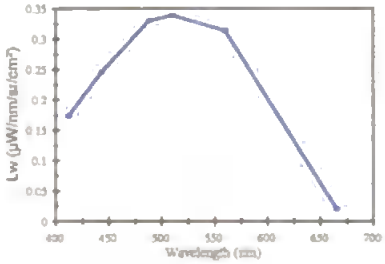

Figure 2: *In-situ* data collected during the overflight period.
a) Plot of SPM for SV1 and SV2.
b) Plot of derived water-leaving radiance for SV1.

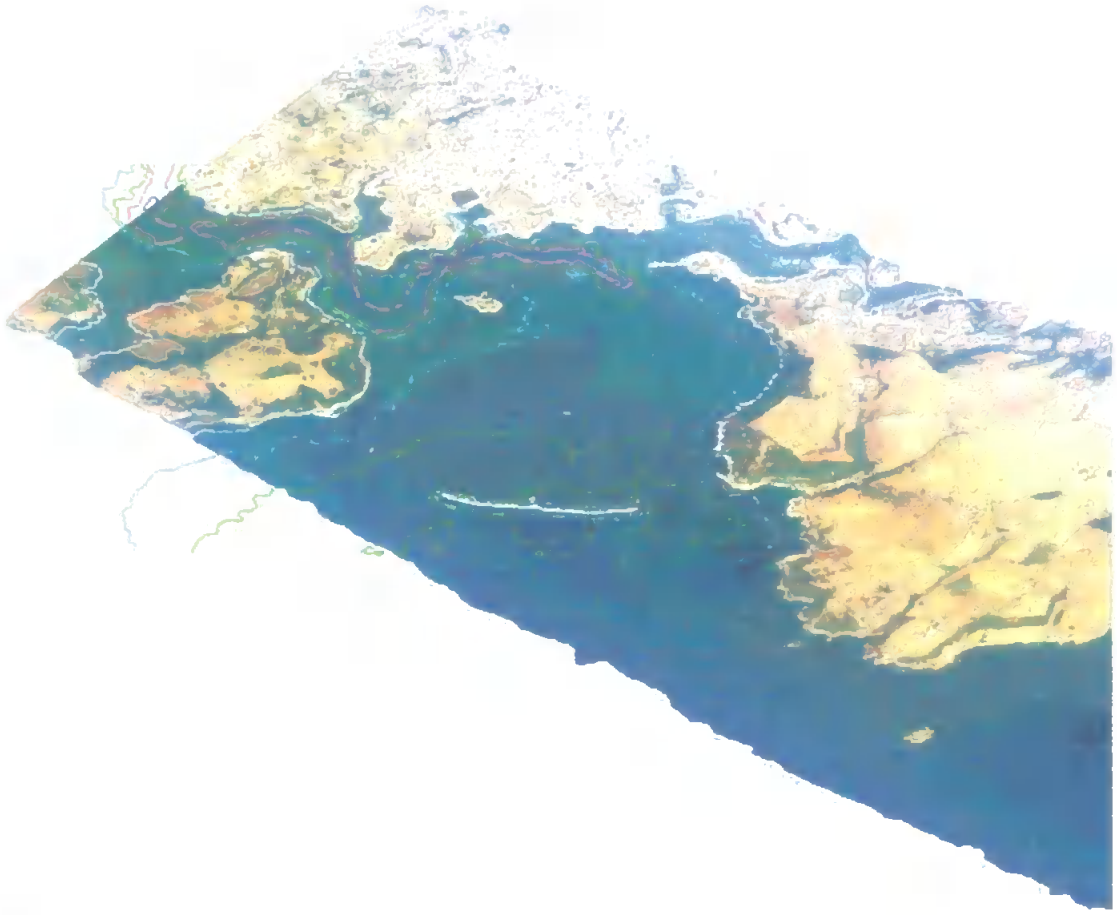

Figure 3: Geometrically corrected CASI colour composite (bands at 669, 555 and 444 nm) of Plymouth Sound overlaid with bathymetry contours, at 5 meter increments.

Discussion.

The fieldwork experiment produced numerous amounts of high quality data, which is being incorporated into a Geographical Information System (GIS). The GIS will provide a means of both storing and cross referencing the data. The ground truth measurements will allow the development of algorithms, e.g. chlorophyll and suspended sediment, from the atmospherically corrected imagery. At present PACE awaits the NERC CASI imagery, which will allow the development of the atmospheric correction procedure and validation with ground truthing data.

Future planned PACE experiments will include imagery from future ocean colour satellite such as SeaWifs, Ocean Colour Temperature Sensor (OCTS) and Medium Resolution Imaging Spectrometer (MERIS).

Acknowledgements.

PACE is grateful for the participation of the following scientists and technicians: Jim Aiken, Graham Carter, John Cook, Keith Dyer, Rod Jones, Andrew Kaye, Pete Miller, Richard Murphy, Matt Pinkerton, Marie-Claire Robinson, Karla Youngs, Andy Whittle and the crew of the survey vessels and aircraft.

References.

Pilgrim, D.A. and Millward, G.E. 1989, Variation in the diffuse optical depth of the bed of a tidal estuary. In BSA Symposium McManus, J and Elloit, M (eds.) **Developments in Estuarine and Coastal Study Techniques**, Denmark, Olsen & Olsen.

Fitzpatrick, F., 1990, **The use of Airborne Thematic Mapper data in the correlation of surface waters and sedimentary environments; Plymouth sound.** Proceedings of the NERC Symposium on Remote Sensing, 235-247.

Hooker, S.B., Esaias, W.E., Feldman, G.C., Greg, W.W. and McClain, C.R., 1992. **An overview of SeaWiFS and Ocean Colour.** NASA Tech. Memo. 104566 vol. 1, S.B. Hooker and E.R. Firestone, Eds., NASA Goddards Space Flight Centre, Greenbelt, Maryland, 24pp., plus colour plates.

Holligan, P.M. and Harbour, D.S., 1977. The vertical distribution and succession of phytoplankton in the western English channel in 1975 and 1976. **Journal of the Marine Biological Association,** 57, 1075-1093.

Holligan, P.M., Violler, M., Dupouy, C., Aiken, J., 1983. Satellite studies on the distributions of chlorophyll and dinoflagellate blooms in the western English Channel. **Continental Shelf Research**, 2, 2/3, 81-96.

Hudson, S.J., Moore, G.F., Bale, A.J., Dyer, K.R. and Aiken, J., 1994. An operational approach to determining suspended sediment distributions in the Humber estuary by airborne multi-spectral imagery. **Proceedings of the First International Airborne Remote Sensing Conference and Exhibition**, Strasbourg, Vol. III, 3, 10-20.

Moore, G.F., Aiken, J., Lavender, S.J. and Bottrell, H., 1996. The Atmospheric Correction of water colour and the quantitative retrieval of biogeochemical variables in Case 2 Waters: application to MERIS. **International Journal of Remote Sensing** (In Press).

Morris, A.W., Bale, A.J. & Howland, R.J.M., 1982. Chemical variability in the Tamar estuary, southwest England. Eastuar. **Coast. Shelf sci.**, 14, 649-661.

Mueller, J.L., and Austin, R.W., 1992. **Ocean Optics Protocols for SeaWiFS validation**. *NASA tech. Memo.. 104566, vol.5*, S.B. Hooker and E.R. Firestone, Eds., NASA Goddards Space Flight Centre, Greenbelt, Maryland, 43pp.

Pinkerton, M., Plymouth Marine Bio-Optical data Buoy (PlyMBODy), 1995. In, Moore, G.F., and S.B. Hooker, 1995: Proceedings of the first SeaWiFS Exploitation Initiative (SEI) Team Meeting. *NASA tech. memo. 104566*, S.B.Hooker and E.R. Firestone, Eds., NASA Goddard Space Flight Centre, Greenbelt, Maryland, 53pp.

Spatial variation in the performance of algorithms for the interpretation of remotely sensed measurements of ocean colour during the first Atlantic Meridional Transect (AMT-1)

A. G. Westbrook[1/2], J. Aiken[2], D.A. Pilgrim[1]

[1]Institute of Marine Studies, University of Plymouth,
Drake Circus, Plymouth, PL4 8AA
[2]Plymouth Marine Laboratory, Prospect Place,
Plymouth, PL4 3DH

Abstract. Coincident biological and radiometric data were collected during the first Atlantic Meridional Transect cruise (AMT-1) from the UK (Grimsby) to the Falklands (Port Stanley). Recently developed algorithms were applied to the data to compare the performance of retrieved in-water properties, the diffuse attenuation coefficient, *Kd*(490nm), and the surface chlorophyll-*a* concentration, with the values measured contemporaneously in situ.

1. Introduction

The Atlantic Meridional Transect (AMT) is a twice yearly survey that traverses the Atlantic Ocean from 52°N to 52°S (see figure 1) using the British Antarctic Survey (BAS) vessel *RRS James Clark Ross* (Robins *et al.*, 1996). In the North Atlantic the AMT course follows the 20° W meridian through the West African upwelling before turning South West at 10°N towards South America.

The AMT covers a wide diversity of bio-physical regimes providing a platform for the assessment of bio-optical variability, and hence the calibration and validation of satellite derived ocean colour measurements. This information is timely that the NASA SeaWiFS sensor on board the Orbital Sciences Corp. Sea Star satellite (Hooker *et al.*, 1992) has been successfully launched (August 1997) and commissioned (September 1997). The water leaving radiances detected by the remote sensor, once atmospherically corrected, are governed by established optical theory describing the physical interaction between the underwater light field and the in-water constituents distributed throughout the surface layer of the water mass (Elachi, 1987; Kirk, 1994).

The objective of algorithm development is to apply contemporaneous biological and optical measurements using in-water radiometry to develop relationships to enable the determination of accurate values of the water constituents from remotely sensed data.

2. Methods

2.1 Optical measurements

The Biospherical Instruments Inc. PRR-600 radiometer was deployed during the daily station in accordance with the SeaWiFS ocean optics protocols (Mueller and Austin, 1995; Robins *et al.*, 1996). Calibration of the instrumentation was traceable to the National Institute of Standards and Technology (NIST), Washington D.C. The PRR-600 consists of a robust pressure housing, with a 7 channel downwelling irradiance sensor, $Ed(\lambda,z)$, in the upper face, and a 7 channel upwelling radiance sensor, $Lu(\lambda,z)$, in the lower, as shown in figure 2. Also contained in the housing are temperature and pressure sensors.

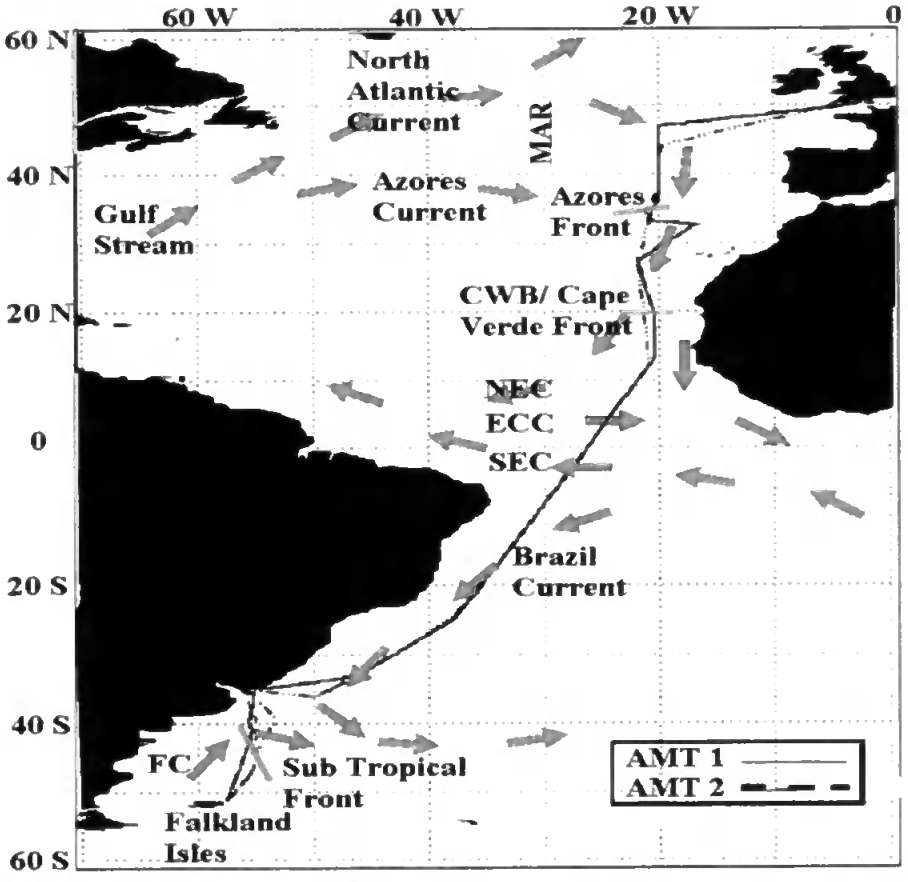

Figure 1. Map showing the track of *RRS James Clark Ross* during AMT-1 (23/09/195 to 24/10/1995), including the major regional current features. Key: NEC-North Equatorial Counter Current, ECC-Equatorial Counter Current, SEC-South Equatorial Counter Current, FC-Falklands Current, CWB-Central Water mass Boundary, MAR-Mid Atlantic Ridge.

The measured intensities for downwelling irradiance, $Ed(\lambda,z)$, and upwelling radiance, $Lu(\lambda,z)$, were used to derive attenuation coefficients, $Kd(\lambda,z)$ and $K_L(\lambda,z)$, by least squares regression analysis of, for $Kd(\lambda)$, $ln[Ed(\lambda,z)]$ where $Kd(\lambda) = d/dz[Ed(\lambda,z)]$, (Pilgrim and Aiken, 1989).

For each profile $Ed(\lambda,z)$ and $Lu(\lambda,z)$ data were extrapolated to just below the surface, (z=0$^-$), to obtain values of the remote sensing reflectance, $R_{RS}(\lambda,0^-)$, from:

$$R_{RS}(\lambda,0^-) = \frac{Lu(\lambda,0^-)}{Ed(\lambda,0^-)} \qquad (1)$$

2.2 Biological measurements

Water samples were collected from the CTD bottle rosette at all sampling stations and filtered onto Whatman GF/F filters with a nominal pore size of 0.7μm, using a positive pressure filtration system. The samples were then stored in liquid nitrogen where they remained at -196°C until analysis. The phytoplankton pigment analysis was carried out using High Performance Liquid Chromatography (HPLC) in accordance with the SeaWiFS protocols (Mueller and Austin 1995; Wright *et al.*, 1991) at the Centre for Hydro-Optics and Remote Sensing (San Diego, California).

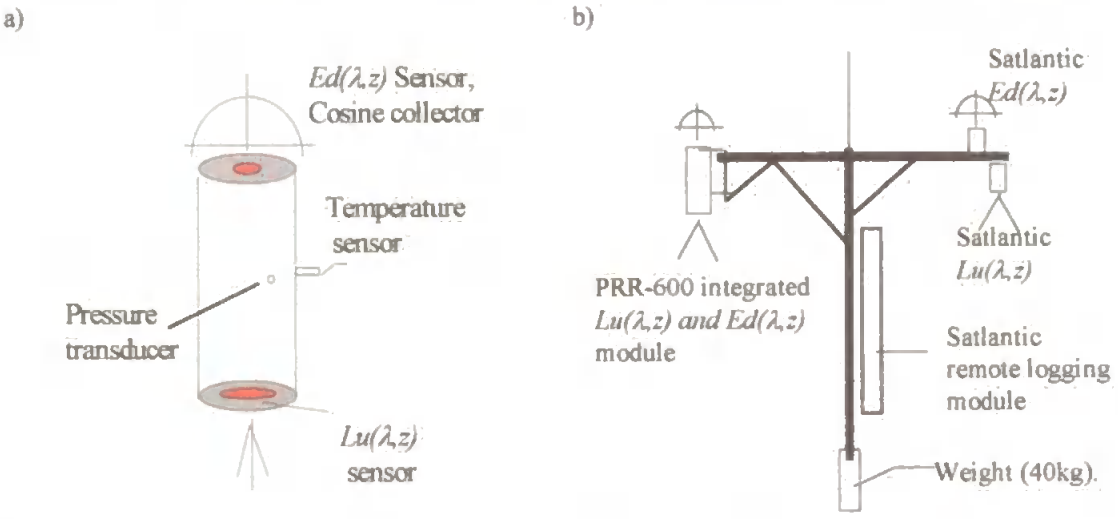

Figure 2. (a) Schematic of the Biospherical Instruments Inc. Profiling and Reflectance Radiometer (PRR-600) underwater unit. (b) The deployment system used during AMT-1 (incorporating an a additional radiometer, the Satlantic SeaWiFS profiler).

3. Algorithms

The algorithms presented are for two products: (i) the mixed layer chlorophyll-*a* concentration and (ii) the vertically downwelling diffuse attenuation coefficient, *Kd*, at 490nm.

(i) The CZCS-type SeaWiFS global pigment algorithm (Moore *et al.*,1997)

This case 1 (Gordon and Morel, 1983) chlorophyll-*a* algorithm was derived from investigations undertaken by Aiken *et al.* (1995) during SeaWiFS calibration and validation exercises, as well as the extensive use of climatological data bases:

$$\text{Chl-}a = \left[\frac{\left(R_{RS}(\lambda_1) / R_{RS}(\lambda_2)\right) - C}{C.(A_1 - A_2).\left(R_{RS}(\lambda_1) / R_{RS}(\lambda_2)\right)} \right]^{B} \qquad (2)$$

where $R_{RS}(\lambda_1)$, $R_{RS}(\lambda_2)$ are the remote sensing reflectances at 443nm and 555nm respectively and revised coefficients by Moore *et al.*(1997) are: $A_1 = 0{\cdot}764$, $A_2 = 32{\cdot}29$, $B = 0{\cdot}88$, $C = 19.63$ (from an analytical fit to an empirical relationship).

(ii) The SeaWiFS Kd(490nm) algorithm (Moore *et al.*,1997)

By developing the relationship between the remote sensing reflectance, $R_{RS}(\lambda)$ and contemporaneous measurements of the diffuse attenuation coefficient at 490nm equation 3 was derived:

$$Kd(490nm) = 0.129 \left[\frac{R_{RS}(443nm)}{R_{RS}(555nm)} \right]^{-1.337} + 0.0192 \qquad (3)$$

where 0.0192 m^{-1} is the diffuse attenuation coefficient of pure water at 490nm (Pope and Fry, unpublished, cited in Moore *et al.*, 1997).

4. Results

Figure 3 (a and b) shows a comparison of the values for chlorophyll-*a* measured and calculated from the radiometry using equation 2. (a) along-track and (b) calculated versus measured, regressions are given for all 19 data and with one 'outlier' removed. Figure 3(c and d) show values for Kd(490nm) measured and calculated from the radiometry using equation 3. (c) along track and (d) calculated versus measured, regressions are given.

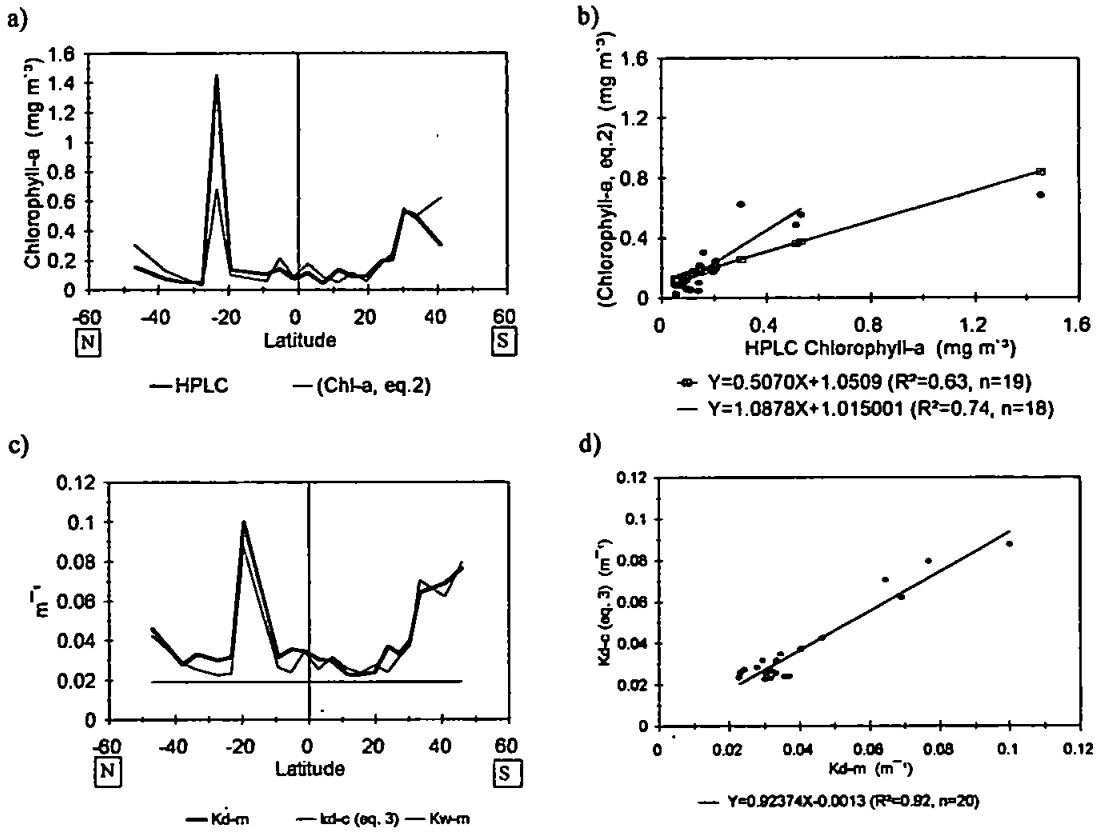

Figure 3. (a) Values of retrieved chlorophyll-*a* from the radiometry compared with the contemporaneous measurements derived by HPLC and (b) a regression analysis of these data. (c) *Kd*(490nm) retrieved from radiometry and the corresponding measured values retrieved from the downwelling irradiance sensor with (d) a regression analysis of these data.

5. Discussion and conclusions

From the results it can be seen that there is good agreement between the bio-optical measurements taken *in-situ* and values derived from the simulated satellite ocean colour data, in terms of $R_{RS}(\lambda, 0^-)$, when applied to the algorithms presented in equations 2 and 3. The calculated and measured variables match each other closely, and clearly define the biological regimes traversed during the cruise in terms of chlorophyll-*a* concentration and *Kd*(490nm) (figure 3a and 3b). The regression analysis of the retrieved and measured chlorophyll-*a* concentrations, illustrated in figure 3(c), is biased by the high value at 20°North, where the calculated value is lower. The regression is improved by removing this data point. The fraction of variance explained by regression of the *Kd*(490nm) data illustrated in figure 3(d) shows good agreement between the calculated and measured values. These algorithms are presented as an effective means of deriving these properties from SeaWiFS scenes of the Atlantic Ocean.

References

[1] Aiken, J., Moore G.F., Trees C.C., Hooker S.B. and Clark D.K., (1995). The SeaWiFS CZCS-Type pigment algorithm. NASA Tech. Memo. 104566, Vol. 29, Hooker S.B. and Firestone E.R., eds., NASA Goddard Space light Centre, Greenbelt, Maryland, 43pp.

[2] Clark D.K., (1981). Phytoplankton pigment algorithms for the NIMBUS-7 CZCS. In Oceanography from Space, J.F.R.Gower, ed., (1981). Marine Science Volume 13, Proceedings of the COSPAR/SCOR/IUCRM symposium on Oceanography From Space. Plenum Press, New York.

[3] Elachi C., (1987). Introduction to the physics and techniques of remote sensing. Wiley Series in Remote Sensing, John Wiley and Sons, New York.

[4] Gordon, H.R. and Morel A., (1983). Remote assessment of ocean colour for interpretation of satellite visible imagery: a review. Springer-Verlag, New York, 114pp.

[5] Hooker S.B., Esaias W.E., Feldman G.C., Gregg W.W. and McClain C.R., (1992). An Overview of SeaWiFS and Ocean Colour. NASA Tech. Memo. 104566, Vol.1 S.B. Hooker and E.R. Firestone, Eds., NASA Goddard Space light Centre, Greenbelt, Maryland, 24pp.

[6] Kirk, J.T.O., (1994). Light and Photosynthesis in Aquatic Ecosystems, second edition. Cambridge University Press, Cambridge.

[7] Moore G.F , Aiken J., Hooker S.B. and Rees N.W., (1997). Remote sensing of Bio-optical Provinces, Proceedings of the Remote Sensing Society, RSS 97, Reading, UK.

[8] Mueller J.L. and Austin, R.W., (1995). Ocean optics Protocols for SeaWiFS validation, Revision 1. NASA Tech. Memo. 104566, Vol.25. Hooker S.B. and Firestone E.R., Eds., NASA Goddard Space light Centre, Greenbelt, Maryland, 66pp.

[9] Pilgrim, D.A. and Aiken, J., (1989). Measurement of the optical diffuse attenuation coefficient. The Hydrographic Journal, **54**, 23-27.

[10] Robbins, D.B., Bale A.J., Moore G.F., Rees N.W., Hooker S.B., Gallienne C.P., Westbrook, A.G., E.Maranon, Spooner W.H., and Laney S.R., (1996). AMT-1 Cruise Report and Preliminary Results. NASA Tech. Memo. 104566, Vol. 35. Hooker S.B. and Firestone E.R., eds., NASA Goddard Space Flight Centre, Greenbelt, Maryland, 87 pp.

[11] Wright, S.W., Jeffrey S.W., Mantoura R.F.C., Llewellyn C.A., Bjornland T., Repeta D. and Welschmeyer N., (1991). Improved HPLC method for the analysis of chlorophylls and carotenoids from marine phytoplankton. Marine Ecology Progress Series, 77, 183-196.

SIMULATED PERFORMANCE OF REMOTE SENSING OCEAN COLOUR ALGORITHMS DURING THE 1996 PRIME CRUISE

A. G. Westbrook[1], M. H. Pinkerton[1], J.Aiken[1] and D. A. Pilgrim[2]

Marine Optics Research Group
[1]Centre for Coastal and Marine Sciences,
Plymouth Marine Laboratory, Prospect Place,
Plymouth, PL1 3DH.

[2]Institute of Marine Studies, University of Plymouth,
Drake Circus, Plymouth, PL4 8AA.

ABSTRACT

Coincident pigment and underwater radiometric data were collected during a cruise along the 20°W meridian from 60°N to 37°N in the north-eastern Atlantic Ocean as part of the Natural Environment Research Council (NERC) thematic programme: Plankton Reactivity in the Marine Environment (PRIME). These data were used to simulate the retrieval of two bio-optical variables from remotely-sensed measurements of ocean colour (for example by the NASA Sea-viewing Wide Field-of-View Sensor, SeaWiFS), using two-band semi-empirical algorithms. The variables considered were the diffuse attenuation coefficient at 490 nm, [K_d(490), units: m^{-1}] and the phytoplankton pigment concentration expressed as optically-weighted chlorophyll-*a* concentration [C_a, units: mg m^{-3}]. It was found that there was good agreement between the measured and the retrieved bio-optical values. Algorithms based on the PRIME data were generated to compare the performance of local algorithms (algorithms which apply to a restricted area and/or season) with global algorithms (algorithms developed on data from a wide variety of water masses). The use of local algorithms improved the average accuracy, but not the precision, of the retrievals: errors were still ±36% (K_d) and ±117% (C_a) using local algorithms.

INTRODUCTION

The Coastal Zone Color Scanner (CZCS) which operated from the NIMBUS 7 satellite between 1978-1986 produced unprecedented basin-scale information on a variety of biological processes, including the development and spatial structure of algal blooms (Esaias *et al.*, 1986; Yoder *et al.*, 1988; Feldman *et al.*, 1989). Based on this success, a number of international space agencies are developing ocean colour observation capabilities. For example the European Space Agency (Europe) are developing the Medium Resolution Imaging Spectrometer (MERIS) and NASA have been operating SeaWiFS since September 1997 and will soon (1999) launch the Moderate Resolution Imaging Spectrometer (MODIS). These sensors have more spectral bands, higher radiometric resolution and better calibration stability than CZCS. Improved bio-optical algorithms must be developed for these new sensors if they are to deliver accurate estimates of bio-optical variables for use in the wider oceanographic research community.

This study considered a number of state-of-the-art algorithms, including those currently used operationally by SeaWiFS. *Two-band band-ratio algorithms* use the ratio of

remote-sensing reflectance just above the sea surface at two wavebands. The algorithms are referred to as *semi-empirical* because the form of the equation is based on the physics of the relationship between the bio-optical variable and the band-ratio, but the constants in the equation are produced by fitting to real data. There are no universally "correct" constants because the relative abundances of various phytoplankton pigments vary significantly with region and season (Aiken *et al.*, 1995). Different pigments have different absorption spectra and consequently the pigment composition affects the relationship between the colour of the ocean and the concentration of phytoplankton in the water. If the empirical constants have been derived from data measured in a variety of oceanic areas over a number of seasons, a *global algorithm* is produced which may be applied universally. Global algorithms will tend to perform well in areas where the composition of phytoplankton pigments is similar to the data used to generate the algorithm, and poorly otherwise. If the algorithm has been generated from data measured only in a specific location and/or at a specific time of the year, the algorithm is called a *local algorithm* and is strictly only applicable to the regions/seasons where the original data were measured. Local algorithms, applicable to the north-eastern Atlantic Ocean in late Spring, were developed using the PRIME data in this study, and these are compared to the equivalent global algorithms.

The two major bio-optical variables derived from ocean colour data are the near-surface chlorophyll-*a* concentration (C_a, units: mg m^{-3}) and the diffuse attenuation coefficient at 490 nm, $K_d(490)$, units: m^{-1}. The former parameter leads to maps of global phytoplankton distribution which can be used as data inputs for models to estimate the role of the oceans in the regulation of atmospheric CO_2 (Aiken *et al.*, 1992), a greenhouse gas. The latter parameter describes the biologically-mediated absorption of light within the surface layers of the sea: a high attenuation coefficient means that light is absorbed rapidly with depth as a result of material in the water. This process can cause significant heating and affect the physical structure of the upper water-column (Sathyendranath *et al.*, 1991). Research by Zaneveld *et al.* (1993) indicates that $K_d(490)$ can also be used to estimate the euphotic zone depth, the depth where the downwelling photosynthetically available radiation (PAR) between 400-700 nm has fallen to 1% of its surface value (Morel and Berthon, 1989). Algorithms for both C_a and $K_d(490)$ have been considered in this study.

The *RRS Discovery* research cruise from Iceland to 37°N 20°W during May and June 1996 was part of the NERC thematic programme Plankton Reactivity in the Marine Environment (PRIME) which was concerned with the role of plankton in the food chain and associated biogeochemical cycling. The cruise was divided into three parts; firstly, a process study on a cold core eddy south of Iceland; secondly, a survey of the physical and biological structure of the waters along the 20°W meridian from 60°N to 37°N; and thirdly, an eight day Lagrangian time-series process survey at 37°N 20°W. The work described here was carried out during the second and third parts of the cruise (Fig. 1).

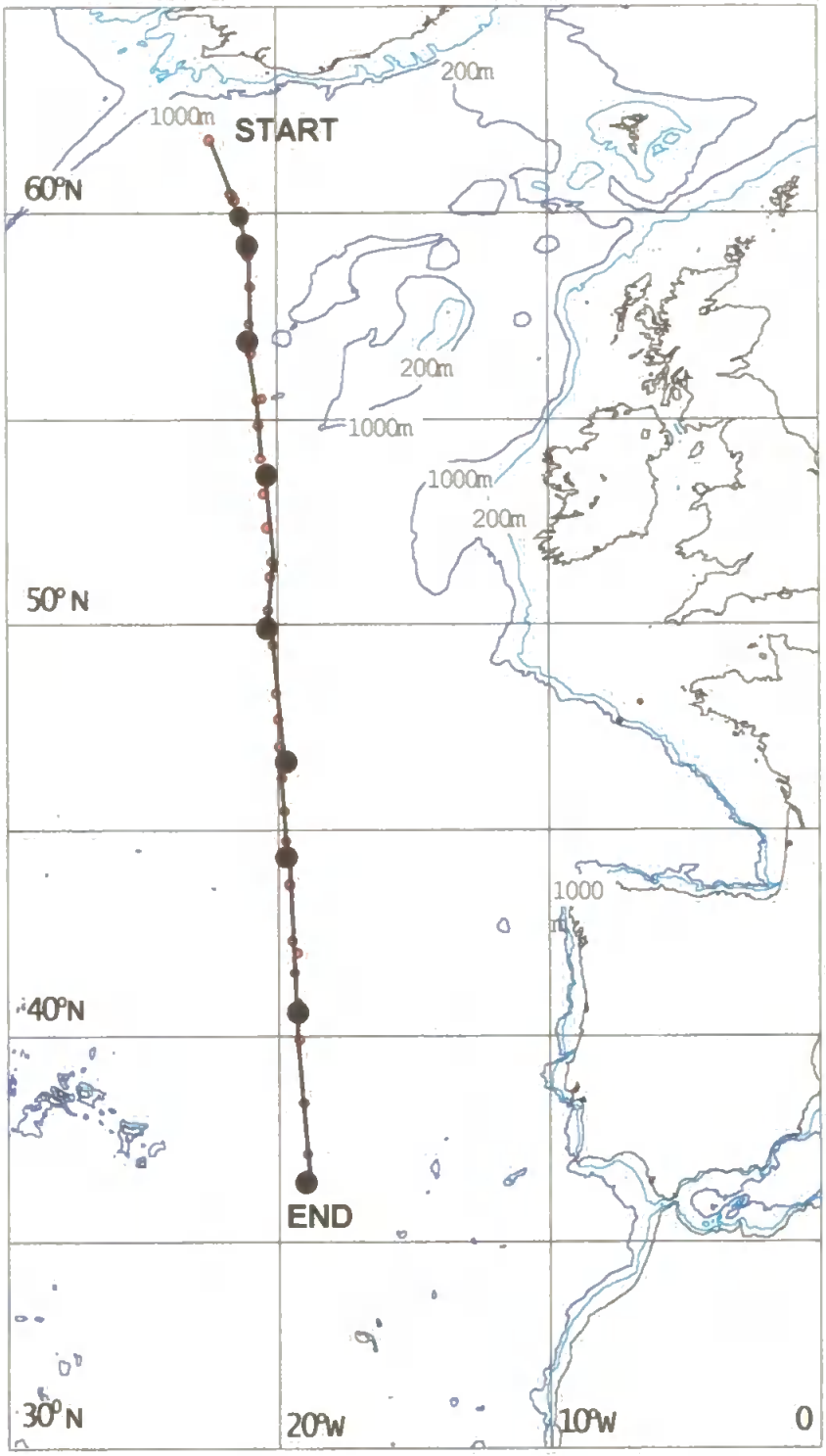

Figure 1. *RRS Discovery* track during the second part of the PRIME cruise; July 2 to July 21 1996. Marked on the chart are the positions of the CTD casts and the optical profiling stations.

METHODS

The general biophysical structure of the water column was characterised by a total of 21 conductivity, temperature, depth and *in situ* chlorophyll-*a* fluorescence (CTDF) casts spaced regularly over the transect (Fig. 1). The underwater light field (profiled downwelling irradiance and upwelling radiance in seven spectral bands) was measured simultaneously with phytoplankton pigment concentrations at 13 bio-optical stations. A mixture of new and existing bio-optical algorithms for C_a and $K_d(490)$ were applied to the optical measurements to investigate how well the bio-optical algorithms would perform with SeaWiFS data. SeaWiFS became operational in September 1997, so no remotely-sensed ocean colour measurements exist for the PRIME study during the period of the cruise and it is not possible to test the retrieval directly.

Phytoplankton pigment measurements

At all bio-optical stations, water samples from typically 12 depths were collected using the CTD bottle rosette. The samples were filtered through Whatman GF/F filters, using a positive pressure filtration system, and stored in liquid nitrogen until analysis at Plymouth Marine Laboratory (PML) using High Performance Liquid Chromatography (HPLC) in accordance with the methodology of Wright *et al.* (1991). The pigment concentrations were optically weighted (Gordon and Clark, 1980) to account for the greater contribution to the optical signal received at the satellite by phytoplankton near the surface. C_a is calculated by optically weighting the total chlorophyll-a concentration produced by summing the monovinyl and divinyl forms.

Optical measurements

Downwelling irradiance and upwelling radiance in seven 10 nm wide bands between 407 nm and 675 nm were measured by profiling a high-precision radiometer through the water column to 100 m. The radiometer used was a Profiling and Reflectance Radiometer (PRR-600) manufactured by Biospherical Instruments (Fig. 2). The optical measurements conformed closely to the SeaWiFS project calibration and validation protocols (Mueller and Austin, 1995). The radiometer was calibrated before and after the cruise using calibration standards traceable to the National Institute of Standards and Technology (NIST), Washington D.C.; the uncertainty was estimated to be less than 5% absolute.

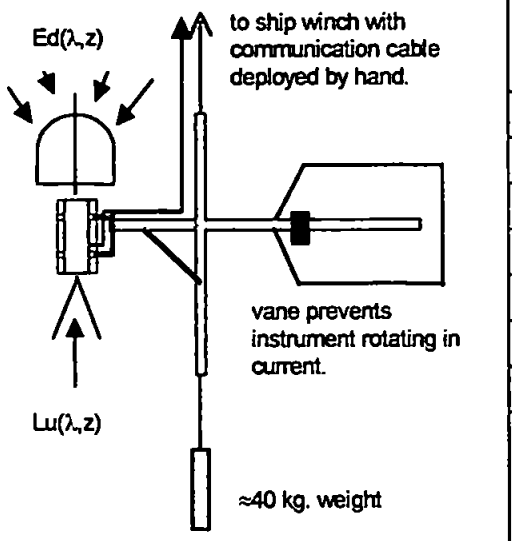

SeaWiFS bands (nm)	PRR600 Bands (nm) Lu(λ,z) and Ed(λ,z)
402 - 422	407 - 417
433 - 453	438 - 448
480 - 500	485 - 495
500 - 520	505 - 515
545 - 565	555 - 565
660 - 680	665 - 675
745 - 785	—
845 - 885	—

Figure 2. The Biospherical Instruments Profiling and Reflectance Radiometer, PRR 600, with spectral bands compared to the NASA SeaWiFS.

Downwelling irradiance at wavelength λ (nm) and depth z (m) is denoted as $E_d(\lambda,z)$ with units: $\mu W\ cm^{-2}\ nm^{-1}$; upwelling radiance is similarly denoted as $L_u(\lambda,z)$ with units: $\mu W\ cm^{-2}\ nm^{-1}\ sr^{-1}$. The diffuse attenuation coefficient is defined as: $K_d(\lambda)=dE_d(\lambda)/dz$. The mean value of $K_d(490)$ for the surface 30 m and the mean downwelling irradiances just below the surface, $E_d(\lambda,0^-)$, were calculated by least squares regression (Pilgrim and Aiken, 1989). A similar analysis gave the upwelling radiance just below the surface, denoted as $L_u(\lambda,0^-)$. The remote-sensing reflectances just below the sea surface, $R_{rs}(\lambda,0^-)$, were calculated as Equation 1:

$$R_{rs}(\lambda,0^-)=\frac{L_u(\lambda,0^-)}{E_d(\lambda,0^-)} \qquad \text{(Equation 1)}$$

The propagation of remote-sensing reflectances through the water surface, to give the remote-sensing reflectance just above the sea surface $[R_{rs}(\lambda,0^+)]$, was taken to be spectrally independent. The SeaWiFS algorithms were tested using ratios of $R_{rs}(\lambda,0^-)$ by application of Equation 2, which also defines $R(\lambda_1:\lambda_2)$:

$$R(\lambda_1:\lambda_2)=\frac{R_{rs}(\lambda_1,0^+)}{R_{rs}(\lambda_2,0^+)}\approx\frac{R_{rs}(\lambda_1,0^-)}{R_{rs}(\lambda_2,0^-)} \qquad \text{(Equation 2)}$$

Where the algorithms use bands different to those measured by the PRR, a correction was applied to reconcile the two, assuming that the underwater light field is spectrally smooth.

Algorithms for $K_d(490)$

The form of the band-ratio algorithm used for the retrieval of $K_d(490)$ from remotely sensed ocean colour imagery has remained unchanged since the CZCS mission (Austin and Petzold, 1981) and is given as Equation 3:

$$K_d(490) = a_w(490) + A\left[R(443{:}555)\right]^B \qquad \text{(Equation 3)}$$

where $a_w(490)$ is the absorption coefficient (units: m^{-1}) of pure water at 490 nm, and A and B are fitted constants. The value of $a_w(490)$ used initially was measured by Smith and Baker (1978) but has been revised following advances in the measurement of the optical properties of pure water (Buiteveld *et al.*, 1994). The empirical constants derived from field measurements have changed as more data have been collected and as instrument technology has improved. This study considered three $K_d(490)$ algorithms (Table 1): the SeaWiFS pre-launch algorithm; the operational SeaWiFS global algorithm; and a PRIME local algorithm generated by least-squares regression in log-space from the 13 PRIME data points.

Table 1. Diffuse attenuation coefficient algorithms used in this study.

$K_d(490)$ algorithm	Reference	Constants		
		$a_w(490)$ [m^{-1}]	A	B
SeaWiFS pre-launch	Mueller and Trees (1995)	0.022	0.127	-1.403
SeaWiFS global	Moore *et al.* (1997)	0.0181	0.129	-1.337
PRIME local	derived in this paper	0.0181	0.135	-1.730

Algorithms for C_a

A variety of forms of algorithm have been used to estimate C_a and three formulations were considered: logarithmic, hyperbolic and polynomial (Table 2).

As with the $K_d(490)$ algorithms, the coefficients were obtained empirically by fitting to data from field measurements. The *global* constants represent the state-of-the-art in semi-empirical band-ratio pigment algorithms. The *local* constants were derived from the 13 measurements made during the PRIME cruise by using a quasi-Newton optimisation routine to minimise the mean-square retrieval error. With only 13 optical stations, it was not possible to divide the data into different areas where the phytoplankton populations or water structure may have been different and the cruise is considered as a whole.

Table 2. Pigment algorithms used in this study.

Pigment algorithm	Formulation	Constants		
			Global	Local
CZCS algorithm after Clark (1981)	*Logarithmic* $C_a = A[R(443{:}550)]^B$	*A*	1.13/π	1.80
		B	-1.71	-2.04
SeaWiFS global CZCS-type algorithm Moore *et al.* (1997)	*Hyperbolic* $C_a = \left[\frac{R(443{:}555) - A}{B.R(443{:}555)}\right]^C$	*A*	19.63	-21.86
		B	-17.29	21.03
		C	0.880	1.706
NASA post-launch SeaWiFS algorithm	*Polynomial* $C_a = A + 10\text{^}(B + Cx + Dx^2 + Ex^3)$ where: $x = \log_{10}\left[R(490{:}555)\frac{F_0(490)}{F_0(555)}\right]$ and: $\frac{F_0(490)}{F_0(555)} = \frac{193.6}{185.9}$	*A*	-0.040	0.0283
		B	0.341	0.173
		C	-3.001	-0.841
		D	2.811	-5.203
		E	-2.041	4.545

* $F_0(\lambda)$ is defined as the mean extra-terrestrial solar irradiance, in $\mu Wcm^{-2}nm^{-1}$, (Neckel and Labs, 1984).

RESULTS AND DISCUSSION

The contoured CTD-F data (Fig. 3) shows the biophysical structure of the water column. The physical structure varied from a weak thermocline at the north end to a shallow mixed surface layer and more pronounced thermocline at the southern end.

The PRIME cruise track crossed a frontal feature at latitude 50°N, as observed in previous studies (Pollard and Pu, 1985) with the different water structures on either side probably resulting from the effect of an eddy on a single water mass (Kraus and Kase, 1984). This feature is considered further by Wade and Heywood (1999). The surface phytoplankton concentrations declined significantly away from the feature on both sides, suggesting that nutrients were being brought into the surface layer adjacent to the front, possibly as a result of divergence. To the north, the phytoplankton maximum was restricted to the surface mixed layer, while south of the front the phytoplankton formed a sub-surface maximum at 60 m. Fig. 4 shows the variation of $K_d(490)$ and C_a along the cruise track and emphasizes the influence of the frontal region at 50°N. The cluster of points at 37°N shows the relative stability of the measurements made throughout the Lagrangian survey; C_a was stable at about 0.08 mg m^{-3}, with a standard deviation of only 0.04 mg m^{-3} compared to 0.38 mg m^{-3} for the cruise as a whole; $K_d(490)$ was approximately 0.026 m^{-1}, with a standard deviation of only 0.002 m^{-1} compared to 0.051 m^{-1} for the whole cruise.

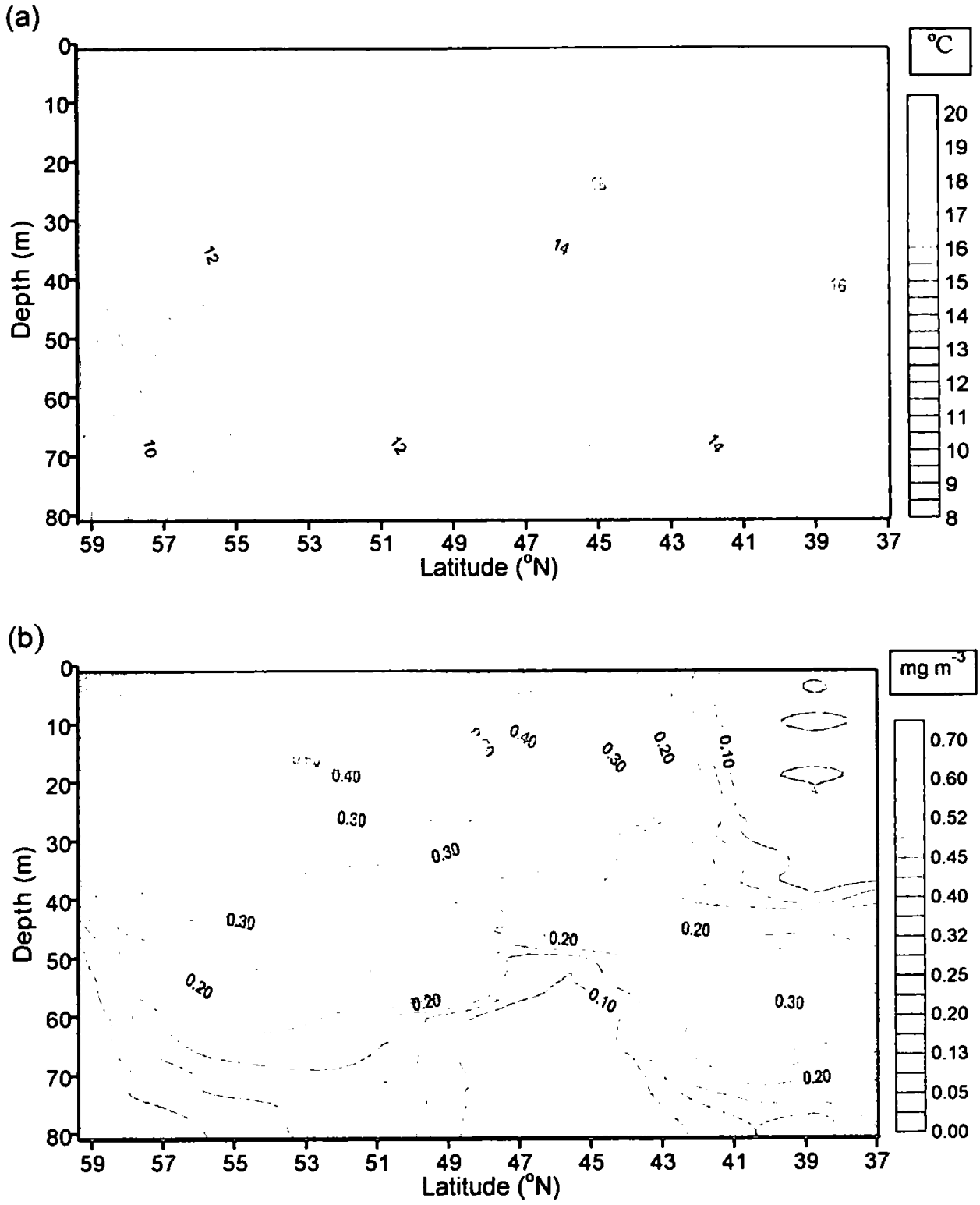

Figure 3. (a) Temperature and (b) Chlorophyll-*a* fluorescence from the CTDF casts during the PRIME transect.

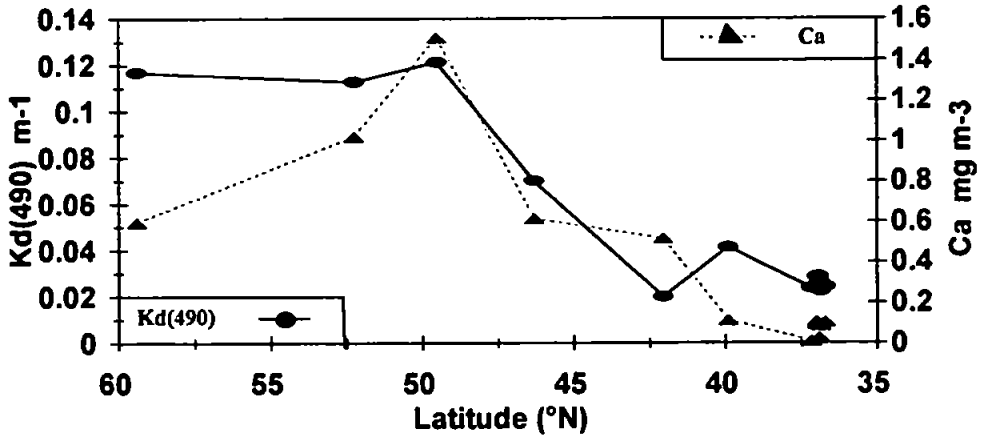

Figure 4. Measured $K_d(490)$ and C_a during the PRIME cruise.

Pigment composition

The pigments in this investigation were grouped as chlorophyll-*a*, chlorophyll-*b*, chlorophyll-*c*, photosynthetic carotenoids and photoprotective carotenoids, the concentrations of which are denoted as: C_a, C_b, C_c, C_{PS} and C_{PP}, respectively (Aiken *et al.*, 1995). Total pigment concentration (C_{TP}) was calculated as $C_a+C_b+C_c+C_{PS}+C_{PP}$ and the ratio of the concentration of each pigment group to C_{TP} was calculated (Table 3).

Table 3. Ratios of the concentrations of pigment groups to total pigment concentration.

	$\frac{C_a}{C_{TP}}$	$\frac{C_b}{C_{TP}}$	$\frac{C_c}{C_{TP}}$	$\frac{C_{PS}}{C_{TP}}$	$\frac{C_{PP}}{C_{TP}}$	$\frac{C_{PS}+C_{PP}}{C_a}$
PRIME mean	0.304	0.025	0.124	0.312	0.171	1.503
Global maximum*	0.544	0.085	0.154	0.377	0.249	1.129
Global mean*	0.475	0.042	0.077	0.276	0.128	0.814
Global minimum*	0.367	0.006	0.020	0.186	0.043	0.522

* Values from the study by Aiken *et al.* (1995). These were used to constrain the SeaWiFS global $K_d(490)$ algorithm and the SeaWiFS global CZCS-type phytoplankton pigment algorithm (both: Moore *et al.* 1997).

The pigment compositions generally lie within the global maximum and minimum values reported in Aiken *et al.* (1995) and consequently the global algorithms of Moore *et al.* (1997) should perform relatively well. The ratio of total carotenoid concentration to chlorophyll-*a* concentration tends to be high, with the mean lying above the global

maximum. This would lead to a lower $R(443:555)$ than expected (Aiken *et al.*, 1995) and hence cause algorithms to over estimate $K_d(490)$ and C_a.

Performance of Algorithms for $K_d(490)$

All three algorithms display the form of the relationship between $R(443:555)$ and $K_d(490)$ well. The relationship between the measured values and the estimates from the different algorithms are compared in Fig. 5 and summarised in Table 4.

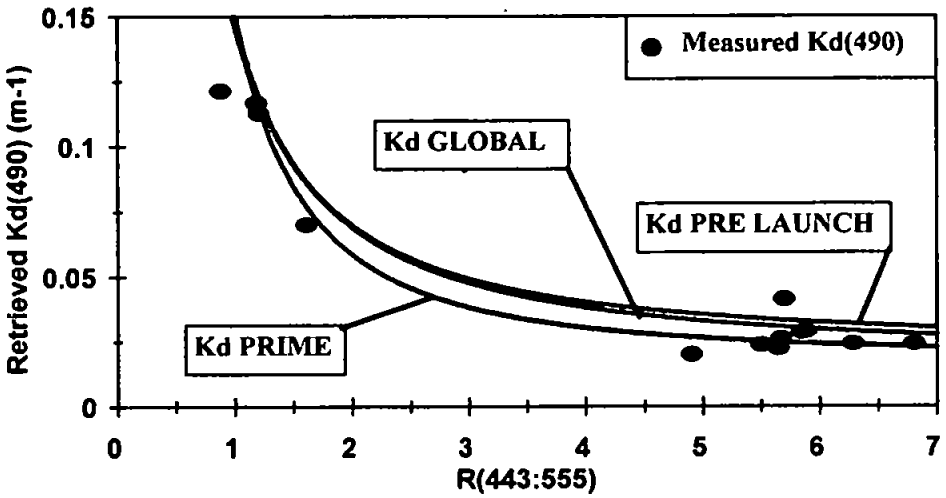

Figure 5. Comparison of measured $K_d(490)$ and retrieved $K_d(490)$ for the algorithms given in Table 1.

Table 4. $K_d(490)$ algorithm performance.

$K_d(490)$ algorithm	$\text{Error} = 100\left[\frac{\text{Retrieved } K_d(490) - \text{Measured } K_d(490)}{\text{Measured } K_d(490)}\right]$			
	Minimum (%)	Mean (%)	Maximum (%)	Standard deviation (%)
SeaWiFS pre-launch (Mueller and Trees, 1995)	-20	+26	+78	24
SeaWiFS global (Moore *et al.*, 1997)	-26	+19	+67	23
PRIME local (this work)	-40	+2.7	+54	23

Both global algorithms for $K_d(490)$ performed relatively well on average (93% of the variance in $K_d(490)$ over the cruise was explained by both the SeaWiFS pre-launch and

SeaWiFS global algorithms) but there was still significant scatter. The magnitude of the scatter is very similar to that observed in previous studies: 90.1% of the variance was explained in the study by Austin and Petzold (1981) and 90% of the variance was explained in the work by Mueller and Trees (1997). The global algorithms tended to over-estimate $K_d(490)$ over the cruise, possibly due to an increasing proportion of carotenoids relative to chlorophyll in the pigment assemblage to the south of the front, giving lower values for the band-ratio than expected. In the relatively clear waters at 37°N, where $K_d(490)$ is low and $R(443:555)$ is high, the algorithms gave estimates of $K_d(490)$ which tended towards the absorption coefficient of pure water at 490 nm.

The local algorithm performed well on average as the same data set were used for derivation and testing. However, the standard deviation of the error is the same as the global algorithms (about 23%), and only 90% of the variance in $K_d(490)$ was explained. This imprecision is either due to random measurement error or actual variability in the relationship between $R(443:555)$ and $K_d(490)$ over relatively small space and time scales. As optical measurements during PRIME conformed closely to SeaWiFS protocols (Mueller and Austin, 1995), measurement error is estimated to be less than 10%: 5% calibration error and about 5% deployment error (for example, due to instrument self-shading and shadowing by the ship). Assuming normally-distributed errors, there is a 95% chance that the true $K_d(490)$ lies within 46% of the retrieved value (twice the standard deviation) and the error due to the algorithms themselves is estimated to be about ±36%.

In summary, estimates of $K_d(490)$ over the north-eastern Atlantic may be obtained which should be accurate on average, but imprecise. The average accuracy of the estimates could be improved from about 20% to near zero using a local algorithm and a more extensive data set, but random errors of ±36% could remain. The value of such data was dependent on the application and the sensitivity of optical and biological oceanographic models to $K_d(490)$ must be considered carefully when inputs derived from ocean colour remote sensing were used. Different algorithm formulations will be required to improve the precision of the estimates; such advanced algorithms are under consideration.

Performance of Algorithms for C_a

All the algorithms display the general form of the relationship between ocean colour and the concentration of phytoplankton in the water, i.e. a high $R(443:555)$ when C_a is low, and vice versa (Fig. 6). Table 5 indicates that there would be good general agreement between near-surface chlorophyll-*a* concentration measured *in-situ* by HPLC, and an estimate obtained from a well calibrated ocean colour sensor in space using any of the algorithms described here. The percentage errors shown in Table 5 should be considered in the context that the ambitious goal of the SeaWiFS mission was to obtain estimates of pigment concentration from space to ±35% (Hooker *et al.*, 1992). The low pigment concentrations sampled during the southern part of the cruise meant that small errors in C_a equated to large percentage errors and drive the poor retrievals obtained using the Clark, (1981) and Moore *et al.*, (1997) algorithms.

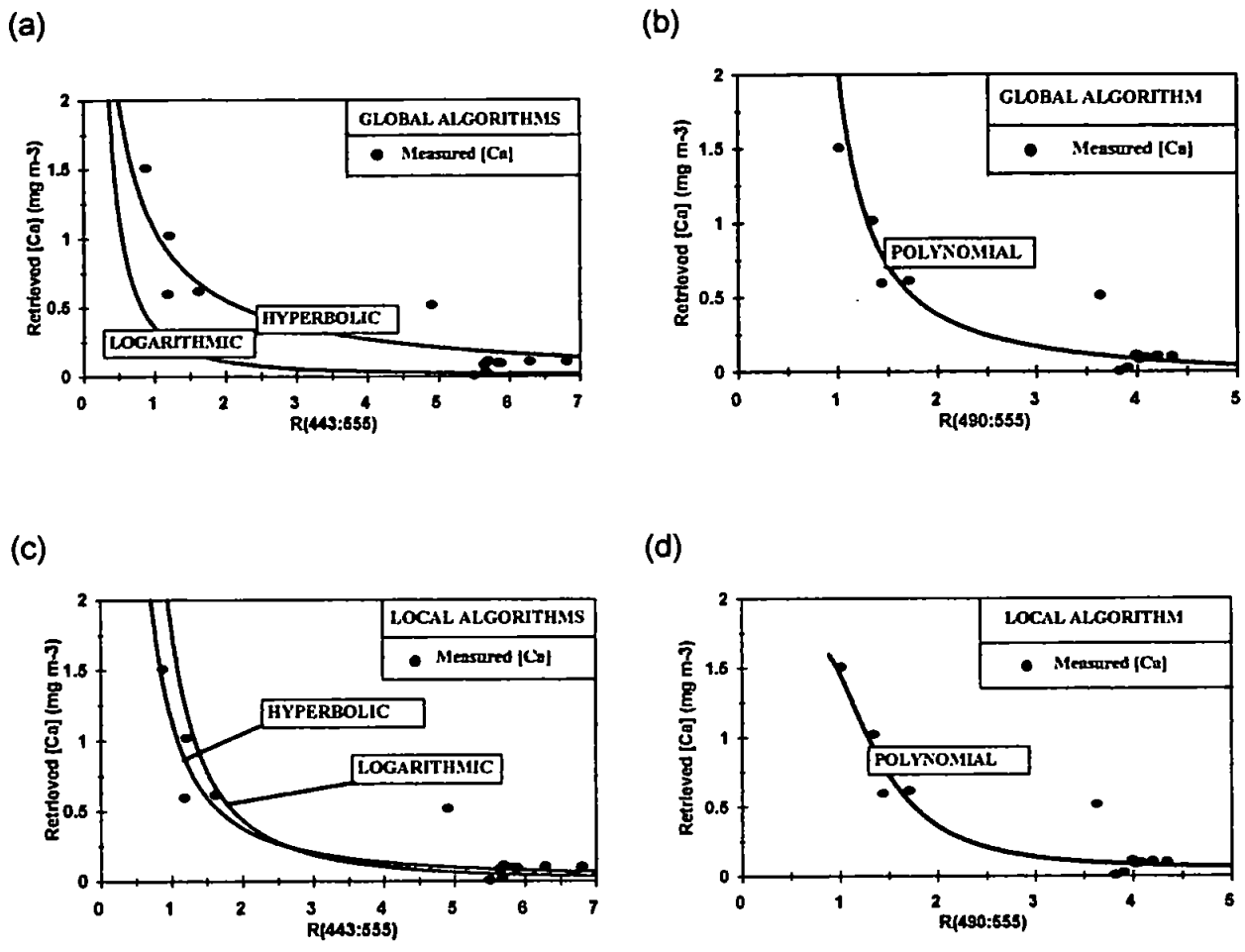

Figure 6. Comparison of measured C_a and retrieved C_a for the algorithms given in Table 2: (a) Global logarithmic and hyperbolic algorithms; (b) Global polynomial algorithm; (c) Local logarithmic and hyperbolic algorithms; (d) Local polynomial algorithm.

Data in figure 6, and the accompanying error analysis summarised in table 5, show the NASA post-launch polynomial algorithm performed best, explaining 90% of the variance in C_a. The SeaWiFS CZCS-type hyperbolic algorithm (Moore *et al.*, 1997) performed well at higher pigment concentrations (0.5-1.5 mg m^{-3}) but overestimated at low concentrations (less than 0.5 mg m^{-3}); the algorithm explained 88% of the variance. The simple logarithmic form developed for CZCS (Clark, 1981) underestimated pigment at all concentrations but still explained 89% of the variance. The proportion of the variance in pigment concentration explained by these band-ratio algorithms is very similar to values reported by previous studies: the chlorophyll algorithm of Clark (1981) explained 90.8% of the variance and the R(443:555) algorithm of Moore *et al.* (1997) explained 87.5% of the variance in chlorophyll concentration (reported in Aiken *et al.*, 1995).

Table 5. Phytoplankton pigment algorithm performance.

Algorithm type	C_a algorithm	% Error = $100\left[\frac{\text{Retrieved } C_a - \text{Measured } C_a}{\text{Measured } C_a}\right]$			
		Minimum (%)	Mean (%)	Maximum (%)	Standard deviation (%)
Global	Clark (1981) logarithmic	-94	-71	-20	19
	Moore *et al.* (1997) hyperbolic	-59	+76	+520	148
	NASA polynomial	-80	-3.1	+190	67
Local	PRIME logarithmic	-82	+5.5	+135	70
	PRIME hyperbolic	-81	-2.2	+183	65
	PRIME polynomial	-82	+0.1	+191	66

The local C_a algorithms were based on the whole PRIME data set. All three forms had mean errors near zero as the same data were used for their derivation and subsequent testing. The standard deviation of the error from the local logarithmic algorithm was greater than the global logarithmic algorithm. This implies that the logarithmic formulation was not well suited to describing the form of the relationship between R(443:555) and C_a in the north-western Atlantic Ocean, irrespective of the amount of data used to constrain it. The local polynomial algorithm error had a standard deviation very similar to that of the global polynomial algorithm; given that this algorithm had 5 fitted parameters and has been fitted to only 13 data points, the lack of a significant reduction of error implies that the NASA SeaWiFS post-launch global algorithm was close to the best performance which could be expected from this form of algorithm. The performance of the SeaWiFS CZCS-type hyperbolic algorithm improved considerably when local parameters were used instead of global values. This could be because the algorithm was developed from measurements in regions which are significantly different in terms of phytoplankton pigment composition than existed during PRIME and implied that the average accuracy could be further improved using more *in situ* data.

The local algorithms were not significantly more precise than the global algorithms; the proportion of the variance explained does not change by more than 1% between the global and local forms. The errors could arise either from fundamental limitations of the technique or random errors in data collection or processing. Total optical measurement error was estimated to be less than 10% as discussed earlier in this paper. HPLC measurements of pigment concentration at PML, using an internal standard, were estimated to be in error by less than 5%. The time lag between the radiometer and CTD deployments will give errors in algorithm performance if the phytoplankton is patchy. Data in Fig. 4 show the stability of the bio-optical structure of the water during the 8-day Lagrangian time series study and suggest that it is unlikely that patchiness on small time scales could account for the large differences in the algorithm performances observed. Data quality can be considered to be good within ±15%, and errors between measured and retrieved pigment concentrations beyond this will arise as a result of the variability of the relationship between C_a and both R(443:555) and R(490:555). The standard deviation of the error in C_a estimated by the local algorithms was about 66% (Table 5).

With 95% confidence we can state that the actual value lies within an interval of ±2 standard deviations from the mean; here, this is ±132% of the estimate, of which about ±117% results from fundamental limitations of two-band ratio algorithms.

In conclusion, there is scope to improve the average accuracy of C_a estimates using local two-band ratio algorithms, but natural variability could still lead to errors of more than ±100% of the estimate. This lack of precision should be considered carefully when data from remote measurements of ocean colour are used. The use of more spectral bands, either in semi-empirical three-band ratio algorithms or using spectral inversion techniques, may improve retrieval precision.

ACKNOWLEDGEMENTS

This work forms part of the Centre for Coastal and Marine Sciences, Plymouth Marine Laboratory Strategic Research Project 1 and was funded by the Natural Environment Research Council under the PRIME Special Topic project P20. This paper is PRIME contribution 52. A. G. Westbrook and M. H. Pinkerton were funded under the SeaWiFS Exploitation Initiative (SEI). The constructive assistance of the reviewers is also gratefully acknowledged.

REFERENCES

Aiken, J., Moore, G.F. and Holligan, P.M. (1992) Remote sensing of ocean biology in relation to global climate change. *Journal of Phycology*, **28**, 579-590.

Aiken, J., Moore, G.F., Trees, C.C., Hooker, S.B. and Clark, D.K. (1995) The SeaWiFS CZCS-Type pigment algorithm. *NASA Technical Memorandum 104566*, Volume 29, Hooker S.B. and Firestone E.R., Eds., NASA Goddard Space Flight Centre, Greenbelt, Maryland, 43 pp.

Austin, R.W. and Petzold, T.J. (1981) The determination of the diffuse attenuation coefficient of sea water using the Coastal Zone Color Scanner. In: *Oceanography from Space*, J.F.R. Gower, Ed. Marine Science Volume 13, Proceedings of the COSPAR/SCOR/IUCRM symposium. Plenum Press, New York, 239-256.

Buiteveld, H., Hakvoort, J.H.M. and Donze, M. (1994) The optical properties of pure water. *Journal of International Society of Optical Engineers* (SPIE) Volume 2258 Ocean Optics XII, 174-184.

Clark, D.K. (1981) Phytoplankton pigment algorithms for the NIMBUS-7 CZCS. In: *Oceanography from Space*, J.F.R. Gower, Ed. Marine Science Volume 13, Proceedings of the COSPAR/SCOR/IUCRM symposium. Plenum Press, New York, 227-237.

Esaias, W., Feldman, G., McClain, C. and Elrod, J.A. (1986) Satellite observations of oceanic primary productivity. *Earth Observing System*, **67**, 835-837.

Feldman, G.C. (1989) Ocean colour: availability of the global data set. *Earth Observing System*, **70**, 634-641.

Gordon, H.R. and Clark, D.K. (1980) Remote sensing optical properties of a stratified ocean: an improved interpretation. *Applied Optics*, **19**, 3428-3430.

Hooker, S.B., Esaias, W.E., Feldman, G.C., Gregg, W.W. and McClain, C.R. (1992) An Overview of SeaWiFS and Ocean Colour. *NASA Technical memorandum 194566*,

Volume 1, S.B. Hooker and E.R. Firestone, Eds., NASA Goddard Space Flight Centre, Greenbelt, Maryland, 24 pp.

Kraus, W. and Kase, R.H. (1984) Mean circulation and eddy kinetic energy in the eastern North Atlantic. *Journal of Geophysical Research*, **94** (C3), 3201-3210.

Moore, G.F , Aiken, J., Hooker, S.B. and Rees, N.W. (1997) Remote sensing of bio-optical provinces, Proceedings of the Remote Sensing Society, RSS 97, Reading, UK.

Morel, A. and Berthon, J.-F. (1989) Surface pigments, algal biomass profiles and potential production of the euphotic layer: Relationships re-investigated in view of remote-sensing applications. *Limnology and Oceanography.*, **34** (8), 1545-1562.

Mueller, J.L. and Trees, C. C. (1995) Revised SeaWiFS pre-launch algorithm for the diffuse attenuation coefficient K(490). CHORS Technical Memorandum 006-96. Center for Hydro-Optics and Remote Sensing, San Diego State University, San Diego, Ca 92120-5005.

Mueller, J.L. and Austin, R.W. (1995) Ocean optics protocols for SeaWiFS validation, Revision 1. *NASA Technical memorandum 104566*, Volume 25, S.B. Hooker and E.R. Firestone, Eds., NASA Goddard Space Flight Centre, Greenbelt, Maryland, 66 pp.

Neckel, H. and Labs, D. (1984) The solar radiation between 3,300 and 12,500 Å. *Solar Physics*, **90**, 205-258.

Pilgrim, D.A. and Aiken, J. (1989) Measurement of the optical diffuse attenuation coefficient. *The Hydrographic Journal*, **54**, 23-27.

Pollard, R.T. and Pu, S. (1985) Structure and circulation of the upper Atlantic Ocean northeast of the Azores. *Progress in Oceanography*, **14**, 443-462.

Sathyendranath, S., Gouveia, A.D., Shetye, S.R., Ravindran, P. and Platt, T. (1991) Biological control of surface temperature in the Arabian Sea, *Nature* (London), **349**, 54-56.

Smith, R.C. and Baker, K.S. (1978) Optical classification of natural waters. *Limnology and Oceanography*, **23**, 260-267.

Smith R.C. and Baker K.S. (1981) Optical properties of the clearest natural waters (200-800nm). *Applied Optics*, **20** (2), 177-184.

Wade, I.P. and Heywood, K.J. (1999) Acoustic backscatter observations of zooplankton abundance and behaviour and the influence of oceanic fronts in the Northeast Atlantic. *This volume.*

Wright, S.W., Jeffrey S.W., Mantoura, R.F.C., Llewellyn, C.A., Bjornland, T., Repeta, D. and Welschmeyer, N. (1991) Improved HPLC method for the analysis of chlorophylls and carotenoids from marine phytoplankton. *Marine Ecology Progress Series*, **77**, 183-196.

Yoder J.A., Esaias W.E., Feldman G.C. and McClain C.R. (1988) Satellite Ocean Colour-status report. *Oceanography*, **1**, 18-35.

Zaneveld, J.R.V., Kitchen, J.C. and Mueller, J.L. (1993) Vertical structure of productivity and its vertical integration as derived from remotely sensed observations. *Limnology and Oceanography*, **38** (7), 1384-1393.